Glass Poly-Vinyl-Phosphonate Cements with Reactive Aluminium Hydroxide Coated Sub-micron Anatase Filler

Paul Alexander Brookbank

June 30th, 2011

Submitted by Paul Brookbank, to the University of Exeter as a thesis for the degree of Doctor of Philosophy in Engineering, June 2011.

This thesis is available for library use on the understanding that it is copyright material and that no quotation from the thesis may be published without proper acknowledgement.

I certify that all material in this thesis which is not my own work has been identified and that no material has previously been submitted and approved for the award of a degree by this or any other University

(Paul Alexander Brookbank)

Abstract

The current generation of Glass Ionomer Cements (GICs) have many advantageous properties over other dental restorative materials but lack the compressive strength of these other materials. The aim of this project is to increase the compressive strength of conventional Glass Poly-Vinyl-Phosphonate cement by inclusion of reactive sub-micron filler particles.

The setting characteristics, chemical reactivity and cement strength have been found using oscillating rheology, infrared spectrometry, nuclear magnetic spectrometry, transmission electron microscopy, potentiometer analysis, laser diffractometry and mechanical analysis.

The addition of sub-micron filler particles in direct weight by weight replacement of aluminosilicate glass of a control material has increased the ultimate compressive strength of the new cement from 206MPa (control) to 250MPa after 365 days of aging. The strength of the new filler enhanced cements were comparable with the control material after 3 hours. The setting chemistry of the filler enhanced cements follows the same order as the control cement but at a decelerated rate.

Theoretical modelling found that a large volume of sub-micron filler could fit into interstitial spacing in formed cement however the alteration of the aluminosilicate glass to polyelectrolyte ratio has been found to drastically alter the cement setting time.
The use of cubic and polyhedral shaped filler particles as supposed to spherical particles may increase the cement strength further as greater packing densities are achieved.

The formulation of a Glass Ionomer Cement with increased compressive strength may find use as a posterior restorative or as a better material for restoration of lesions and cavity liners.

Acknowledgments

I would like to express my gratitude to my supervisors Dr Oana Ghita, Dr Michele Barbour and Professor Ken Evans for firstly giving me the opportunity to undertake this research and their continued support and guidance during this research project.

This research has been funded by the Great Western Research fund and Associated Dental Products (Kemdent, Swindon). I would like to thank Tony Cook of Kemdent for his knowledge of quality control for water based dental cements and providing me with materials to perform my research.

A special thank you is extended to Mr Ian Moon and Mr Peter Jerry for their skill, hard work and technical guidance provided when producing parts and supervising myself in the workshop environment; their tuition has evolved into a firm friendship.

My love goes to my partner Ailichia and daughter Lilly for all their unwavering encouragement, motivation and patients without which, none of this would have been possible.

Content

List of Tables

List of Figures

List of Abbreviations

Al – Aluminium

$Al(OH)_3$ – Aluminium Hydroxide

Al_2O_3 – Aluminium Oxide

ASG – Aluminosilicate Glass

Asym – Asymmetrical

$BaSO_4$ – Barium Sulphate

BF – Bright Field (Specific Reference to TEM)

BO – Bonding Oxygen

$C_5O_4H_4$ – Acrylic Acid Monomer

Ca – Calcium

CaO – Calcium Oxide

CaOH – Calcium Hydroxide

DC – Diamond Carve

FE – Field Emission

GIC – Glass Ionomer Cement

h – Hour

HAAF – High Angle Annular Dark-Field (Specific Reference to TEM)

IR – Infrared Spectroscopy

MAD – Mean Absolute Deviation

Min – Minute

NBO – Non-bonding Oxygen

NMR – Nuclear Magnetic Resonance

P – Phosphorus

PAA – Polyacrylic Acid

P:L – Powder to Liquid Ratio

s – Second

$\hat{S}$ – Estimate of Variance

SEM – Scanning Electron Microscopy

Sr – Strontium

SRO – Strontium Oxide

SS – Solid State

Sym – Symmetrical

TA – Tartaric Acid

TEM – Transmission Electron Microscopy

TiGIC – Titanium Dioxide Incorporated Glass Ionomer Cements

TiO_2 – Titanium Dioxide

χ_i – *i* th Term in the Data Set χ

χ_0 – Suspected Outlier Value

$Y_2(SO_4)_3$ – Yttrium Sulphate

σ_C – Compressive Strength (Maximum Achieved Stress per Unit Area)

Chapter 1

Introduction

The aim of this research project is to develop a new type of glass polyalkenoate cement (GIC) based on conventional glass poly-vinyl-phosphonate cement with the addition of reactive filler particles. The filler particles are based on titanium dioxide (TiO_2) and coated in a reactive metal hydroxide layer believed to help their incorporation into the polymer matrix (Figure 1.1).

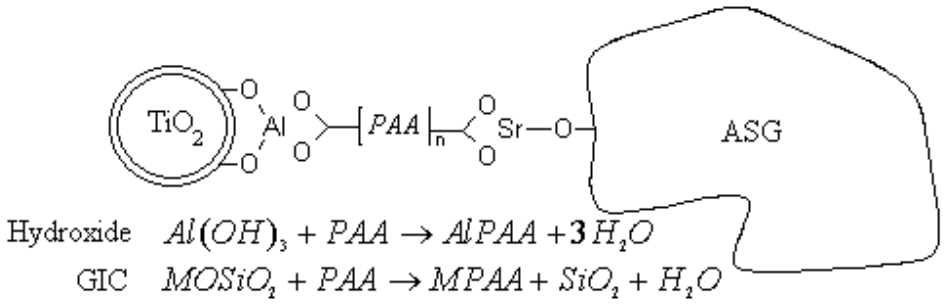

Figure 1.1: Proposed Mechanism for Al(OH)3 Coated Filler Incorporation into A Conventional GIC (M is a Metal Ion and PAA is Polyacrylic Acid)

Conventional glass polyalkenoate cements are already accepted, and widely used within clinical dentistry and have now begun to find a range of applications outside of dentistry which exploit their good biocompatibility. These include artificial ear ossicles, bone substitute plates, and more recently, as a cement for fixation of cochlear implants and for sealing defects in the skull (Gu *et al*, 2005). GICs are becoming more important outside of clinical dentistry and will continue to become increasingly important for years ahead (Gu *et al*, 2005).

Recent attempts to improve the physical properties of GICs for tooth restoration have focused on the combination of composite resin (polymerisation) technology with GIC acid – base (chemical salt formation) technology, often resulting in the deterioration of mechanical properties (*see* Chapter 2).

Chapter 1: *Introduction*

The addition of a reactive filler is believed to enhance the physical properties: by enhancing the mixing (mechanical lubrication), increasing compressive strength due to increased packing and enhanced chemical bonding (Gorman & Hill, 2003) and reducing the film thickness size for use as a luting cement. All without disrupting the properties of the original cement (i.e. chemical bonding to tooth & fluoride release / recharge).

This research focuses on a selection of new cement compositions classified as reinforced glass polyalkenoate cements (RGIC).
Several techniques have been employed to study the cements. Particle size analysis (*see* Chapter 3) was performed as the size of the particles taking place in the acid – base reaction are known to influence the handling and setting properties of the cement (Wilson & Nicholson, 1993).
Oscillating rheology (*see* Chapter 4) using traditional (Wilson) and modern equipment was used to define and improve the working / setting times and short term (< 60 min) strength increase of cements. These are of particular interest to dental professionals.
The compressive strength (*see* Chapter 5) was calculated using a universal testing machine at chronological increments to find mid- to long-term (ultimate) strength, important when classifying the restoration material.
Transmission electron microscopy and potentiometric titrations have been performed to identify reactive material and estimate reactivity thereof (*see* Chapter 3).
Mid-infrared (IR) (*see* Chapter 6) and solid state nuclear magnetic resonance (NMR) (*see* Chapter 7) spectroscopy were used to study the chemical reactions taking place during the early setting (0-24 hours) stages.
A theoretical model has been developed (*see* Chapter 8) to aid the explanations of experimental results and suggest an optimum cement formulation.

The data from each technique is presented in separate chapters, in which the results for the various cement compositions are compared, discussed, and where relevant – related to previous literature. The results from each technique are later drawn together to form a short discussion (Chapter 9). Finally, areas for further related research are suggested.

Chapter 2

Literature Review

Aim

The aim of this chapter is to report and discuss all literature relevant to the current research project.

2.1 Introduction

This literature review describes the main aesthetic dental restoratives materials currently in common use. Their composition, development, advantages and disadvantages are discussed in order to show the need for ongoing dental material research.

A full account of the development, physical properties and setting mechanism of Glass Ionomer Cements (GICs) is given as this material has been used as the starting point for the research in this thesis.

A major component of the new dental cements in this research is the incorporation of reactive coatings on inert filler materials. The results of previous attempts to enhance the physical properties of Glass Ionomer Cements by filler incorporation are discussed.

A description of human teeth, their associated health problems and use of restorative materials with relation to tooth degradation is not given as comprehensive literature is available elsewhere (Simmelink, 1994; Van Noort, 1994; Ten Cate, 1994; Jones, 1995; Smith, 1998; Holt *et al*, 2000; Jones, 2001; Grippo *et al*, 2004).

2.2 Dental Restorative Cements

Ideally, a dental restorative cement should fulfil the following criteria (Nicholson & Anstice, 1999):

a. Easy mixing and placement as an unset paste
b. Convenient working times but short setting times
c. Rapid development of mechanical properties
d. High strength (tensile and compressive)
e. Match of the thermal expansion properties with original tooth
f. Good adhesion to tooth structures with minimal cavity preparation
g. Low polymerisation shrinkage
h. No taste
i. Dimensional stability
j. Optimum levels of fluoride release
k. High resistance to effects of saliva, food/drink, brushing and flossing
l. Biologically inert but preferably bioactive
m. Match of colour and translucency with original tooth
n. Colour stability
o. Low cost
p. Long shelf life

There are many qualities that dental restorative cements should posses and although there are currently several acceptable types of white dental cements available, none are perfect as none satisfy all the above listed criteria. Therefore, it is necessary for ongoing research and development to improve existing materials with an aim to ascertain all the qualities listed above.

The four main types of 'white' filling materials currently in use are: glass ionomer cements (GICs), composite resins (CRs), resin modified glass ionomer cements (RMGICs) and polyacid modified composite resins (PMCRs or compomer).
The general composition, chemistry, developments and advantages/disadvantages of these filling materials will be discussed with particular emphasis on GICs as they are most relevant to this research.

2.2.1 Glass Polyalkenoate Cements (Glass Ionomer Cements)

Glass ionomer cements have literature present from 1968 to 2010 (Wilson, 1968; Coughian, 2010; Li *et al*, 2010) which covers every aspect of their chemistry, physical properties and modifications made from the conventional cement.

This section will focus on the structure and chemistry of conventional GICs. The structure of the glass and polyelectrolyte as well as the addition or modification of the conventional GIC formulation by filler addition / modification will also be included.

A brief description of how the GIC system works is given in Equation 1,

$$MOSiO_2 + H_2A \rightarrow MA + SiO_2 + H_2O \qquad \text{Equation 1}$$

where M represents the cement-forming cation from ASG and A the cement-forming anion from cement forming liquid. The cement-forming reaction is one where hydrogen bridges in the liquid phase are progressively replaced by more rigid metal ion bridges, a process which causes the liquid to gel and the gel to harden (Wilson, 1978).

2.2.1.1 A Brief History

GIC's were first created in 1965 when Alan Wilson, Brian Kent and Brian Lewis where commissioned by the Laboratory of the Government Chemist to investigate the structure and properties of dental silicate cements.

Wilson's initial investigation showed that aluminium and calcium phosphates may form part of the silicate cement matrix and it was not solely due to the formation of a silica gel as was previously believed (Skinner & Phillips, 1960). The knowledge that phosphate might play a role in the setting reaction of the dental silicate cement suggested that replacing phosphoric acid with a less reactive, chelating acid might lead to the improvement of the silicate cements properties (Wilson, 1968).

Wilson prepared a range of cements using the aluminosilicate glass powder from the existing silicate cements and mixed them with tartaric, pyruvic, tannic, fluoboric, glycerol phosphoric and tetraphosphoric acids in 35 to 50% solutions. All the chelating acids formed cements within 2 to 8 minutes showing that cements could be formed with multifunctional hydrogen bonded acid. Regrettably none of the cements formed were hydrolytically stable and when stored in water degradation or total disintegration occurred (Wilson, 1968).

The investigation into alternative liquid cement formers also included a 25% solution of polyacrylic acid (PAA) which unlike the other acids in the study formed a cement that had little or no working time with a slow increase in viscosity to an indefinite setting point but, when left to harden for 24 hours it proved to be hydrolytically stable (Wilson, 1968).

In 1968 Wilson & Kent resumed the study of alternative cement formers as a new laboratory with the facilities to make aluminosilicate glasses had just been completed (Wilson, 1996) enabling the two to make aluminosilicate glasses with varying reactivity's to suit the chosen chelating acid.

Brian Kent was the first to find that the aluminium to silica ratio of the glass was the key to controlling the reactivity of the calcium aluminosilicate glass. The normal ratio was 0.5 but a more reactive glass was needed to form a cement with the relatively weak PAA so ratios upwards of 0.57 were used.

The decision was made to use more concentrated solutions of PAA (40% to 50%) based on the work of Smith (1968) who had shown that increased concentrations of PAA were needed to form satisfactory cements.

The more reactive aluminosilicate glass and the increased concentration of PAA formed a cement that set in under 5 minutes which sparked interest from the British technology group and led to a patent (Wilson & Kent, 1969) being filed.

2.2.1.2 Chemical Environments in Aluminosilicate Glass (ASG)

Aluminosilicate glass is a general term used for a range of glasses that contain alumina and silica. The glass used throughout this study is a fluro- strontium- phosphorus-aluminosilicate because its dominant constituents are silica (SiO_2 – 42.63%), alumina (Al_2O_3 – 27.84%), phosphorous (P_4O_{10} – 6.39%) and fluorine (from the fluorides SrF_2, CaF_2, NaF and $AlPO_4$ – 6.79%) (Fennell *et al*, 1998).

The structure of aluminosilicate glasses and similar glasses have undergone extensive study to understand the aluminium, oxygen, silicon, phosphorus, calcium/strontium/sodium and fluoride environments within reacted & un-reacted glasses (Sourial *et al*, 1999; Stebbins & Zeng, 2000; Stebbins *et al*, 2000; Takaishi *et al*, 2000; Sakida *et al*, 2001; Youngman & Dejneka, 2002; Singh *et al*, 2002; Kiczenski *et al*, 2004; Poirier, 2005; Venkataraman & Varma, 2006; Matsuya *et al*, 2007; Mountjoy, 2007).

The formulation of ASG controls the chemical and mechanical properties of conventional GICs. It is important to fully understand the constituent parts and the role they play in the glass/cement.

The most fundamental description of the aluminosilicate glass used in GICs was given by Kent *et al* in 1979. They describe the aluminosilicate glass as a three-dimensional, random network of SiO_4 and AlO_4 tetrahedra that are linked only at the vertices, and each vertex is shared by two tetrahedra coordinated to a cation, this has the effect of minimising the electrostatic repulsion at oxygen sites (Figure 2.1) within the glass network.

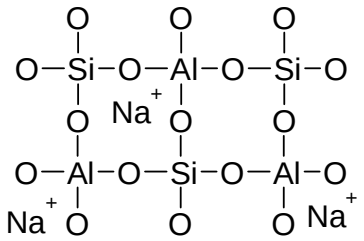

Figure 2.1: Example of a Sodium Aluminosilicate Glass, Al2O3:SiO2 = 1 (Wilson & Nicholson, 1993)

The ions present in aluminosilicate glass each perform a different role within the glass structure giving the glass its characteristics. Each ion is therefore discussed separately in order to fully understand their importance.

2.2.1.2.1 Silica (^{29}Si)

Silica is a tetravalent ion (Si^{4+}) that forms a quartz glass network when SiO_2 is heated to form a magma (≈2000ºC) then shock cooled by immersion in water. Quartz is unreactive therefore network modifying cations such as aluminium, calcium and strontium are added to the glass melt in order to stress the silica structure. The addition of network modifiers permits acid hydrolysis of the glass. Silica is the network former within aluminosilicate glasses.

Silica has been shown to occupy a tetrahedral shape within different fluoro-aluminosilicate glasses (Dupree *et al*, 1989; Matsuya *et al*, 1996; Griffin & Hill, 2000; Stamboulis *et al*, 2004; Hill *et al*, 2006; Stamboulis *et al*, 2006; Kelsey *et al*, 2008; Zainuddina *et al*, 2008). Silica can have multiple network arrangements within the glass network consisting mostly of bridging (bonding) oxygens with a lower concentration of non-bridging oxygens (Figure 2.2) dependent on the individual glass composition.

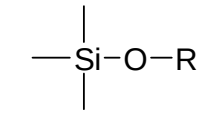

Bridging Oxygen

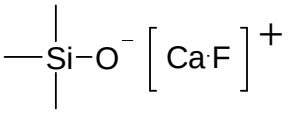

Non-Bridging Oxygen

Figure 2.2: Bridging and Non-Bridging Oxygen's (R – Al or Si) (Stebbins & Xu, 1997)

2.2.1.2.2 Aluminium (^{27}Al)

Aluminium is a trivalent ion so it generally forms compounds where it is coordinated by three other ligands but when it is added to the glassy melt it is able to replace Si in the quartz matrix, this is because it is small enough to replace Si isomorphically. For Al to form part of the glass, which is a tetrahedral network it too must take on a tetrahedral configuration which means that it is coordinated by four oxygen atom causing it to exceed its valence and possesses an overall negative charge (Nicholson, 1998; Cody *et al*, 2001; Mysen & Cody, 2001; Hill *et al*, 2004; Pires *et al*, 2004; Criscenti *et al*, 2005; Matsuya *et al*, 2007). The net negative charge must be balanced out otherwise it is not energetically favourable for Al to take on a tetrahedral configuration; the negative charge is counterbalanced by a modifying cation, typically calcium or sodium (Figure 2.3).

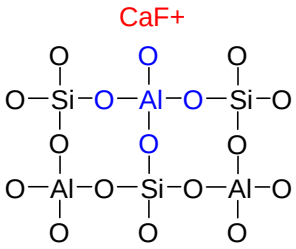

Figure 2.3: Structure of fluoro-aluminosilicate glass

Stebbins et al (2001), Stamboulis *et al* (2004), Hill *et al* (2006) and Matsuya *et al* (2007) have identified the formation of high energy, five and six fold, aluminium species (Al-F-Ca/Sr/$Na_{(n)}$) that occur naturally in low concentrations within ASGs (Figure 2.4).
Al (V) and Al (VI) can also be caused by the glass not containing enough network modifying cations to maintain aluminium in the IV state and can occur when the glass melt has been incorrectly formulated or as a result of excess fluorine and phosphate content which leads to the complexing of sodium, calcium and strontium in the form CaF^+ etc (Stebbins *et al*, 2001).

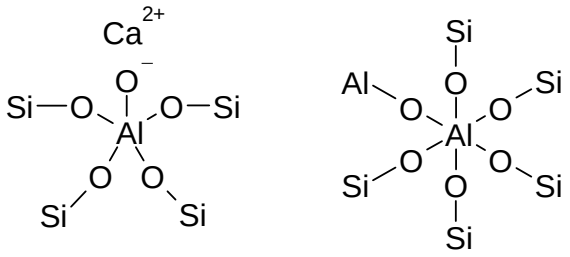

Figure 2.4: Example V and VI Coordination of Aluminium

Lee & Stebbins (2000), Hill *et al* (2006), Matsuya *et al* (2007) and Kelsey *et al*, 2008 have all confirmed the existence of high energy Al-O-Al bonds present in aluminosilicate glasses. Lee & Stebbins (2000) noticed that the field strength of the modifying ions have a pronounced effect on the concentration of aluminium rich phases dispersed throughout the glass, their NMR study used lithium (Li – high field strength) and sodium (Na – low field strength) to demonstrate these findings. Only high field ions can stabilise the highly reactive Al-O-Al bond because of the high charge density they carry.

2.2.1.2.3 Oxygen (^{18}O)

Oxygen has the highest concentration in any aluminiosilicate glass and the studies of Stebbins & Xu (1997), Stebbing *et al* (2001) and Mountjoy (2007) suggest that it might have the most complex chemistry of the glass. Oxygen either occupies Bridging (BO) or non-bridging (NBO) sites (Figure 2.2). BOs bridge two AlO_4 or SiO_4 tetrahedra providing a strong, long lived covalent bond that connects the smallest structural units throughout the aluminosilicate network. NBOs form a weak ionic bond between either an Al or Si tetrahedra with one or more modifier cation such as sodium or calcium therefore connecting the network dweller to the aluminosilicate network.

2.2.1.2.4 Phosphorus (^{31}P)

Introduction of phosphorus in the form of a phosphate into the ASG network introduces multiple structural possibilities dependent on the quantity of phosphate introduced (Cody *et al*, 2001). Hill *et al* (2006) and Matsuya *et al* (2007) have both found evidence that phosphorus charge-balances discrepancies in the network caused by the addition of aluminium; it also preferentially binds to non-bridging oxygens in the glass network forming Al-O-P bonds. Dollase *et al* (1989), Stamboulis *et al* (2004), Stamboulis *et al* (2006), Hill *et al* (2006) and Matsuya *et al* (2007) have found evidence of the existence of Al-O-PO_3. Disagreement has been voiced between Dollase & Stamboulis and Hill & Matsuya over the existence of further Al-O-P or Si-O-P bonds with the same phosphate group. The results of Hill *et al* (2006) and Matsuya *et al* (2007) showed that the addition of phosphate to aluminosilicate glasses cause the quartz network to re-polymerise, whereas Dollase *et al* (1989) and Stamboulis *et al* (2004/2006) found that a aluminium pyrophosphate is formed with a single phosphorus atom surrounded by up to 3 Al-O- bonds (NMR study).

Phosphorus was found to enter an aluminosilicate glass as a network modifier preferentially Matsuya *et al* (2007) also found that the addition of fluoride caused an increase in Al-O-P linkages which strongly agrees with the work of Stebbins & Zeng (2000), Lee & Stebbins (2000) and Hill *et al* (2006) where they found that the addition of fluoride increases the amount of NBO's

2.2.1.2.5 Network Dwelling Ions (Na, Li, Ca, Sr)

Network dwelling (or network modifying) ions' primary role is to facilitate the substitution of Al in place of a Si in the formation of aluminosilicate glass'. The size and charge density of network dwelling ions needs to be considered when formulating dental ASGs. Alkaline earth metals have a large atomic radius and relative charge density compared with alkaline metals therefore favour negative charge concentrations. The inclusion of alkaline earth metals has been reported to induce aluminium dense areas (in the form Al-O-Al) and excessive formation of NBOs when compared with alkaline metals (Stebbins & Xu, 1997; Lee & Stebbins, 2000).

Modern ASG contain strontium as a modifier cation, strontium replaces calcium in ASG and has the benefit of being radiopaque so when x-rays are performed on a patient with a filling of this type the filling margins can be seen in the x-ray and distinguished from healthy and carious tooth tissue (Van Noort, 1994).

Lee & Stebbins (2000) found that substituting strontium for calcium in ASG has virtually no effect on the ensuing structure of the glass, this is because the formation of Al–F–Sr species are favoured at the expense of F–Metal species. Hill *et al* (2006) found that the addition of strontium to the glass progressively causes an increase in Ca-F.
Matsuya *et al* (2007) suggested that fluoride associates with calcium to form CaF_2 but preferentially tries to be associated with both calcium and aluminium to form Al–F–Ca species. If Hill *et al* (2006) and Matsuya *et al* (2007) are both correct then strontium increases the formation of Al-F-Ca species present and lowers the extent of NBO contrary to the belief of Lee & Stebbins (2000).

2.2.1.2.6 Fluoride (^{19}F)

Fluoride was originally added to the glass melt to reduce melting temperature and decrease viscosity to help handling of the molten glass (Nicholson, 1998).

Stebbins & Zeng (2000), Lee & Stebbins (2000), Hill *et al* (2006), Matsuya *et al* (2007) all found evidence of the existence of F–Ca, Al–F–Ca, Al–F–Na, F–Sr, Al–F–Sr, AlO_3F, AlF_3 species formed in ASG using ^{19}F MAS-NMR. The formation of calcium fluoride was found to increase proportionally with increasing fluoride content. Partially complexed calcium, CaF^+, is still available to charge balance Si-O-Al bonds and NBO's.

Hill *et al* (2006) found that increasing fluoride content increased the proportion of Al-F-M (M = Modifier cation) and lowered the amount of NBOs because it consumes the modifier ions and stops them stabilising NBO groups.
Hill *et al* (2006) also found evidence that fluorine forms complexes with modifier cations of highest charge to size ratio preferentially.

2.2.1.2.7 Example of a Aluminosilicate Glass

It is possible to envisage a generalised ASG based on the information about the individual environments of network formers and the effects of increasing network dwelling ions.

The structure is predominantly made of an Al-O-Si backbone with the occasional NBO (-Si-O^- Ca^{2+}) which is stabilised by a network modifying cation (Na, Ca, Li…etc) which can include pentavalent and hexavalent aluminium (Hill *et al*, 2006).
The addition of fluorine to the glass increases the amount of 5- and 6- coordinate aluminium, reduces the amount of NBO and encourages the formation of Al-F-M species. The observed concentration of pentavalent and hexavalent aluminium in charge-balanced glasses are not high enough to compensate for the amount of NBO observed so the formation of oxygen tri-clusters where oxygen is either bonded to three aluminium ions (Figure 2.5) or a mixture between silicon and aluminium.
Increased modifier concentrations leads to the formation of NBO in order to satisfy the modifier ions coordination. In these cases it appears that the distortion of SiO_4 tetrahedra is preferable to the under-co-ordination of modifiers (Matsuya *et al*, 2007).

The composition and structure of the aluminosilicate glass used to form glass ionomer cements is critical to cement formation and eventual properties.
Kent and Wilson originally identified that the Al:Si ratio of the glass was critical in determining the reactivity of the glass and subsequent cement properties but Hill *et al* (2006) have identified that in modern, more complex glasses containing fluorine and phosphate the Al:Si ratio is much less important.

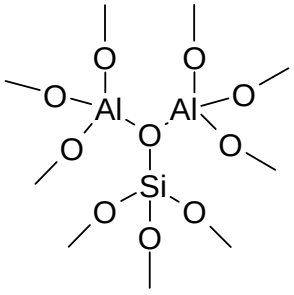

Figure 2.5: Aluminium Tri-cluster

2.2.1.3 Matrix-Forming Polyacids

The nomenclature used throughout academic reports including this thesis can sometimes be confusing when describing the acid(s) used in conjunction with basic aluminosilicate glass to form a GIC. This is because of the multiple ways in which the acids (e.g. polyacrylic acid, PAA) can be described. These acids are either described by their specific nature as alkenoic, (hence the name polyalkenoic cement) or by a more understandable, but still general, description such as polycarboxylic acid or polyelectrolyte solution. The use of 'liquid' is also frequent in discussion where it is used to describe the acidic liquid solution that is mixed with basic glass powder to form a GIC. The use of alkenoic acid, although the most precise description, is seldom used throughout this thesis because it has become somewhat rare and archaic in the literature and might therefore be unfamiliar to likely readers, whereas polycarboxylic acid (polyacid), polyelectrolyte solution and liquid are in common use and are therefore adopted here by convention.

Three types of polycarboxylic acids are commonly used in GICs either as homogeneous polymers or co-polymers where the two acid monomers (Figure 2.6) are polymerised together. Polyacrylic acid is always present in GICs as either a homo- or co- polymer (Wilson & Kent, 1969; Wilson & Nicholson, 1993; Coughian, 2010). There is a linear relationship between the physical strength of a GIC and the polyacid concentration however increasing the ionic strength deteriorates handling properties (Wilson *et al*, 1989; Wilson & Nichols, 1993). The strength of the polyacid is determined by the number of carboxylic acid groups present on the monomer. This is why co-polymers of maleic, and more recently, (vinyl)phosphonic acid (PAA-PVPA) have been introduced during the development of the GIC.

Diamond Carve GIC, the GIC used as the starting point for the experimental work described in this thesis, contains a small amount of PAA-PVPA co-polymer (1.25% PAA-PVPA when compared to PAA content)to produce a hydrolytically more stable cement (Ellis *et al*, 1991; Nicholson, 1998), reduce early water solubility (Smith, 1998), improve translucency (Smith, 1998) and overall mechanical performance because of the polymers high molecular weight (Ellis *et al*, 1991; Nicholson, 1998).

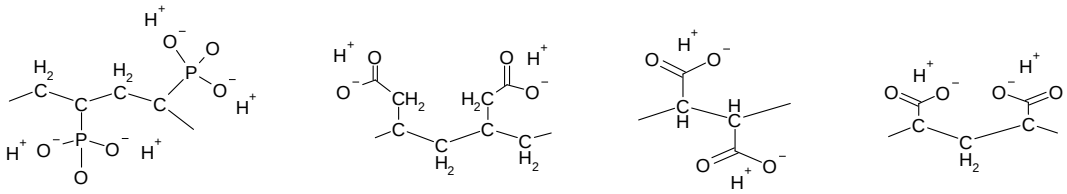

Figure 2.6: Vinyl Phosphonic Acid, Itaconic Acid, Maleic Acid and Acrylic Acid

Increasing the molecular weight (polymer length) has been found to increase the mechanical performance of GICs (Wilson *et al*, 1989; Ellis *et al*, 1991; Nicholson, 1998). Increasing the molecular weight of the polyacid was found to have a pronounced influence on the setting rate, acid erosion rate, toughness, fracture toughness and wear resistance (Wilson *et al*, 1989). The molecular weight affects the viscosity of the polyacid and therefore the handling characteristics of the cement. It is therefore important to get a good balance between concentration, molecular weight, and viscosity (Wilson *et al*, 1989). The development of water hardening cements has helped to alleviate the effects of having to mix high viscosity liquid with aluminosilicate glass powder (Van Noort, 1994).

Steric hindrance appears to be one of the factors preventing GIC's from reaching their full potential. The polymer chains are initially flexible coils (which could be likened to a slinky spring) that are able to move past each other with limited interaction. However when the pH is raised towards neutrality this forces the coils to expand and become like rigid rods that are unable to move past one another(Balasubramanlan & Mlsra, 1977), this then limits the number of cross-links that can be formed between polymers and carboxyl groups. This is because the cations in solution are unable to move freely due to a hydration shell caused by electrostatic forces which increases their size and the polymer is unable to move because its carbon backbone has become rigid (Wilson & Nicholson, 1993). It is assumed that aluminium will only be able to form two of its three available bonds with carboxyl groups from PAA in a GIC because of these steric effects (Nicholson, 1998).
Itaconic acid was used in an attempt to reduce the steric effects by increasing the distance between carboxylic acid groups and contain the carboxyl group as a side chain that is free to move around; however, these modifications had minimal affects (Nicholson, 1998).

2.2.1.4 Acid-Base Setting Mechanism

The setting reaction has been described by Wilson & Nicholson (1993) as consisting of three phases that overlap one another.

Phase 1: When the powder and liquid are mixed, hydrated protons are formed from the ionisation of the polyacrylic acid in water. These ions attack the surface of the glass particles around the oxygen atoms which causes the release of calcium (Ca^{2+}), strontium (Sr^{2+}), fluoride (F^-), aluminium (Al^{3+}) and possibly phosphate (PO_4^{3-}) ions. The release of these ions results in the formation of a silica-based hydrogel around the involved glass particles (Figure 2.7) (Wilson & Nicholson, 1993; Williams *et al*, 2002; Stamboulis *et al*, 2004).

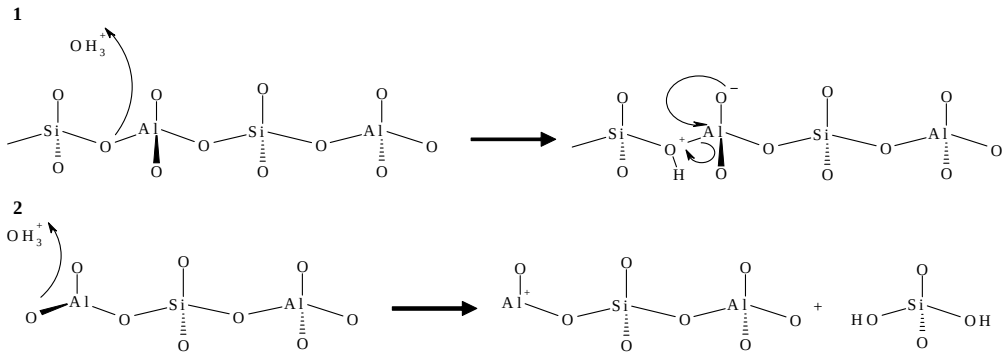

Figure 2.7: The initial stages in the setting reaction of a GIC. The reaction continues until the Al^{3+} ion is release.

Phase 2: In the second phase of the reaction, the Ca^{2+}, Sr^{2+} and Al^{3+} ions migrate from the silica hydrogel into the aqueous cement phase where, as the pH increases, they precipitate out as polysalts (specifically as polycarboxylates). The polycarboxylates ionically crosslink the conjugate acid chain and cause the cement to harden (Figure 2.8) (Wilson & Nicholson, 1993).

The cross-linking mechanism is described as being ionic (Nicholson, 1998; Griffin & Hill, 2000; Culbertson, 2001; Jones *et al*, 2003; Billington *et al*, 2006) however Wilson & Nicholson (1993) believe that there may be some degree of covalency present in the Al-PAA structure due to the high polarising power of the small, highly charged, aluminium ion.

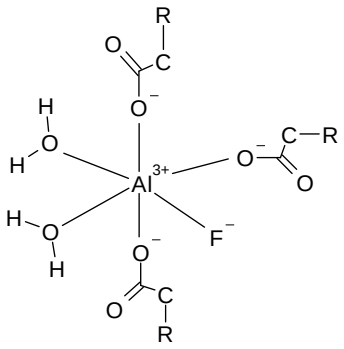

Figure 2.8: Example of Fully Set Glass Ionomer Cement

The order in which calcium / strontium and aluminium is released from the glass network and the form it takes when released is a matter of debate (Nicholson, 1998).

Early infrared studies have shown the formation of calcium / strontium polyacrylate salt (Ca/Sr-PAA) forming earlier than the equivalent aluminium salt (Al-PAA). It is believed that calcium / strontium ions are released first because they are preferentially attacked as they are not covalently bound to the glass structure (Nicholson *et al*, 1988). However, subsequent studies have shown the release of aluminium and calcium / strontium simultaneously (Wasson & Nicholson, 1990; De Maeyer *et al*, 2002*;* Young *et al*, 2004) although aluminium is believed to be initially released in a form which does not readily produce Al-PAA.

The initial setting mechanism (working time) is due to the formation of calcium / strontium polycarboxylates which form over the first five minutes of the reaction (Wilson & Nicholson, 1993). During the first 24 hours of cement maturation the relatively unstable calcium / strontium polycarboxylate is replaced with aluminium polycarboxylate because a stronger, more stable, bond is formed (Wilson & Nicholson, 1993; Nicholson, 1998).

The role of the fluoride ions initially released from the glass in the setting mechanism is not fully understood (Nicholson, 1998). Its been suggested that fluoride ions form soluble complexes with aluminium such as AlF^{2+} and Al_2^{+}, which may prevent the premature gelation of the polyanions with aluminium (Wilson *et al*, 1976; Wilson & Nicholson, 1993; Nicholson, 1998). Another possibility is that fluoride ions bind to the carboxylic acid groups via strong hydrogen bonds (Nicholson, 1998). In the final cement, it seems to be accepted that the fluoride ions coordinate to the cross-linked metal ions, thus maintaining the charge neutrality of the system (Figure 2.8) (Wilson *et al*, 1974; Prosser *et al*, 1982; Culbertson, 2001).

Phase 3: A slow hydration of both the silica-based hydrogel (Figure 2.9) and the polycarboxylates (Figure 2.8) occurs which results in a further improvement in the cement's physical properties; this phase of the reaction may continue for several months (Wilson & Nicholson, 1993).

A secondary hydrated silica (phosphorus) structure (resulting from secondary GIC reactions) has been reported to form in the cement matrix increasing mechanical properties over time (Wasson & Nicholson, 1993; Matsuya *et al*, 1996) although this is not generally accepted (Tomlinson, 2007).

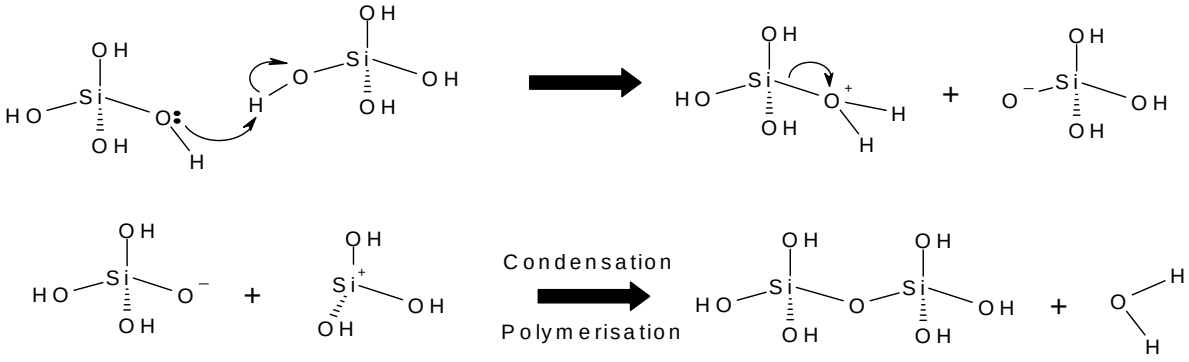

Figure 2.9: Rebuilding of the Silicon Glass Network

Water is essential for the acid-base reaction to occur as it allows the acid to dissociate. It also enables the various metal cations to entre the liquid phase resulting in the formation of metal cross-links.

Water is known as either ‘bound’ or ‘unbound’ within the GIC system. Unbound water is coordinated as a secondary hydration sheath around the polyacid chains and is able to be removed via evaporation. Bound water is coordinated via its oxygen atom to the metal ions (Figure 2.8) in the polycarboxylate bonds adding stability to the system; this water can not be removed by evaporation (Wilson & Nicholson, 1993; Van Noort, 1994).

The cement strengthens gradually over the period of weeks / months, as the ratio of the cements bound to unbound water increases and as the cement forming cations diffuse through the cement, cross-linking further polyacid chains (Wilson *et al*, 1979; Wilson & Nicholson, 1993; Matsuya *et al*, 1996; Smith, 1998; Nicholson & Anstice, 1999; Culbertson, 2001).

2.2.1.5 Reaction Controlling Additives

Early GICs increased viscosity rapidly after cement activation (mixing) making the mixing and placement of restorations not viable (Wilson & Nicholson, 1993; Wilson, 1996). A great amount of work was performed on finding a suitable multifunctional carboxylic acid that would delay the setting mechanism without altering the physical properties of the cement (e.g. water solubility) (Wilson & Crisp, 1975, 1976, 1980; Wilson *et al*, 1976; Crisp & Wilson, 1976; Crisp *et al*, 1979; Cook, 1982; Prosser *et al*, 1982; Nicholson *et al*, 1988).

Wilson *et al* (1976) and Prosser *et al* (1982) both found that only (+) tartaric acid (TA) (Figure 2.10) had desirable effects including the introduction of a ‘snap set’ property where the cement remained at a lower viscosity than not TA containing cements but then experienced a much more rapid hardening than non TA containing cement which can be imagined as having a linear increase in viscosity over the early stages of reaction. Other desirable effects included increased cement strength and the decrease in the formation of Ca-PAA (Nicholson, 1998).

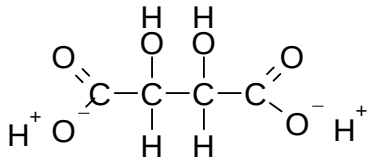

Figure 2.10: Tartaric Acid

The exact way in which (+) TA works within the GIC system is not fully understood, small amounts of TA accelerate the working time where as larger amounts delay the working time. The other multifunctional carboxylic acids (e.g. citric acid) including the isomers of tartaric acid, meso and (-), do not have the same affect as the (+) isomer instead they shorten the working time and elongate the setting time (Nicholson, 1998).

TA is known to react preferentially with ASG compared with PAA because of its increased acidic strength. TA is able to form its metal carboxylate complex at a lower pH than PAA therefore 'capturing' the metal cations that are released initially from the ASG preventing the premature setting reaction between calcium and PAA (Nicholson *et al*, 1988). The increased acidity of TA aids in the breakdown and release of Al from ASG increasing the formation of Al-PAA accelerating the hardening of the cement (Wilson & Nicholson, 1993).

2.2.1.6 GIC Properties

GICs have several advantageous properties which include the relative ease of use, little to no exothermic reaction, low shrinkage when compared with CRs due to the lack of polymerisation (Feilzer *et al*, 1995; De Gee, 1999), low coefficient of thermal expansion, acceptable aesthetic quality, the ability to store and release fluoride and the ability to chemically adhere to dentin and enamel. The latter two advantages are unique to GICs therefore their importance is discussed further.

GICs have the advantage of being able to store and release fluoride; they can be thought of as rechargeable fluoride 'reservoirs'. Fluoride is known to help prevent further tooth decay via a number of mechanisms (Preston *et al*, 1999).

These include the transformation of hydroxyapatite to the harder, more acid-resistant fluorapatite, the enhancement of remineralisation, the disturbance of ionic bonding during pellicle and plaque formation and the inhibition of microbial growth and metabolism, thus reducing the amount of bacterial acid produced (Xu & Burgess, 2003). The majority of fluoride release from the cement occurs in the first 3 days after mixing (Xu & Burgess, 2003). Therefore, the ability of GICs to uptake, store and release fluoride obtainined from other sources such as toothpaste is very beneficial, as this provides long-term protection against tooth decay (Preston *et al*, 1999). Fluoride also seems to improve the compressive strength of GICs (Nicholson, 1998).

GICs have the valuable property of being able to adhere chemically to both dentine and enamel. This is considered extremely advantageous because good adhesion between restoration and tooth minimises marginal leaks, thus reducing the possibility of secondary decay (Tomlinson, 2007). Secondly, adhesive materials are more clinically conservative. This is because the dentists does not need to remove excessive amounts of healthy tissue to create an undercut as is often the case with dental amalgams (Van Noort, 1994) nor is the necessity to perform an acid etch to remove the enamel layer and expose dental tubules which is the case with CRs (Wilson & Nicholson, 1993; Nicholson, 1998). Several mechanisms have been proposed for the adhesion of GICs to tooth structures (Wilson & Nicholson, 1993). It has been suggested that GICs bond to the mineral (hydroxyapatite) phase of the enamel and dentin via the cement forming a chelate with the calcium cations at the surface of the hydroxyapatite (Wilson & Nicholson, 1993). Another theory is that polyacrylate displaces phosphate and calcium ions on the surface of the hydroxyapatite, producing an intermediate layer of calcium and aluminium phosphates and polyacrylates between the tooth and the cement (Wilson & Nicholson, 1993; Van Noort, 1994; Tanumiharja *et al*, 2000). In addition, hydrogen bonds may form between the carboxylic groups and amino acid groups of the collagen, primarily present in dentin (Van Noort, 1994; Jones, 1995). The most recent theory is that GICs adhere via hydrogen bonds between the polyacrylic acid or polyacrylate ion and water molecules that are tightly bound to the surface of the tooth (Nicholson, 2000).

Despite these advantages, GICs do suffer from some shortcomings. The first main disadvantage is their sensitivity to moisture and desiccation during the initial setting stages (Van Noort, 1994). Secondly, GICs are relatively brittle, weak in tension, have poor wear characteristics and have a low modulus of elasticity and fracture toughness (McLean, 1992; Russ, 1999; Gu *et al*, 2005). The relatively poor mechanical properties limit their use to non-load bearing applications.

Despite these disadvantages, the characteristics of GICs still make them a suitable material for the restoration of anterior teeth, tunnel restorations, cavity liners, bases under amalgam and composite resins and the attachment of stainless steel crowns and bridges. They are also used as a general repairing material for erosion lesions, abrasions and temporary anterior / posterior restorations (Culbertson, 2001).

2.2.1.7 Filler Technology

There have been two general approaches to the improvement of the mechanical properties of GICs. The first focused on the filler technology, while the second focused on the matrix surrounding the fillers. The latter has been the most successful with the combination of the existing composite resin system with the GIC system leading to the development of resin modified GICs (RMGIC) and polyacid modified composite resin (PMCR).

The advancement of the filler technology used within the original GICs focuses on either the modification of the existing glass, introduction of glass fibres and the addition of metal particles, flakes and fibres (Simmons, 1983; McLean & Gasser, 1985; Walls *et al*, 1987; Kerby & Bleiholder, 1991; Wasson, 1993; Wilson & Nicholson, 1993; Smith, 1998; Rafferty *et al*, 2000; Gu *et al*, 2005).
Wilson *et al* (1972) found that aluminosilicate glasses can undergo amorphous phase separation during the quenching process governed by the rapidity of the process. It was subsequently found that GICs made with glasses that had undergone amorphous phase separation produced cements with greater compressive strength than single phase glasses (Crisp & Wilson, 1974).

The phases may consist of discrete droplets or two essentially continuous phases (Nicholson, 1998) that are believed to consist of calcium and fluoride (Hill & Wood, 2000). The amorphous separated phase can be envisaged as consisting of a central core of fluorite surrounded by and amorphous region, which is readily etched by acid, a less readily etched subsurface layer and an outer layer which is rapidly etched (Hill Wood, 2000).
The separated phase is less reactive than the original single phase therefore attempts have been made to control the setting rate by controlling the level of phase separation within the glass (Barry *et al*, 1979; Wood & Hill, 1991a, 1991b). All modern GIC glasses contain some amount of an amorphous separated phase which has been purposefully generated by controlling the quenching process to improve the compressive strength of the cement (Nicholson, 1998).
During the same period of development Schmitt *et al* (1983) patented a GIC incorporating calcium depleted ASG particles as filler particles. The particles are washed in an acidic solution (hydrochloric, sulphuric, nitric, acetic, propionic and perchloric acids may be used) to deplete the outer 10-100 μm of the powder particles of calcium. Sulphuric (H_2SO_4) and nitric (HNO_3) acids have also be used to deplete the surface of boro-aluminosilicate glasses however these acids dissolved much more of the glass and caused adverse setting effects (Wilson & Combe, 1991).
Little is known about the properties of these acid depleted cements other than they reduce early water sensitivity and elongate the working time (Schmitt *et al*, 1983) compared to the same untreated cement.

The largest volume of research with respect to the filler technology used in the GIC system has been focused on reinforced glass ionomer cements (RGIC). RGICs are based on the original GIC system but with the addition of either un/reactive particles or fibres that have been introduced with the hope that their presence will impart some of their properties into the resultant cement.

Attempts to increase the physical properties of the GIC system include the addition of amalgam powder (Simmons, 1983; Bayls, 1991), metal fibres and flakes (Wilson & Prosser, 1984), stainless steel, metal oxide and silver particles (Kerby & Bleiholder, 1991; Gu *et al*, 2005), sintered metallic and glass particles (Walls, 1987; McKinney *et al*, 1988; Wasson, 1993), hydroxyapatite (Arita *et al*, 2003; Gu *et al*, 2005), un/reactive glass fibres (Kobayashi *et al*, 2000; Lucksanasombool *et al*, 2002; Lohbauer *et al*, 2003) and ytterbium fluoride & barium sulphate nano particles (Prentice *et al*, 2006).

A large amount of work has been competed on GIC systems including amalgam powder and silver sintered glass, the so called 'miracle mix' and cermet-ionomer cements respectively (Simmons, 1983; McLean. & Gasser, 1984). Miracle mix contains silver-tin-copper and mercury amalgam-alloy which has been mixed with ASG glass powder until a homogeneous mix is achieved (Tomlinson, 2007). Cermet glass powders are made by mixing equal volumes of ASG and metal particles (typically silver), compressing them in a pelletiser and fusing the system at 800ºC so that the metal becomes sintered into the glass powder (Wasson *et al*, 1993). The compressive, flexural, tensile and bond strength of these two materials have been tested as well as the release of fluoride and silver (Miller *et al*, 1984; Wilson *et al*, 1984; El-Mallakh *et al*, 1987; Walls *et al*, 1987; Irie & Nikai, 1988; Tjan & Morgan, 1988; Kerby & Bleinholder, 1989; Williams *et al*, 1989; Williams *et al*, 1992).

The change in the ISO requirements for sample sizes over the duration of several different studies have lead to inconsistencies in the test methods therefore results cannot be easily compared (McCabe *et al*, 1990; Wasson, 1993). The inconsistency between experimental techniques has made the identification of an increase in compressive, flexural or tensile strength unobtainable (Wasson, 1993). The fluoride release of RGICs has the similar profile (slightly lower in some cases) as conventional GICs over a 100 day period however silver is also release which is known to cause tooth discoloration (Sarkar *et al*, 1988; Bowen & Marjenhoff, 1992; Ruse, 1999; Nicholson, 2000). The supposed slight improvement in mechanical properties, poor aesthetics and tooth discolouring silver release have limited their use to low load bearing applications (Russ, 1999).

Further to the inclusion of amalgam powders and metal fibres, addition of hydroxyapatite (HA), HA / zinc oxide agglomerations, ytterbium fluoride and barium sulphate have been tested for suitability as orthopaedic and dental cements. The addition of hydroxyapatite was shown to improve the flexural strength of the RGICs the extent of which was controlled by the shape of the particle, HA whiskers (fibres) or spheres (Arita *et al*, 2003; Gu *et al*, 2005). However, large volumes were needed (≈ 25%) in order to achieve a noticeable difference which in turn affected the working & setting times, compressive strength and solubility of the cement (Arita *et al*, 2003). The addition of an insoluble zinc oxide core in the centre of HA agglomerates was found to increase micro-hardness and compressive strength (Gu *et al*, 2005).

The inclusion of reactive ytterbium fluoride to the GIC system accelerated the working and setting times. Interestingly, small quantities of un-reactive barium sulphate were found to accelerate the working and setting time where as larger quantities had a diluent effect and decelerated the working and setting time (Prentice *et al*, 2006). The inclusion of both ytterbium fluoride and barium sulphate reduced the compressive strength at 1 and 24 hours (Prentice *et al*, 2006).

The discovery that RGICs reinforced with glass fibres failed at the fibre matrix interface (Nagaraja & Kishore, 2005) has lead to the development of reactive short glass fibres which can react with the cement forming liquid (Kobayashi *et al*, 2000 Lohbauer *et al*, 2003). These short glass fibre RGICs have been found to have increased compressive, tensile and flexural strength when compared to their equivalent GIC (Kobayashi *et al*, 2000 Lohbauer *et al*, 2003). The glass used has an effect on the volume needed to obtain maximum mechanical properties. Kobayashi *et al* (2000) found that up to 60 vol% was needed to obtain maximum mechanical properties compared to 20 vol% found by Lohbauer *et al* (2003). No data is available for wear resistance, fluoride release or mixing parameters of these reactive fibre RGICs however with incorporations of up to 60 vol% the cement are not expected to mix, carve or take burnish well.

2.2.2 Composite Resins

CRs can be thought of as glass filled plastics made up of three major components: an organic resin, inorganic filler particles and a coupling agent (Van Noort, 1994). The resin polymerises to form a rigid solid matrix binding the individual filler particles within the matrix via the coupling agent.

The first CRs were developed in the 1950s and made from poly(methyl methacrylate) (PMMA) incorporating quartz filler particles (Van Noort, 1994). These CRs provided an aesthetic alternative to metallic amalgams and were found to adhere to acid etched enamel and dentin (Buoncore, 1955; Buoncore *et al*, 1956). However, the CRs based on PMMA suffered from high polymerisation shrinkage despite the presence of filler powders. This shrinkage can lead to the formation of a gap between the composite and the cavity wall, which can fill with oral fluids (microleakage) containing bacteria possibly leading to further decay (Nicholson & Anstice, 1999; Deliperi & Bardwell, 2002). The polymerisation shrinkage usually results in a weaker bond strength between the composite and tooth, thus reducing the longevity of the filling (Van Noort, 1994).

In order to combat the polymerisation shrinkage the PMMA resin was replaced with bis-GMA (2,2-bis[4(2-hydroxy-3-methacryloxypropoxy) phenyl]-propane), a high molecular weight dimethacrylate resin which was found to reduce shrinkage (Bowen, 1961). Bis-GMA based composites are still in common use today (Smith, 1998) along with urethane dimethacrylate (UDMA) resin (Van Noort, 1994).
These high molecular weight resin monomers are very viscous making high filler loading difficult so, the bis-GMA and UDMA are diluted with small amounts of lower molecular weight monomers such as methyl methacrylate (MMA) or tri/ethylene glycol dimethacrylate (T/EGDMA). These diluents' are methacrylate terminated so polymerise in the same way as bis-GMA becoming incorporated into the set resin (Nicholson, 1998). The addition of the MMA and T/EGDMA allows for greater filler loading and better handling properties however, these materials increase the amount of polymerisation shrinkage. Therefore, a delicate balance exists between handling properties and shrinkage which is further complicated by high filler loading, lowering the polymerisation shrinkage.

As the CRs continued to develop so too did the way in which they cured. Initially, CRs were supplied as two separate pastes, one containing an activator, the other an initiator so upon mixing the cement would chemically set. A later development, which proved popular with dentists, was a single paste that could be set on demand by exposure to ultraviolet (UV) light (Buonocore & Davila, 1973; Rock, 1974; Wilder *et al*, 1983). The replacement of the chemical initiator with the photoninitiator, benzoin methyl ester, meant that the setting reaction occurred when a source of UV radiation was shone on the restoration (Rock, 1974). The use of UV radiation introduced a depth of penetration issue, meaning that only 1-2 mm of cement could be cured at a time resulting in the restoration having to be built up in layers (Van Noort, 1994). The move away from UV radiation was driven by the safety concerns regarding corneal exposure to UV radiation (Rock, 1974) which lead to the development of visible light activated composites. The replacement of the photoninitiator with an α-diketone initiator system (e.g. camphorquinone) and amine reducing agent. These are cured by exposure to high intensity blue light of wavelength 470 nm (Nicholson, 1998) which negated the UV hazard and also increased the depth of penetration up to 3-4 mm. This reduced the need for incremental placement of the cement, although for very deep fillings this is still required (Van Noort, 1994). However, it should be noted that, the incremental placement of CRs may reduce the effects of polymerisation shrinkage, although this is debated (Versluis, 1996).

There has been much discussion over the use of high- versus low-intensity light sources in dentistry (Unterbrink & Muessner, 1995; Davidson-Kaban *et al*, 1997; St-Georges *et al*, 2003; Hofmann *et al*, 2003). High-intensity curing lamps are convenient for dentist as they provide a quick set however, their use increases polymerisation shrinkage (Hofmann, 2003) and reduces polymer chain length and level of cross-linking ultimately resulting in weaker composites. The use of low-intensity (soft start) light sources results in greater levels of cross-linking and polymer chain length, thus improving the mechanical properties of the composite (Rueggeberg, 1999).

There are several different classes of CR's available currently, each with their associated advantages and disadvantages. Individual discussion of each CR modification is beyond the scope of this review and in depth literature is available elsewhere (Van Noort, 1994; Nicholson & Anstice, 1999; Frankenberger *et al*, 1999; Bayne *et al*, 1998; Labella *et al*, 1999; Abe *et al*, 2001; Leinfelder & Prasad, 1998; Leinfelder *et al*, 1998; Lee *et al*, 2003; McCabe & Rusby, 2004)

2.2.2.1 Summary

Composite resins are a white coloured dental restorative that can obtain compressive strength comparable with amalgam restorations (Van Noort, 1994); amalgams reach compressive strengths in excess of 400MPa (Phillips, 1949), above the compressive breaking strength of tooth (Lee & Park, 2000). The cavity preparation is simple consisting of an acid etch with ortho-phosphoric acid to remove enamel and expose dental tubules for keying with resin tags. This is an improvement on the undercut method employed with dental amalgams resulting in the loss of healthy dentin (Van Noort, 1994).
CRs can be command set using visible radiation however, they are susceptible to a high degree of polymerisation shrinkage increasing the placement time to minimise micro-leaks occurring. The ultimate strength of the restoration is also technique sensitive; a well packed restoration must be made in order for the CR to reach a compressive strength similar to a dental amalgam (Leinfelder & Prasad, 1998).
Despite their shortcomings, CRs are very popular (Nicholson, 2000), especially due to their high aesthetics.

2.2.3 Resin Modified Glass Ionomer Cement (RMGIC)

RMGICs can be considered as a hybrid of GICs and CRs because they consist of the conventional GIC components and photopolymererisable monomers and suitable polymerisation initiators. They have a duel set mechanism which encompasses the acid-base and polymerisation reactions. A cement is formed made up of filler particles embedded in two types of matrices, an ionic matrix from the acid-base reaction and a polymer matrix due to the added monomer (Nicholson & Anstice, 1999).

2.2.3.1 Development and Properties

RMGICs were first developed in the late 80's in an attempt to combine the advantageous properties of both CRs and GICs whilst minimising their previous individual disadvantages (Antonucci *et al*, 1988; Mitra, 1989; Mathis & Ferracane, 1989).

The first RMGICs simple consisted of conventional GIC components with added water-miscible monomers (often 2-hydroxyethyl methacrylate, HEMA) and a suitable polymerisation initiator. The cements therefore have a duel setting mechanism: the acid-base reaction of the GIC components and the polymerisation reaction (Nicholson & Anstice, 1999). The final set cement consists of filler particles embedded in two types of matrices, an ionic metrix from the acid-base reaction and a polymer matrix due to the polymerised monomers (Nicholson & Anstice, 1999).

RMGICs were further developed by the replacement of some carboxylic acid groups within the PAA with pendant groups containing C=C bonds (Brown & Mallakh, 1992). The C=C bonds are able to undergo polymerisation, thus covalently cross-linking PAA to the polymer matrix. Therefore, in these RMGICs compositions, the PAA takes part in the acid-base neutralisation and the polymerisation reactions. RMGICs contain modified acids, still usually containing some added monomer, usually HEMA (Wilson, 1990; Nicholson, 1998; Nicholson & Anstice, 1999). The HEMA not only undergoes polymerisation to form polyHEMA, it is also able to copolymerise with the modified PAA (Wilson, 1990).

Polymerisation in RMGICs is often photoinitiated (light activated), allowing a degree of command over the setting. Light-activated RMGICs, in particular, were hoped to have the benefit of extended working times with a 'snappy' setting (with use of a dental lamp) (Wilson, 1990; Kan *et al*, 1997; Qvist *et al*, 2004). However, in-vitro experiments to prove this 'snappy' setting mechanism have been difficult due to practical problems of simultaneously exposing the cement to light and using e.g. an oscillating rheometer (McCabe, 1998).

In general, the mechanical properties of most RMGICs lie between those of the CRs and GICs (Uno *et al*, 1996; McCabe, 1998).RMGICs are reported to have significantly higher flexural / tensile strength and fracture toughness (Mitsuhashi *et al*, 2003) than GICs (McCabe, 1998). Unfortunately, some RMGICs have much lower flexural strengths than CRs (McCabe, 1998). The polymerisation reaction in RMGICs has been found to contribute significantly to the early development of strength (Mathis & Ferrace, 1989; Eliades, 1993), but research has shown that after 1 week of ageing, GICs and RMGICs have similar compressive strengths (Xie *et al*, 2003). The early development of strength is advantageous because it prevents the susceptibility of becoming damaged. The rapidly forming polymer network also serves to protect the cement from moisture contamination (Wilson, 1990; Hse *et al*, 1999), desiccation, both common problems experienced by GICs. The short term micro-hardness of RMGICs has been found to be either similar or much reduced compared to GICs dependent upon product and setting mechanism employed (Peutzfeldt *et al*, 1997; Xie *et al*, 2000; Ellakuria *et al*, 2003).

Unfortunately, RMGICs have been found to have generally unimproved or sometimes much poorer (abrasive) wear resistance in comparison to GICs (Momoi *et al*, 1992; Peutzfeldt *et al*, 1997; Futatsuki *et al*, 2001). This is likely to be linked to the lower hardness (Peutzfeldt *et al*, 1997). These results have been suggested to result from the weaker bonding between the fillers and matrix in RMGIC than GICs, due to the partial replacement of polysalts matrix with polymer (De Gee, 1999; Xie *et al*, 2000). Any areas of unreacted polymer matrix may also contribute to the decreases in wear resistance for the RMGICs (Xie *et al*, 2000).

RMGICs have been found to release similar amounts of fluoride to conventional GICs, although there is variation between products (Mitra, 1991; Momoi & McCabe, 1993; Forss, 1993; Kan *et al*, 1997; Nicholson & Anstice, 1999). In some cases fluoride release for RMGICs has been found to be higher than that of GICs (Preston *et al*, 1999). Another important advancement from the GIC is their improved aesthetics due to the polymers high translucency (Nicholson & Anstice, 1999; Mount *et al*, 2002).

RMGICs have been found to retain their beneficial GIC property of being able to adhere to tooth structures (Nicholson & Anstice, 1999), although there seems to be some conflicting views / results on the extent of their bonding abilities in comparison to conventional GICs (Fritz *et al*, 1996; McCabe, 1998; Nicholson & Anstice, 1999; Saito *et al*, 1999; Nicholson, 2000). In general RMGICs have been found to bond more strongely to dentin than GICs although most manufactures still recommend the use of a preconditioned to achieve maximum strength (Rusz *et al*, 1992; McCabe, 1998; Hse *et al*, 1999).

RMGICs are tolerated well by tooth pulp (Fenton *et al*, 1991; Gaintantzopoulou *et al*, 1994) but there are some concerns over biocompatibility (Hamid *et al*, 1998; Palmer *et al*, 1999), because of the release of uncured resin (monomer), which is cytotoxic (Bruce *et al*) and can delay hypersensitivity reactions (Katsuno *et al*, 1995).

Unfortunately, the problem with polymerisation shrinkage experienced by CRs is still prominent within the RMGICs (Attin *et al*, 1995; Irie *et al*, 2002) and therefore it has been suggested that the product should be applied and cured in increments (Hse *et al*, 1999), although the effectiveness of this method is debated (Versluis *et al*, 1996). Another resin related problem with RMGICs is high levels of water sorption (Feilzer *et al*, 1995; Kanchanavasita *et al*, 1997) which causes swelling of the restorative leading to discomfort and possible fracture of the tooth itself.

2.2.4 Polyacid Modified Composite Resin (PMCR)

PMCRs, otherwise known as 'compomers', were developed in the early-to-mid 1990s and were another attempt to combine the advantageous characteristics of CRs and GICs. They contain all the major components from both CRs and GICs except for the addition of water (McCabe, 1998). The name compomer comes from the combination of ***comp****osit resin* and *glass ion****omer*** (Ruse, 1999).

PMCRs come as a single paste containing photo initiators that are activated by visible light (470 nm). The composition of the resin phase of PMCRs varies between brands (Nicholson & Alsarheed, 1998) but the filler powder is always an ion-leachable glass, usually a calcium- fluoro-aluminosilicate glass as used in GICs. The monomer present is usually a bulky modified, methacrylate monomer such as UDMA or bis-GMA. In addition, bi-functional monomers, containing two carboxylic acid groups and two carbon double bonds (e.g. TCB, DCDMA) are included (Meyer *et al*, 1998). These monomers are able to be involved in both the polymerisation and acid-base reactions.
The setting reaction in compomers is not a duel setting mechanism like that of an RMGIC. This is because of the absence of water preventing the acid-base reaction taking place until water sorption occurs after monomer polymerisation. Therefore, the extent of the acid-base reaction that takes place may be limited by the rigidity of the polymeric network (McCabe, 1998; Meyer *et al*, 1998).

The polymerisation of PMCRs has been found to suffer from similar levels of polymerisation shrinkage as CRs (Chen *et al*, 2003). The sorption of water was believed to initiate the acid-base reaction and increase the strength of the restoration however, this is not the case; strengths have remained roughly constant regardless of the acid-base reaction taking place (Eliaded *et al*, 1996; Nicholson *et al*, 2003). Therefore, it seems that wet conditions allow the acid-base reaction to take place but significant uptake of water may weaken the resin phase offsetting any gains from the acid-base reaction. Similar flexural strength values have been reported for PMCRs stored in wet conditions over the course of one year (Torabzadeh & Aboush, 1996).

Despite the effects of water, the strength of water stored PMCRs have been found to exceed that of RMGICs and GICs but remains inferior to that of CRs (Mayer *et al*, 1998; Saito *et al*, 1999; Xu & Burgess, 2003)

The micro-hardness of PMCRs has been found to be similar to that of GICs (Peutzfeldt *et al*, 1997; Zimehl & Hannig, 2000). There seems to be mixed reports on wear resistance of PMCRs in comparison to RMGICs and GICs (Peutzfeldt *et al*, 1997; Nicholson & Anstice, 1999). However, reports agree that PMCRs wear resistance is inferior to that of CRs (Peutzfeldt *et al*, 1997).

PMCRs have two major disadvantages when compared to GICs and RMGICs. Firstly, they lack the ability to bond tooth structures, a well known advantage of GICs and some RMGICs (Ruse, 1999). Secondly, they have been found to release significantly less fluoride than GICs and RMGICs (Ruse, 1999).

Despite PMCRs disadvantages, they are easy to handle and highly aesthetic making them widely accepted by dental practitioners (Chen *et al*, 2003).

2.2.5 Conclusion

The advantages and disadvantages of the available “white” dental restorative materials have been discussed. The four materials discussed can be considered compositionally as GIC and CRs being the extremes with RMGIC and PMCRs intermediate cements with compositional similarities to both the extremes (Guggenberger *et al*, 1998).

It is clear that all the available cement types have their uses but also their limitations; none of them satisfy all of the ideal criteria listed in Sec. 2.2. .This is the driving force behind all of the research, which is clearly being approached from many angles to produce a wide variety of interesting materials with different properties.

2.3 Cement forming Metal Oxides

There are a large range of metal oxides able to form cements although not all can be formed with water based polyelectrolytes.
Metal oxides previously investigated for the uses as a dental restorative include oxides of: boron, bismuth, barium, beryllium, cobalt, copper, cadmium, chromium, calcium, iron, indium, lanthanum, lead, magnesium, mercury, molybdenum, manganese, strontium, tin, tungsten, yttrium and zinc (Wilson & Nicholson, 1993).

Metal oxides capable of forming hydrolytically stable cements are ZnO, CuO, SnO, HgO and PbO. Non-hydrolytically stable cement formers include MgO, CaO, BaO and SrO (Wilson & Nicholson, 1993).
Crisp *et al* (1976) found that the reaction between bivalent metal oxides and PAA goes to completion where as Hornsby (1977) found that trivalent metal oxides such as Al_2O_3, La_2O_3, Bi_2O_3 and Y_2O_3 are capable of forming polycarboxylic cements but the reaction is only partial.

In order for a cement to form from a metal oxide, that oxide must be capable of releasing a cation into acidic solution. The best oxides were found to be amphoteric (posses both basic and acidic properties) for use as cement formers (Kingery, 1950).

Aluminium is capable of forming several different oxide and hydroxides (Wefers & Misra, 1987) each with subtle structural differences. The oxides and hydroxides of aluminium are amphoteric (Wefers & Misra, 1987) but as afore mentioned, aluminium is trivalent and therefore the reaction between PAA and Al_2O_3 does not go to completion (Hornsby, 1977; Wilson & Nicholson, 1993).
However, tri-hydroxides of aluminium ($Al(OH)_3$), aluminium hydroxide) have been found to react with PAA and form stable cements (Saniger, *et al*, 1991; Hu & Saniger, 1992; Wu *et al*, 1997; Vermohlen *et al*, 2000; Alexandera *et al*, 2001). The tensile strength of $Al(OH)_3$-PAA cements is comparable with conventional GICs (Hu & Saniger, 1992; Bresciani *et al*, 2004) however, more prudent data such as compressive strength, wear resistance etc is not available.

The stability of freshly precipitated $Al(OH)_3$ is however a cause for concern. $Al(OH)_3$ is known to condense over relatively short periods of time to form Al_2O_3 (Wefers & Misra, 1987). It is reported that a sample of freshly precipitated $Al(OH)_3$ will convert completely to Al_2O_3 in under a year at room temperature (Sato, 1972).

2.4 Particle Packing in Cement and Resin Based Materials

Particle packing has been a subject of theoretical and experimental interest for some time and has been extensively studied and documented (Gray, 1968; Cumberland, 1987; German, 1989) particularly in the field of building cements (Jones *et al*, 2002).
A good introduction to particle packing in polymer composites can be found in 'Advances in Composite Materials - Analysis of Natural and Man-Made Materials (2011)' and further information on theoretical packing models can be found in Appendix 4 owing to the amount of text.
Chapter 8 (Theoretical Modeling of Filler Enhance GICs) concentrates on the optimization of packing density so a general discussion of current particle packing literature of concrete / cement systems (industrial building material e.g. Portland Cement) and packable composite resins is presented in lieu of relevant GIC literature which concentrates on porosity due to mixing technique variation. (Mitchell & Douglas, 1997; Nomoto *et al*, 2004; Coldebella *et al*, 2011).

2.4.1 GIC Porosity

Mitchell & Douglas (1997) have found that the method used to mix GICs has a pronounced effect on the porosity of the resulting cement. They reported that surface porosity of hand mixed cements is greater than the equivalent encapsulated cements.
This conflicts with the results of Nomoto *et al* (2004) who found large bubbles inside encapsulated cement samples. Nomoto *et al* reported the porosity of hand mixed cements to be approximately 0.1 % / vol whilst encapsulated cements had a porosity of 2-3 % / vol.
An attempt to improve packing density of GICs by decreasing porosity has been made through the application of ultrasound to setting restorations.

Tanner *et al* (2006) and Coldeballa *et al* (2011) found that the application of ultrasound to a GIC can be used to command set the restorative and reduce the porosity by 25-50% compared to control materials.

2.4.2 Packing Optimization

Previously the packing density of cement systems has been increased as the result of tailoring the particle size distribution (Dinger & Funk, 1993; Lange *et al*, 1997; Brouwers & Radix, 2005; Cho *et al*, 2006) of cements using a continuous Andreasen and Andersen (1930) approach. Jone *et al* (2002) and Brouwers (2006) have both written reviews of the theoretical models used to identify the porosity of cements based on the particle size distribution of hardcore used. They conclude that the use of a perfect, continuous power law distribution will yield the maximum packing fraction for the various models reviewed.

Dental composites as reviewed in *sections 2.2.2 & 2.2.3* closely resemble epoxy resins and filled polymer matrices. Research has been conducted into particle loading and surface interactions of glass, calcium carbonate and silica micro / nano fillers used with these resin / polymer phases (Suetsugu & White, 1983; Kitey & Tippur, 2005; Prentice *et al*, 2006; Fleming & Goodboy, 2006; Fu *et al*, 2008; Adachi, 2008; Elbishari *et al*, 2011).

Prentice *et al* (2006) have shown that the addition of nano sized ytterbium fluoride and barium sulphate has the undesirable effect of shortening the working time of GICs. This is expected to be due to the surface interactions of the filler particles with the matrix forming polyacid as found in thermoplastic research (Suetsugu *et al*, 1983), epoxy resin development (Kitey & Tippur, 2005; Adachi *et al*, 2008; Fu *et al*, 2008) and composite resin dental cements (Elbishari *et al*, 2011). There is no reference made to the packing of fillers in these resin phase systems because the addition of particulate material is intended only to increase toughness, fracture strength and flexural strength (Fu *et al*, 2008).

Glass Ionomer Cements are a unique and dynamic material where the properties of the final cement can be influenced by the size of ASG particles, the packing of ASG particles, and the chemical make-up of the glass as well as the molecular weight of the matrix forming polyelectrolyte. These factors independently influence the strength of the final restoration when prepared in a controlled environment.

The above literature would suggest that the effect of sub-micron filler addition to an already heavily packed cement may cause variation from the original handling properties due to surface interactions leading to increased viscosity. However, these effects are not expected to be pronounced given the level of particulates already in the polymer dispersion.

Chapter 3

Materials & Method

Aim

The aim of this chapter is to present the method in which the control material and filler incorporated cements have been manufactured and the correct mixing procedure for sample preparation.

3.1 Introduction

Commercially available Diamond Carve (DC) is produced by Associated Dental Products Ltd (Kemdent) and is a class I and II semi-permanent restorative material. DC is a glass polyalkenoate cement containing poly(vinyl phosphonic acid) in addition to the more commonly used polyacrylic acid; this hybrid GIC was first patented by Alan Wilson in (EP0340016B1) 1989 and further worked on under his supervision by John Ellis in 1991 (Ellis *et al*, 1991).
DC has been used throughout experimentation as the base material for filler incorporation and as such has been studied in conjunction with the filler enhanced hybrid.

The use of TiO_2 (anatase) as the base particle for coating with $Al(OH)_3$ was made because of its inert nature and small particle size. These properties are of significance because biocompatibility with the original tooth substrate is an important property required of dental restorations to prevent immediate or delayed reaction with the tooth pulp. The high compressive strength of TiO_2 (single crystal ≈ 850 - 950 MPa; Vahldiek, 1967; CERAM Research Limited, 2010) and sub-micron size of the particles will allow the particles to fill interstitial voids left in fully set cement. Anatase was supplied to Kemdent by Langfang Pairs Horses Chemical Company, product number – SA120.

The increased packing density and high compressive strength of the filler particles are intended to increase the compressive strength of the set TiGIC.
The introduction of a reactive substrate on the surface of the TiO_2 filler particles is hoped to enhance the particles incorporation into the Glass–Polyelectrolyte salt lattice.

Information on the sol-gel coating of titanium dioxide (TiO_2) particles with aluminium hydroxide ($Al(OH)_3$) and the preparation of DC and filler incorporated cements is provided with some analytical data identifying key properties of the base materials.

3.2 Coating Procedure

The coating process is separated into three steps,

1. Dispersion

Particles in an aqueous solution carry an electrical charge which is caused by:

- Differential loss of ions – if either titanium or oxygen atoms were to dissociate from the TiO_2 particle into solution this would cause a resultant charge on the surface of the particle (similar to electrolysis).

- Structural inequality – the internal structure of TiO_2 has non-bonding species (Ti^{4+} or O^{-2}) causing resultant charges to occur (Restori *et al*, 1987). These inequalities lead to a dominant charge being exhibited by the particle.

The surface charge of TiO_2 in neutral solution is reported to be slightly negative (Wiese & Healy, 1974; Imae *et al*, 1991) so a dispersing agent is needed to stop coalescing and sedimentation occurring. The large density difference between TiO_2 and H_2O meant that constant mechanical stirring was needed to prevent sedimentation due to gravity (weight of particles).

2. Precipitation

The aluminium species used during the coating process is stable as hydrated Al^{3+} and SO_4^{-2} ions in acidic solution but as the pH is raised to neutrality the Al^{3+} ion is no longer stable and 'crashes' out of solution as $Al(OH)_3$ (Wefers and Misra, 1987).

The basic solution used to raise the pH of the aluminium solution to neutrality will affect the salt formed during the process and the extent of neutralisation. It is therefore ideal to use a strong monobasic species to drive the reaction to completion avoiding multiple ionisations and complex salt formation. Sodium hydroxide (or caustic soda) is an ideal base with a pK_B of 0.2 (Borkowski, 2005)

3. Filtration

The final coated product must be separated from the final liquor which was achieved using a combination of centrifugation and vacuum filtration. The filtration steps were performed multiple times to remove the salt of neutralisation from the coated particles.

3.2.1 TiO_2 Suspension

The coating process is performed using a colloidal suspension process; the titanium dioxide particles must be suspended in solution before the aluminium species can be added to the TiO_2 slurry. The dispersant used in the coating process was monoisopropanolamine (MIPA) which is a surface-active substance (surfactant).

The TiO_2 suspension was made by mixing a 0.012 mol dm^{-3} solution of MIPA in a constant 1:104 molar ratio with a 1.25 mol dm^{-3} suspension of TiO_2. A propeller stirrer was used to continually mix the suspension to prevent sedimentation.

3.2.2 Aluminium Hydroxide Precipitation

Aluminium sulphate is an amphoteric aluminium species that when dissolved in water forms an acidic solution of approximately pH 3.1 – 3.7.

A 9% w/w coating of $Al(OH)_3$ was to be laid down on the surface of the TiO_2 particles in solution. The coating percentage was chosen because positive identification of coating webs at this concentration was made using a transmission electron microscope (*see* section 3.5.2). This was achieved by adding solid aluminium sulphate to the TiO_2 suspension so that a molarity of 5.77×10^{-2} mol dm^{-3} was achieved (e.g. into a 1 litre TiO_2 suspension, 19.74g of $Al_2(SO_4)_3$ would be needed)

A peristaltic pump was used to add a 0.1 molarity solution of sodium hydroxide to the aluminium/titanium slurry at a rate of 2ml per minute until neutrality was reached. This process took approximately 2 hours to complete.

3.2.3 Separation of Coated Particles

The suspension is first centrifuged and the solids removed from the supernatant. The coated particles are then washed by re-suspension in distilled water. The conductance of the supernatant was measured and the process was repeated until a constant conductance was reached at which point the damp particle cake was free from salts of neutralisation. The particles were dried, ground and stored in a desiccator at 22±2°C to prevent accelerated aging of the $Al(OH)_3$ gel coating (due to elevated temperatures).

3.3 Diamond Carve Cement

Diamond Carve is a duel component, chemically setting cement consisting of a powder blend and an acidic polyelectrolyte solution. DC was supplied from Kemdent® in hand mixed and encapsulated varieties.

The powder is a blend of a strontium based fluoroaluminosilicate glass (ASG), (L)-Tartaric acid (TA), polyacrylic acid (PAA) and a small amount of copolymer vinylphosphonic acid and acrylic acid (PVPA/AA). The weight-average molecular weight of PAA is approximately 60,000 $gmol^{-1}$ while that of PVPA/AA is approximately 73,000 $gmol^{-1}$ (Fennel *et al*, 1998). The powder has an average particle size of 16-37 μm cross-sectional diameter as determined by particle size analysis (Figure 3.7).

The liquid used in DC is a mix of high molecular weight PAA (60,000 g mol^{-1}) and TA in the ratios presented in Table 3.1.

3.3.1 Diamond Carve Manufacture

The ASG used in DC is supplied as a course frit (approximately 3mm in diameter) which is first milled in a ceramic mill filled with large ceramic balls (10-30mm diameter) for 6 hours until an average particle size between 100-200μm is achieved.

The reagents (Table 3.1) are further milled mixed together in a mill containing a range of ceramic balls between 5–20mm in cross-sectional diameter for 4 hours. The milled cement powder is then passed through a 100μm sieve to remove any oversized particles. The average particle size of DC powder is 16-37 μm cross-sectional diameter (Figure 3.7).

The polyelectrolyte solution is produced by mixing the reagents from Table 3.1 in an orbital mixer for 2 hours. The resultant solution contains no solids and is translucent with a slightly yellow colouration.

Diamond Carve Reagents and Percentage Weight Ratio's (g)					
	Aluminosilicate Glass (%)	Polyacrylic Acid (%)	Tartaric Acid (%)	PAA-PVPA co-polymer (%)	Water (%)
Diamond Carve Powder	87.824	8.932	2.365	0.878	N/A
Polyelectrolyte Solution	N/A	61.7385	11.249	N/A	27.0135

Table 3.1: Reagents and Mixing Ratios used to Produce DC Powder and DC Liquid

3.3.2 Cement Preparation

DC is able to be prepared using two different mixing techniques; automated mixing using encapsulated cement and hand mixing. The mixing technique used throughout experimentation was performed using encapsulated cements. The technique for hand mixing is described in Appendix 1 and is presented because exploratory tests during the early stages of research highlighted the increased repeatability of encapsulated cements when compared to hand mixed.

Only the powder to liquid (P:L) ratio of encapsulated DC differs from the hand mixed samples. The P:L ratio of hand mixed DC is 4:1 where as that of the encapsulated cement is 3.7:1 because a slightly less viscous cement is required to aid extrusion from the capsule. The implications of the lower P:L ratio in capsules is a decrease in compressive strength (Cook, 1982; Fleming *et al*, 2003)

The capsule consists of a mixing chamber, a sachet of cement liquid & securing cap, a plunger and a twist open nozzle (Figure 3.1).

The liquid sachet sits on the exterior of the mixing chamber above a breach in the chamber and secured in place using the cap; the chamber is filled with cement powder. The reaction is initiated when the capsule is crimped forcing the cement liquid into the mixing chamber.

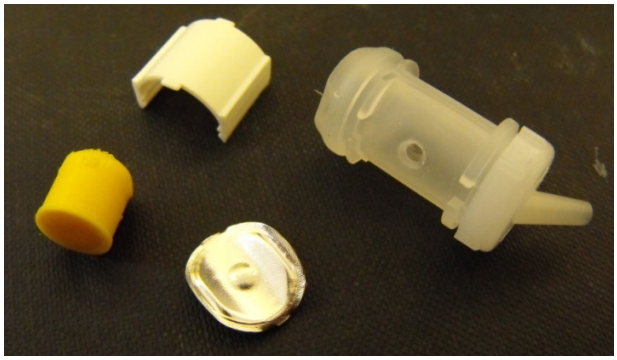

Figure 3.1: Components of a DC Capsule (Securing Cap (Top Left), Mixing Chamber (Top Right), Plunger (Mid-Left), Acid Sachet (Bottom-Mid)

The capsules are activated and mixed following steps 1-3 below,

1. Cement capsule crimped for 10 seconds (Stopwatch Started)
   0 – 15 Seconds
2. Capsule loaded into a dental amalgamator and mixed for 10 seconds
   15 – 30 Seconds
3. Capsule is extruded
   30 – 60 Seconds

A dental amalgamator is used to mix the activated capsules. The amalgamator used throughout capsule mixing was a Vivadent Silamat operating at 3280 rpm; identified by stroboscope.

The mixed cement should posses,

a. Putty like consistency
b. Non-sticky to instruments
c. Slight translucency

3.4 Titanium Filler Incorporated Cement (TiGIC)

The filler incorporated cements are based on DC with small quantities of ASG directly replaced with the same weight of coated and un-coated TiO_2.

3.4.1 TiGIC Manufacture

The filler incorporated cements (TiGICs) were prepared using the same method as described in section 3.3.1. Filler incorporated cements (TiGICs) were formulated so that the ratios in Table 3.2 were maintained. ASG is removed and replaced on a weight by weight basis with titanium dioxide.

TiGIC Formulation (Percentage Incorporation)					
	DC	1.00%	2.50%	7.50%	10.00%
Aluminosilicate Glass	87.825	86.947	85.629	81.238	79.042
Polyacrylic Acid	8.932	8.932	8.932	8.932	8.932
Tartaric Acid	2.365	2.365	2.365	2.365	2.365
PAA-PVPA co-polymer	0.878	0.878	0.878	0.878	0.878
Titanium Dioxide	0.000	0.879	2.197	6.588	8.783

Table 3.2: Formulation of TiGIC Cements (Percentage Reagent Incorporation)

The TiGIC powder was brilliant white in colour due the high refractive index of TiO_2 which is widely used as a white pigment in a multitude of applications.

3.4.2 TiGIC Preparation

The capsules, as supplied by Kemdent® were pre-filled with DC so needed to be cleaned before use. The disassembly and cleaning procedure is explained in steps1-5 below.

1. Plunger is removed from the rear of the capsule and the DC cement powder discarded.
2. Capsule is disassembled into constituent parts (Capsule body, twist open nozzle, plunger, liquid sachet and sachet securing panel (Figure 3.1)).

3. All the individual parts are placed in 1 litre of distilled water and ultrasonically agitated for 5 minutes.
4. The individual parts are then rinsed with distilled water and placed on a clean glass slab in an oven at 37ºC.
5. Once the capsules have been cleaned and are dry they are reassembled with exception of the plunger.

The capsules were then filled with 0.4600 ± 0.005g of TiGIC powder and the plunger is replaced to seal the capsule.
The TiGIC capsules are mixed in the same manner as in section 3.3.2.

3.5 Coating Identification

The identification of a coating on the surface of the TiO_2 base particles was achieved using a Field Emission Transmission Electron Microscopy (FETEM) at the University of Nottingham Nanotechnology and Nanoscience Centre.

A JEOL 2100F microscope operating at 200kV (field emission gun source) equipped with a Gatan Orius camera and Oxford Instruments INCAEnergy EDX system.
The microscope was used in two operating modes, Scanning TEM (STEM / Bright Field) and High Angle Annular Dark Field (HAADF) (used to highlight Z-contrast difference in structures).

Samples prepared for TEM investigation included 1%, 3% and 9% coated TiO_2 particles. The results from the analysis of all three coating percentages are presented in Appendix 1 whereas only results from the 9% w/w coated samples are discussed here.

This is due to the analysis failing to identify a coating on 1% w/w coated particles unlike was achieved by Scanning Electron Microscopy (SEM) performed by Rochelle *et al* (1980).

Identification of a possible coating material was seen for 3% w/w coated TiO_2 particles but the positive identification was not possible because the instrument was operating near its limit of detection and distinction between $Al(OH)_3$ and other possible artefacts could not be made (*see* Appendix 1).
The positive identification of a coating at a 9% w/w was possible using the FETEM so was therefore chosen as coating percentage to be used throughout cement manufacture and further analysis.

3.5.1 Titanium Dioxide

Uncoated TiO_2 was found to have a mixture of particle sizes all forming agglomerates on the polymer backing film. Large particles were selected to perform both brightfield (BF) and HAADF analysis on because this avoided excessive magnifications and the amount of time per sample for thermal stability to be reached. **Error! Reference source not found.** is BF image of un-coated TiO_2 and is shown to highlight the difficulty associated with determining whether a coating is present at the particles edges or not. It would be an easy mistake to look at **Error! Reference source not found.** and identify a small uniform oating around the entire particle. The HAADF image of un-coated TiO_2 (Figure 3.3) identifies no different atomic number contrasts.

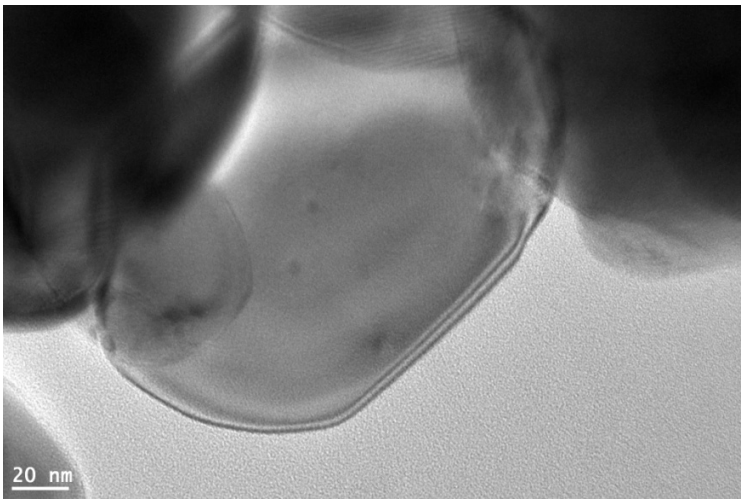

Figure 3.2: Uncoated TiO_2 (100,000 x Magnification, Bright Field Image)

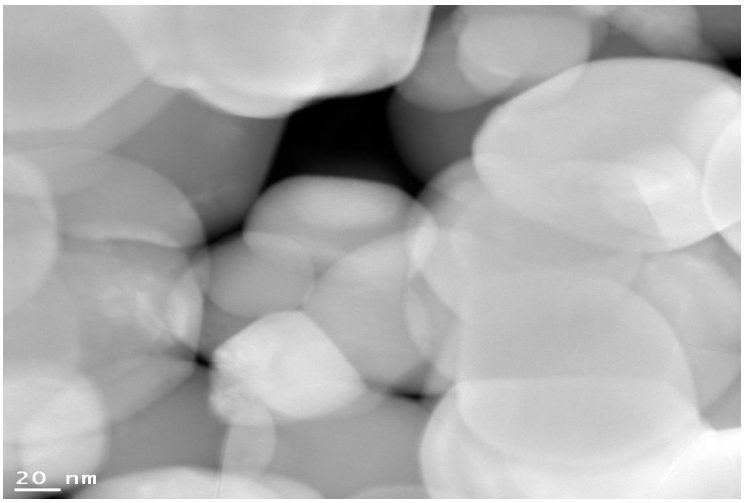

Figure 3.3: Uncoated TiO2 (50,000 x Magnification, HAADF Image)

3.5.2 Coated TiO_2 (9% w/w)

BF images of coated TiO_2 identify a web of material covering multiple particles. Rochelle *et al* (1980) found from SEM analysis that $Al(OH)_3$ forms 'webs' covering multiple particles therefore the 'webs' seen in Figure 3.4 are positive identification of a coating and not a spectra artefact. Evidence supporting the hypothesis that the $Al(OH)_3$ is acting as a 'glue' causing congregation of multiple TiO_2 particles is found in the HAADF spectra presented in Figure 3.5. $Al(OH)_3$ is a lighter material than TiO_2 so appears as a darker colour within a HAADF image. It is possible to see an Al rich, dark ring, around the meeting point between small particles with a larger particles and as a seam between the denser TiO_2 particles. Energy Dispersive X-rays (EDX) confirmed these dark rings and seams as being aluminium rich confirming their identity as ($Al(OH)_3$ (Figure 3.6).

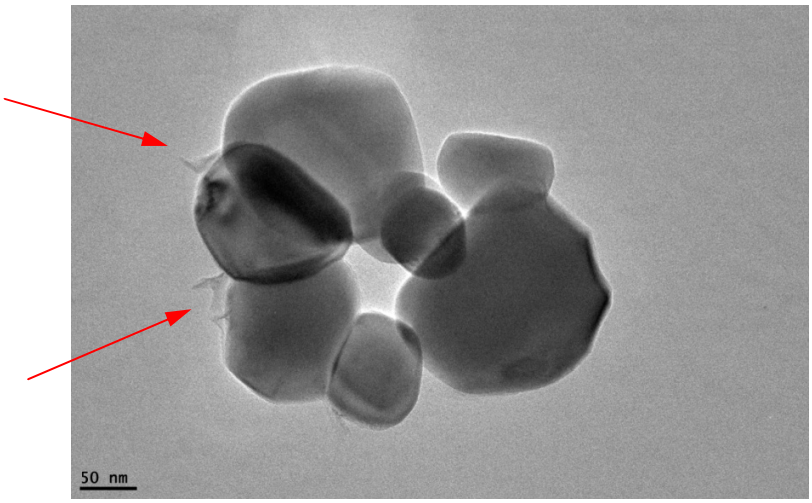

Figure 3.4: 9% coated TiO_2 (40,000 x Magnification, Bright Field Image)

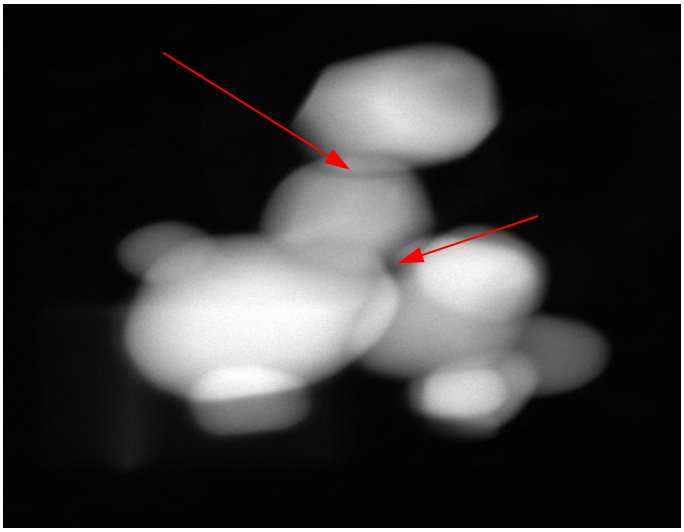

Figure 3.5: 9% coated TiO_2 (20, 000 x Magnification, HAADF Image)

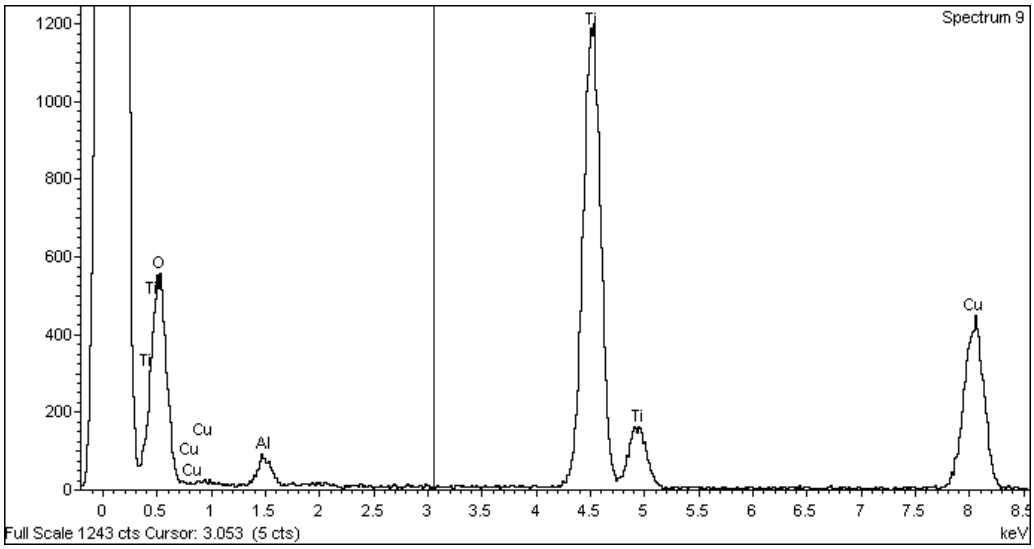

Figure 3.6: EDX taken at a Fringe of Two Overlapping Particles Confirming the Presence of Aluminium

3.6 Glass and Filler Size Characterisation

The manufactured cement powders and base materials were analysed for particle size distribution using a Micromeritics Saturn Digisizer™ 5200. The dispersion liquid for manufactured TiGIC powder was methylated spirits (95% ethanol, 5% methanol). This was used, rather than water, to prevent the acid-base reaction taking place within the instrument and clogging the inlet / outlet pipes. The auto-sampler exposed each sample to 60 seconds of mechanical mixing, during which the samples were sonicated for 30 seconds to ensure a homogeneous dispersion with no agglomerates. Each sample was analysed three times to check the consistency of the results and to allow a (more accurate) average determination.

The particle size distribution of ASG and TiO_2 can be seen in Figure 3.7. The particle size range of ASG is 250.0-1.0 µm with a mode at 37.5-16.0 µm. TiO_2 has a particle size range of 12.0-0.1 µm with the bulk of particles in the range 2.0-0.1 µm; the mode is present in the range 0.25-0.1 µm. The Saturn Digisizer was unable to detect particle sizes smaller than 0.1 µm so if, for example, a Gaussian distribution is present with a mean centred around 0.1 µm then it is reasonable to predict the presence of particle sizes smaller than 0.1µm in TiGIC samples.

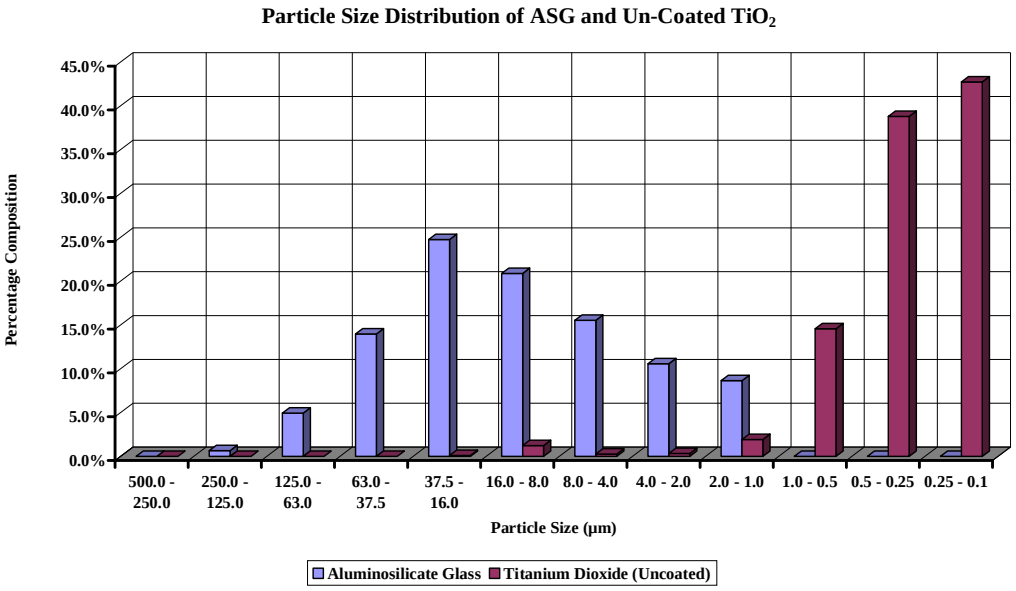

Figure 3.7: Particle Size Distribution of ASG and Un-Coated TiO_2

The coating process has caused the TiO_2 particles to form larger conjoined particles held together by the $Al(OH)_3$ precipitate which is visually evident from Figure 3.4. There is no obvious trend to the way in which the coated particles have increased in size however the particle size range has changed from 12.0-0.1 µm to 187.5-0.1 µm although the modal particle size remains in the range 0.25-0.1 µm (Figure 3.8).

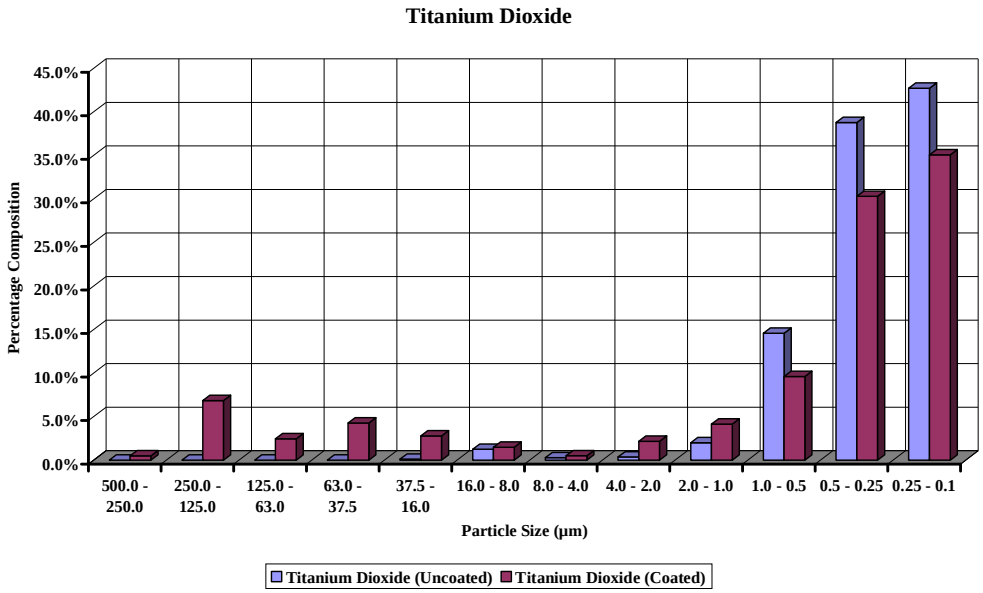

Figure 3.8: Particle Size Distribution of Coated and Un-Coated TiO_2

The particle size distribution of coated and un-coated 2.5% incorporated cements can be seen in Figure 3.9. The coated and un-coated cements have similar particle size distributions with the only discernable difference being the slightly higher concentration of larger particles 8.0-250 µm in the coated filler cements.

As previously seen, the uncoated TiO_2 had a larger frequency of particles sized 0.25-0.1 µm than coated TiO_2. This was expected to be true in TiGICs however Figure 3.9 does not show this trend. The unexpected frequency reversal and the absence of any particles in the range 1.0-0.5 µm suggests that the samples had not been agitated properly before analysis. This is possible given that these samples were the last to be analysed and therefore had the largest amount of time to agglomerate and settle.

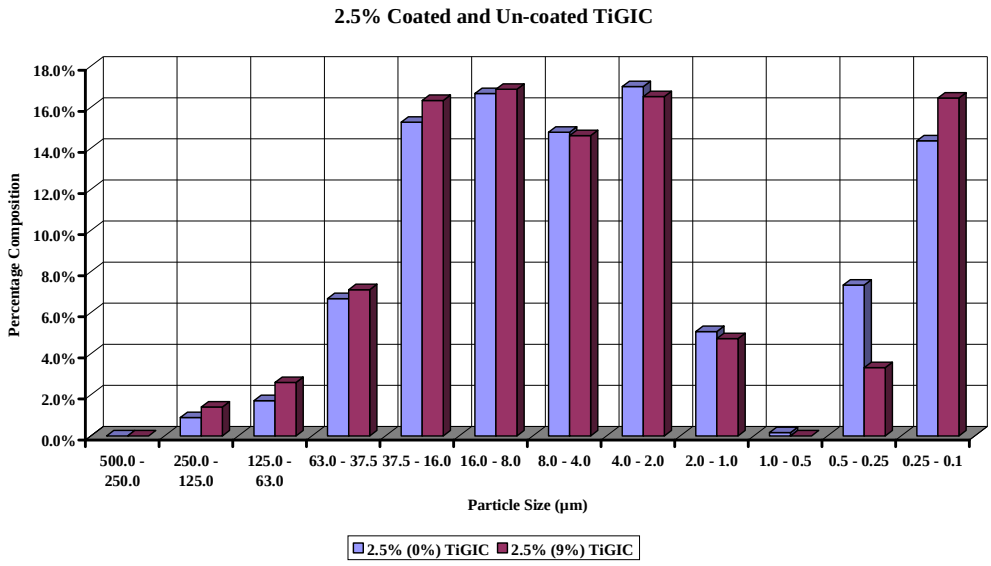

Figure 3.9: Particle Size Distribution of 2.5% TiGICs Incorporating Coated and Un-Coated Filler Particles

The general difference between the coated and un-coated filler cements is the higher frequency of larger particles as a result of conglomeration caused by filler precipitation.

3.7 Coating Reactivity

$Al(OH)_3$ is known to react and neutralise strong acids however the acids used in GICs (PAA, PVPA-PAA and TA) are not strong (pKa < -2). It is therefore important to find out if the coating on the surface of the filler particles in new TiGICs is capable of reacting with the polyelectrolyte solution.

The measured pH of solutions characteristic of the concentrations found in DC liquid are presented in Table 3.3 along with their reported pK_A values (Balasubramanlan & Mlsra, 1977; Wilson & Nicholson, 1996; CRC Handbook, 1992; Peacock & Calhoun, 2006).

pH of Solutions (in correct concentration) used in DC and Reported pK_A Vales		
Acid	pH	pK_A
PAA	1.89	5 to 6
PVPA/AA	3.70	2 and 8
TA	1.54	2.96 and 4.16
HCl	1.00	-3 to -5

Table 3.3: Acid Properties of Solutions used in and for the Analysis of DC Liquid

$Al(OH)_3$ has previously been reported to react with PAA and form a stable cement (Hu & Saniger, 1992; WU *et al*, 1997; Lewandowski & Koglin, 2000; Pefferkorn, Pefferkorn *et al*, 2001). It was therefore believed that its presence on incorporated fillers would 'cement' them into the control cement.

There are many pharmaceutical methods for determining the reactivity of $Al(OH)_3$ used as antacids (Rossett- Rice, 1954, Hem, 1975; Washinton, 1991; Peterson, 1992) all of which are titrametric methods.

The Rossett-Rice acid reactivity test was chosen to find the acid reactivity of $Al(OH)_3$ as it provided time dependent data which was of particular importance as DC undergoes rapid neutralisation during the setting reaction.

The same method adapted to use acetic acid has been successfully used to characterise the reactivity of ASGs used in GICs (De Maeyerl *et al*, 1998).

3.7.1 Rossett-Rice Reactivity

The Rossett-Rice time is the length of time a quantity of dry $Al(OH)_3$ gel (equivalent to 300mg of aluminium hydroxide) dispersed in 70 millilitres of 0.1N hydrochloric acid and 30 millilitres of water at a temperature of 37ºC is able to remain at a pH between 3 to 5 as additional 0.1N hydrochloric acid is added to the mixture at a rate of 4 millilitres per minute via a peristaltic pump. The temperature used in the pharmaceutics adaptation is 37ºC to mimic the core temperature of the human body; experimentation was conducted at 20ºC ±1ºC to mimic average room temperature. The solution was constantly agitated using a magnetic stirrer at 300 RPM. The target dwell time for a commercial antacid is 60 minutes (Peterson, 1992).

Freshly precipitated $Al(OH)_3$ was prepared as in section 3.2 without the need for a TiO_2 suspension. The reaction between the precipitated aluminium species and 0.1N HCl can be seen to be slow (Figure 3.10), taking between 25-30 minutes to reach equilibrium. The Rossett-Rice time achieved by the fresh precipitate after equilibrium was 6 minutes 20 seconds (Figure 3.11) which is poor when compared to other commercial antacids available (Washinton, 1991; Peterson, 1992).

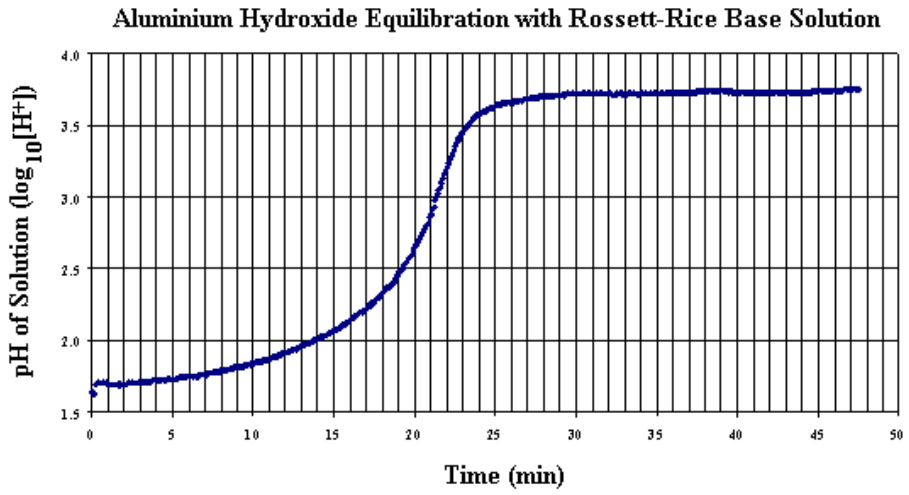

Figure 3.10: Aluminium Hydroxide Equilibrium with 0.1N HCl Solution

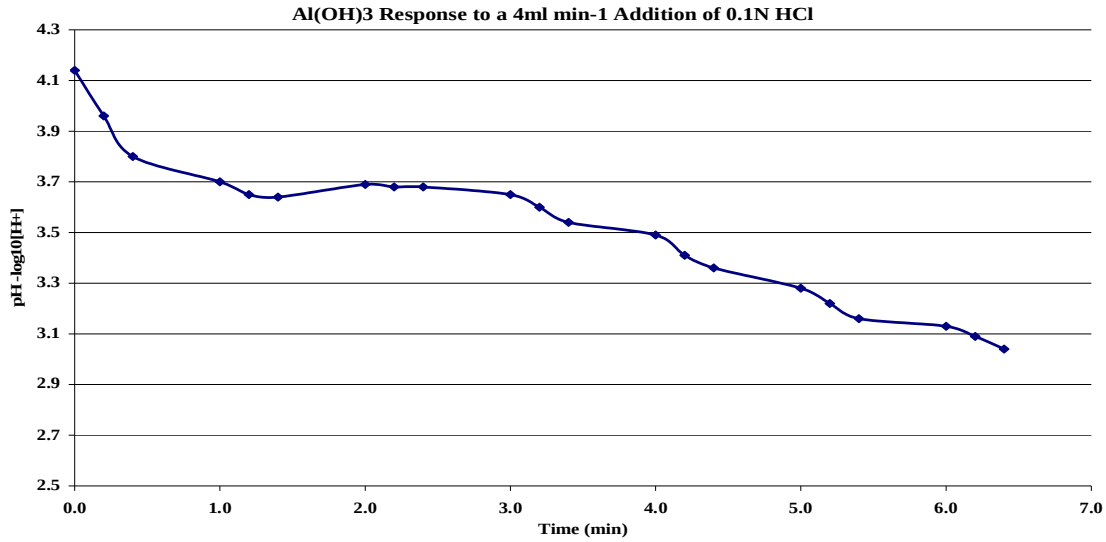

Figure 3.11: Rossett-Rice Reactivity Test Performed on Freshly Precipitated $Al(OH)_3$

The Rossett-Rice test identified the presence of a slow reaction between the $Al(OH)_3$ coating with a strong, dilute acid. In Figure 3.10 the $Al(OH)_3$ is in excess compared to H^+ ions identifying an activation energy deficiency; not enough energy is available to drive the reaction to completion. Elevated temperatures like found in the mouth would increase the amount of energy in the system ultimately increasing the speed of reaction if normal reaction kinetics are observed.

The likeliness of a reaction between $Al(OH)_3$ and any of the polyelectrolyte's found in DC is minimal. Additionally, the rapid neutralisation of polyelectrolyte's takes place in the first 120 seconds after mixing in which time a cement is formed.

3.7.2 $Al(OH)_3$ Titration

In order to confirm or refute a slow reaction taking place between $Al(OH)_3$ and the matrix forming polyacrylic acids, a simple potentiometric test was prepared. A colloidal dispersion that contained a great excess of $Al(OH)_3$ was prepared into which PAA was added. The pH was then monitored with time to identify a neutralisation reaction taking place.

The $Al(OH)_3$ dispersion consisted of 10ml of distilled water and 6 mg of dry $Al(OH)_3$ gel. A PAA solution was made by tenfold dilution of PAA used in DC cement with distilled water to reduce complications arising from viscosity increases during neutralisation. The pH was monitored after 0.1 ml of dilute PAA solution was added to the $Al(OH)_3$ dispersion and a plateau was reached.

The pH of the solution before PAA addition was 3.94, this decreased to 3.21 immediately after addition 0.1 ml of PAA. The pH of the $Al(OH)_3$ – PAA solution then slowly recovered to 3.91 after approximately 20 minutes (Figure 3.12). Although no quantitative data was produced during this quick test it has positively identified a reaction between PAA and $Al(OH)_3$ although the speed of the reaction that would take place between these two species during the setting of TiGICs can not be implied.

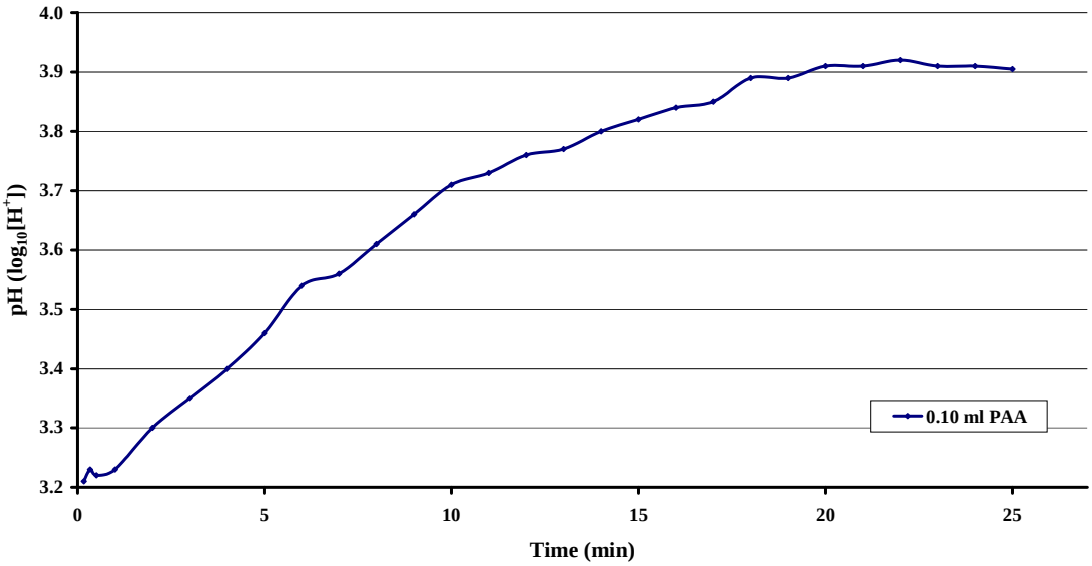

Figure 3.12: Time Delay between 0.1 ml PAA Addition and pH Response of an $Al(OH)_3$ dispersion

The speed with which PAA and $Al(OH)_3$ react in TiGICs would aid the understanding of the initial working and setting times as well as filler incorporation into the GIC network however, such low levels of coating are present it is unlikely that a noticeable difference will be found. Therefore, at the levels of coating used in TiGIC cements the coating will only aid the incorporation of the filler into the GIC matrix regardless of reactivity.

Chapter 4

Rheological Analysis of TiGICs

Aim

The aim of this chapter is to establish the working, setting times and short term strength increase (<1 hour) of DC and experimental TiGICs using a Wilson and modern, technologically advanced, ossiclating rheometers.

4.1 Introduction

Methods for the elucidation of handling properties of Glass Ionomer Cements (GICs) for clinical use are contained within the European Standard for water based dental cements – EN ISO 9917-1.

The working time is found using an oscillating rheometer, coined the 'Wilson Rheometer' after the involvement of A. D. Wilson throughout the development of the apparatus (Bovis, Harrington & Wilson, 1971; Wilson, Crisp & Femer, 1976) and invention of the glass ionomer cement (Wilson & Kent, 1972; Wilson & Nicholson, 1996; Wilson, 1996).

A technologically advanced oscillating rheometer is used in conjunction with a Wilson rheometer to find additional cement properties during the setting reaction better aiding the understanding of handling properties.

4.2 Experimental Methods

Experimental parameters such as oscilation frequency and plate seperation (*see* Section 4.2.2) used with the AR2000 advanced rheometer have been found from preliminary tests and have been implimented to mimic the Wilson rheometer and provide the most defined and repeatable results (*see* Appendix 3).

Experiments carried out on the Wilson rheometer were performed at both room temperature (23±1°C) and 15ºC so that a comparision with the results obtained from the AR2000 could be made as experiments could only be performed at 15ºC using the AR2000. This was due to the speed at which the automated plates on the AR2000 came together allowing the GIC sufficient time to form a hard cement preventing the plates from closing at room temperature.
Ten repeats were performed for each sample using both techniques and averaged results are presented.

4.2.1 Wilson Rheometer

The Wilson rheometer consists of the main oscillating body and a pen plotter that records the amplitude of the oscillation via a transducer (mechanical signal to electrical signal).

All cement samples prepared for analysis on the Wilson rheometer were encapsulated cements. Encapsulated cements were found to be the most repeatable way in which to mix the control and TiGICs (*see* Appendix 2). It was noticed that the viscosity of encapsulated TiGICs was greater than the control material immediately after mixing. The viscosity increased with increasing filler content. This will be as a result of particle loading (DuPont Titanium Technologies, 2010) outweighing the shear thining effect of the amalgamator on the PAA polymer (Flory & Osterheld, 1954; Sundstrom, 1983; Yang *et al*, 2001).
The cements were prepared as described in Chapter 3.

The following steps describe the experimental method used with the Wilson rheometer,

1. The pen plotter must be started at the same time as the cement capsule is crimped and the reaction is initiated.
2. The mixed cement is extruded onto the bottom oscillating plate of the rheometer.
3. The top platen is manoeuvred into place sandwiching the sample in place.
4. The top plate is fastened into place using a quick threading nut.
5. The experiment is left to run until the amplitude of the resultant pen plot reaches approximately 2% of the initial amplitude.

6. The cement sample is detached from the rheometer plates by removing the top plate and leaving the cement in air for 1-2 minutes.

When performing tests at 15ºC a refrigerated water bath with a programmable thermostat was connected to the top brass platen and allowed to reach and maintain a constant 15ºC. The temperature was continuously monitored using a thermocouple.

4.2.2 Advanced Rheometer

The set-up (calibration) of the AR2000 rheometer is performed according to the operation manual.

Aluminium plates were used instead of brass plates like on the Wilson rheometer, this decision was made after comparison between aluminium and brass plate materials in the investigatory experiments which showed that the cement adhered best to aluminium and slipped less at high viscosities (*see* Appendix 2). The plates have a contact diameter of 10mm so are comparable with the Wilson rheometers plates. The plates used on the advanced rheometer have a flat surface instead of a serrated surface (as on Wilson rheometer) to avoid complex angular velocities being created and complicating subsequent calculations of viscous and elastic moduli.

The user defined parameters are the oscillation frequency, plate separation (experimental and back of distances), applied shear stress (torque), ETC temperature and data acquisition length.

Parameters defined by user,

1. ***Oscillation frequency –*** set at 0.1667 Hz to mimic the Wilson rheometer.
2. ***Applied shear stress*** – set at 2000Pa after investigatory experimentation (*see* Appendix 2)
3. ***Plate Separation*** - The experimental distance was set at 1mm to mimic the distance between the Wilson rheometer plates. The back off distance was 10mm to allow placement of the sample cement.
4. ***Acquisition length*** – A length of 40 minutes was used with DC and a length of 60 minutes was used with the TiGICs.
5. ***ETC temperature*** – set at 15ºC to avoid condensation forming on the plates.

All experimentation was started 90 seconds after the activation of the capsule and the loading process proceeded,

1. Capsule activated and mixed (*see* Chapter 3)
   0-30 seconds
2. Capsule extruded onto the rheometer plates
   30-50 seconds
3. Rheometer plates closed to experimental distance
   50-70 seconds
4. ETC closed and allowed to activate
   70-80 seconds
5. Acquisition Began
   90 seconds

4.2.3 Data Analysis (Wilson Rheograms)

4.2.3.1 Working Time(s)

The working time of a GIC from a Wilson rheogram has been defined using two separate methods that produce only slightly different results (Bovis, Harrington & Wilson, 1971; Wilson, Crisp & Ferner, 1976).

The method chosen and used throughout calculations is defined by Bovis, Harrington & Wilson (1971) and is described as the amount of time needed for the initial amplitude at the beginning of experimentation to decrease by 5%.
The working time was found as follows (Figure 4.1),

1. Measure the amplitude at the beginning of experimentation.
2. Calculate 95% of the initial amplitude and mark the length on the fringes of the rheogram.
3. Measure vertically upwards from the baseline to the point where the 95% amplitude marks have been made. The vertical length is converted into the working time.
4. An average between sides is taken and this average is the final reported working time.

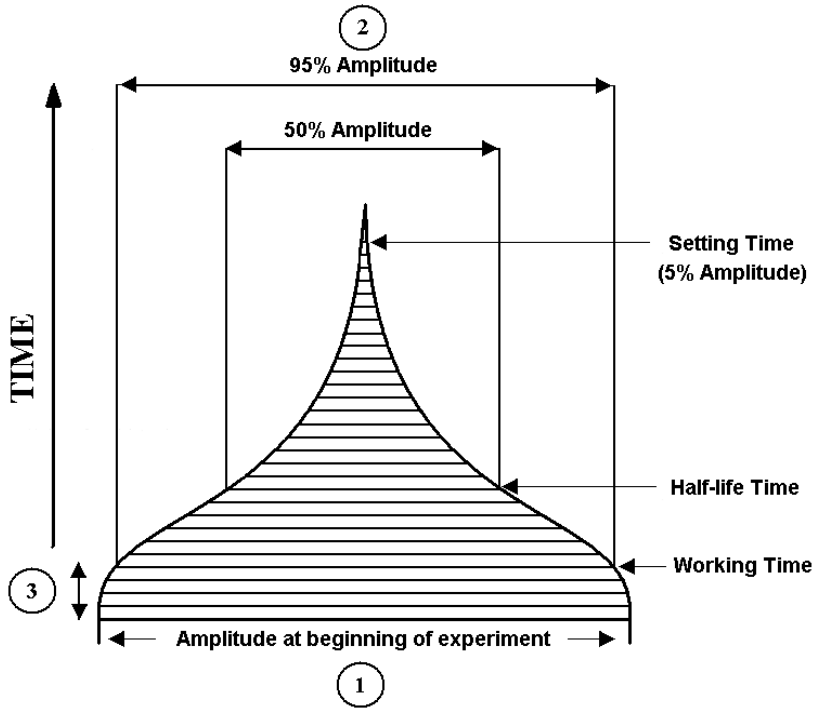

Figure 4.1: How to Calculate the Working Time of A GIC using the Bovis *et al*, 1971 Method

The Bovis *et al* method was found to produce a tighter standard deviation than the Wilson *et al* method although 'in practice very little difference is observed in the working times from oscillating rheometry obtained by either of these construction methods' (Wilson and Nicholson, 1993).

4.2.3.2 Setting Time

The setting time is calculated (Figure 4.2) by the following steps,

1. Measure the amplitude at the beginning of experimentation.
2. Calculate 5% of the initial amplitude and place two lines extending from the baseline until the line intersects with the rheogram.
3. The vertical length to the point of intesection is then converted into the setting time.

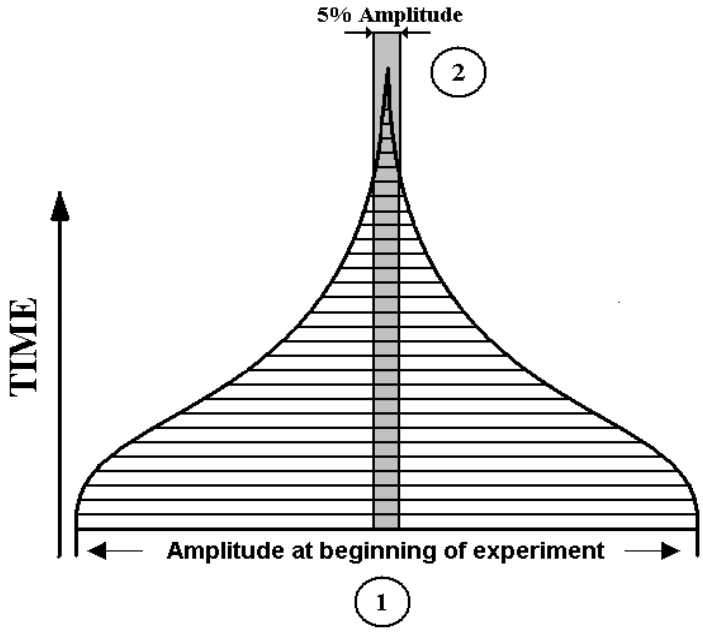

Figure 4.2: How to Calculate the Setting Time of a GIC

4.3 Results and Discussion

A large amount of preliminary work was performed on the advanced rheometer to identify the cause of inconsistent results, the formation of a periodic increase in phase seperation as the cement continued to harden and the most suitable way to retard the setting reaction. Additionally, the best operating parameters were established including the most suitable plate material. These results are presented in Appendix 2.

4.3.1 Wilson Rheometer

Clinically, the results from the Wilson rheometer at 15ºC are of minor importance because standard measurements are taken at 24ºC (Wilson & Nicholson, 1993). However, calculation of the working and setting times at 15ºC from the Wilson rheometer will allow the correlation with data obtained from the AR2000 rheometer providing a better understanding of the viscoelastic properties of the sample cement.

The temperature dependence of the observed working and setting times is shown in Table 4.1. It can be seen that there is a variation of between 40 and 66 seconds in the working and setting times of the control cement with a temperature difference of 1ºC respectively. Decreasing the temperature by approximately 7ºC causes the working and setting times to elongate by 273 and 335 seconds respectively. Whilst performing experiments using the Wilson rheometer the ambient and water bath temperatures fluctuated by 1.9 ºC and 1.7 ºC respectively introducing uncertainty into the recorded working and setting times.

The working time of uncoated TiGICs decreases with increasing filler incorporation opposite to the working time of coated TiGICs which increased with increasing filler volume. A significant temperature difference between higher and lower concentration, coated, TiGICs may cause this effect so a direct comparison is not made. The shortening of the working time with increasing filler volume is currently attributed to mechanical filler effects of TiO_2. A personal communication from Dr L H Prentice who has previously reported similar results (Prentice *et al*, 2006) is in agreement with this hypothesis. It follows that PAA is strongly absorbed onto the surface of TiO_2 and $Al(OH)_3$ which will have a similar effect as the cross-linking mechanism, restricting the movement of polymer (Strauss *et al*, 1993; Buleva *at* al, 2001; Liufu *et al*, 2005; Chen & Wei, 2007). The increased viscosity of the particle loaded polymer therefore means that less salt bridges (cross-linking) are required to reach the viscosity known as the working time.

The average values of setting time displays the same trend as the working times, allowing for temperature differences. The inclusion of $Al(OH)_3$ as a coating on the filler has the effect of prolonging the setting time when compared to the same volume of uncoated filler incorporation. There is a large error associated with the setting times because of the way in which it is measured. When making and taking results at 5% amplitude slight errors (e.g. 0.5 mm horizontal error equates to 2.8 mm vertical error or 17 seconds assuming a 80º gradient) can result in large errors when dealing with large gradients.

The powder to liquid ratio (P:L) is known to affect the setting profile of GICs (Lewis & Wilson, 1976; Fleming *et al*, 2003). A decrease in the P:L has been shown to increase the setting time of conventional GICs whilst decreasing the mechanical strength of the cement. The replacement of ASG with an inert (TiO_2) or low reactivity ($Al(OH)_3$) filler particle is effectively the same as decreasing the powder to liquid ratio and is therefore the most likely cause of the elongation of the setting time.

Working and Setting Times of Sample Cements			
Sample	**Temperature (ºC)**	**Working Time (s)**	**Setting Time (s)**
Diamond Carve	15.5±0.8	478±18	747±29
	22.0±0.3	205±10	412±21
	23.3±0.3	165±15	346±38
2.5% (0%)	16.7±0.5	411±14	1168±63
	23.9±0.5	102±8	528±33
2.5% (9%)	17.2±0.9	305±8	984±73
	23.1±0.2	106±6	545±19
7.5% (0%)	16.4±1.0	270±13	1084±20
	23.3±0.3	116±14	663±73
7.5% (9%)	16.5±0.8	356±24	1122±83
	23.4±0.3	165±15	811±64

Table 4.1: Working and setting times of Diamond Carve (Control) and Experimental TiGICs

4.3.2 Advanced Rheometer

The information provided by the advanced rheometer includes the extent of cure, how strong (in compression) the cement is at a given point and how these two properties develop as the cement sets. The increased sensitivity of the advanced rheometer allowed it to be used to follow the curing reaction for 40-60 minutes where the Wilson rheometer wasn't able to follow the reaction past 20 minutes with any accuracy.

The extent of cure can be imagined as the amount of cross-linking present in the cement. This process suppresses viscous flow and enhances elastic character. In its most basic terms, cure is the transition from viscous to elastic character (Hough *et al*, 2009). This change can be monitored using the phase separation (δ) between an applied sinusoidal stress and the resultant strain (Figure 4.3). A lag of 90º is representative of a Newtonian fluid (all energy dissipated) whereas a lag of 0º represents a Hookean solid (all energy is stored).

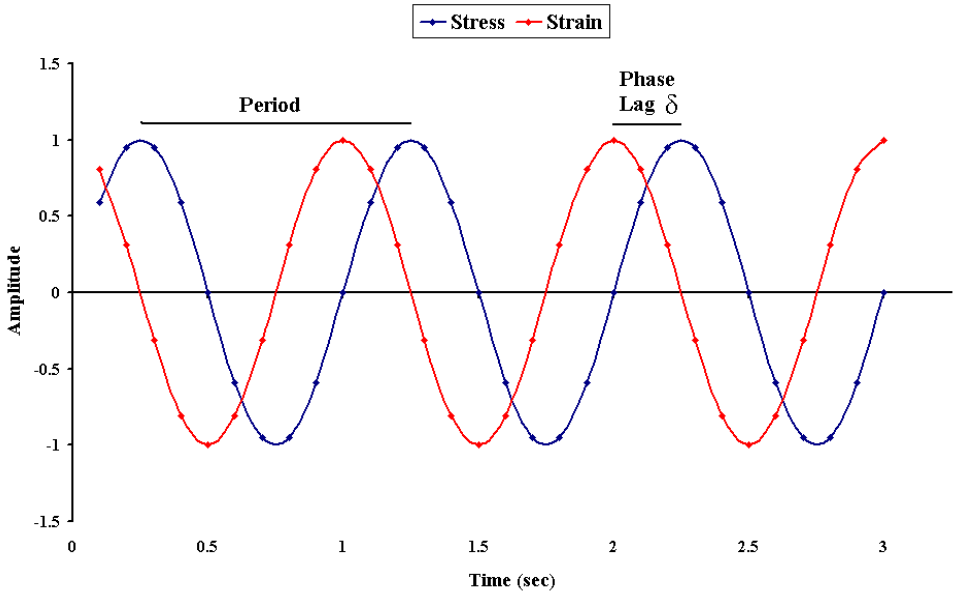

Figure 4.3: Illustration of the Phase Lag between an Applied Stress and Resultant Strain Measured by AR2000 Rheometer

The delta angle does not take into account the rigidity of the material (complex modulus, G^*) therefore the storage modulus (G') will be a better way to measure the extent of cure. The storage modulus (Eqn 2) is a way of measuring the amount of elastically stored energy in the system; given that cure has been defined as the change from viscous to elastic character this modulus is an ideal way to monitor the cure.

$$G' = \frac{\sigma_0}{\gamma_0}\cos\delta = G^* \cos\delta \qquad \text{Equation 2}$$

where σ_o is the stress at maximum amplitude, γ_o is the strain at maximum amplitude, G^* is the complex modulus and δ is the phase angle between the applied and resultant oscillating stress and strain.

The loss modulus (G'') provides information about how the sample is 'flowing' during the test. Interpreting both the storage and loss modulus (Eqn 2 & 3) together is the best way of predicting the cements properties (e.g. elastic, brittle) and strength as it cures e.g. A cement with a large G' and G'' would be stronger in compression than a cement with a large G' but small G'' because of the ability to loose energy through heat and vibration.

$$G'' = \frac{\sigma_0}{\gamma_0}\sin\delta = G^* \sin\delta \qquad \text{Equation 3}$$

Graphical representation of the data generated by the advanced rheometer is the best way to visualise the physical changes undergone by sample cements during the curing process. Figure 4.4, Figure 4.6 and Figure 4.7 show the phase lag, storage modulus and loss modulus of DC and all TiGICs.

Data is presented for 40 minutes for the control material because the sample begins to slip and come away from the rheometer plates after this period. Data is presented for 60 minutes for the TiGIC samples because they adhere to the rheometer plates; data becomes increasingly noisy around 60 minutes due to the plates slipping and internal noise so experimentation was stopped.

4.3.2.1 Phase Lag

All TiGICs from Figure 4.4 show a smaller phase lag at the beginning of acquisition than the control material. This has previously been found during the Wilson rheometer analysis of working time and confirms the increased viscosity during first 5 minutes of cure.

The phase separation for the 2.5% (9%) TiGIC has a lower value than the other TiGICs which was not expected from the working times. The rate of cure can be seen to be approximately the same as the other TiGICs but offset by approximately a minute (Figure 4.4). Elevated room temperature during mixing (Average – 23.7±0.3ºC; 2.5% (9%) - 25.3±0.8ºC) is expected to have caused increased levels of cure before loading into the rheometer explaining this observation.

The control material experiences a periodic increase in phase separation around 5 minutes for a period of approximately 200 seconds after which the value comes back into line with the TiGICs and then precedes below it (Figure 4.4). This periodic increase in delta would suggest that the control material had become less or stopped increasing in viscosity for a short period during the curing reaction. This is believed to be due to the snap set characteristic of the control material instilled by TA which has been lost in the TiGICs. The periodic increase in delta seems to be a precursor for cement to become a rubbery material for a short period of time after 10 minutes as shall be seen later in from Storage and loss moduli data. The occurrence of a competing chemical reaction may be identified using infrared spectrometry.

The final values of delta indicate that the control material had cured further (greater solid contribution) than the TiGICs.

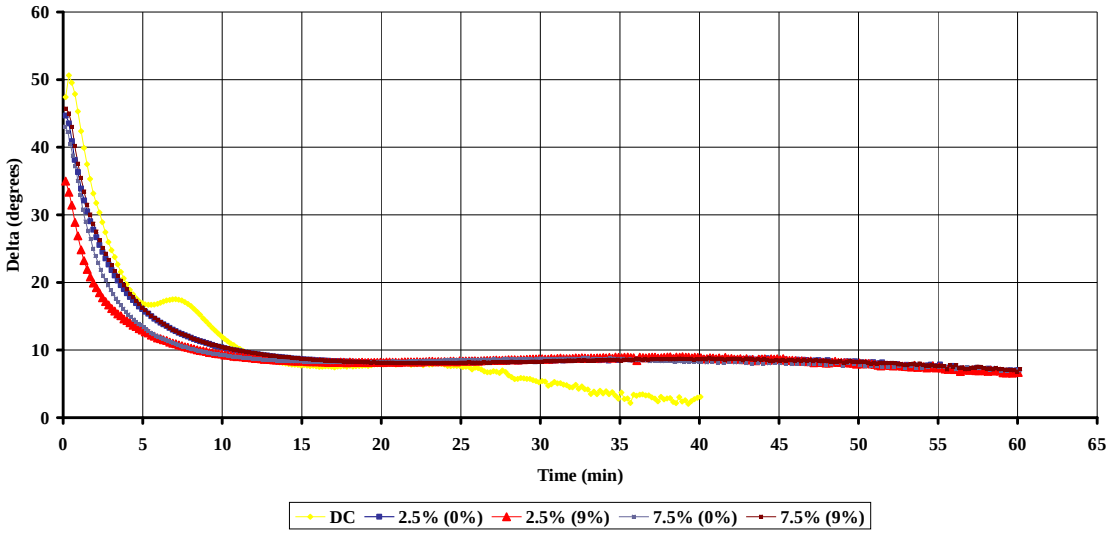

Figure 4.4: Phase Lag between Applied Stress and Resultant Stain of Curing TiGICs and DC

4.3.2.2 Storage Modulus

The control material can be seen to have a low storage modulus for the first 8 minutes of observation which is then followed by a sharp increase in viscosity (Figure 4.6). This characteristic is known as a 'snap set' which has been introduced by TA which preferentially reacts with cations preventing the gelation of the polyacids. The snap set provides a long working time allowing easy placement of the cement followed by a rapid increase in cure speed reducing water susceptibility and the likeliness of damage from opposing forces.

The control material displays a characteristic s-shaped graph (Figure 4.5) which is typical of a neutralisation reaction (Clayden *et al*, 2000). The storage modulus deviates from this s-shaped curve during 0-10 minutes where it maintains a low viscosity and then during 10-15 where it increases faster than the fitted curve; the rapid increase in G' after 10 minutes coincides with the downturn in the periodic increase of δ. After this sharp increase in modulus the rate of increasing G' returns to follow the perceived s-shape.

The maximum continual linear increase in viscosity is seen between 20 – 30 minutes and the rate of increasing G' is 10.329 MPa s^{-1} (R^2 = 0.9992). The trace begins to crest after this point and it is assumed that a plateau will occur shortly after 40 minutes where the curing reaction is considered complete.

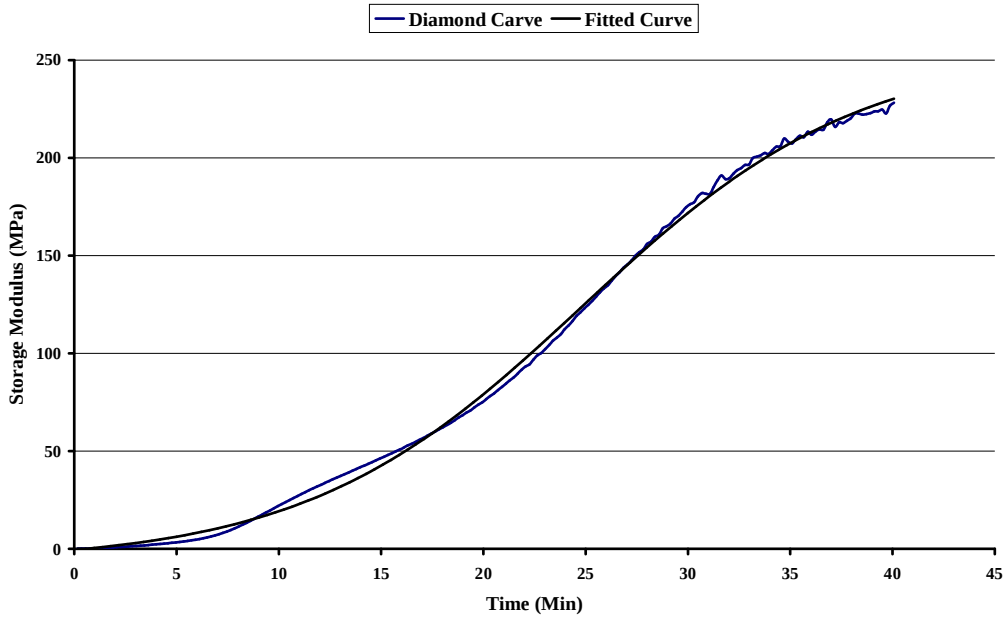

Figure 4.5: Storage Modulus of Diamond Carve with a Curve Fitted to the Data Representing a Typical Neutralisation Reaction

The TiGICs have a continuous linear increase in storage modulus and experience only a small change in gradient around 35 minutes (Figure 4.6). The TiGICs have lost the 'snap set' characteristic although the same level of TA has been used within these cements. The rate of G' increase during the initial 35 minutes of reaction in all the TiGICs is approximately 10% that of the control material (Table 4.2). The curing progress during the later 25 minutes was approximately 20% that of all TiGICs. Prosser *et al* (1982), Cook (1982) and Wilson & Nicholson (1993) have reported that a snap set is not present when excessive levels of TA are present. The addition of large concentrations of TA also increase the setting time of conventional GICs.

The advanced rheometer has identified that the curing speed in the TiGICs is severely retarded by the removal of ASG and addition of TiO_2 / $Al(OH)_3$.
Trends found in the Wilson rheometer are mimicked in the results from the advance rheometer. Increasing the filler volume increases the viscosity (possibly due to sub-micron particle loading); the presence of a coating appears to reduce the viscosity when compared to the same volume of non-coated filler.

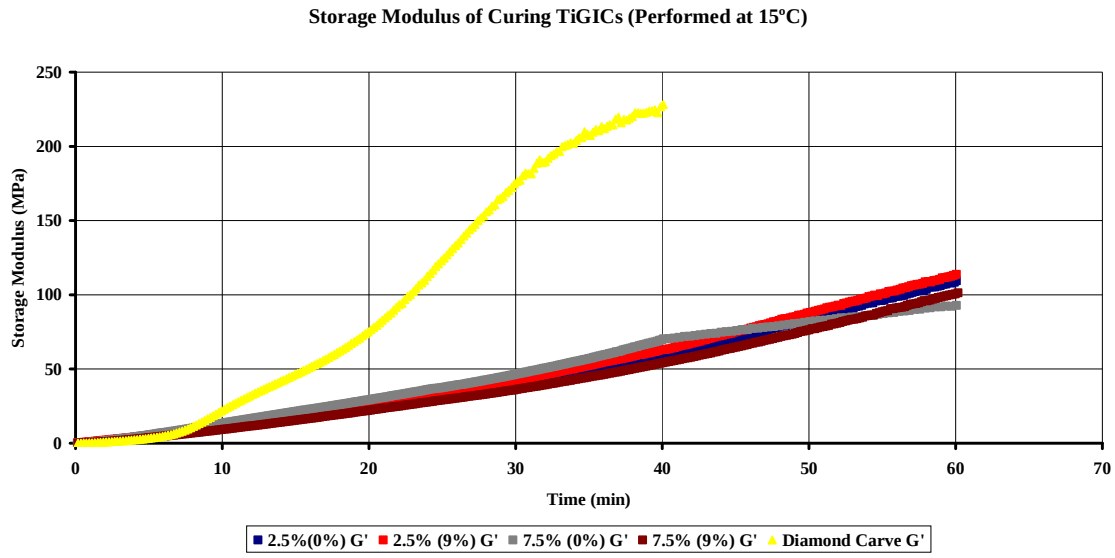

Figure 4.6: Storage Modulus Change over Time in Curing TiGICs

Sample		Gradient (MPa s^{-1})
Control	20-30 min	10.329
2.5% (0%)	0-35 min	1.418
	35-60 min	2.446
2.5% (9%)	0-35 min	1.483
	35-60 min	2.490
7.5% (0%)	0-35 min	1.276
	35-60 min	2.012
7.5% (9%)	0-35 min	1.301
	35-60 min	2.278

Table 4.2: Gradient Values for Linear Elastic Modulus Increase(s)

The loss modulus can be used in conjunction with the storage modulus results to gain an insight into the structure of the cement which can be used to predict the strength of the sample in compression.
The viscosity remains low during the first 8 minutes of cure in the control material, the combination of low G' and G'' moduli (Figure 4.7) and greater δ values when compared to the TiGICs provide evidence that the material is less viscous and able to flow more readily than the TiGICs. The control cement is still dominated by its elastic modulus during the first 8 minutes so the user needs to be aware that subtle, low force changes in placement geometry may result in the cement returning to its original shape.

The viscosity of the control material quickly increases at the beginning of the 'snap-set' which can be seen in the loss modulus as a large increase due to the higher amounts of energy being dissipated (G* is dominated by the sinδ term). This is because the polymer matrix is still able to flow ($0<\delta$) but it takes a larger amount of energy to force the polymer chains past one another due to increasing cross-linking. A peak is reached by the G'' modulus of the control material after 28 minutes which is believed to be caused by the total entanglement (cross-linking) of the polymer analogues to a rubbery to glassy phase transition (Macosko, 1994). The downturn in the G'' of the control material is therefore as a result of decreasing energy losses due to the formation of a solid cement network with increasing hardness and brittle nature. At the end of monitoring the control material, the storage modulus was over an order of magnitude greater than the loss modulus (Table 4.3).

The loss moduli for the TiGICs have not peaked after 60 minutes unlike the control material. The lack of a maxima combined with the low relative storage modulus and greater delta values compared with the control material clearly indicate that all TiGICs have not completely cured and will be much softer at 60 minutes than the control material at 40. This will be directly reflected in the compressive strength values.

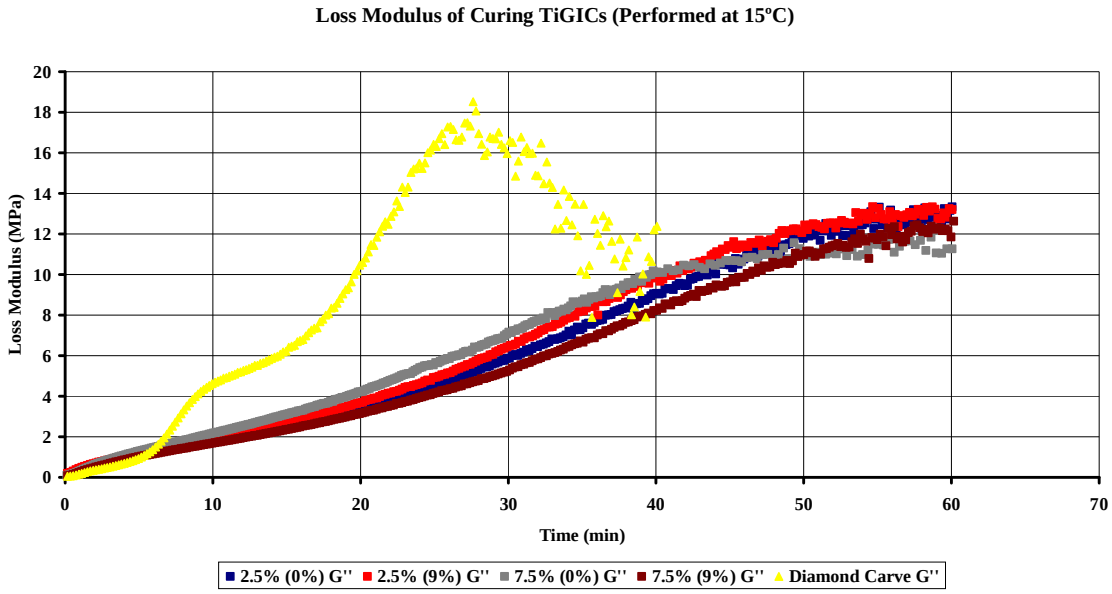

Figure 4.7: Loss Modulus Change over Time in Curing TiGICs

The maximum storage and loss moduli of DC and all TiGIC samples are presented in Table 4.3. The values of storage modulus suggest that the compressive strength of the TiGICs will be approximately half that of DC at 60 minutes. There isn't a TiGIC sample that produces noticeably greater G' or G'' values because of the overlapping deviation in results. As previously found in the investigatory tests (*see* Appendix 3) and the Wilson rheometer results there appears to be a natural variability in the cements which is complicated by the slightest fluctuation in temperature.

Maximum Storage and Loss Moduli (15ºC) of Novel TiGICs		
Sample Material	**Storage Modulus (MPa)**	**Loss Modulus (MPa)**
Diamond Carve	228.19±18.24	18.52±2.18
2.5% (0%) TiGIC	109.39±16.46	13.33±1.76
2.5% (9%) TiGIC	113.85±22.29	13.56±2.18
7.5% (0%) TiGIC	92.87±15.14	11.27±1.18
7.5% (9%) TiGIC	101.29±14.54	12.63±1.08

Table 4.3: Storage and Loss Moduli of Diamond Carve and Experimental TiGICs performed at 15ºC

4.4 Conclusion

The working and setting times of the control material (Diamond Carve) were established as 165 and 346 seconds respectively at room temperature (22±1°C). (reported working time of 135 seconds and setting time of 310 seconds at 23ºC (Kemdent LTD)). Lowering the temperature by approximately 7ºC has a large effect on the curing properties of the cement. The working time has been elongated by 313 seconds (478) and the setting time by 401 seconds (747). Therefore, lowering the temperature to 15ºC means that the progress of the reaction can be monitored at a greatly decelerated rate.

The inclusion of filler material to the original DC cement has caused a shortening of the working time and an elongation of the setting time. The role of $Al(OH)_3$ coating is unclear, the coating elongates the working time but shortens the setting time. This may be due to differing degrees of absorption between TiO_2 and $Al(OH)_3$ with PAA causing varying degrees of polymer entanglement / mobility. The shortening of the setting time may be due to a continued reaction between the coating and polymer matrix.

The changes in working and setting times are believed to be caused by the alteration of the powder to liquid ratio, poor reactivity of $Al(OH)_3$ and sub-micron filler interaction with the polymer matrix. However, the possibility of the reaction being altered chemically due to equilibrium or compositional changes has not been eliminated.

Chapter 5

Compressive Strength

Aim

Compressive analysis has been carried out on TiGIC cement samples with the intention of identifying and following increases in mechanical strength over a year of observation.

5.1 Introduction

Introduced into the dental standards in the 1930s, the compressive strength (σ_c) test has become one of the most common mechanical tests for dental cements (Wilson & Nicholson, 1993; Fennell *et al*, 1998). The σ_c test is relevant because it partially mimics the load implants are subject to in the mouth; as Wang has noted, the predominant masticatory forces are compressive in nature (Wang *et al*, 1999).

The σ_c measurement serves as a valuable screening and quality control procedure to evaluate the build up of strength in GICs and to ensure consistency between samples. It has been noticed that there is a large variation between samples due to minor defects in the final σ_c samples which result in localised stress concentrations thereby affecting the magnitude of the result (Yap *et al*, 2002; Tomlinson, 2007).

The failure of fully set GICs in compression is often ‘catastrophic brittle failure’ where the sample fractures and bursts apart making identification of the mode and plane of failure outside the scope of this chapter. Failure may occur by plastic yielding, cone failure due to secondary shear forces, or axial splitting from secondary tensile forces (Kendal, 1978; Wilson & Nicholson, 1993).

5.2 Method

5.2.1 Sample Preparation

The method used to prepare and test samples of DC and TiGIC is contained in BS EN ISO 9917-1:2003. A split stainless steel mould (Figure 5.1) was used to produce σ_c test samples of cylindrical shape with dimension 4mm (Ø), 6mm high; these dimensions minimise buckling during testing (BS EN ISO 9917-1:2003).

The method used to mix the tests samples is described fully in Chapter 3, page 40-43. The mixed cement was placed in a stainless steel mould then sandwiched and clamped between two polished stainless steel plates; excess cement was expelled by pressure between the plates. The clamped moulds were placed in an oven at 37ºC for one hour after which time they are removed and the cements top and bottom surfaces are polished using wet 1200 grit wet and dry paper whilst in their moulds. The solid cylindrical samples are removed from their moulds and placed in distilled water at 37ºC for long term testing unless used straight away.

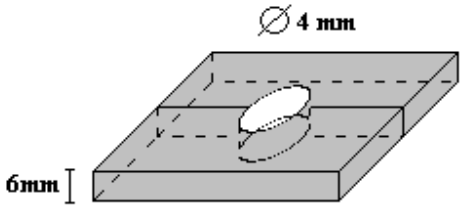

Figure 5.1: Representation of Mould used for Compressive Strength Sample Preparation

5.2.2 Compressive Analysis

The σ_c analysis was performed on a Lloyd Instruments EZ20 universal testing machine controlled remotely by QMat software.

The samples were placed between two platens that had moist Nº 1 Whitman filter paper on their faces. The samples were tested using either a 1 kN or 10 kN load cell dependent upon the samples age and maximum load / displacement they were able to withstand. The load cell was chosen so that measurements took place within the mid 80% of the cell's range to minimise erroneous results that could arise when measurements are recorded in the upper or lower extremes of the cell.

The calculations of compressive strength were performed automatically by the QMat software from the force 'vs' time curve generated during testing. A typical load 'vs' time curve can be seen in (Figure 5.2).

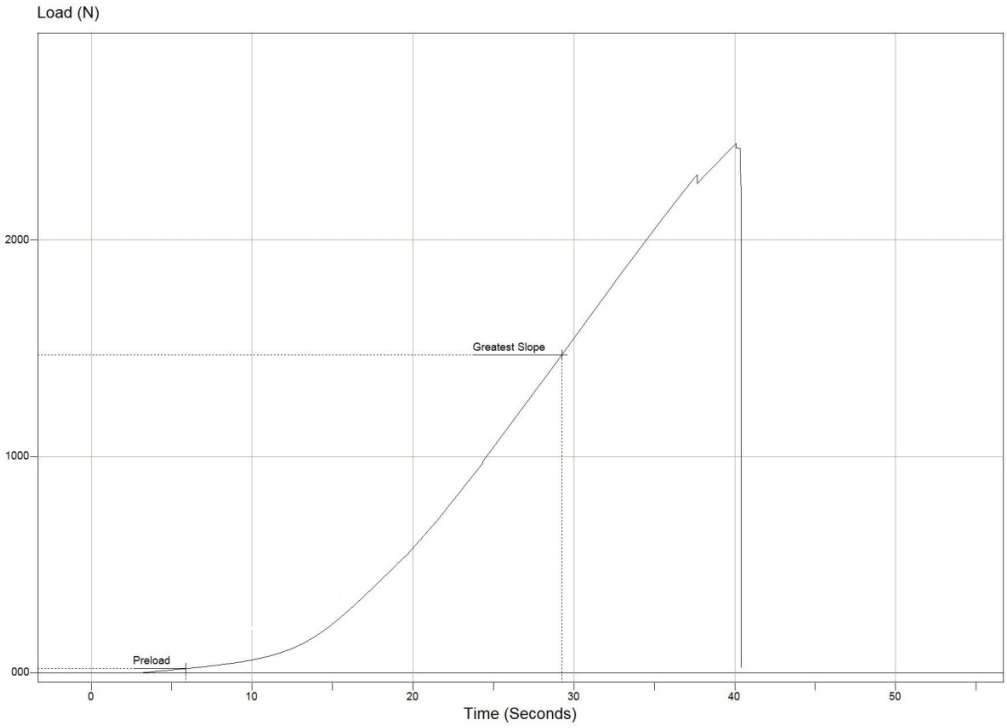

Figure 5.2: Typical Load 'V' Displacement Curve recorded using QMat Software

The QMat software calculates the compressive strength σ_c from the maximum load *F* (in Newtons, N) and the initial radius *r* (in mm) using equation 4:

$$\sigma_c = \frac{F}{\pi r^2} \qquad \text{Equation 4}$$

Ten repeats of each sample were performed before post-experiment manipulation.

5.2.3 Data Manipulation

Initially unfiltered data had a considerable spread of values producing large standard deviation values. The 'Robust' weighting of untreated data using a distance function quickly identifies multiple outlying data points and then establishes a mean based on 'reliable' results (Miller & Miller, 2000).
Data is filtered using a median absolute deviation (MAD) calculation using Equation 5 which finds the median value of the individual deviations from the mean.

$$MAD = median\left[\left|\chi_i - median\left(\chi_i\right)\right|\right] \qquad \text{Equation 5}$$

where χ_i is the *i*th term in the data set χ.

Possible outliers are detected and then rejected if the results from Equation 6 are greater than the integer 5 (Miller & Miller, 2000).

$$\left|\chi_0 - median(\chi_i)\right| / MAD \qquad \text{Equation 6}$$

where χ_0 is the suspected outlier(s).

An estimate of variance (§) is then found using Equation 7 and is the source of sensitivity. Large errors skewing the mean are down-weighted in accordance with the variance estimate.

$$\hat{S} = 1.5\left[\frac{MAD}{0.6745}\right] \qquad \text{Equation 7}$$

The down-weighting process is best described using an example therefore Table 5.1 includes the unfiltered results from the ten multiple repeats of Diamond Carve at 1 Hour.

Unfiltered	93.2	94.3	95.1	96.3	98.8	99.3	102.3	104.0	104.2	113.0

Table 5.1: Compressive Strength Results from Diamond Carve after 1 Hour

This series of data points is not considered to contain any outliers however the value 112.99 can be seen to vary from the bulk of the results when using a dot-plot (Figure 5.3).

Figure 5.3: Dot-plot of the Values Presented in Table 7

The median of this data was taken as 99.05 and the estimate of variation (§) can be calculated as 9.65. The deviation of the individual values from the median can be seen in Table 5.2.

Deviation	5.8	4.8	3.9	2.8	0.2	0.2	3.2	4.9	5.2	13.9

Table 5.2: Calculated Deviation from the Median of the Data Presented in Table 7

Deviations greater than ŝ are weighted via the addition or subtraction of ŝ from the original value depending on its position above or below the median respectively. The deviation of 13.94 caused by the suspect value 112.99 is greater than ŝ therefore is changed to 103.34. The alteration of this value generates a new *pseudo-value* and therefore a new data set. Further iterations of the procedure are the same as before but the deviation values are calculated from the mean and not the median.

The iteration process is continued until a *pseudo -data set* with all deviations below ŝ has been calculated. An estimate of the 'reliable' mean can be found from this *psudo - set*.

5.3 Results and Discussion

The results section has been split into short term (0-28 days) and long term (28-365 days) observations. Short term tests proceeded long term test because of the completion of simultaneously running theoretical modelling and chemical reactivity tests, therefore insufficient time was available to carry out long term analysis of these samples.
Short term tests were performed on Diamond Carve and TiGICs containing 1%, 2.5%, 7.5% and 10% filler. Long term tests were performed on Diamond Carve, 2.5% and 7.5% TiGICs.

5.3.1 Short Term Observations

The strength increase directly after restoration placement and the ensuing hours after placement are an important property of dental restorations. The normal mastication force exerted at the occlusion is approximately 25MPa whilst the limit of elasticity for enamel is 125 MPa (Lee & Park, 2000). Although a threshold value is not given for which dental restorations must reach it is reasonable to want the restoration to withstand mastication forces. A compressive strength of 80MPa would therefore be desirable before the restoration is considered strong enough for use.

The immediate strength increase over the first hour of setting can be indirectly predicted from rheological data produced in Chapter 4, page 66 and suggests that the compressive strength at 1 hour should follow the order DC, 2.5%(9%) TiGIC, 2.5%(0%) TiGIC, 7.5%(9%) TiGIC and 7.5%(0%). A comparison between all TiGIC formulations with the control material after 1 and 3 hours show that there is a significant shortfall in the compressive strength of new TiGICs aged 1 hour (Figure 5.4). After 1 hour, Diamond Carve had reached a σ_c of 99.1MPa whilst the TiGICs ranged in strength from 50.1 to 68.1MPa from maximum to minimum filler incorporation (Table 5.4).

The data contains considerable variation and it is only possible to identify a clear difference between TiGICs containing 1% and 2.5% filler with those that contained 10% w/w filler.

The strength of the control material increases slowly between 1 to 3 hours in comparison to the TiGICs. DC increases by 9.6MPa from 99.1 MPa to 108.7 between 1 and 3 hours whereas the TiGICs, on average, increase by 45.5MPa. This is most likely caused by the loss of the 'snap set'. After 3 hours of ageing all the TiGICs had comparable strength with the control material. The slow increase in strength and loss of a 'snap set' has previously been confirmed by rheological measurements (*see* Chapter 4). The presence of $Al(OH)_3$ appears to hinder the increase in compressive strength initially however, there is no statistical differences as non-coated and coated cement deviations overlap.

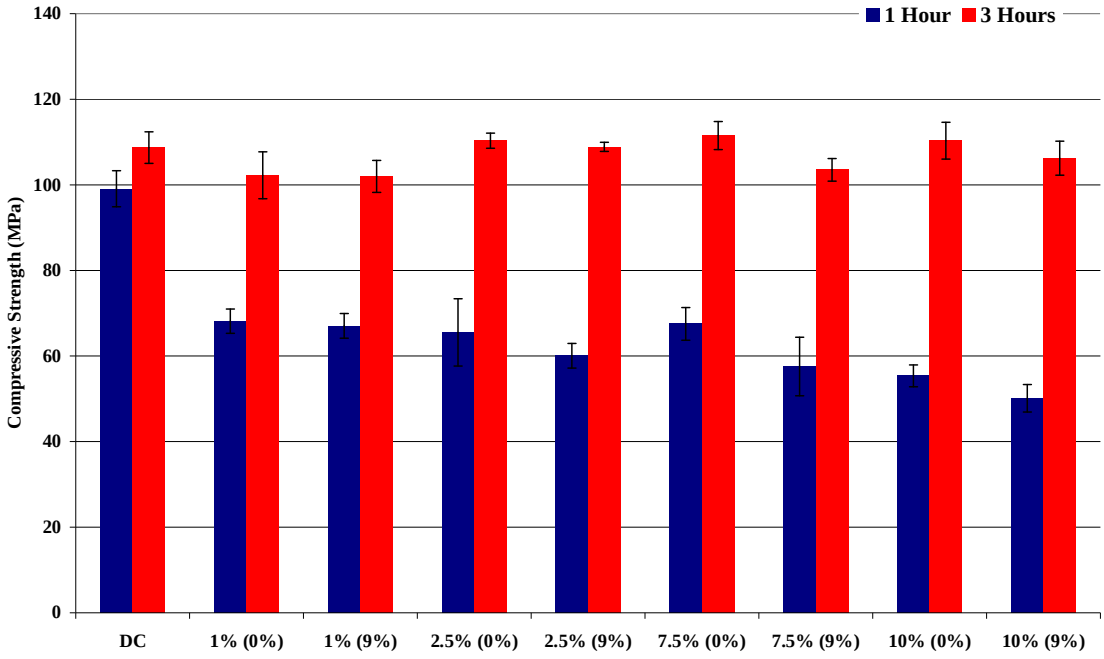

Figure 5.4: Compressive Strength Values for Diamond Carve and all TiGIC Formulations after 1 and 3 Hours

The compressive strength of the control material and all TiGICs continues to increase over the 28 day observation period. Uncoated (Figure 5.5) and coated (Figure 5.6) data is shown separately without error bars to better highlight the average increase in σ_c. This data can be found additionally in Table 5.3.

The onset of strength in DC is seen to level off after approximately 4 days; the compressive strength of DC increases by 7MPa between day 3 and day 28. The average strength increase after 3 days in the TiGIC samples appears to continue to increase at a greater rate than in DC with the exception of 10% TiGICs. This not statistically true as the majority of standard deviation values overlap with DC throughout the 28 day period.

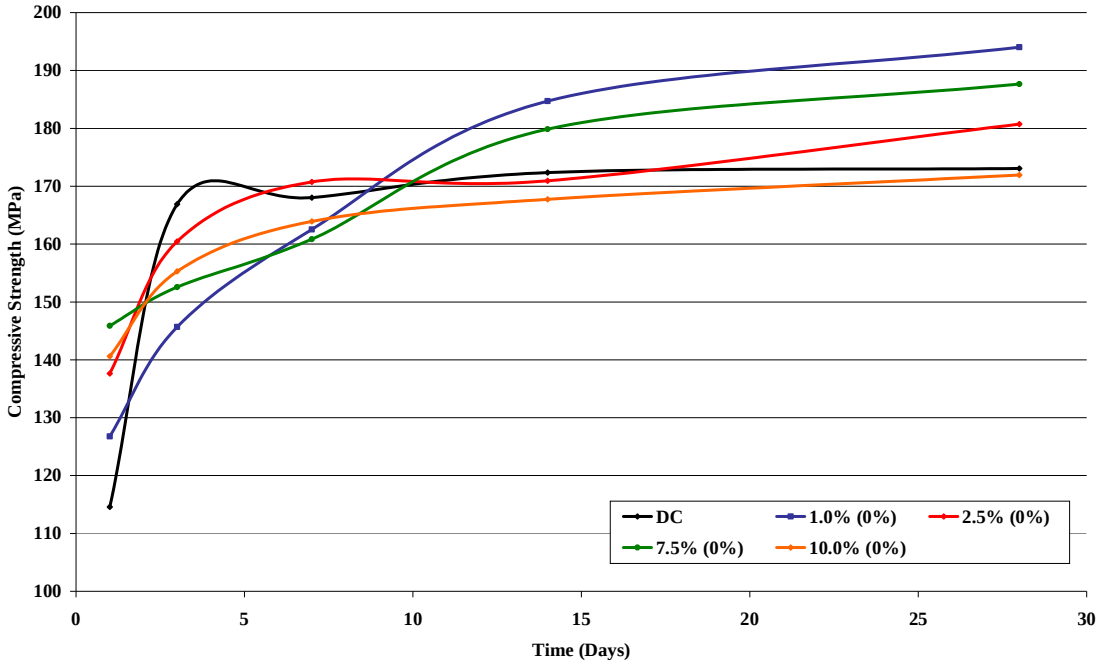

Figure 5.5: Compressive Strength Increase of Diamond Carve and Uncoated TiGIC Formulations over 1 - 28 Days

Time (Days)	1	3	7	14	28
DC	115 ± 7	167 ± 4	168 ± 11	172 ± 20	173 ± 4
1% (0%)	127 ± 10	146 ± 17	163 ± 10	185 ± 10	194 ± 9
1% (9%)	126 ± 10	147 ± 10	163 ± 3	185 ± 5	197 ± 14
2.5% (0%)	138± 6	160 ± 5	171 ± 15	171 ± 12	181 ± 32
2.5% (9%)	140 ± 3	164 ± 12	174 ± 4	182 ± 13	195 ± 18
7.5% (0%)	146 ± 3	153 ± 2	161 ± 9	180 ± 4	188 ± 12
7.5% (9%)	136 ± 9	153 ± 10	160 ± 5	184 ± 5	187 ± 11
10% (0%)	141 ± 7	155 ± 6	164 ± 9	168 ± 8	172 ± 12
10% (9%)	141 ± 5	158 ± 5	166 ± 9	168 ± 10	172 ± 18

Table 5.3: Average Compressive Strength (MPa) Values of Diamond Carve and all TiGIC Formulations from 1-28 Days

Statistically, the only cements that had achieved a greater compressive strength than the control material after 28 days was coated and uncoated 1% TiGIC. In both Figures 33 & 34 the 1% cement had the greatest compressive strength continually and at the end of data collection the strength increase showed no indication of slowing down.

The coated TiGICs show a similar trend as uncoated TiGICs with the exception of 2.5%(9%) TiGIC. 2.5%(9%) TiGIC (0-7 days) displays the greatest compressive strength of the coated TiGICs initially and then maintains a high rate of increase throughout the 28 days.

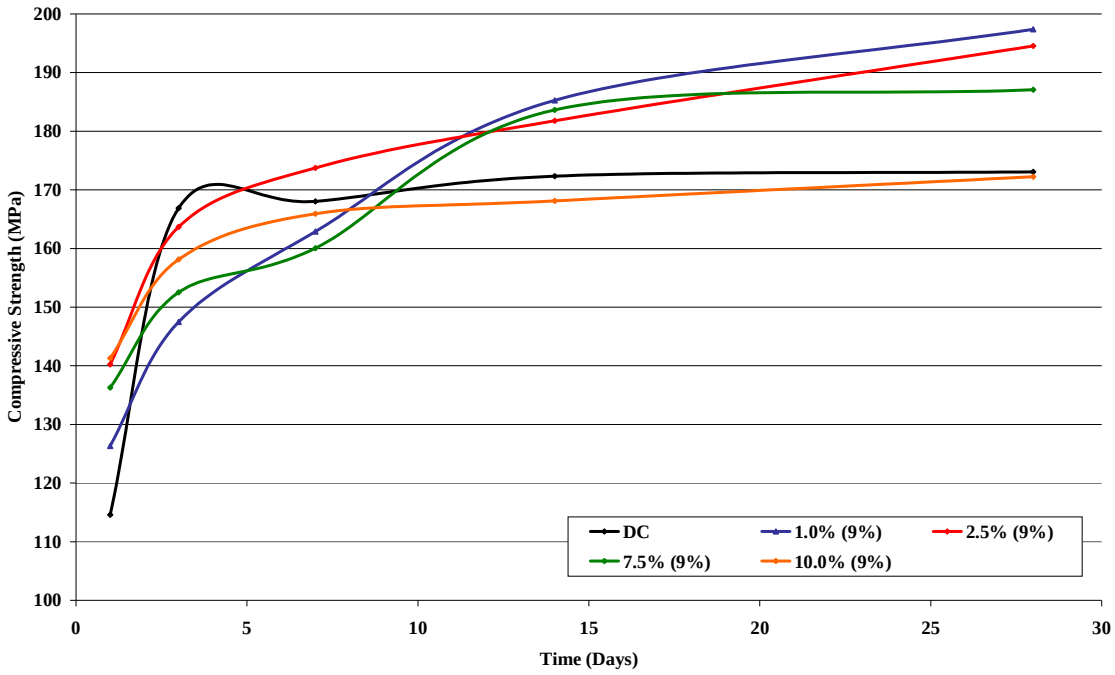

Figure 5.6: Compressive Strength Increase of Diamond Carve and Coated TiGIC Formulations over 1 - 28 Days

The addition of $Al(OH)_3$ has not affected the strength of the cements statistically however, if comparison is made between just the average values (Table 5.3) then the coating is generally increasing the compressive strength especially in samples aged longer than 14 days.

5.3.2 Long Term Strength Increase

The long term strength increase of GICs is well documented and is believed to be due to water becoming tightly bound to cement salts, stabilising the bonds (Wilson & Nicholson, 1993; Liu *et al*, 1999). It is also believed that the increasing compressive strength over large periods of time is caused by the continuation of the acid-base reaction (Fennell *et al*, 1998).

The continued increase in compressive strength can be seen in Figure 5.7 and Table 5.4. The standard deviations are not included in Figure 35 as this makes the graph hard to read. The standard deviation values are included in Table 10.

The ultimate compressive strength reached by DC, 2.5%(0%), 2.5%(9%), 7.5%(0%) and 7.5%(9%) after 365 days of ageing have been recorded as 206±4, 215±11, 250±15, 221±5 and 206±5 MPa respectively (Figure 5.7).

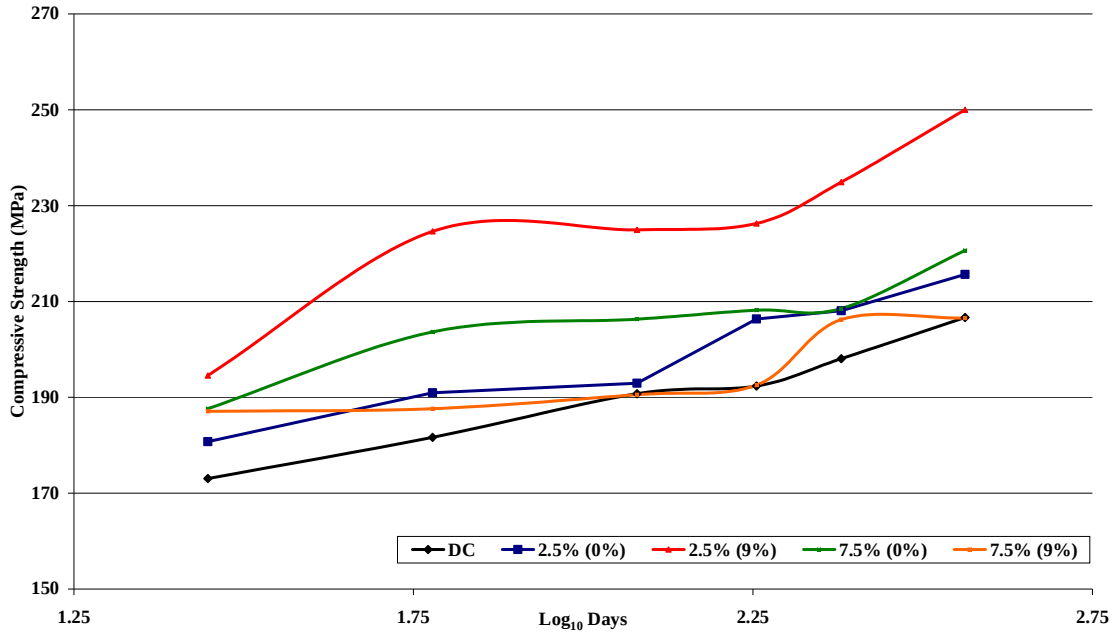

Figure 5.7: TiGICs and DC Maturation over a 1 Year Period

The standard deviations from TiGIC formulations overlap the values obtained for control samples at extremes making the positive identification of an improvement in σ_c difficult. There is however, a significant increase in TiGIC strength above the control samples for cement formulations based on 2.5%(9%) and 7.5%(0%) which is statistically true (Table 5.4). 2.5%(9%) TiGIC has a greater compressive strength than DC in samples aged longer than 180 days whilst 7.5%(0%) has intermittently higher values from 60 days.

Age (Days)	Sample				
	DC	**2.5% (0%)**	**2.5% (9%)**	**7.5% (0%)**	**7.5% (9%)**
28	173.06 ± 3.86	180.75 ± 31.70	194.54 ± 18.37	187.64 ± 11.86	187.08 ± 10.86
60	181.64 ± 14.39	190.93 ± 15.57	224.62 ± 20.47	203.65 ± 5.26	187.64 ± 17.77
120	190.75 ± 12.70	192.93 ± 26.58	224.93 ± 22.99	206.29 ± 10.95	190.54 ± 6.00
180	192.38 ± 7.94	206.36 ± 7.40	226.28 ± 6.29	208.19 ± 2.02	192.54 ± 6.54
240	198.05 ± 3.97	208.07 ± 8.54	234.90 ± 21.43	208.52 ± 11.12	206.25 ± 9.23
365	206.64 ± 4.34	215.65 ± 10.92	249.98 ± 14.74	220.63 ± 5.12	206.54 ± 4.78

Table 5.4: Long-term Compressive Strength Increase over a 1 Year Period

The volume of filler and its effect on compressive strength is unclear. The average values suggest that larger volumes of uncoated filler produce higher σ_c's whilst lower volumes of coated filler produce greater σ_c. The large standard deviations and relative closeness of the σ_c values coupled with the presence of an $Al(OH)_3$ coating make the only possible assumption that, the lower filler volume produces the greatest compressive strength.

Average data from Table 10 provide no further indication of the $Al(OH)_3$'s role in the build-up of strength as the values of compressive strength at 365 days show opposing results for the two volumes of filler used. 2.5% (9%) TiGIC has a greater σ_c compared with 2.5% (0%) TiGIC whereas 7.5% (0%) TiGIC has a greater σ_c than 7.5% (9%) TiGIC. These differences are significant as the standard deviations do not overlap.

The standard deviation values highlight the variation between samples (up to 17.5% deviation from the mean in long term samples) even though the mixing technique was tightly controlled. This may be caused by an increase in brittle nature as the cements age which emphasises any defects in the sample leading to greater variability in strength (Yap *et al* 2002; Fleming *et al*, 2003).

Generally, the average compressive strength of all TiGICs reaches a greater value than that of the control material which is believed to be due to the increased packing density as a result of sub-micron filler incorporation.

The maximum value of compressive strength obtained for DC after 365 days of ageing in distilled water was 207±4MPa, considerably less than the 350MPa quoted in the product brochure.

5.4 Conclusion

The compressive analyses of Diamond carve and various formulations of TiGICs have shown that a significant difference in initial and long term strength exists. The initial (1h) samples show that DC had a superior σ_c than any of the TiGIC formulations tested. The strength of the TiGICs continued to increase at a greater rate than DC and comparable values were reached after 3 hours.

No statistical differences were found between DC and any TiGIC until after 180 days when 2.5%(9%) and 7.5%(0%) became noticeably stronger. Average values of σ_c indicated that all long term TiGIC samples had reached greater values than DC however this could not be confirmed.

Large variations were present in this data even after statistical manipulation, therefore further tests should be performed on multiple samples (>30) to reduce standard deviations and increase confidence in values obtained.

The fracture mechanism cannot be determined as the cement samples underwent catastrophic brittle failure as expected.

Chapter 6

Infrared Investigation of Curing Mechanism

Aim

The aim of this chapter is to confirm the setting mechanism of Diamond Carve and identify any changes in the mechanism caused by incorporation of TiO_2 filler material or $Al(OH)_3$ coating material.

6.1 Introduction

Analysis of general GICs has previously been carried out using mid-infrared (mid-IR) spectroscopy to identify the formation of polyelectrolyte salts (Nicholson *et al*, 1988; Young, 2002; Young *et al*, 2003; Tomlinson *et al*, 2007) as acid – base neutralisation proceeds (*see* chapter 2).

The mid-IR of GICs has many overlapping peaks that cannot be separated or resolved by chemical or mathematical manipulation. The use of mid-IR can only be used in a semi-quantitative manner because a reference peak of known concentration is not present within the spectra.
The identification of dominant salt peaks and the rate of change during the observation period can be used to suggest a setting mechanism for DC and filler incorporated cements (Young *et al*, 2004).

6.2 Experimental Methods

6.2.1 Control Materials and Solutions

Diamond Carve has been used as the control material for the IR analysis of the setting mechanism of novel filler incorporated cements (TiGICs).

A full description of the materials used in DC and all subsequent TiGIC variations can be found in Chapter 3.

6.2.2 Experimental Procedure

A Bruker Vector 22 mid-FTIR spectrometer fitted with a Specac Golden Gate Attenuated Total Reflectance accessory was used throughout analysis. A personal computer with Bruker spectral analysis software, OPUS 6, was used to control the IR spectrometer and analyse subsequently recorded spectra.
Spectra of cement samples were recorded at both ambient temperature (21.5 ± 1.5ºC) and at a controlled temperature of 15.25 ± 0.25ºC. The temperature was lowered using a chilled, polished stainless steel plate secured in place over the sample using the ATR clamp.

All spectra were an average of 32 scans collected between 600-4000 cm^{-1} with a resolution of 4 cm^{-1}.

The ambient experimental procedure can be summarised by steps 1–5,

1. The ATR diamond window was cleaned using distilled water and acetone to remove dust and grease; the window was cleaned before each recorded sample.
2. A background spectrum was performed.
3. The samples were prepared and mixed as described in section chapter 3.
4. The mixed cement was placed on the ATR window and pressed firmly against the window using the accessory clamp with a domed or diamond head tip. The head was chosen to provide the strongest contact with the ATR window.
5. Acquisition was begun.

Chilled experiments were performed in the same way as ambient samples with the exception of a chilled stainless steel plate being used to press the samples against the ATR window. The plate temperature was recorded by means of an attached thermocouple on the rear of the plate. Five separate acquisitions were performed on each of the formulations and average spectra were generated.
The acquisition of spectra was automatically performed at 1 minute intervals throughout the experimental duration of 60 minutes. Spectral manipulation was performed using Bruker OPUS 6 software.

ATR spectra were converted to absorbance spectra so the concentration of cement salts could be predicted applying Beers law (Equation 8).

$$A = \varepsilon c \ell \qquad \text{Equation 8}$$

where A is absorbance, ε is the molar absorptivity coefficient, c is the analyte concentration and ℓ is the path length.

The ATR spectra are converted into absorbance spectra using Equation 9.

$$AB = ATR\frac{1000}{x} \qquad \text{Equation 9}$$

where x is the wavelength expressed as a wavenumber ($x = 1/\lambda$, cm^{-1}).

Monitoring the extent of cure was difficult because of the lack of a stationary (un-reacting) peak within the spectrum to act as a reference (Cambridge Polymer Group, 2004).
The change in peak intensity is an indication of the change in concentration of reaction products within the cement (Young *et al*, 2004) however; the contact with the ATR window will affect the amount of absorbed radiation altering the recorded spectral intensity (*see* Appendix 3). The constantly changing nature of all the peaks in the spectra due to heavy overlapping and different rates of reaction make the use of spectral intensity for calculation of degree of cure difficult to assess.

The subtraction of the spectra at t_0 from the spectra at t_i (Equation 10) will reduce the effects of contact with the ATR window and return the change in intensity over a given time with respect to the spectrum taken at the beginning of observation. Another advantage of using the absorbance difference spectra is the separation of overlapped positions within the spectra (1100 – 600 cm^{-1}) (Tomlinson, 2007).

$$\Delta I = I_0 - I_t \qquad \text{Equation 10}$$

The difference spectra must also be used with care because it does not account for the reaction rate or progress within the sample before the acquisition is begun.

6.3 Results and Discussion

Previously, the setting mechanism of general GICs have been identified using mid-IR and solid state nuclear magnetic resonance spectroscopy (Prosser *et al*, 1982; Nicholson *et al*, 1988; Dupree *et al*, 1996; Matsuya & Ohita, 1996; Griffin & Hill, 2000; Young *et al*, 2004; Stamboulis *et al*, 2006; Tomlinson *et al*, 2006; Billington *et al*, 2006). IR is used qualitatively for the purpose of identifying cement salt formation and the relative rates of formation during the observation period.

The order of reaction is widely believed to be (Wilson & Nicholson, 1996; Nicholson, 1998):

1. TA preferentially binds to bivalent cations that are released from ASG first preventing premature gelation of PAA (Sr/Ca-TA).
2. TA binds to trivalent aluminium when released from ASG to prevent gelation of PAA although there are conflicting views over its availability for binding to PAA initially (Al-TA) (Nicholson, 1998).
3. Once TA has been consumed by reaction with bivalent cations these cations then form cement salts with PAA (Sr/Ca-PAA).
4. Finally, PAA binds with aluminium and Sr/Ca-PAA bonds are slowly replaced by the more stable Al-PAA bonds.

The added acidic strength of TA also aids in the degradation of ASG promoting reaction with PAA. The reaction is supposed to occur in series with PAA reacting after TA however this is a matter of dispute (Nicholson, 1998).

6.3.1 Control Materials Peak Assignment

Preliminary experiments were performed to aid the identification and assignment of the characteristic absorbencies within Diamond Carve; both powder and liquid (*see* Appendix 5). The identification of the aluminium species precipitated on the surface of the TiO_2 filler particles is also able to be understood.

6.3.1.1 Diamond Carve Liquid

Solutions of polyacrylic acid, tartaric acid and vinylphosphonic-acrylic co-polymer were prepared from distilled water and deuterium oxide separately in order to separate the carboxyl (1706 cm^{-1}) and water (1633 cm^{-1}) absorbance's in the range 1500 – 1800 cm^{-1} (Figure 6.1 & Figure 6.2). Infrared spectra were recorded for each acid and the peaks found (*see* Appendix 3) have been identified are applied to DC liquid (Figure 6.1). The peak allocations are presented in Table 6.1 and discussed in Appendix 5.

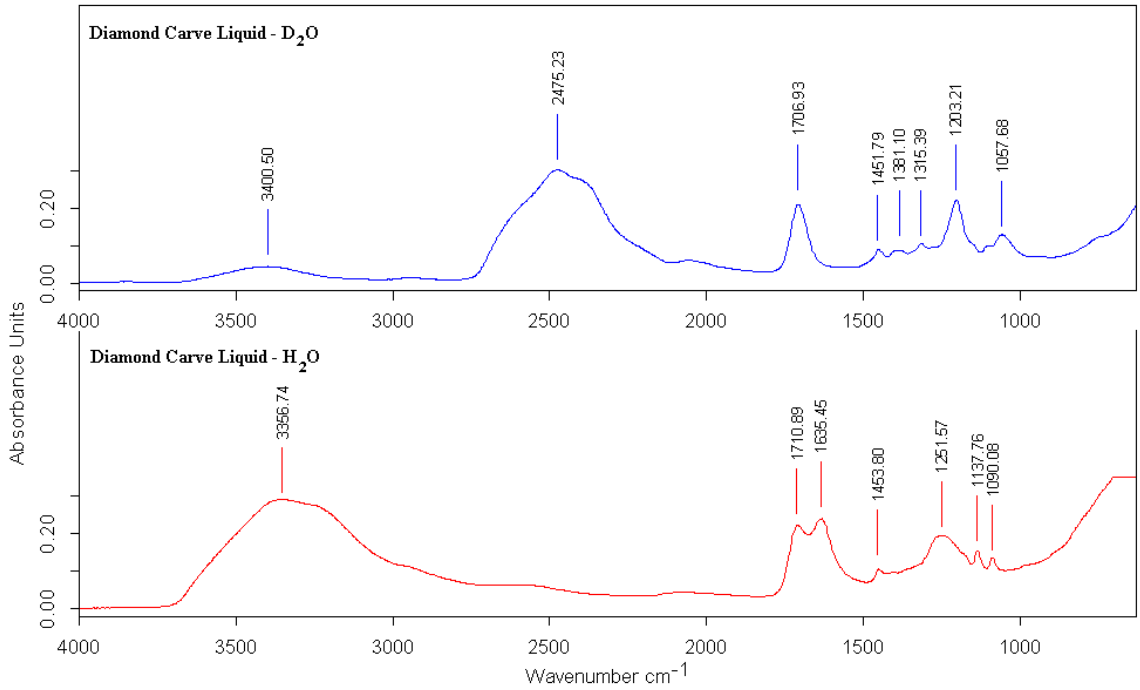

Figure 6.1: Diamond Carve Liquid Prepared from Distilled Water and Deuterium Oxide

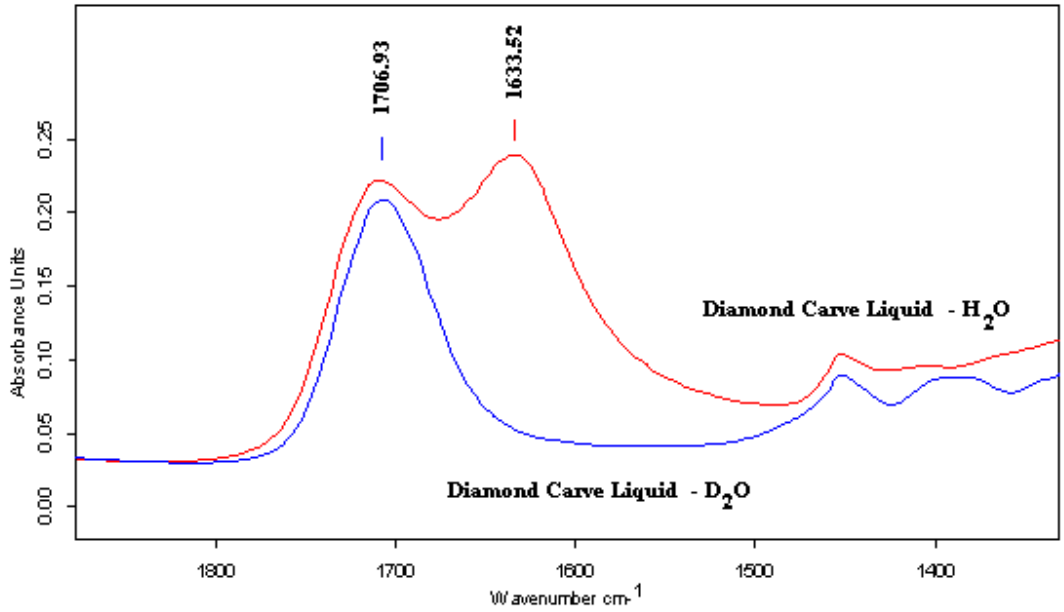

Figure 6.2: Comparison of Polyacid Solvent Selection. Removal of H_2O Scissoring at 1633 cm^{-1}

DC liquid contains a large –OH stretch at 3354 cm^{-1} with a broad shoulder at 3244 cm^{-1} caused by bound and free water respectively (Young *et al*, 2003).

Broad water peaks in the spectra range 3000 – 3850 cm^{-1} mask $–CH_3$ stretching vibrations from PAA and –OH stretching from secondary alcohol groups present in TA (Kozhevina *et al*, 1980; M'Bareck *et al*, 2004). The shoulder at 2943 cm^{-1} is caused by –C-O stretching from carboxyl groups of both PAA and TA (Young *et al*, 2004). The absorbance at 1708 cm^{-1} is a combination of the –C=O stretch found in PAA and TA (Nicholson *et al*, 1988; Young *et al*, 2004). The –C=O stretch of PAA is believed to dominate this peak position because of greater concentration and an absorption frequency closer to PAA than that of TA. The characteristic scissoring vibration of water is observed at 1633 cm^{-1} which forms a doublet with –C=O. A small peak at 1451 cm^{-1} is from a $–CH_2$ stretch located on the PAA carbon backbone (M'Barec *et al*, 2004). The broad peak at 1249 cm^{-1} is believed to be widened by the combination of absorbance's from a –C-O stretch from PAA and a –HCOH deformation combination band from PAA and TA (Crisp *et al*, 1973; Kozhevina *et al*, 1980). The two smaller absorbencies at 1135 cm^{-1} and 1088 cm^{-1} are from asymmetric and symmetric –C-OH stretches from the secondary alcohol groups present in TA respectively (Kozhevina *et al*, 1980).

Wavenumber and Allocated Functional Species – Diamond Carve Liquid			
Peak Assignment		**Wavenumber (cm^{-1})**	**Remarks**
H_2O	D_2O		
-OH	$-CH_2$, -OH	3400 - 3354	Methyl vibration from PAA, -OH vibration of secondary alcohol from TA and H–OH stretch
-OH	-O-D	2475, 1633	Scissoring Vibration
-C=O	-C=O	1708	Combination of carboxyl group from PAA (1700 cm^{-1}) and TA (1724 cm^{-1})
$-CH_2$	$-CH_2$, -CH	1451	Carbonyl carbon and methyl groups
-C-O	-C-O	1249, 1381 & 1315	Carboxylate Group
-C-OH	NA	1135	Asymmetric –C-OH stretch from TA alcohol
-C-OH	-C-OH	1088, 1057	Symmetric –C-OH stretch from TA alcohol

Table 6.1: Peak Assignment for Diamond Carve Liquid (Tomlinson, 2007)

6.3.1.2 Diamond Carve Cement

The peak vibrations of fully cured DC have been presented in Table 6.2. Peak allocations agree with Nicholson (1998) and Tomlinson (2007) (Table 6.2).

The identification of a symmetric stretching vibration from aluminium tartrate at 1410 cm^{-1} was not made as this frequency was observed in $Al(OH)_3$ – TA cements. Instead the occurrence of Al-TA is expected to be around the same wavenumber as Sr/Ca-TA at 1383 cm^{-1} causing a broadening of the Sr/Ca-PAA absorbance at 1410 cm^{-1} (*see* Appendix 3).

Absorbance Wavenumber and Allocated Functional Species – H_2O Cements			
Peak Assignment	**Vibration Mode Wavenumber (cm^{-1})**		**Remarks**
	Mode 1	**Mode 2**	
-C=O	1720 - 1693	1324, 1255	Carboxyl and carboxyl ions (PAA, TA)
Sr/Ca – TA	1598 - 1582	1416 - 1402	Combination bands
Sr/Ca – PAA	1552	1407	Symmetric stretch not observed
Al – TA	1646	1380	Asymmetric and Symmetric Stretch
Al – PAA	1560	1473, 1436	Methyl overlap with symmetric stretch
$-CH_2$	1455	1416	
-CHCO	1403	1235, 1170	

Table 6.2: Final Allocation of Specific Absorbencies in Water Based Diamond Carve Cement (Tomlinson, 2007)

Water based DC cement (Figure 6.3 and Figure 6.4) has a combination peak corresponding to un-reacted carboxylic acid groups (PAA, TA & PVPA-PAA) at 1693 cm^{-1}, a –OH scissoring vibration present from water at 1633 cm^{-1} and a asymmetric Sr/Ca-TA stretch at 1597 cm^{-1} (Appendix 5). A shoulder present at 1552 cm^{-1} on the Sr/Ca-TA peak is due to the formation of Sr/Ca-PAA (Nicholson, 1998). Tomlinson (2007) also assigns the absorbance at 1552 cm^{-1} to Al-PAA however this peak was not seen in $Al(OH)_3$-PAA spectra (*see* Appendix 5). The reaction of ASG and PAA is relatively slow when compared to the reaction between ASG and TA which accounts for the low intensity seen in spectra during early cement development.

Two peaks are present from $–CH_2$ scissoring and –CHCO bending vibrations at 1453 cm^{-1} and 1405 cm^{-1} from the PAA backbone (Wu *et al*, 1997; Tomlinson, 2007). Al-PAA is present as a shoulder at 1473 cm^{-1} (Nicholson, 1998, Young, 2002 and Tomlinson, 2007).

The –CHCO bending from PAA changes intensity and shape during the setting reaction which has been attributed to an overlap with a calcium polyacrylate at 1410 cm^{-1} and a mixture of Sr/Ca tartrate 1405-1372 cm^{-1} and Al-TA at 1385-1372 cm^{-1} (Saniger *et al*, 1991; Appendix 5).

The increasing peak at 1058-1048 cm^{-1} is believed to be due to the condensation of silicic acid (Si-OH) rebuilding the Si-O-Si glass network (Crisp *et al*, 1974; Young *et al*, 2003).

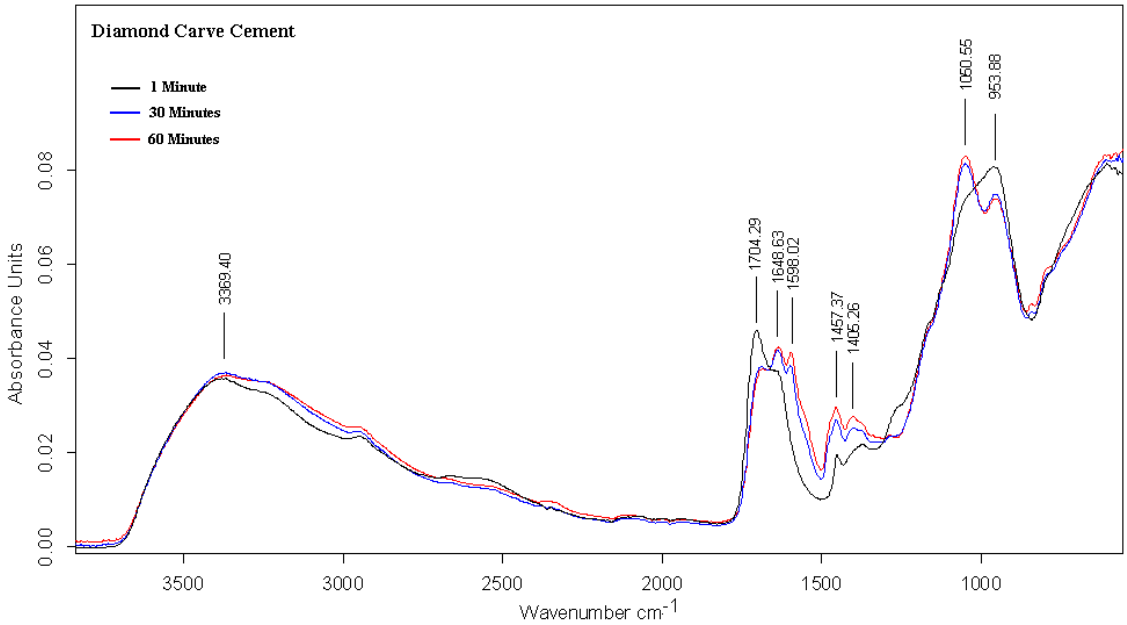

Figure 6.3: Cure Monitoring of Diamond Carve Cement from 1-60 Minutes

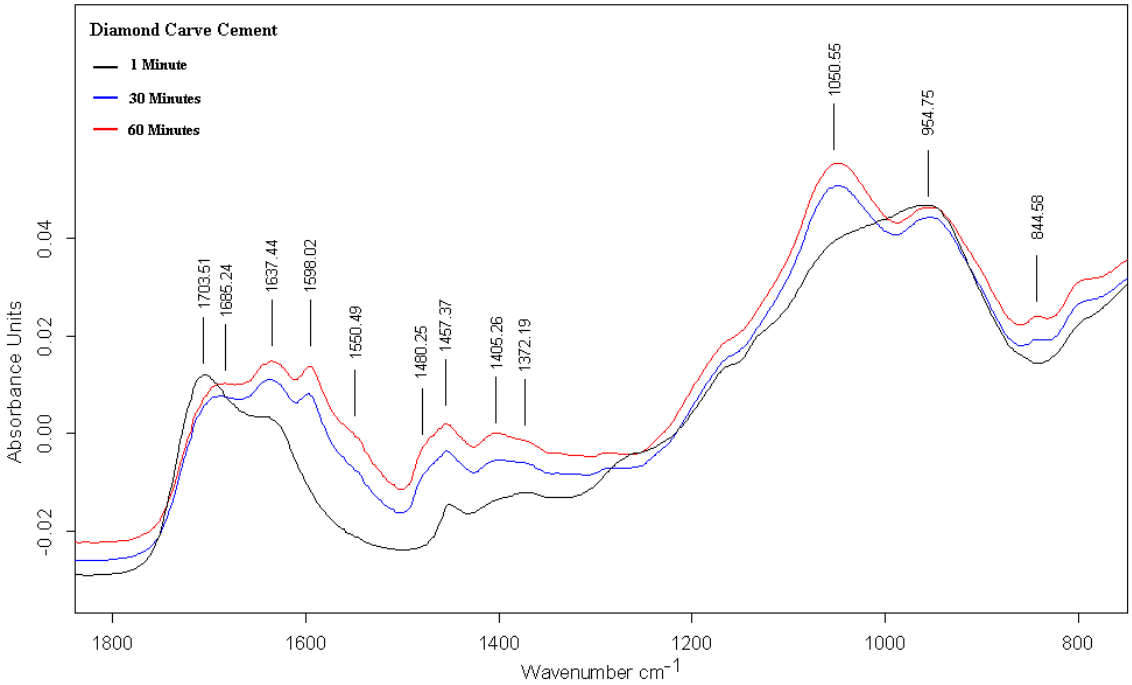

Figure 6.4: Cure Monitoring of Diamond Carve (Zoomed between 800-1800 cm^{-1})

Deuterated DC (Figure 6.5) has the equivalent H-O-H scissoring (D-O-D) vibration at 1203 cm^{-1} which is overlapped by the strong absorbance's of –Al-O and Si-O(Si) from ASG. The removal of the H-O-H vibration from 1633 cm^{-1} allows the positive identification of peaks in the range 1300-1800 cm^{-1} as previously performed by Nicholson *et al* (1988). The deuterated cement exhibits the same peaks as water based DC with the addition of a shoulder present at 1646 cm^{-1} caused by the formation of Al-TA (Nicholson, 1998) and the development of a shoulder (1560 cm^{-1}) on the strong Sr/Ca-TA absorbance at 1598 cm^{-1} assigned to Al-PAA.

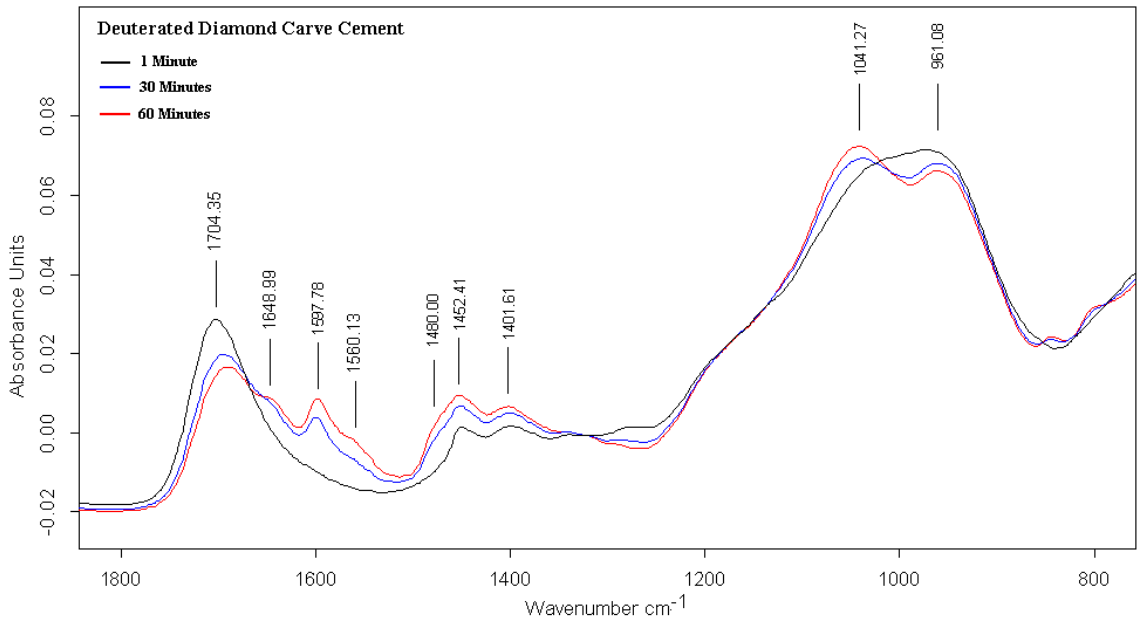

Figure 6.5: Diamond Carve Cement made with Deuterated DC Liquid

Identification of characteristic absorbance frequencies is difficult due to overlapping peaks, vibration modes and competing reactions. The final allocation of specie absorbencies are given in Table 6.2 and are used throughout this thesis.

6.3.1.3 Aluminium Hydroxide

Aluminium Hydroxide was freshly prepared as described in Chapter 3. Identification and conformation of the coating species is important because the many different forms of aluminium oxide(s) and hydroxide(s) have varying acid reactivity's (Wefers & Misra, 1987).

The positive identification of a crystalline structure is not possible without the aid of x-ray crystallography which was unavailable. Therefore, the identification of the structure will be made by comparison of IR data with previous literature. The degree of crystallinity and structural order is known to cause a decrease in acid reactivity with increasing dehydroxylation (Wefers & Misra, 1987).

Amorphous $Al(OH)_3$ has a less distinguished spectrum than crystalline aluminium hydroxide because of the disordered distribution of vacancies and the continuous distribution of bond lengths means there is no long range structure (Shek & Lai, 1997).

The peaks located at 1087 cm^{-1} and 977 cm^{-1} (Figure 6.6) are assigned to the –OH bend of Al-OH (Sato, 1981). The peak at 1633 cm^{-1} is present because of the –OH bending of absorbed water. The large convoluted peak based around 3350 cm^{-1} is due to a combination of –OH stretches from Al-OH believed to be present at 3600 cm^{-1}, 3540 cm^{-1} and 3420 cm^{-1} from a localised structure within the gel, probably Bayerite.

The identification of –OH stretches in the precipitated $Al(OH)_3$ is confirmation that surface hydroxyl groups are present and total dehydrolysis has not occurred. The broad nature of the combination peak around 3374 cm^{-1} would suggest that no long range ordering has yet been established in the precipitate and that it may be predominantly amorphous. The occurrence of a defined peak at 1638 cm^{-1} suggests the presence of a Gibbsite or Boehmite structured arrangement.

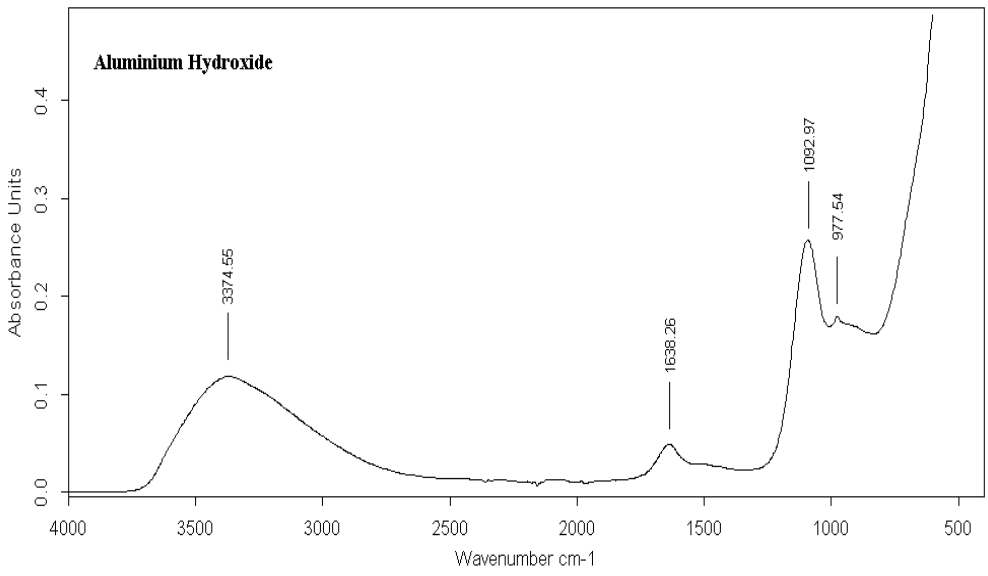

Figure 6.6: Spectrograph of Freshly Precipitated Aluminium Hydroxide

$Al(OH)_3$ has characteristic absorbencies in the range 977 – 1638 cm^{-1} which are obscured by the vibrations associated with cement salts and ASG. The concentration of ASG and cement salts are vastly in excess of $Al(OH)_3$ so observation of decreasing peak absorbance due to reaction / consumption is not visible.

6.3.2 Absorbance Change Spectra and Setting Mechanism

To clarify how the peaks within DC change and to help detect the production of cement salts, absorbance change (difference) spectra (Young *et al*, 2004) have been generated using the "spectrum calculator" function within the OPUS software. Peaks (absorbance values > 0) represent an increase in intensity throughout setting, whereas troughs (absorbance values < 0) represent a decrease in intensity throughout setting.
The difference spectra have been used to highlight changes in the dominant cement salts being formed relative to their intensity at t_0. The difference spectra can provide details of intensity increase over time that can be directly related to a given frequency enabling the rate of formation to be found. This data can be combined with the first appearance of characteristic metal-salt frequencies to aid in the identification of the setting mechanism.

6.3.2.1 Diamond Carve Setting Mechanism

In order to gain a full understanding of the setting mechanism and the relative rates of salt formation, the water absorption around 1637 cm^{-1} was removed by use of deuterium oxide as a solvent for polyelectrolyte production (Figure 6.7) that is known to mask the formation of Al-PAA at 1650 cm^{-1}.
The early (0-1 min, mixing period) rate of reaction and dominant salt species in DC is unable to be found because IR observation did not begin until 1 minute after the initiation of mixing.

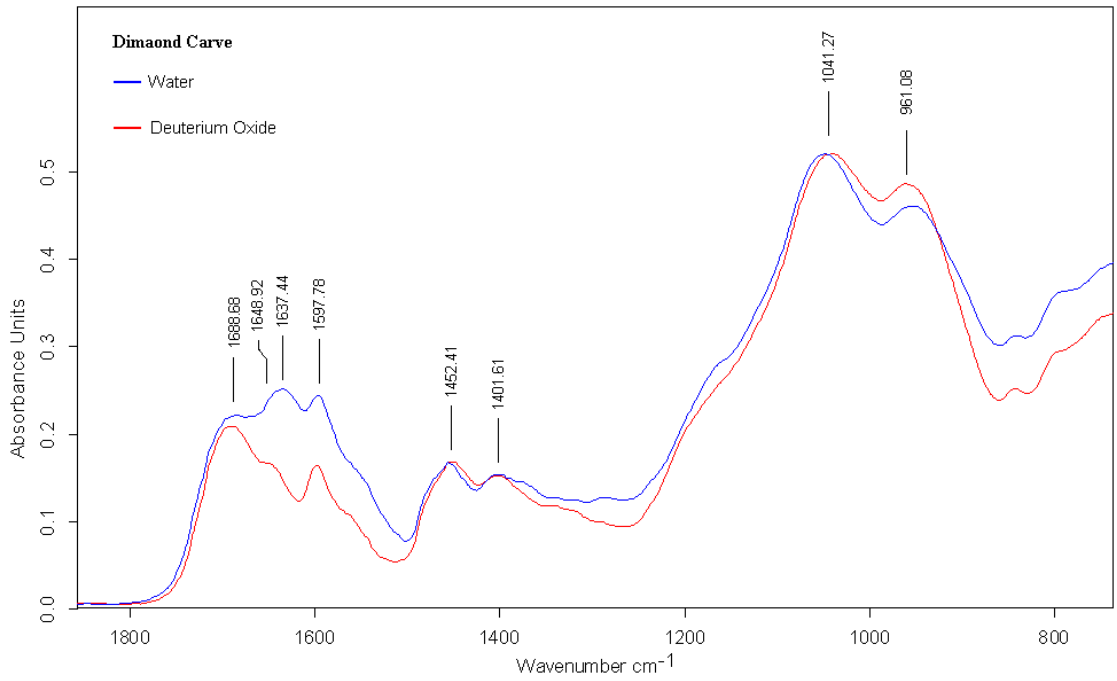

Figure 6.7: Fully Set Diamond Carve (t=60 min) with H_2O and D_2O Solvents

The cements reacted at room temperature (21.5 ± 1.5ºC) have been found to react 2.5 times faster than those reacted at 15ºC when comparing working times (*see* Chapter 4). The initial increase in viscosity is commonly believed to be caused by the formation of Sr/Ca/Al – TA salts neutralising the cement causing the coiled PAA to expand into rod shaped molecules increasing viscosity (Mandel, 1992) and the formation of Sr/Ca-PAA cross-linking the high molecular weight polyacid (Nicholson, 1998). The gradual increase in strength is attributed to the replacement of Sr/Ca salts with Al-PAA salts (Nicholson, 1998; Wilson & Nicholson, 1993) and then the formation of an inorganic hydrated silicate / phosphate network (Nicholson *et al*, 1993 & Wilson, 1996). The IR analysis is able to identify if the dominant salt concentration changes during the first 1-60 minutes of reaction.

The first spectrum (1 minute) shows a small shoulder at 1598 cm^{-1} due to Sr/Ca-TA already present in the spectra (Figure 6.8). The occurrence of Al-TA at 1649 cm^{-1} is masked by the C=O peak at 1701 cm^{-1} but is expected to already be present because of the strong symmetric absorbance at 1389 cm^{-1} due to the combination peak from Sr/Ca/Al-TA. Al-TA becomes apparent in the spectra at 15 minutes when the intensity has become great enough to raise above the decreasing carboxyl stretch.

The occurrence of Sr/Ca-PAA first becomes present in the spectra at 2 minutes as a small peak at 1543 cm^{-1}. The formation of PAA salts causes the gelation of the cement (Nicholson, 1998) however no PAA salt peak is observed until 2 minutes but the viscosity is known to be increasing. The early PAA salt formation causing the increase in viscosity (working time) must therefore be concealed in the moving baseline.

The intensity (concentration) of Sr/Ca-PAA grows over time as a shoulder on the, now well formed, Sr/Ca-TA peak at 1599 cm^{-1} which additionally overlaps the asymmetric Al-PAA stretch. Al-PAA is apparent in the spectra at approximately 3 minutes as a peak at 1560 cm^{-1} and 1467 cm^{-1}.

The difference spectra (Figure 6.9) can provide information about the rates of increase over the period 2-60 minutes which can be used to highlight how the individual salt species are behaving during the setting reaction.

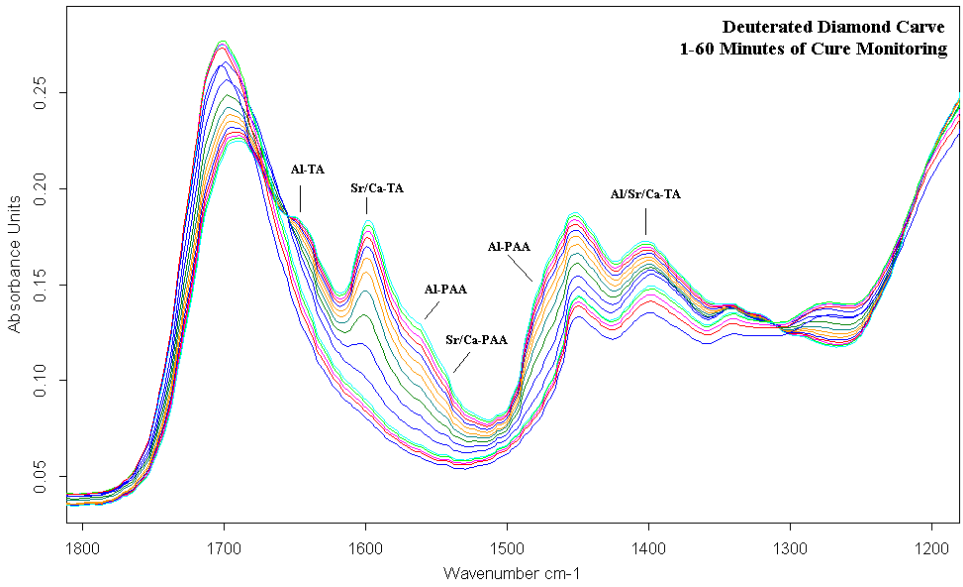

Figure 6.8: Deuterated Diamond Carve Cement over a 1-60 Minute Period (15°C)

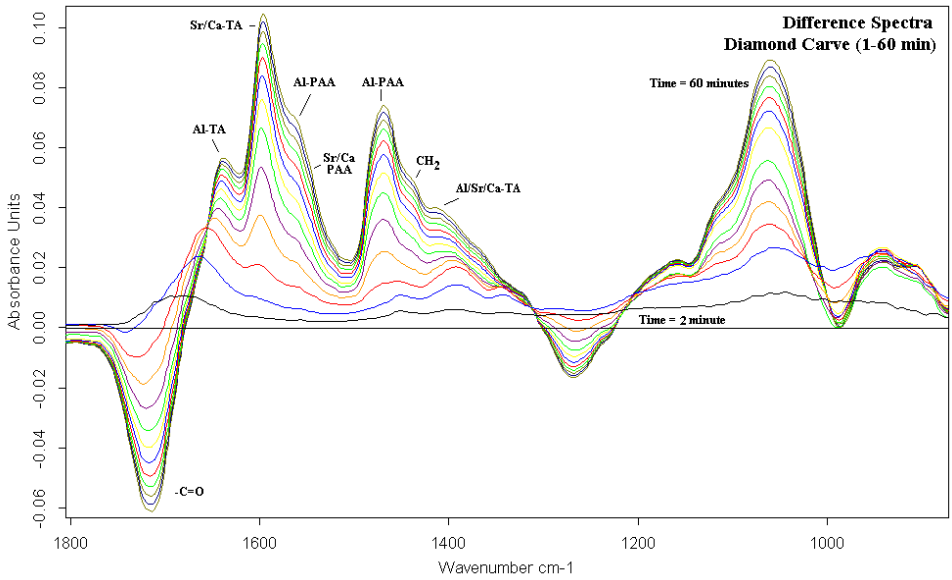

Figure 6.9: Difference Spectra from the Cure of Deuterated Diamond Carve (5 Minute Increments – 2, 5, 10 etc, 15ºC)

The difference spectrum shows that Al-TA may be forming quicker in the early stages of reaction than Sr/Ca-TA (Figure 6.10). The early appearance of Sr/Ca-TA in the IR spectrum (Figure 6.8) is apparent because it is sufficiently far away from the large –C=O as to not be concealed by it. The Al-TA peak however is closer to the –C=O absorbance so early formation has been hidden. The formation of Al-TA slows down rapidly after 2-3 minutes of reaction whereas the rate of Sr/Ca-TA continues to increase for over 25 minutes of reaction. Difference spectra from the later stages of reaction (around 60 minutes) (Figure 6.8) show that the distance between consecutive measurements is much smaller in Al-TA than in Sr/Ca-TA (rate of change is smaller) although the intensities are comparable.

The way in which the intensity values are extracted from the spectral data for rate analysis produces ambiguity because of the way the base-line is ‘pulled’ up by rapidly forming salts. It is therefore recommended that Figure 6.10 is used to identify general trends rather than explicit rates. Confidence in data increases with time as individual peaks become distinguished from the base-line and therefore become independent of influencing forces.

Monitoring the development of Sr/Ca-PAA is difficult because of overlapping peaks of Sr/Ca-TA and Al-PAA.

The results would indicate that Sr/Ca-PAA is present in the cement in low concentrations (as indicated by low intensity) and continues to increase over the observation period at a slower rate than the other salts of neutralisation. Nicholson (1998) reported that early cement hardening is due to Sr/Ca-PAA formation therefore it is assumed that only small concentrations are needed to cause a significant increase in viscosity.

The order of salt appearance, and therefore the order of reaction, is believed to be Al-TA → Sr/Ca-TA → Sr/Ca-PAA → Al-PAA however; more research is required to confirm the presence of Al-TA during the early stages of reaction.
The reaction begins to slow down after 25 minutes but is still proceeding at 60 minutes. It has been proposed that the acid-base reaction will never cease and continues indefinitely throughout the restorations life span (Wilson & Nicholson, 1993).

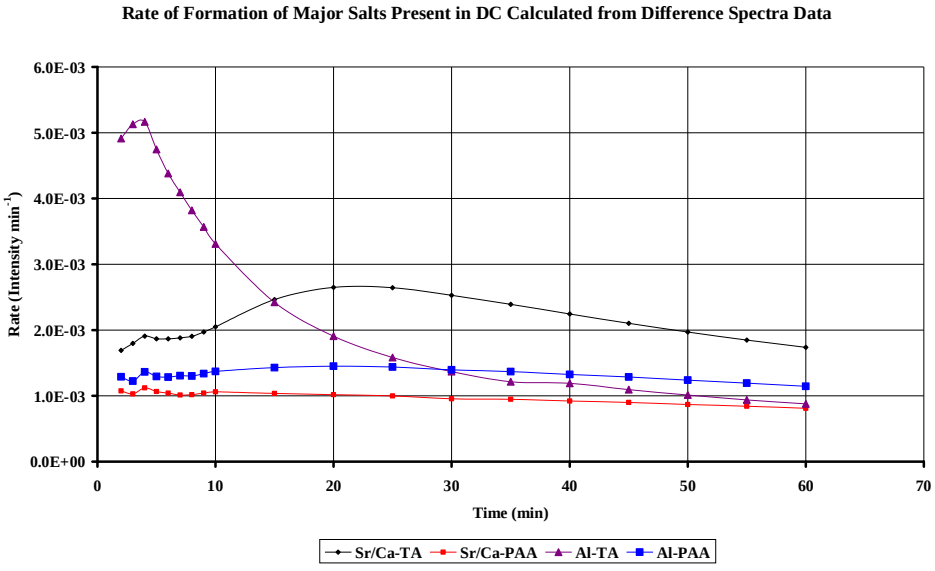

Figure 6.10: Rate of Formation of Major Salts in Deuterated Diamond Carve

The setting mechanism of Deuterated DC at 15ºC has been found to follow the same order of reaction as RT cured cements but at a reduced rate.

6.3.2.2 Effect of Temperature on Reaction Mechanism

The difference spectra has been particularly useful at identifying the changes occurring in the region 850-600 cm^{-1} which were previously not observed in Figure 6.3 because of the high amount of overlapping of salt peaks. The difference spectra of DC curing at ambient temperatures (21.5 ± 1.5ºC) (Figure 6.11) shows a trough at around 729 cm^{-1} and two small peaks at 804 cm^{-1} and 840 cm^{-1} which have previously been assigned by Hamilton *et al* (2001), Maeyer *et al* (2002), Andrade *et al* (2004) although the spectra is noisy at this frequency so a quantitative analysis of this data is not presented. The trough present at 729 cm^{-1} is thought to be due to the symmetric stretch from Si-O-Al which is breaking during acid attack. The two peaks at 804 cm^{-1} and 840 cm^{-1} are assigned to the symmetric stretching vibration of the Si-O-Si bond as silicic acid condenses rebuilding the silica / phosphorus type network (Nicholson, 1998; Hamilton *et al*, 2001; Maeyer *et al*, 2002 & Andrade *et al*, 2004).

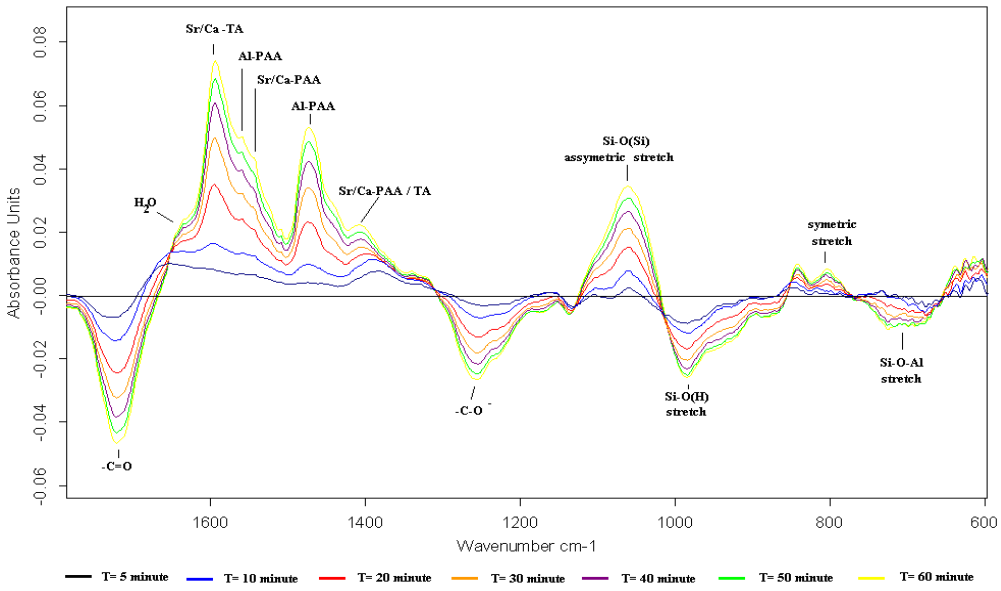

Figure 6.11: Absorbance Difference Spectra of DC Cured at 21.5 ± 1.5ºC for 60 Minutes

Comparison between DC samples analysed at 21.5 ± 1.5ºC and reduced temperatures identifies the distinct difference between the reactivity of PAA and TA towards bivalent and trivalent metal cations.

Figure 6.11 shows the presence of Al-PAA (1560 cm^{-1}) as a relatively distinguished shoulder on the much larger Sr/Ca-TA peak where as this shoulder is not present in refrigerated samples (Figure 6.12) instead a much wider combination peak from Sr/Ca/Al-PAA is seen with almost equivalent intensity to Sr/Ca-TA. Wu *et* al (1997) have previously found that the reaction between PAA and aluminium is not effected by temperature whereas bivalent Sr and Ca have slightly reduced reactivity. severely retarded by reduced temperatures. The reduced temperature caused the reaction between Sr/Ca-TA to be retarded whilst the production of Sr/Ca/Al-PAA remained approximately the same thus the combination peak has not been dwarfed by the normally much larger Sr/Ca-TA peak.

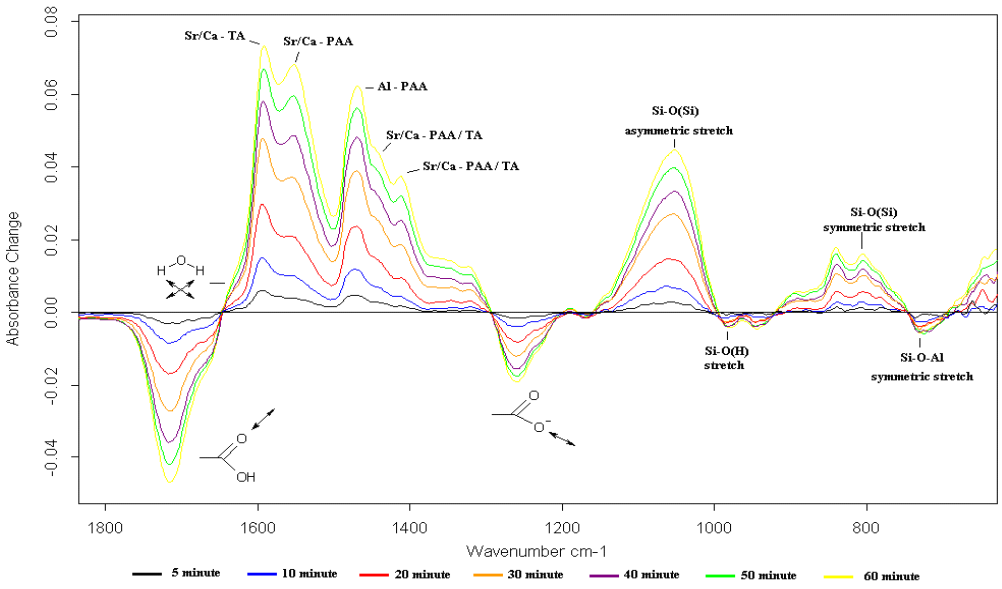

Figure 6.12: Difference Spectra of DC Cured at 15ºC between 5 - 60 Minutes

The occurrence of Al at both characteristic absorbencies (1560 cm^{-1} & 1473 cm^{-1}) within the 15ºC samples suggests that the ASG network is being broken down to release the Al cation but without the generation of Si-O(H). The rebuilding of the Si-O-Si structure without going through the Si-O(H) condensation intermediate is a possible explanation for this observation. The implication of this proposal is that the rebuilding of the ASG network does not proceed via the condensation of silicic acid. There is no reported evidence to support this proposal and without further investigation it is unable to propose an alternative mechanism of ASG rebuild.

6.3.3 Filler Incorporated Cements

The viscosity of TiGICs was found to increase at a greater rate than DC over the first 100 seconds of reaction from rheological results. The working time is reached by 2.5% TiGIC at 102 seconds, 7.5% TiGIC at 116 seconds and DC at 165 seconds.

The direct analysis of spectra containing un-coated and coated filler particles compared with DC is ambitious as interpretation of minute differences (Figure 6.13) is subjective. Figure 6.13 shows the spectra of uncoated TiGICs compared with DC over a 30 minute period. The only, clearly, distinguishable differences are is the early appearance of Al-PAA and Sr/Ca-TA at 1480 cm^{-1} and 1596 cm^{-1} in 7.5% (0%) TiGIC respectively.

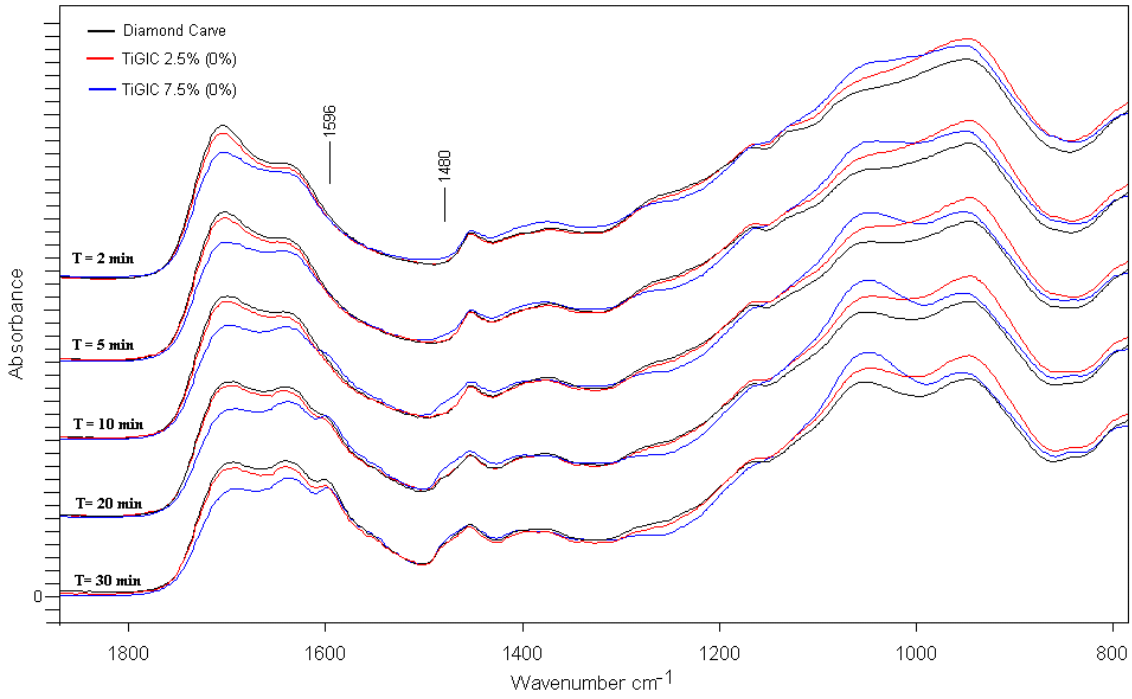

Figure 6.13: Reaction Comparison between DC (Blue), 2.5% (0%) TiGIC (Red) and 7.5% (0%) TiGIC (Black) - 30 Minutes

This would suggest that the 7.5% (0%) cement was reacting quicker than the control or the 2.5% (0%). A valid measure of cement reactivity is the decrease, or conversion, of –C=O to cement forming salts therefore can be used to approximate the rate of reaction.

When the data is taken apart and the rates calculated it can be seen (Figure 6.14) that DC is reacting the quickest and 2.5% (0%) and 7.5% (0%) have similar rates of reaction during the first 5 minutes of reaction.

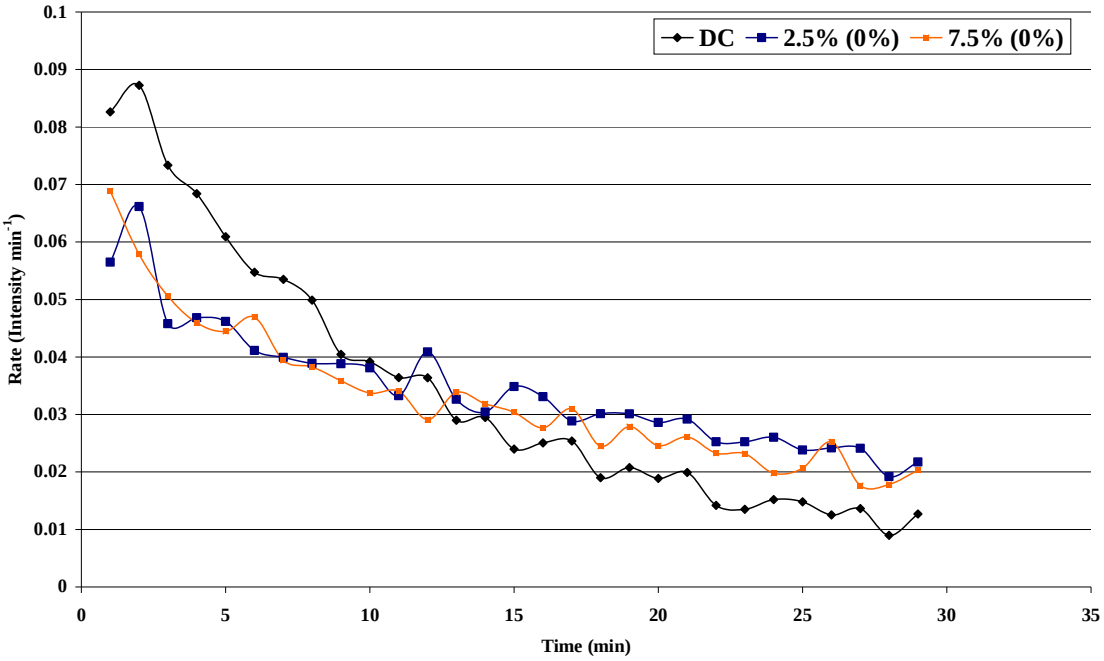

Figure 6.14: Rate of Carboxyl Consumption in Uncoated TiGICs and DC

A similar trend is seen in 2.5% (9%) TiGICs however 7.5% (9%) has a severely reduced rate of reaction compared to DC. This is unexpected as the Wilson rheometer produced a working time comparable with DC.

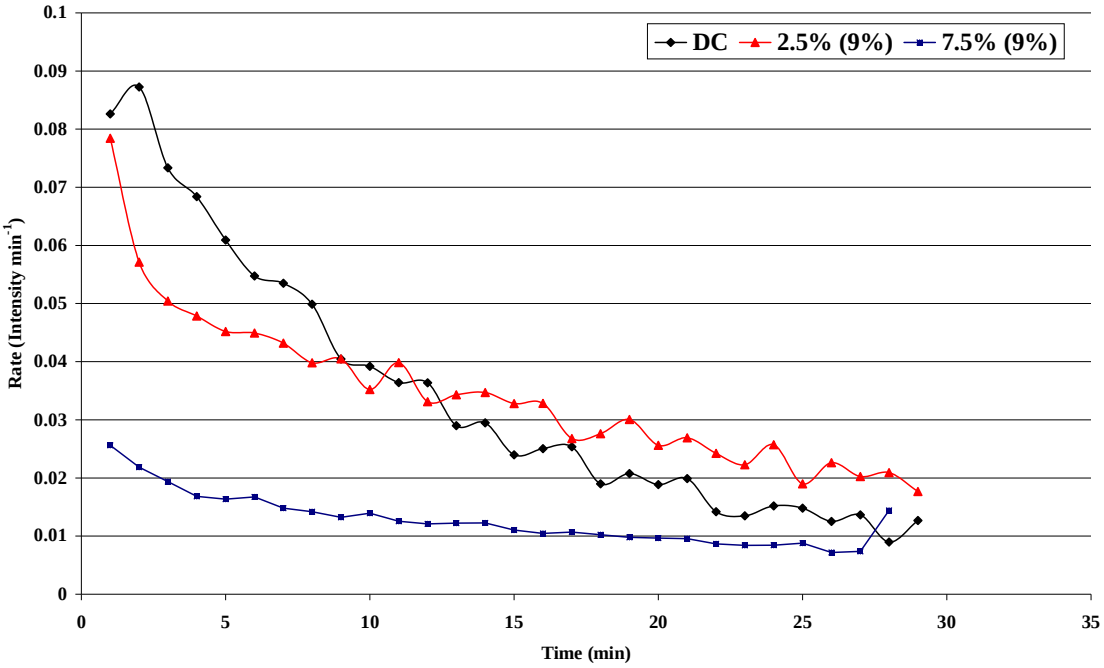

Figure 6.15: Rate of Carboxyl Consumption in Coated TiGICs and DC

The TiGICs have a slow rate of reaction during the first 5 minutes of reaction when compared to the control material. The rate of carboxyl consumption in the control material reduces rapidly and reaches a slower rate compared with the majority of the TiGICs after 15 minutes. This is in agreement with the AR2000 advanced rheometer results that found that the rate of reaction in the TiGICs is greater than DC after 10 minutes and continues at approximately the same rate until observation was stopped at 60 minutes. The rate of strength increase in the control cement had reached a plateau after 50 minutes where the reaction was assumed to have almost stopped.

High Al-TA reactivity during the first 5 minutes of reaction (Figure 6.16 & Figure 6.17) was an unexpected result as this salt isn't considered to become reactive until after strontium and calcium have become depleted (Nicholson, 1993). This result indicates that Al-TA is present at the beginning of acquisition and is reacting faster than Sr/Ca – TA which has previously not been reported.

The concentration of various cement salts cannot be directly identified from IR spectra due to the high degree of overlapping peaks and the dynamism of the curing cement. This may mean that Al-TA may be present in low concentrations although reacting faster than the other cement salts.

All TiGICs show the same trend in salt reactivity and are therefore only a single example of a coated and un-coated TiGIC is presented here (Figure 6.16 & Figure 6.17).

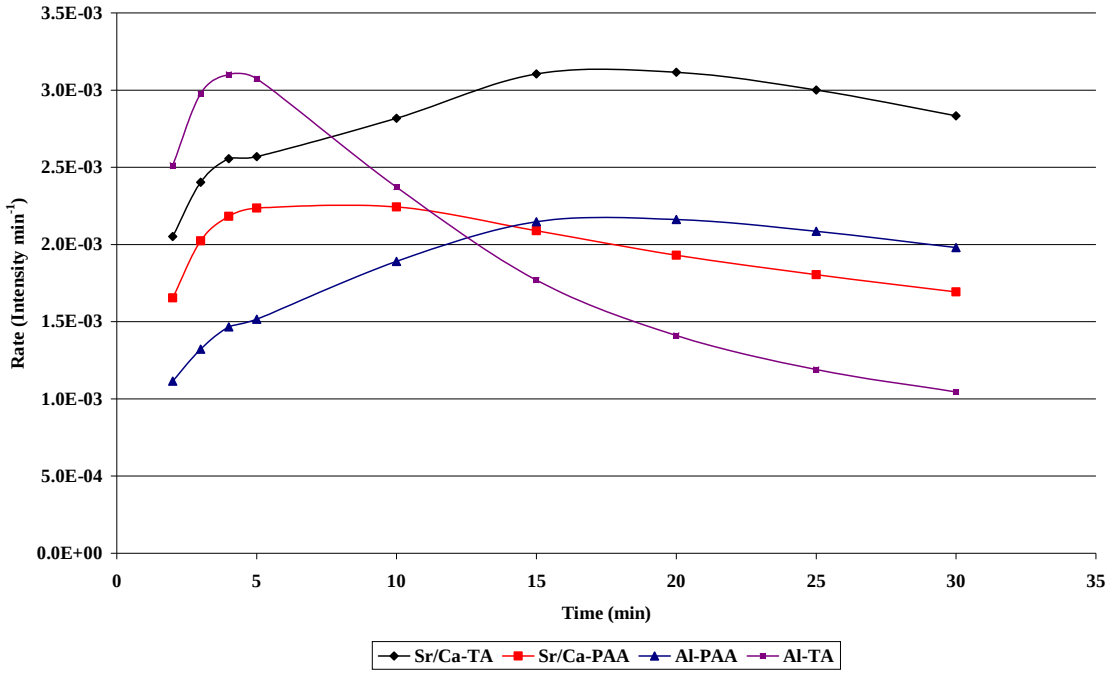

Figure 6.16: Rate of Major Salt Formation Calculated for 2.5% (0%) TiGIC from Difference Spectra

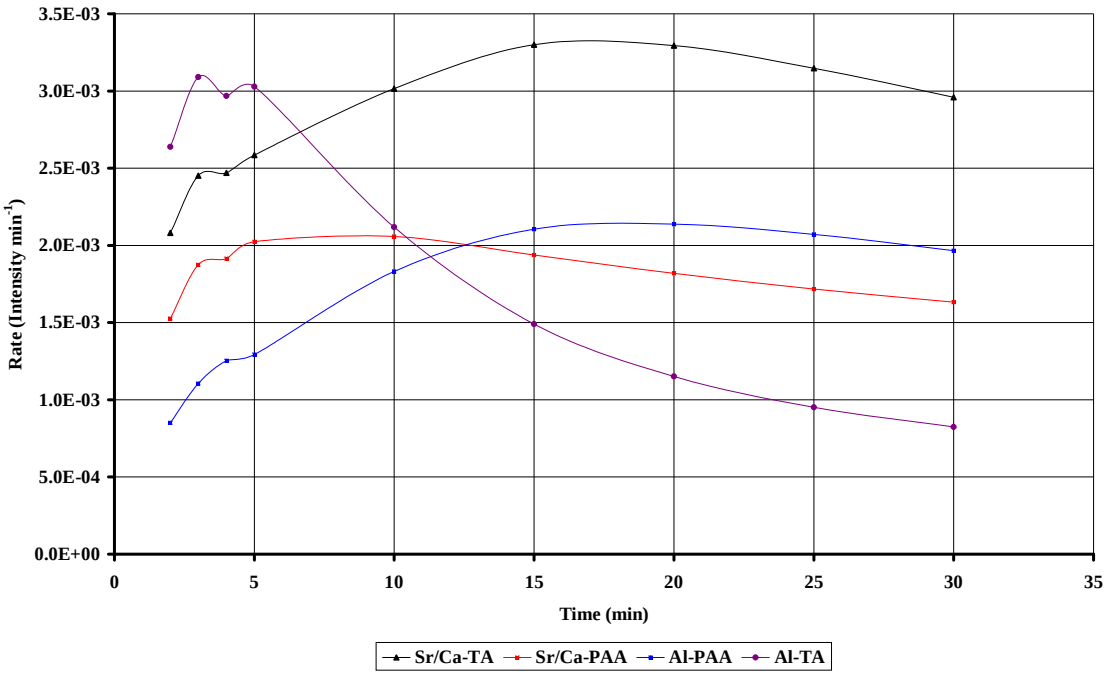

Figure 6.17: Rate of Major Salt Formation Calculated for 2.5% (9%) TiGIC from Difference Spectra

The extent of reaction was calculated from the decrease in the carboxyl peak at 1703 cm^{-1} (Figure 6.18) because this is the precursor for all the reactions taking place in DC and TiGICs. The consumption of the carboxyl groups is initially greatest in DC but this rate begins to slow after 4 minutes of monitoring caused by a decrease in available reagents and an increase in the mobility of polyions. The rates of reaction in the coated TiGICs coincide with the observed cement salts from the IR spectra (Figure 6.18) confirming the rate of reaction progress as DC → 2.5% (9%) → 7.5% (9%). As the reaction continues, DCs rate of reaction decreases however the rate of deceleration is not mimicked by the coated TiGIC cements. The 2.5% (9%) and 7.5% (9%) TiGICs rate of reaction become greater than DC after 10 and 22 minutes respectively. This is expected to be caused by the decreased powder to liquid ratio (ASG:PAA) allowing more steric freedom and greater available carboxyl groups for reaction with ASG.

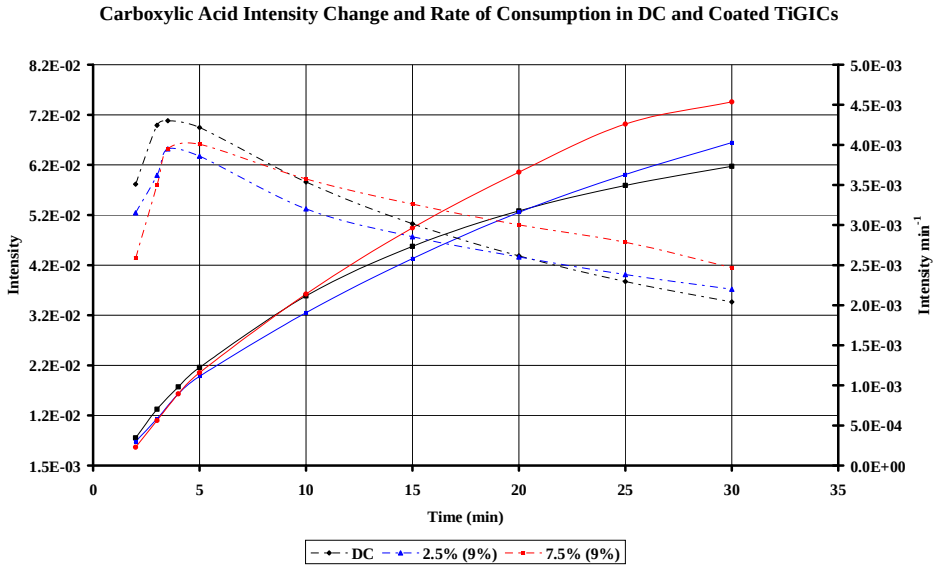

Figure 6.18: Intensity Change and Rate of Carboxyl Group Conversion in DC and Coated TiGICs

6.4 Conclusions

The IR investigation of DC, coated and un-coated TiGICs has identified the order of reaction with regard to the rate of initial formation of the cement salts. The dominant salt species identified in both the IR spectra (first appearance) and from the rate of formation (difference spectra) is Al-TA in all cement combinations except 7.5% (9%) TiGIC. The identification of Al-TA before that of Sr/Ca-TA has not been reported for other GICs and may be caused by the addition of the more acidic PVPA/AA co-polymer. The PVPA/AA was not expected to significantly influence the setting of the GICs because of its low concentration and absence of a reaction when just ASG and PVPA/AA were mixed together (*see* Appendix 3). The early dominance of Al-TA is soon replaced by Sr/Ca-TA as the rate of Al-TA production rapidly decreases but Sr/Ca-TA continues to increase and remain the highest reacting salt species throughout the rest of cement observation. Sr/Ca-PAA and Al-PAA are both found in the cements during the early stages of reaction from difference spectra. Their presence isn't detected in the IR spectra until the salt intensity has increased enough to become distinguished from the baseline.

The baseline is constantly increasing in intensity because of the formation of overlapping salts therefore, in order for a salt peak to become distinguished from another close absorbance the difference in intensity needs to be large enough so that a single peak can be observed and not a large broad, undefined absorbance. The increase in the formation of Al-PAA is slower than the other cement salts so as the peak reaction rate is reached the other cement salts are well in decline. These results in a switch between the dominant PAA salt being formed from Sr/Ca-PAA to Al-PAA which is expected (Crisp & Wilson, 1973; Wilson and Nicholson, 1996).

The addition of slow or non reacting filler particles has the apparent effect of reducing the powder to liquid ratio. This may be as a result of TiO_2 density being greater than ASG and therefore the w/w inclusion reduces the volume of powder or, the removal of the highly reactive ASG (De Maeyerl, 1998) has the effect of reducing the reactive species ratio (ASG:DC liquid). Prosser *et al* (1982), Wilson & Nicholson (1996) and Nicholson (1998) have shown that decreasing the powder to liquid ratio increases the working and setting time by increasing the number of carboxyl sites available for cross-linking and decreasing the readily available glass cations.

The early increase in viscosity in the TiGICs over DC has not been identified as the result of salt formation (chemical) with PAA as DC has the greater rate of salt formation over all TiGIC formulations. Therefore, early increases in viscosity are likely caused by the addition of micro-nano sized filler particles (mechanical) as described in Chapter 4.

Rheology has shown that IR of DC cements aged for 24 hours, powdered and pressed to form a KBr disk for transmission analysis would show a dominant peak from Al-PAA because of the relative concentrations of PAA and Al. The energetic stability of aluminium polyacrylate compared with the other salts of neutralisation is favourable and rearrangement to this form during maturation has been observed in NMR studies (Matsuya *et al*, 2007).

Chapter 7

Nuclear Magnetic Resonance Spectroscopy

Aim

The aim of this chapter is to identify new aluminium species caused by the reaction between the polyelectrolyte solution and $Al(OH)_3$ coating. The identification of evidence to support the expected cause of a shortened working and elongated setting time as mechanical and concentration effects respectively.

7.1 Introduction

The use of Fourier Transform Nuclear Magnetic Resonance (FT-NMR) and Magic Angle Spinning Nuclear Magnetic Resonance spectroscopy (MAS-NMR) have been used extensively by several studies to probe the setting mechanism of glass ionomer cements (GICs) (Hill *et al*, 2006, Stamboulis *et al*, 2006 and Zainuddina *et al*, 2008)

Coated TiO_2 particles have a 9% w/w aluminium hydroxide ($Al(OH)_3$) layer which is thought to react with the polyelectrolyte solution used with acid - base cements (TiGIC) to enhance the setting reaction and link the TiO_2 base material into the polysalt network of the fully set cement.

Aluminium and phosphorus nuclei have been probed in cements aged between 1 hour and 1 day. Aluminium was chosen because of its vital role in the cross-linking of polyacrylic acid (PAA) and its distinct coordinate states in the aluminosilicate glass (ASG) and cement forming salt bridges. The identification of aluminium hydroxide as a coating material would make the identification of reactions taking place with the coating and cement forming solution possible. Identification of competing reactions occurring simultaneously with the acid-base reaction of the control material would further aid the understanding of the complex setting chemistry.

Phosphorus was chosen because the addition of polyvinylphosphonic acrylic acid co-polymer (PVPA/AA) has not previously been studied in GICs using NMR and may identify a chemical cause for the decreased working time.

7.2 Experimental Method

7.2.1 Sample Preparation

The prepared cement (*see* Chapter 3) was placed in stainless steel moulds complying with ISO 9917-1 (3mm x 6mm). The moulds were clamped between two pieces of polished stainless steel and placed in an oven at 37ºC for 1 hour. They were removed from the moulds and further aged in distilled water at 37ºC to prevent dehydration.

The acid-base reaction was terminated as follows,

1. The test samples were quenched in liquid nitrogen to stop the reaction progressing at its normal rate.
2. The frozen pellets were then ground into a fine paste in ethanol to displace any free water not associated with any reaction products.
3. The cement paste was then desiccated at 60ºC to dry excess ethanol solvent leaving a dry sample powder.
4. The dried sample powder was then stored in an evacuated dedicator containing self indicating silica gel.

The acid-base reaction must be stopped at specific times before the NMR analysis. The experiment is stopped otherwise continuation of the hardening process within the GIC fragments will lead to erroneous results.

Powdered samples were prepared from Diamond Carve, coated and uncoated 2.5% TiGIC and 7.5% TiGICs. The setting reaction was stopped at 1 hour, 3 hours and 1 day for each sample set.

7.2.2 Magic Angle Spinning Nuclear Magnetic Resonance (MAS NMR)

A Bruker AVANCE DSX 400 MHz NMR spectrometer (9.4 Tesla) was used to carry out MAS-NMR spectroscopy of DC and TiGICs to probe the aluminium and phosphorus environments within the cement samples. The spectrometer was used with a low capacity (4 mm), multi-nuclear probe head (^{6}Li to ^{31}P, max spin speed 15 KHz) and a rotor speed of 4 kHz. Sample powders were packed into a 4mm zirconia rotor and sealed with a chloro-trifluoroethylene (Kel-F) end cap.

The spectrometer was calibrated for ^{27}Al nuclei using aluminium chloride hexahydrate ($AlCl_3.6H_2O$) as a standard reference material and the chemical shift was adjusted to 0 ppm. ^{27}Al spectra were recorded at 104.3 MHz with a pulse width of 2.8 ps and a delay time of 0.5 s, 1024 scans were collected per spectrum.

The spectrometer was calibrated for ^{31}P nuclei using 85% phosphoric acid (H_2PO_4) as a standard reference material and the chemical shift was adjusted to 0 ppm. ^{31}P spectra were recorded at 161.98 MHz with a pulse width of 2.8 ps and a delay time of 30 s, 1024 scans were collected per spectrum.

Spectra were recorded using the spectrometer controlling Bruker software. Spectral manipulation and image preparation was performed using SpecManager from ACD/Labs.

7.3 Results and Discussion

7.3.1 Aluminium Environment

Aluminium is a trivalent cation that is removed from basic aluminosilicate glass by acid hydration of the silica network. Aluminium is released immediately (*see* Chapter 6) in low concentrations (Zainuddina *et al*, 2008*)* which gradually increases until neutralisation of the polyelectrolyte solution occurs (Nicholson, 1998).

Aluminium forms 1 - 2 covalent (Lee *et al*, 1996) bonds with the carboxyl group of the polyelectrolyte solution and is then surrounded by water taking up a hexahedral arrangement (Nicholson, 1998) (Figure 2.8); the increase of compressive strength over time is attributed to the complex formation with loosely bound water molecules (Wilson & Nicholson, 1996). The reaction progress can be monitored using the changing signal strength of tetrahedral bound aluminium in the aluminosilicate glass and liberated hexahedral aluminium in polymer cross-links (Stamboulis *et al*, 2006; Zainuddina *et al*, 2008).

7.3.1.1 Diamond Carve

Aluminosilicate glass has an asymmetric peak at 56.84 ppm (Figure 7.1). The intensity values for this peak were normalised to 1 so identification of changes in the DC cement could be easily detected. The signal is representative of aluminium co-ordinated by 4 oxygen's (Al(IV)) in the un-reacted glass; small quantities of Al(V) cause the asymmetry by forming a small tail centred at 12.37 ppm (MacKenzie & Smith, 2002; Stamboulis *et al*, 2006).

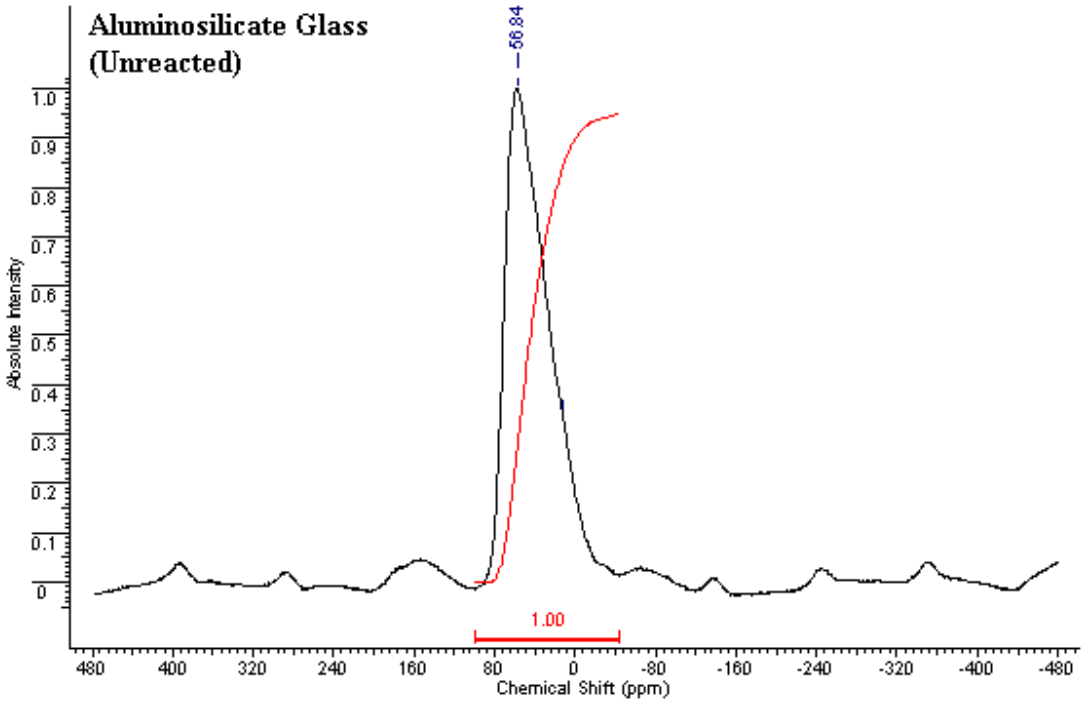

Figure 7.1: Aluminium Solid State NMR Spectra of Un-reacted Aluminosilicate Glass (Control)

Mixing ASG with the polyelectrolyte solution causes the single 4 co-ordinate aluminium to form a doublet of changing intensity (Figure 7.2). Two peaks are located at 63.86 ppm and 12.82 ppm which are assigned to Al(IV) and Al(VI) respectively. The deconvolution performed by Zainuddina *et al* (2008) suggests that the shoulder present on the strong Al(IV) peak at around 39–42 ppm is caused by Al(V) from ASG. The Al(V) signal intensity remains approximately constant throughout cement maturation.
The signal intensity of the Al(IV) peak has decreased rapidly from the un-reacted ASG during the first hour of reaction identifying the rapid breakdown of the glass structure. The peak intensities displayed in Table 7.1 fluctuate as a result of a rolling baseline presumed to be caused by a quadrapolar interaction because of the amorphous aluminium glass environment (loss of symmetry and long range structure; Matsuya *et al*, 2007). Therefore, the most robust measure of reaction progress is the ratio between Al(IV) and Al(VI) peak intensities as this indicates the extent of ASG degradation and subsequent aluminium release.

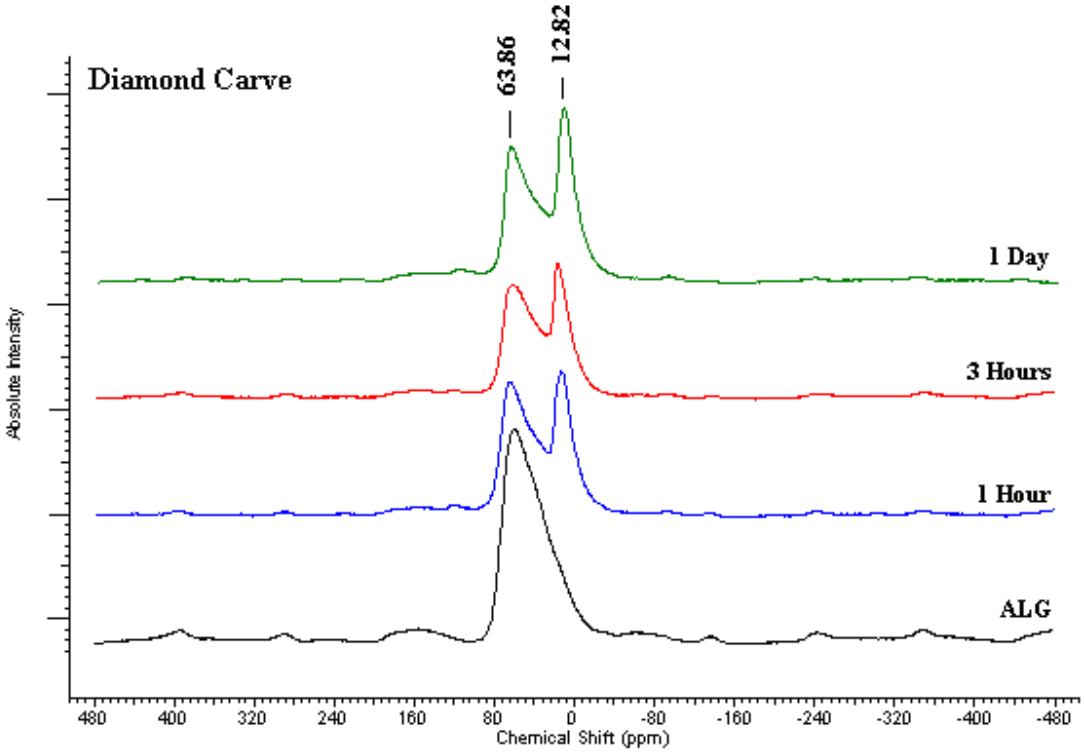

Figure 7.2: ^{27}Al MAS-NMR Analysis during the Acid-Base Curing Process of DC

As time proceeds the concentration of Al(VI) increases relative to Al(IV) therefore, the ratio increases. The release of Al(IV) from ASG is greatest during the first hour as represented by the decrease in the Al(IV) peak intensity value from 1 to 0.628. Al(IV) is continually removed from the ASG over the next 23 hours but at a slow, decreasing rate confirming the continuation of the acid-base reaction for over a 24h period. Zainuddin *et al* (2008) have found the intensity of the Al(IV) peak to decrease and the Al(VI) increase quickly over 24 hours but continually over a year. Crisp *et al* (1976) have stated that the acid base reaction may continue indefinitely.

Sample	DC (1 Hour)		DC (3 Hours)		DC (1 Day)	
Aluminium Species	Al(IV)	Al(VI)	Al(IV)	Al(VI)	Al(IV)	Al(VI)
Peak Intensity	0.628	0.680	0.530	0.632	0.637	0.820
Ratio (VI:IV)	1.083		1.192		1.287	

Table 7.1: Intensity Changes in Al(IV & VI) during the Curing Process of DC

7.3.1.2 Filler Incorporated Cements

The Infrared analysis (*see* Chapter 4) has shown that the TiGICs follow a similar reaction pathway to the original GIC however no explanation for the decreased setting rate could be directly identified.

The NMR spectra collected for all TiGIC combinations (Figure 7.3 - Figure 7.8) show that the reaction progresses in the same way as DC (Figure 7.2). The acid attack upon the ASG liberates aluminium from the basic glass lowering the intensity of Al(IV). The subsequent formation of aluminium cement salts after liberation increases the intensity of Al(VI) visible in the spectra. The differences between TiGIC samples are small when represented graphically (Figure 7.3 - Figure 7.8) and are therefore better illustrated in a data table (Table 7.2).

Sample	Sample Age / Aluminium Species					
	1 Hour		3 Hour		1 Day	
	Al(IV)	Al(VI)	Al(IV)	Al(VI)	Al(IV)	Al(VI)
DC	0.628	0.680	0.530	0.632	0.637	0.820
Ratio (VI:IV)	1.083		1.192		1.287	
2.5% (0%)	0.556	0.635	0.543	0.646	0.574	0.740
Ratio (VI:IV)	1.143		1.189		1.290	
2.5% (9%)	0.534	0.617	0.555	0.649	0.543	0.694
Ratio (VI:IV)	1.154		1.170		1.279	
7.5% (0%)	0.547	0.603	0.527	0.658	0.484	0.630
Ratio (VI:IV)	1.102		1.247		1.301	
7.5% (9%)	0.540	0.580	0.536	0.640	0.539	0.714
Ratio (VI:IV)	1.075		1.195		1.323	

Table 7.2: ^{27}Al (IV & VI) Peak Height of Coated and Uncoated TiGICs

The 2.5% and 7.5% cements (Figure 7.3 & Figure 7.4) 1 hour after initiation show an greater rate of ASG breakdown and subsequent salt formation than DC. The 2.5% cement has a greater difference than the 7.5% cement suggesting that the removal of ASG is encouraging accelerated degeneration of the ASG when compared to DC. However, direct comparison of DC with the TiGICs (Figure 7.5 & Figure 7.6) identifies a decrease in aluminium concentration in the TiGICs when compared to DC. If the aluminium content of the TiGICs were equal or greater than DC the sum of the Al(IV) & Al(VI) peak heights would be equal or greater than DC independent of reaction speed; this is not apparent in Table 7.2.

The removal of ASG from uncoated TiGICs has clearly causes a reduction in the aluminium content of the cement which is proportional to the % ASG removal (Figure 7.6). A reduction of 10g ASG equates to a loss of 1.48g Al^{3+} (Fennell *et al*, 1998) effecting the active ASG to PAA ratio. The difference between the Al(IV) and Al(VI) peak intensities remains constantly greater within the uncoated TiGICs samples throughout the 24h's of ageing suggested a further degree of degradation of the ASG network when compared to the original GIC.

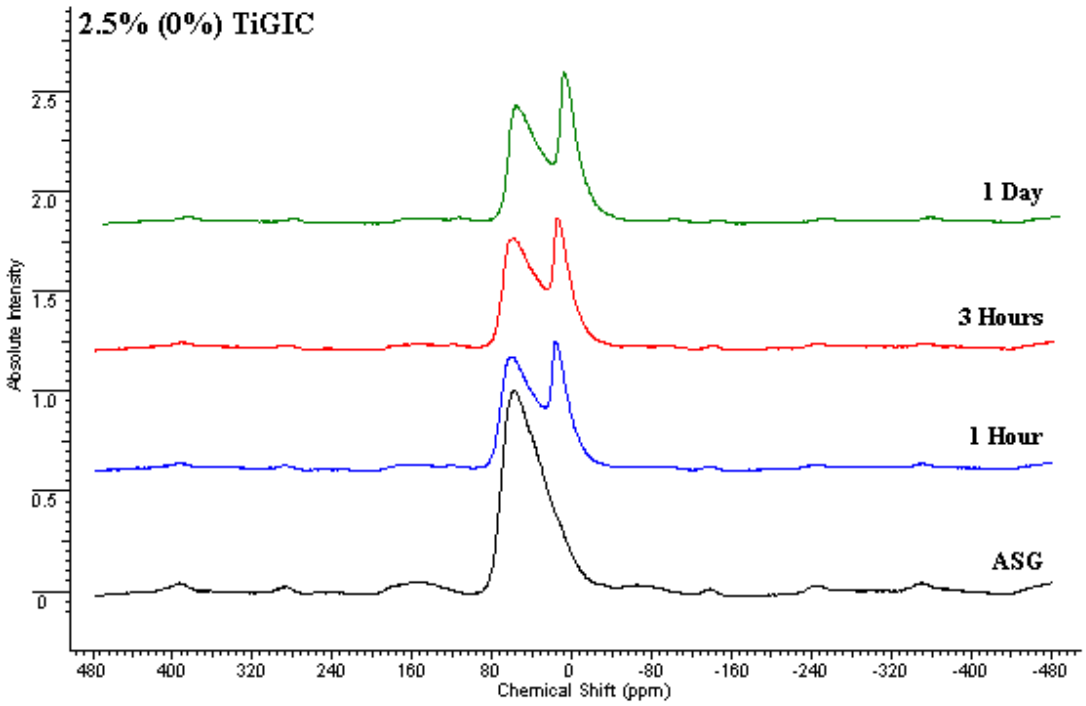

Figure 7.3: ^{27}Al MAS-NMR Analysis during the Acid-Base Curing Process of 2.5% Uncoated TiO_2

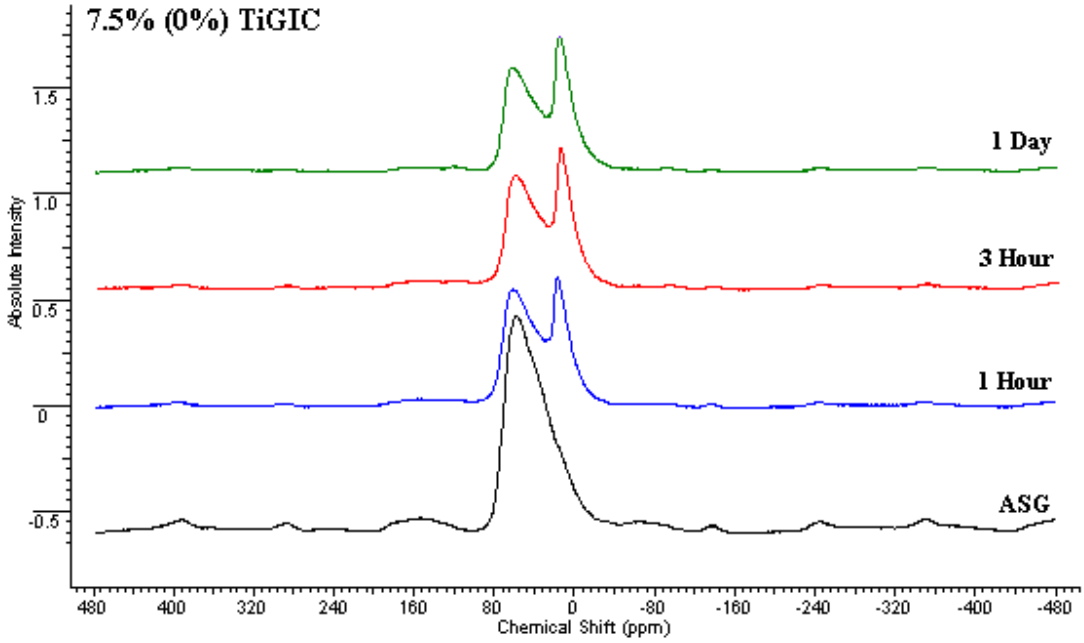

Figure 7.4: ^{27}Al MAS-NMR Analysis during the Acid-Base Curing Process of 7.5% Uncoated TiO_2

The reduction in available aluminium for reaction will have changed the equilibrium of the reaction by moving the position to the right (products) temporarily. The accelerated degradation of the ASG in the TiGICs during the early stages of reaction is consistent with the results presented in Figure 7.3, Figure 7.4 and the shortening of the working time from rheological experiments (*see*, Chapter 4).

The concentration of both Al(IV / VI) is greater in the original GIC 1 hour after activation although the apparent breakdown of the ASG structure (indicated by ratio in Table 7.2) is not as great as in the TiGICs.

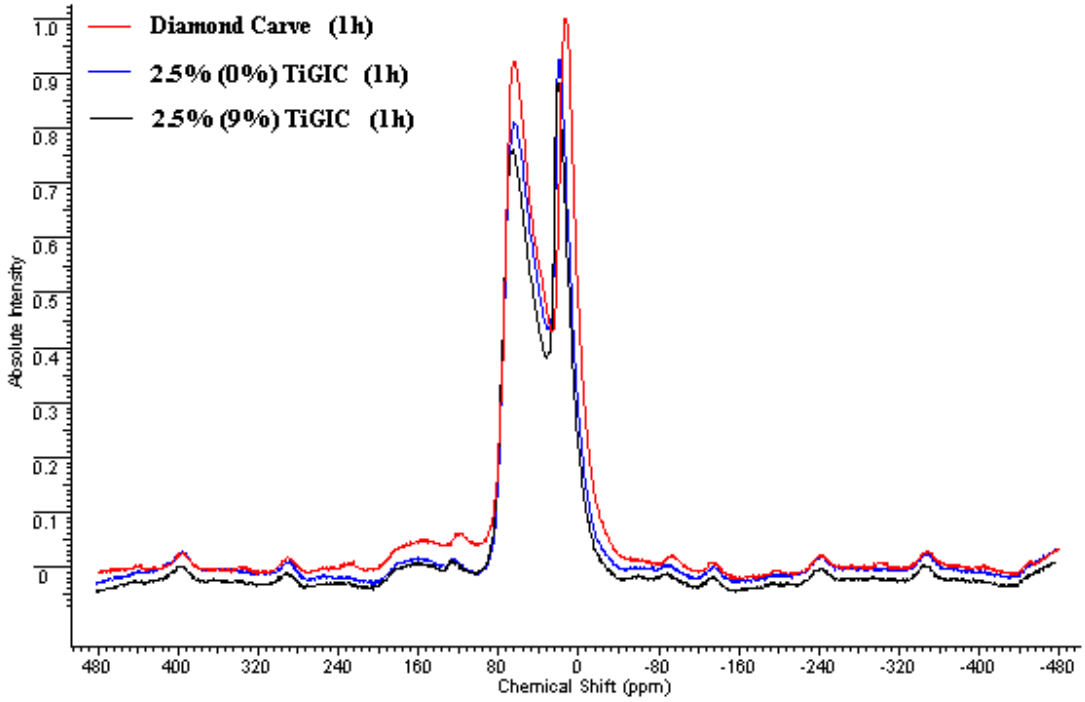

Figure 7.5: Comparison of Un/Coated 2.5% TiGIC with DC at 1 Hour

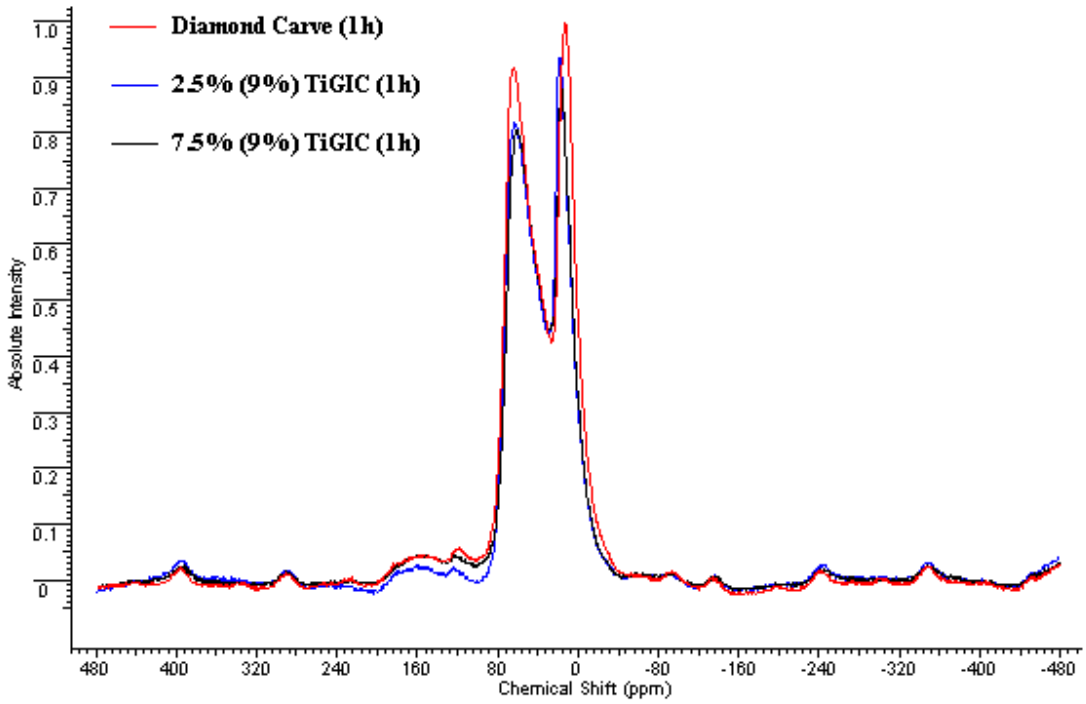

Figure 7.6: Comparison of 2.5% & 7.5% Coated TiGIC with DC at 1 Hour

The addition of a 9% w/w $Al(OH)_3$ coating to the inactive TiO_2 base particle has had little effect on the peak intensity differences over a 24 hour period.

Consider the removal of 10g of ASG which, as previously mentioned (*see* Section 2.2.1.2, page 7), is composed of 52.66% Al_2O_3 and 6.79% $AlPO_4$. The removal of 10g of ASG is the equivalent of removing 1.65g of aluminium. This is then replaced with 10g of 9% w/w coated TiO_2 which has the equivalent of 0.9g of $Al(OH)_3$ and only 0.31g of aluminium. The replacement of ASG with 9% w/w coated TiO_2 is effectively removing 80.85% of the aluminium in the system on a weight by weight basis. The TiGICs have a w/w replacements of 2.5% and 7.5% so the majority of the reactive aluminium available in the glass is maintained for reaction.

The reaction progresses the same way in the coated TiGICs (Figure 7.7 & Figure 7.8) as it has done in the uncoated TiGICs and original GIC.

The coating is known to react slowly with PAA (*see* Chapter 3) however its presence in the cement, although slight, has failed to react with PAA and boost the intensity of the Al(VI) peak to greater values than in the uncoated TiGICs after 24h of reaction; Table 7.2 suggests that the coating is hindering the production of Al(VI).

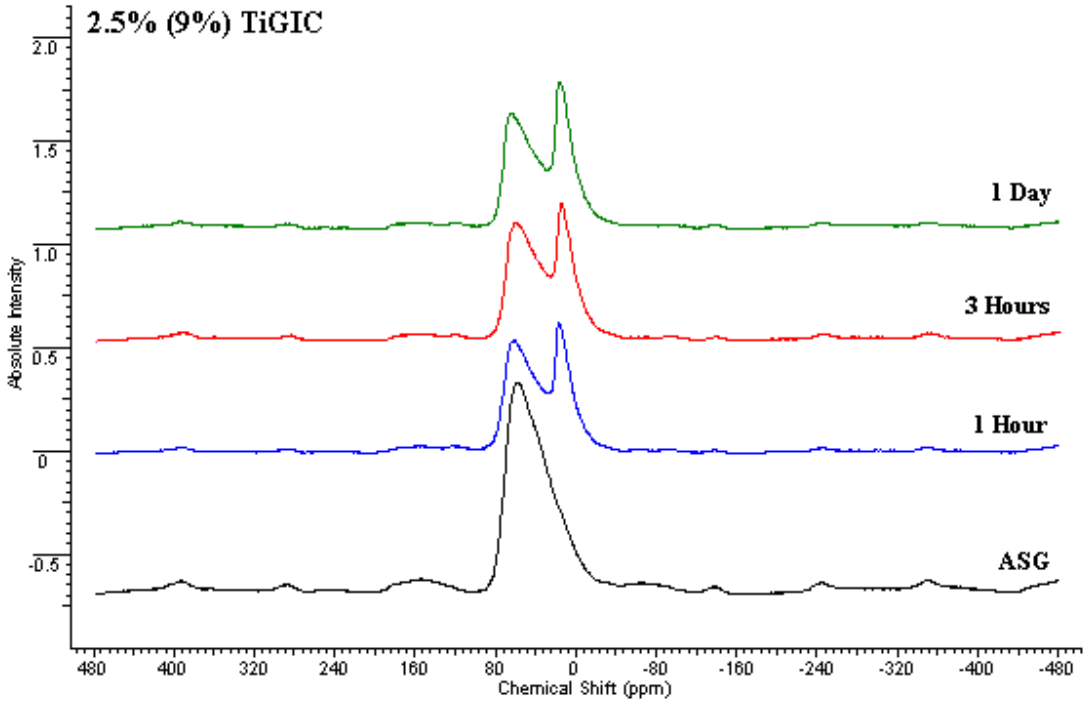

Figure 7.7: ^{27}Al MAS-NMR Analysis during the Acid-Base Curing Process of 2.5% Coated TiO2

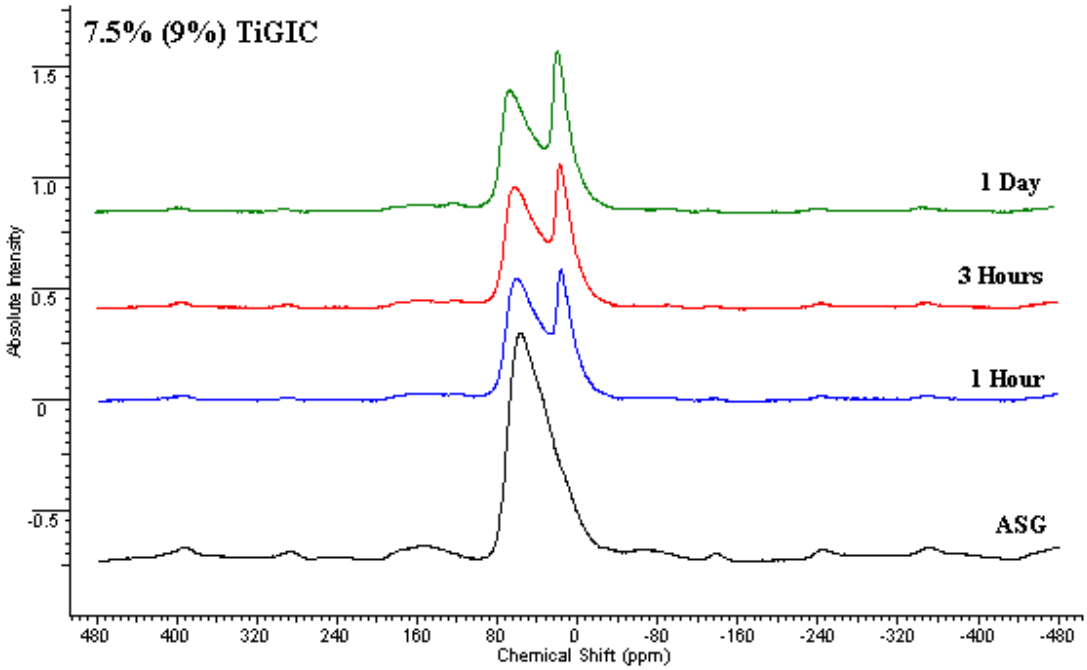

Figure 7.8: ^{27}Al MAS-NMR Analysis during the Acid-Base Curing Process of 7.5% Coated TiO2

7.3.2 Phosphorus Environment

The control material for the analysis of the phosphorus environment was the co-polymer polyvinylphosphonic acrylic acid (PVPA/AA) found in DC. It was hoped that the additional acidic strength of the PVPA component of the polymer would react preferentially with $Al(OH)_3$ during the acid base reaction. PVPA/AA (Figure 7.9) has a symmetrical peak based at 32.05 ppm caused by the phosphoric acid group of the co-polymer (Figure 7.10).

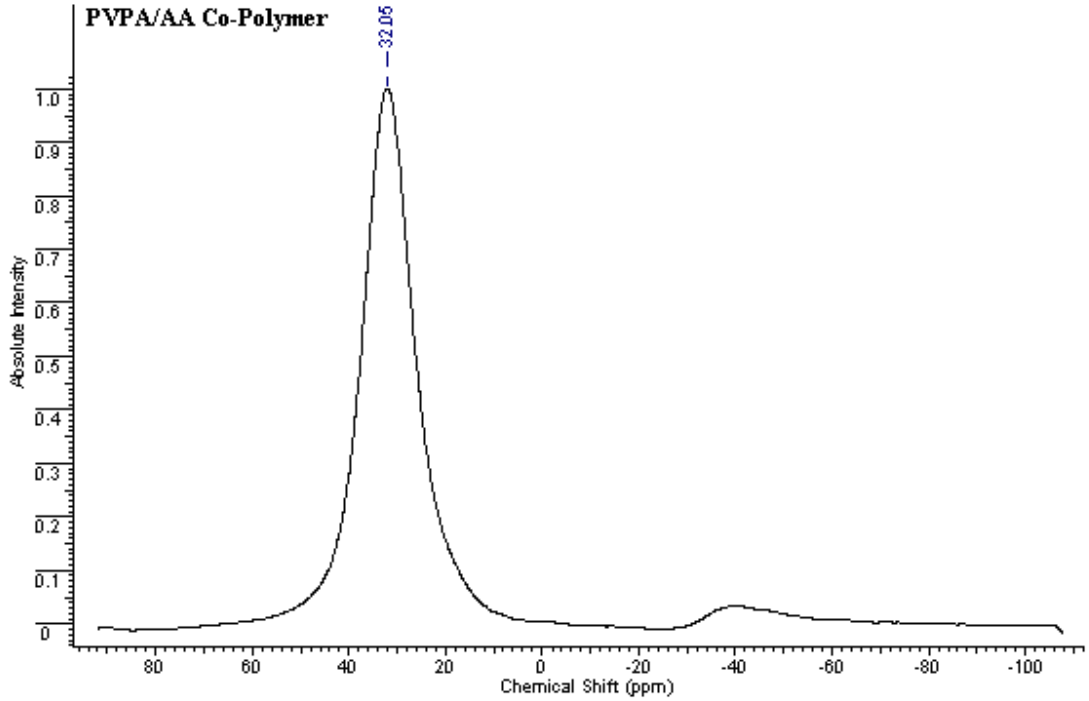

Figure 7.9: Control Spectra of PVPA/AA Co-Polymer (Unreacted)

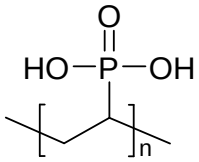

Figure 7.10: PVPA

The use of PVPA/AA as a control material was a poor choice because such low levels are used in DC GIC that the control measurement was in great excess therefore no quantitative comparison between the control and sample GIC / TiGICs could be made and only a qualitative analysis has been performed. A more suitable control material would have been ASG as the amount of reported phosphorus pentoxide (Fennell *et al*, 1998) is in excess of the phosphorus content in PVPA/AA and would be quantitatively comparable.

The peak separation between the PVPA/AA control material and the peaks found in the original GIC (Figure 7.13) spectra indicate a dominant phosphorus environment from ASG in the GIC rather than from PVPA/AA.

DC at one hour has a peak at -12.20 ppm which has been attributed to phosphorus in an $[Al–PO_4]^{3-}$ pyrophosphate-type environment Stamboulis *et al* (2004). The peak at -12.20 ppm is asymmetrical with a slight shoulder at -25.15 ppm. The shoulder is presumed to be caused by the formation of P(*n*Al) species where increasing *n* decreases the chemical shift e.g. P(4Al) is a PO_4 tetrahedron surrounded by 4 Al and has a chemical shift of -29 ppm (Figure 7.11) (Dollase *et al*, 1989). Therefore, the cause of the shoulder is believed to be a P(2Al) pyrophosphate group (Figure 7.12) (Stamboulis *et al*, 2006).

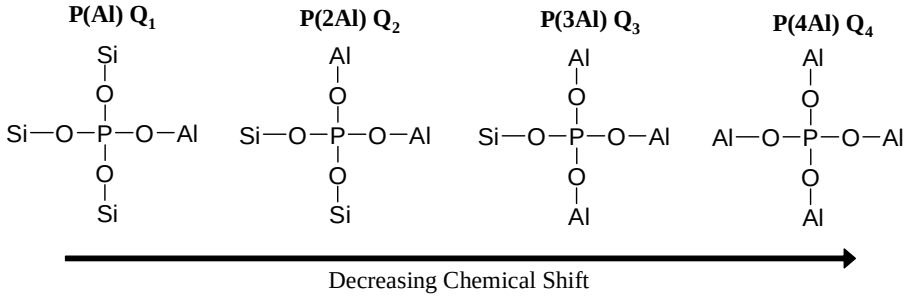

Figure 7.11: Phosphorus Coordination with Aluminium

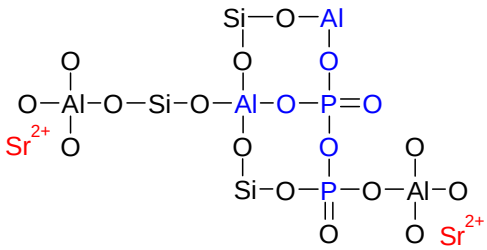

Figure 7.12: Example of a Pyrophosphate Group Surrounded by 2 Al-O Tetrahedrons (Blue) in a Partially Degraded ASG Network

The spectra of DC after 3 hours of reaction show little change in the intensity of $[Al–PO_4]^{3-}$ however the peak location has shifted slightly to -12.64 ppm suggesting a slight change in the environment around the PO_4 tetrahedron as the reaction progressed; Stamboulis *et al* (2006) have reported a shift in pyrophosphate peak position of multiple cements containing different ASG's as they were aged. This is believed to be caused by an increase in the number of AlO_4 around the PO_4 environment as a result of the removal of strontium continues throughout hydrolysis of the ASG.

The shoulder on the original pyrophosphate (-12.20 ppm) peak at -25.15 experiences a substantial increase 3 hour after mixing which subsides over the remaining 24 hours (Figure 7.13). The chemical shift of P(Al) and P(4Al) is -8 ppm and -29 ppm respectively (Stamboulis *et al*, 2004) so the temporary shoulder at -25.15 may be caused by a P(3Al) pyrophosphate species meaning that the concentration of network dwelling cations is in slight excess of the amount needed to balance the negative aluminium in ASG at this point. The highly co-ordinated PO_4 tetrahedron is present at low levels throughout cement maturation causing the asymmetry of lower co-ordinated PO_4 peak at -12.20 however a step in the reaction between 1 and 24 hours generates highly co-ordinated phosphates. The cause of the increased intensity at -25.15 ppm is not known, the removal of Sr/Ca into the polyelectrolyte solution causes the chemical shift to decrease and so does an increase in the number of bonding oxygen's which all stem from the level of network modifiers (Cody *et al*, 2001).

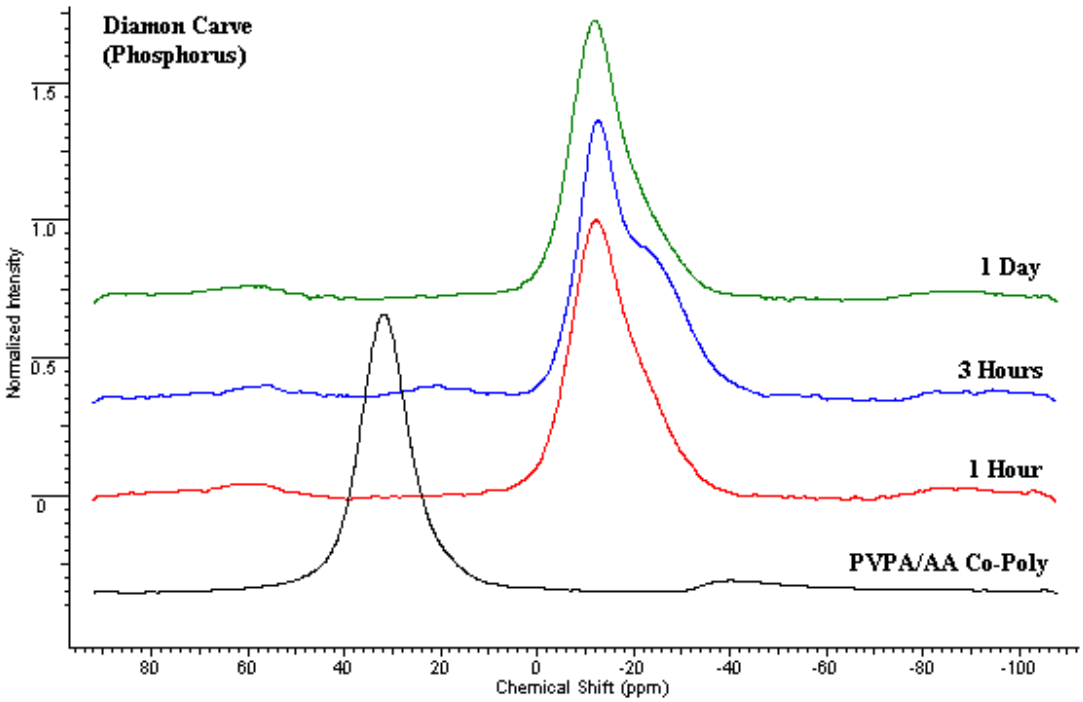

Figure 7.13: Phosphorus Solid State NMR Analysis of the Maturation of Diamond Carve

The phosphorus analysis of the TiGICs only includes the 7.5% cements because of time constraints. It was felt that analysing the greatest filler incorporated cements would show any differences better than the lower, 2.5%, incorporated cements.

The 7.5% uncoated TiGIC (Figure 7.14) show the same pyrophosphate peak found in DC GIC at -12.51 ppm which does not change intensity considerably (baseline shift) over the 24h duration. The temporary shoulder from the DC GIC is permanently in the spectrum of 7.5% (0%) TiGIC at -25.15 ppm, the intensity of which decreases as the samples age. The shoulder has a greater width in the 7.5% (0%) TiGIC than in the DC GIC samples suggesting multiple phosphorus complexes (O'Neill *et al*, 1982). The presence of a second shoulder at approximately -30 ppm in the sample aged 24h confirms the presence of at least 3 different phosphorus complexes at -12.20 ppm, -25.15 ppm and -30 ppm. The P(4Al) peak at -30 ppm (Dollase *et al*, 1989) remains constant over 24h where as the peak at -25.15 decreases relative to it. This decrease is not a result of a transformation from one P(*n*Al) complex to another as the intensity of the other two signals remain constant.

The reduction in the -25.15 ppm signal may be as a result of acid hydrolysis of the P(*n*Al) bond causing the signal to diminish however, this is a natural step in the reaction as seen in DC GIC.

Griffin & Hill (2000) have reported that the Al:P ratio of the ASG close to 1 will cause a reduction in the amount of Al released from the ASG because the Al-O-P bond is no longer susceptible to acid hydration; addition of P_2O_5 stabilises the AlO_4 bond (O'Donnell, 2008). The cause of the increased shoulder width and the generation of a complex at -30 ppm may therefore be caused by the increased acid hydrolysis of the ASG removing a greater number of network modifiers forcing the AlO_4 to take up an arrangement around a / multiple phosphorus tetrahedron for stability (Cody *et al*, 2001).

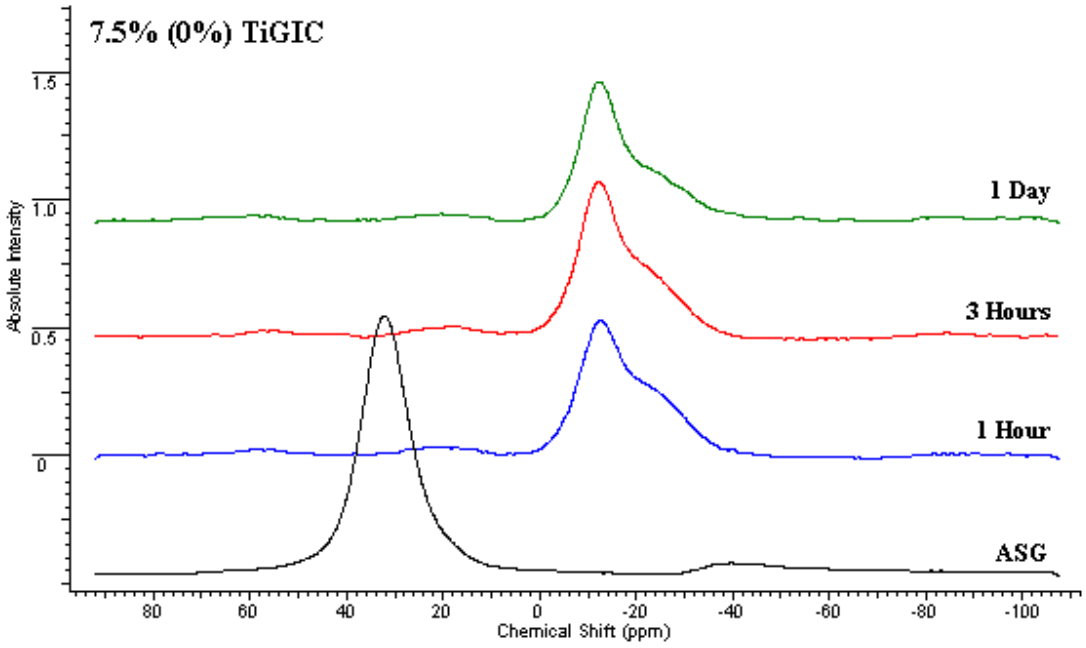

Figure 7.14: Phosphorus Solid State NMR Analysis of the Maturation of 7.5% Uncoated TiGIC

The ^{31}P coated 7.5% TiGIC results show similar peaks to both the DC GIC and uncoated 7.5% TiGIC. A strong signal is found at -12.78 ppm which is attributed to P(2Al) pyrophosphate (Figure 7.15). The intensity of the P(2Al) peak decreases slightly as the cement aged over the remaining 3 and 24 hour samples.

The peak position also moves to more negative values (-12.79 → -14.02 ppm) over 24h which, given previous discussion, may mean that the PO_4 environment is becoming surrounded by AlO_4 tetrahedron to stabilise the loss of network dwelling ions. The intensity of the shoulder present at -21.23 ppm increases between 1 – 3 hours but then decreases over 3 – 24 hours as seen in DC GIC. The width of the shoulder increases from the initial measurement at 1 hour in the 3 and 24 hour samples. This was seen in the uncoated 7.5% TiGICs and is possibly caused by the removal of network dwelling ions or the breakdown in Al-O-P bonds causing the formation of multiple phosphate species (O'Neill *et al*, 1982).

Higher coordinated PO_4 complexes initially have a much greater intensity in the 1 hour sample than the 3 or 24 hour samples suggesting a greater concentration of P(*n*Al) species in the 7.5% coated TiGICs compared to uncoated TiGIC and DC GIC.

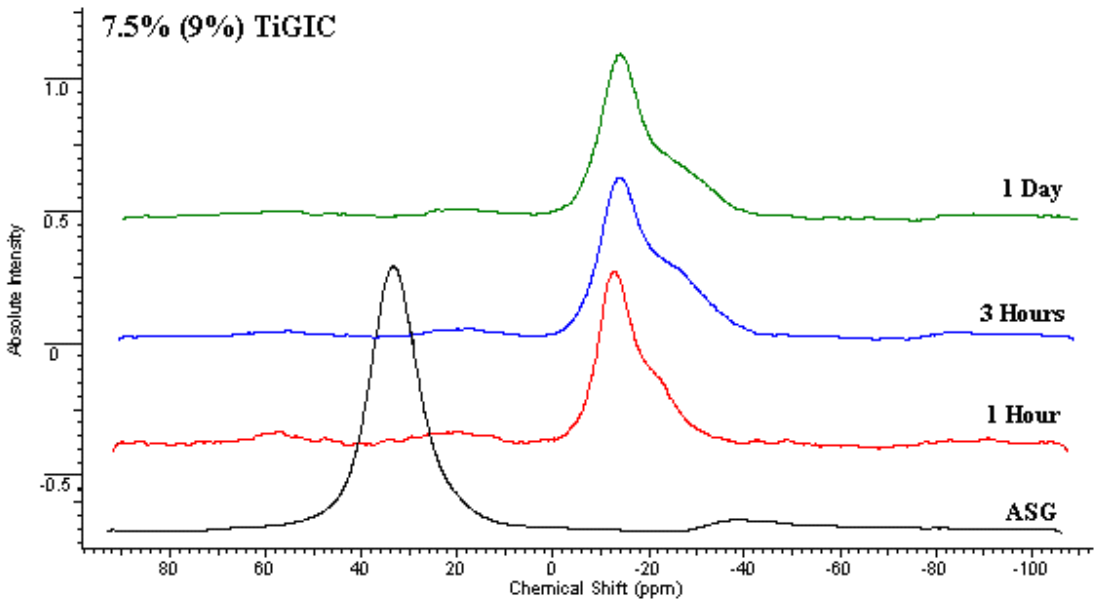

Figure 7.15: Phosphorus Solid State NMR Analysis of the Maturation of 7.5% Coated TiGIC

7.4 Conclusion

The SS NMR analysis of ^{27}Al and ^{31}P nuclear sites in DC GIC and un/coated TiGICs has identified the breakdown of ASG, subsequent formation of Al-PAA and Al-TA (Al(VI)) and the formation of multiple pyrophosphate type species.

The ^{27}Al spectroscopy of DC found that aluminium in an ASG network is predominantly in a tetrahedral environment, Al(IV). As the ASG is acid hydrolysed by the polyelectrolyte solution aluminium is removed from the tetrahedral orientation and forms a hexagonal, Al(VI) orientation with available carboxylic groups and water in the acid solution. The breakdown of the ASG environment and subsequent removal of Al(IV) has been found to occur in the same way as the control material but at an increased pace in the TiGICs however, the removal of ASG means that the concentration of Al(IV) and Al(VI) is always greatest in DC GIC. The reduction in aluminium concentration has effectively caused a reduction in the powder to liquid ratio which is known to cause an elongation of setting time (Wilson, 1976; Cook, 1983; Billington *et al*, 1990). Therefore, the cause of setting time elongation is a consequence of ASG removal.
The accelerated degradation of the ASG network in the TiGICs may be the cause of premature gelation of the PAA solution and subsequent reductions in working time however measurements around that time have not been performed.

The ^{31}P spectroscopy of DC GIC has found that phosphorus is always present in a pyrophosphate type arrangement with aluminium (Figure 7.12). There is a periodic increase in P(*n*Al) species, where *n* is greater than 2, during the setting reaction which is believed to be caused by the removal of network dwelling ions forcing AlO_4 tetrahedron to take up orientation around a PO_4 tetrahedron for stability before breakdown of the Al-O-P bond. The TiGICs always have these P(*n*Al) species, where *n* is greater than 2, present in all samples tested. The rapid breakdown of the ASG network in the TiGICs, as indicated by ^{27}Al results, may mean that greater amounts of Sr^{2+} have been removed from the ASG causing the formation of P(4Al) tetrahedron followed by the breakdown of the Al-O-P bond resulting in aluminium cation release.

The addition of $Al(OH)_3$ as a coating on the TiO_2 filler particles has not caused the formation of additional peaks in the ^{27}Al spectra from the un-reacted material or from reaction products. This is believed to be due to the concentration being below the limit of detection for the spectrometer or the concealment of any new peaks by the existing ASG peaks.

Chapter 8

Theoretical Modelling of Filler Enhanced Glass Ionomer Cements

Aim

The aim of this chapter is to predict the optimum volume of filler needed to achieve the best possible packing density. This will be achieved using basic theoretical modelling using idealised conditions and computer simulated random conditions.

8.1 Introduction

The optimisation of Glass polyalkenoate cements (conventionally called Glass Ionomer Cements, GICs) has been investigated for over 25 years. The previous work can be divided into three separate work ethics; (i) alteration of the aluminosilicate glass structure (Prosser *et al*, 1986; Nagaraja & Kishore, 2005) (ii) investigation of alternative electrolytes or modification / enhancement of the original polyacrylic acid e.g. co-polymers or additives (Prosser *et al*, 1982; Smith, 1998; Xie *et al*, 2004) (iii) or the inclusion of filler materials (McLean, 1988; Nagaraja & Kishore, 2005; Prentice *et al*, 2005).
No attempts have previously been made to theoretically optimise filler particle size or shape with the intention of enhancing existing GICs. This is likely due to the relative low experimental costs involved with small batch experiments providing 'real' physical data or, the difficulty to accurately model the composite structure without heavy idealisation and computational strength.

Work in this chapter consists of three parts, firstly idealised packing conditions and particle sizes will be used to calculate ideal filler size and incorporation percentage. Secondly, the best filler particles shape to optimise the surface area to volume ratio. Thirdly, modelling random packing of spheres, plates, cubes and triangular shaped particles to optimise the filler content and shape so as interstitial voids will be reduced within the final packed cement.

Nomenclature

The terms solvent and solute are used throughout metallurgy and ceramic text. The term solvent refers to the atoms / particles of the lattice (e.g. all spheres in an empty body centred cubic lattice are solvent molecules) where the solute is smaller atoms or particles that fit in the interstitial gaps of the solvent structure.

8.2 Method

The method for calculating the unit cell dimensions, unit cell volume, particle (sphere) volume, void space, packing factor and interstitial gap size(s) have previously been studied (Olmsted, 1947; King, 1971; Mackay, 1973; Sickafus & Mackay, 1974; Hale, 2008). A full understanding of this theory and useful equations can be found in Appendix 4.

A brief introduction to the theory of crystal lattice structures including their shapes, volumes, nomenclature and equations is given to provide the novice reader with enough information to follow calculations made throughout this chapter.

8.2.1 Unit Cell(s)

Crystalline materials such as metals and ceramics are made up of a repetitive structure called a crystal lattice. The smallest divisible unit that possesses the symmetry and properties of the entire crystal lattice when stacked together in three dimensions is called the unit cell.

The atoms in the unit cell may be at the corners, on the edges, on the faces, or wholly enclosed in the box, and each cell in the crystal is identical.

There are three general unit cells that can be used to describe most crystalline structures;

Body Centred Cubic (BCC)

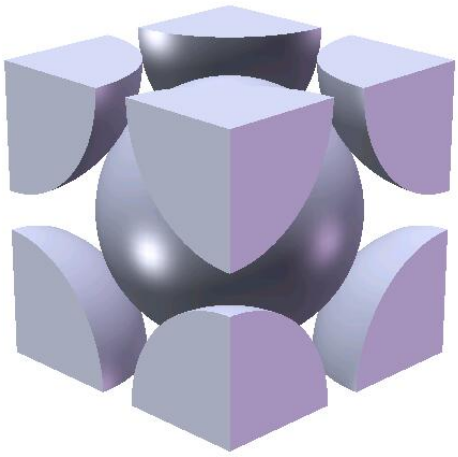

Figure 8.1: Body Centred Cubic Unit Cell (BCC)

The BCC unit cell is made up of two complete spheres; one complete sphere in the middle of the lattice and eight eighths in each corner of the cubic lattice.

Face Centred Cubic (FCC)

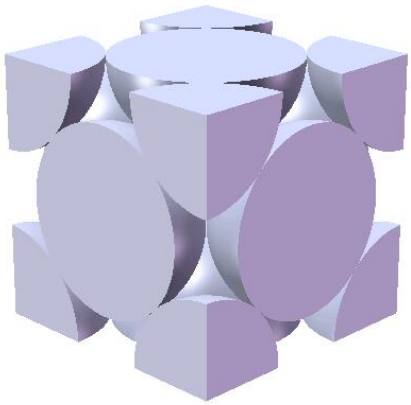

Figure 8.2: Face Centred Cubic Unit Cell (FCC)

The FCC unit cell is made from four complete spheres; six half spheres on each face of the unit cell and eight eighths in each corner of the cubic lattice.

Hexagonal Close Packed (HCP)

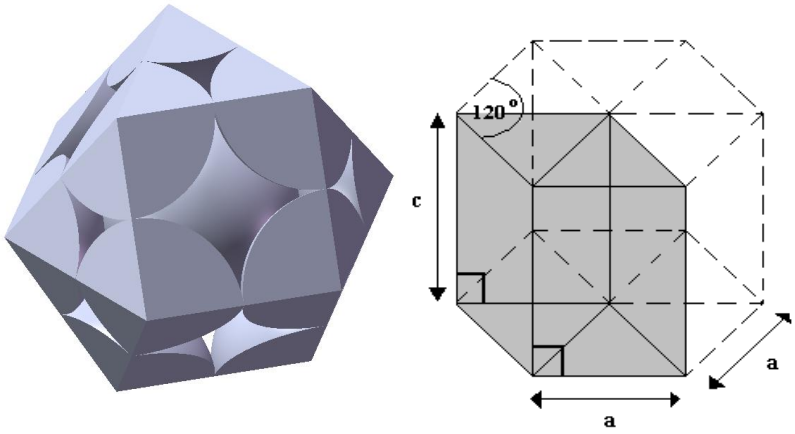

Figure 8.3: Hexagonal Close Packed Unit Cell (HPC)

The HCP unit cell is made from three complete spheres; one whole sphere and twelve sixths on each plane intersection.

Unit cells differ in appearance but the number of spheres and size of the cells differ only slightly providing optimal packing is applied. The highest possible packing factor for a BCC lattice is 0.68 and for a FCC & HCP lattice is 0.74 (William & Callister, 2000).

The unit cell dimensions and volume are calculated using the equations in Table 8.1.

	BCC **a = b = c**	**FCC** **a = b = c**	**HCP** **a = b ≠ c**	
Unit Cell Dimensions	$a = \frac{4r}{\sqrt{3}}$	$a = 2r\sqrt{2}$	$a = 2r$	$c = 4r\sqrt{\frac{2}{3}}$
Unit Cell Volume	$\left(\frac{4r}{\sqrt{3}}\right)^3 = \frac{64r^3}{\sqrt{27}}$	$\left(2r\sqrt{2}\right)^3 = 16r^3\sqrt{2}$	$\left(6\sqrt{3}r^2\right)\left(2\left(2r\sqrt{\frac{2}{3}}\right)\right)$	

Table 8.1: Unit Cell Dimension and Volume Equations for BCC, FCC and HCP Unit Cells – *r* is the Radius of the Solvent Particle

HCP has two lattice constants because a = b ≠ c unlike BCC and FCC where a = b = c.

The void volume* (unoccupied space) within the unit cells can be found using equation 11;

$$V_{void} = V_{Cell} - V_{Sphere} \qquad \text{Equation 11}$$

The packing fraction (PF) (packing density) is found using equation 12;

$$\text{PF} = \frac{v_{Sphere}}{v_{Cell}} \qquad \text{Equation 12}$$

8.2.2 Interstitial Gaps

Interstitial gaps are the spaces found between solvent particles. Solute particles are able to fill these spaces (e.g. Figure 8.4) without disrupting the existing lattice, increasing the packing of the unit cell.

The inclusion of spherical particles into existing unit cells has previously been investigated (King, 1971). There are two locations (orientations) in the unit cells that can accommodate different sized particles (octahedral & tetrahedral, *see* Figure 8.4 & Appendix 4). The radius of spherical particles able to fill existing interstitial spacing in BCC, FCC and HCP lattices' can be found using the relations in Table 8.2.

	BCC	**FCC**	**HCP**
Octahedral Spaces	$0.067a$ or $0.274a$	$0.1464a$	$0.207a$
Tetrahedral Spaces	$0.126a$	$0.0794a$	$0.1124a$

Table 8.2: Relationship between Unit Cell Dimension and Maximum Solute Particle Size
(Note: BCC has two Octahedral Spacing's (*see* Appendix 4))

* The volume of a sphere is calculated - $V_{\text{Sphere}} = \frac{4}{3}\pi r^3 = \frac{1}{6}\pi d^3$

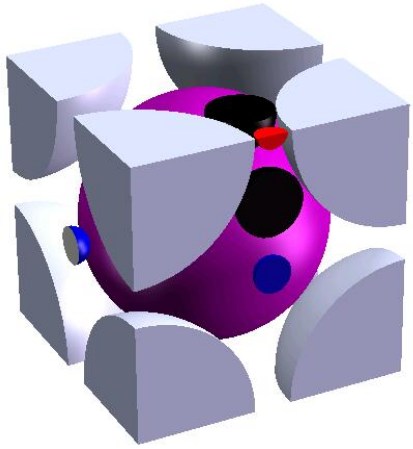

Figure 8.4: Illustration of the Interstitial Spaces in a BCC Lattice Able to Accommodate Spherical Particles with Dimensions Calculated from Table 8.2 (Black – Tetrahedral, Red & Blue – Octahedral)

Filler particles with square and triangular cross sections have also been investigated. Equations for calculating the maximum size of uniform geometric shapes in regular BCC, FCC and HCP lattices are presented in Table 8.3.

The locations and orientations of some square and triangular particles fitted into interstitial spacing's are shown in Figures 76 – 79.

Lattice Structure	Filler Shape	Dimensions		
		Height	Width / Hypotenuse	Depth
BCC	Square Plate	$\left(\sqrt{\frac{32}{3}}r\right)-2r$		$\frac{2r}{\sqrt{3}}-r$
	Triangular Plate	$\frac{4r}{\sqrt{3}}-2r$	$\left(\sqrt{\frac{32}{3}}r\right)-2r$	$\sqrt{2}\frac{2r}{\sqrt{3}}-r$
	Triangular Bar	$\left(\sqrt{\frac{32}{3}}r\right)-2r$	$\frac{2\left[\sqrt{2}\frac{2r}{\sqrt{3}}-r\right]}{\sqrt{3}}$	$\sqrt{2}\frac{2r}{\sqrt{3}}-r$
FCC	Cube	$2r\left(\sqrt{2}-1\right)$		
	Triangular Bar	$2r\left(\sqrt{2}-1\right)$	$2\left[r\sqrt{2}-\sqrt{r^2-r\left(\sqrt{2}-1\right)^2}\right]$	$2r\left(\sqrt{2}-1\right)$
		$2r\left(\sqrt{2}-1\right)$	$\sqrt{\left(6-4\sqrt{2}\right)r^2}$	$r\left(\sqrt{2}-1\right)$
	Square Bar	$2r-r\sqrt{3}$	$\frac{\sqrt{3}}{2}\left(2r-r\sqrt{3}\right)$	$\sqrt{2}\frac{2r}{\sqrt{3}}-r$
HCP	Square Bar	$2r-r\sqrt{3}$	$\frac{\sqrt{3}}{2}\left(2r-r\sqrt{3}\right)$	$\sqrt{2}\frac{2r}{\sqrt{3}}-r$
		$2r\left(\sqrt{2}-1\right)$		$r\left(\sqrt{2}-1\right)$
	Triangular Bar	$4r-2r\sqrt{3}$		$\sqrt{2}\frac{2r}{\sqrt{3}}-r$
		$2r\left(\sqrt{2}-1\right)$	$2\left[r\sqrt{2}-\sqrt{r^2-r\left(\sqrt{2}-1\right)^2}\right]$	$r\left(\sqrt{2}-1\right)$

Table 8.3: Maximum Filler Size of Irregular Shaped Filler Particles able to be Accommodated into Interstitial Spacing's in BCC, FCC and HCP lattices (*r* – Radius of Solvent Particle)

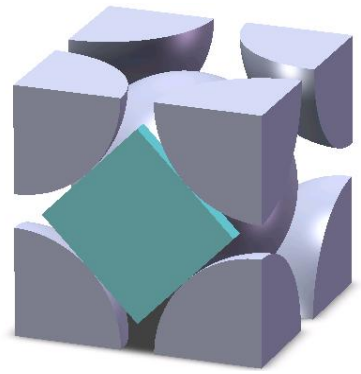

Figure 8.5: Square Plate Particle Fitted Into an Interstitial Space in a BCC Lattice

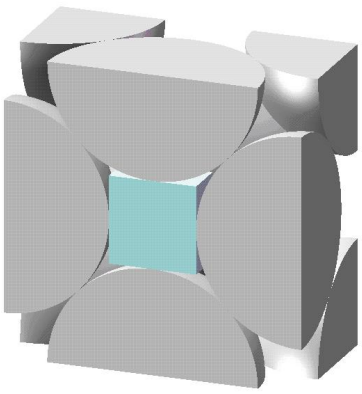

Figure 8.6: Cubic Particle Fitted into an Interstitial Space in a FCC Lattice

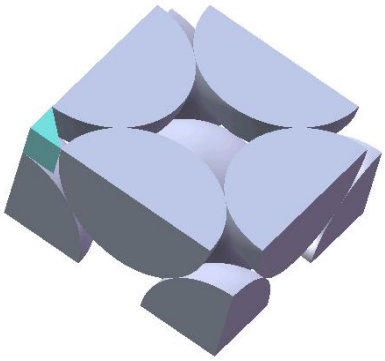

Figure 8.7: Triangular Rod Particle Fitted into an Interstitial Space of a FCC Lattice

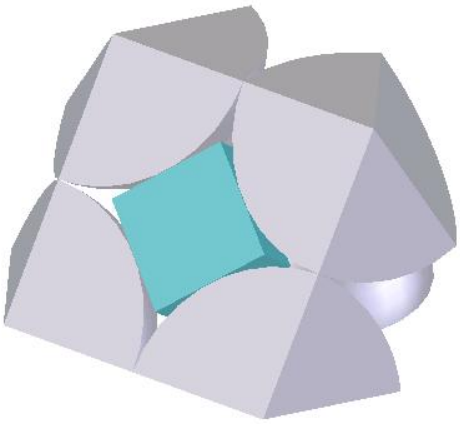

Figure 8.8: Cubic Particle Fitted into an Interstitial Space of a HCP Lattice

8.2.3 Computer Simulated Random Packing

The way in which GIC's and TiGICs are prepared (*see* Chapter 3) means that ideal packing is highly unlikely to occur, therefore computer simulated random packing will be employed to gain a better understanding of how a 'real cement' is more likely to form. This allows for the modelling of complete poly-dispersed cement systems rather than heavily idealised mono-dispersed systems.

MacroPac was chosen to perform random packing simulations as it offers a range of random algorithms and the ability to design advanced polyhedral shaped particles should further work be required.

The three algorithms which were investigated for suitability are,

(i) Dynamic Drop Pack
(ii) Monte-Carlo Simulation
(iii) Overlap Minimization Pack

Full explanations of these algorithms can be found in text and academic papers such as Nolan & Kavanagh (1992), Leach (2001), Chang (2010). A brief outline of each can also be found in Appendix 4.

Periodic boundary conditions were used throughout all simulations to avoid wall effects.

8.3 Results

The theory included in Section 8.3 is to illustrate how the particles in idealised models will pack together and the placement of interstitial filler particles. It is however not necessary to consider a single unit cell in the development of the GIC model, rather the maximum packing fraction obtained by each lattice.

8.3.1 Idealised Modelling (Packing)

An arbitrary amount of ASG (1g) will be used to model the packing. The packing fraction of a mono-dispersed lattice will therefore remain constant for a known volume of ASG.

The filler particles are two orders of magnitude smaller than the ASG particles so it has been assumed that they are able to fill the interstitial spaces of the ASG lattice almost entirely leaving only the void volume from packing of the filler itself.

The weight of TiO_2 filler able to be incorporated into an ideal BCC, FCC and HCP lattice without disrupting the solvent packing is considered with and without polyelectrolyte solution. The volume of polyelectrolyte solution that would typically be used with 1g of ASG is 0.23 cm^3 (ml) maintaining a 4:1 (weight) ratio (*see* Appendix 4 for calculation).

8.3.1.1 Spherical Filling Particles

A density of 2.54 gcm^{-3} is used in these calculations (Lower *et* al, 2004) which are based on a sodium aluminosilicate glass; this is because the density of the control ASG is not known. The unit and void volumes have been calculated for 1g of ASG and are shown in Table 8.4. The density of Rutile used in calculation is 4.23 gcm^{-3} (MTI Corporation, product NP-TiO2-R-20).

TiO_2 Filler Incorporation - No Polyelectrolyte				
Lattice	Unit Volume (cm^3)	Void Volume (cm^3)	TiO_2 Weight (g)	Final Void Vol (cm^3)
BCC	5.79	1.85	5.33	1.26
FCC / HCP	5.32	1.38	4.33	1.02

Table 8.4: Weight of TiO_2 Filler Incorporation and Resultant Space after Packing of an ASG Lattice with No Polyelectrolyte

It is possible to incorporate 5.33g (32% v/v) or 4.33g (26% v/v) of TiO_2 into the interstitial gaps of a uniform BCC, FCC/HCP ASG lattices composed of 1g of glass. The addition of this amount of TiO_2 will increase the packing density in the BCC lattice from 0.68 to 0.78 and FCC/HCP lattice from 0.74 to 0.81, a significant increase.

It should be noted that this concentration of TiO_2 would severely hinder or stop a GIC from forming as the powder to liquid ratio (ASG : Polyelectrolyte) would effectively become skewed towards lower values (*see* Chapter 4).

8.3.1.2 Non-Spherical Filler Particle Incorporation

TiO_2 used in experimental cements was non-uniform in shape (*see* Chapter 3) therefore geometries other than spherical need to be considered. The relationship between maximum solvent and solute particle size has been calculated in Table 8.2 & Table 8.3.

It was assumed that small particles will tend to congregate together and form agglomerates that will resemble a single large particle that possesses similar properties to that of a single large solid particle (similar to simply adding a large solid particle although it is constructed from smaller particles with the same geometries). Therefore, to obtain a fair comparison between which shaped filler particles occupy the greatest volume in a BCC, FCC and HCP lattice the maximum calculated particle size of each is used.

A single unit cell composed from 40 μm spherical ASG solvent particles is considered for packing by spherical, square and triangular particles.

A 40 µm BCC, FCC and HCP unit cell has a void volume of $3.15x10^4$, $4.70x10^4$ and $7.05x10^4$ μm^3 respectively. The size, location and therefore quantity difference between filler particles means the total filler volume must be deducted from the void volume. The number of filler particles able to fit into the different unit cells is presented in Table 8.5.

Lattice	Particle			
	Sphere		Square / Cubic	Triangular
	Octahedral	Tetrahedral		
BCC	(*a*) 12 (*b*) 6	24	(*Plate*) 6 (*Rod*) 12	12
FCC	16	8	(*Intern*) 1 (*Extern*) 12	(*Intern*) 1 (*Extern) 12*
HCP	16	8	(*Small*) 8 (*Large*) 6	(*Small*) 8 (*Large*) 6

Table 8.5: Number of Filler Particles Able to be Incorporated into a Single BCC, FCC, HCP Lattice

The assumption that smaller filler particles will agglomerate to form a larger adaptation of themselves means that all filler sizes (different location) can be included in a single unit cell. The final void volume from a 40 µm ASG unit cell ideally packed in a BCC, FCC or HCP lattice configuration and packed with the maximum volume of filler able to fit interstitial voids has been presented in Table 8.6.

Lattice	Sphere	Square / Cubic	Triangular
BCC	28.89	13.85	17.70
FCC	24.95	15.91	19.11
HCP	24.89	20.01	20.51

Table 8.6: Percentage Void Volume after Spherical, Square / Cubic and Triangular Filler Addition

Lattice	Sphere	Square / Cubic	Triangular
BCC	0.711	0.861	0.823
FCC	0.750	0.840	0.810
HCP	0.750	0.800	0.790

Table 8.7: Packing Fraction Obtained after Filling BCC, FCC and HCP Glass lattices with Spherical, Square / Cubic and Triangular

The BCC lattice has a packing fraction of 0.68 before packing with spherical, square / cubic and triangular fillers.

The introduction of spherical filler particles has increased the packing fraction to 0.71 (Table 8.7). Similarly the addition of square / cubic and triangular filler particles has increase the packing fraction to 0.86 and 0.82 respectively, a considerable improvement.

It had previously been found (*see* section 8.3.1.1) that introduction of smaller sized spherical particles (0.1 μm) could increase the packing fraction to 0.78, an improvement on the results found here (0.71). This is because the filler particles used here are the same order of magnitude as the solvent particle and are therefore unable to occupy all interstitial space as was assumed with filler particles two orders of magnitude smaller than the solvent particles. In an ideal model it would therefore make sense to use filler particles many orders of magnitude smaller than the solvent particle to achieve the maximum compressive strength. If ideal conditions are not achieved ('real' conditions) then larger filler particles are believed to increase the compressive strength to a greater extent than smaller particles because they are unable to move past other solvent and solute particles as readily as small particles.

The FCC lattice has increased packing fraction from 0.74 (unfilled) to 0.75, 0.84 and 0.81 when using spherical, square / cubic and triangular particles respectively.

Filler incorporation into a HCP lattice has the smallest effect on the reduction in void volume. An unfilled lattice has 25.96% void space which when filled with square / cubic filler particle geometries has an improvement of 5.95%. The packing fractions after filling with spherical, square / cubic and triangular particles are 0.75, 0.78 and 0.80 respectively.

In all instances, the use of square / cubic filler particles has increased the packing fraction to the greatest extent assuming ideal packing conditions are applied. The nature of poly-dispersed particles is not ideal therefore random packing results would give a greater indication of the size and geometry needed to increase the packing fraction of a 'real' GIC.

Filler material with a uniform geometry and sub-micron size is however currently unavailable so these calculations are purely theoretical and cannot be tested.

8.3.1.3 Polyelectrolyte Addition

The packing fractions of uniform geometry filler particles entering ideally packed ASG lattices has been calculated in sections 8.3.1.1 & 8.3.1.2. These values are now applied to 1g of ideally packed ASG in a BCC, FCC or HCP arrangement. The powder to liquid ratio has been taken as 4:1 mimicking the control cement. Therefore, 0.25g of polyelectrolyte solution would be used with 1g of ASG which has a fluid volume of 0.23 cm^3 (ml).

The polyelectrolyte solution contains no void space so the volume can be deducted from the final void volume of the optimised cements and the final packing fraction can be calculated.

The introduction of polyelectrolyte solution has a standard effect of increasing the packing fraction of spherically filled BCC, FCC and HCP by 0.04. An increase of 0.05 is seen in other geometric filled cements because there is a lower volume to be filled by polyelectrolyte (Table 8.9).

ASG Lattice	Filler Particle Shape	Packing Fraction	
		Dry Cement (No Polyelectrolyte)	Full Cement (Polyelectrolyte)
BCC	Sphere	0.71	0.75
	Square / Cubic	0.86	0.91
	Triangular	0.82	0.87
FCC	Sphere	0.75	0.79
	Square / Cubic	0.84	0.89
	Triangular	0.81	0.86
HCP	Sphere	0.75	0.79
	Square / Cubic	0.80	0.85
	Triangular	0.79	0.84

Table 8.8: Packing Fraction for BCC, FCC, HCP Lattice Filler Combinations With and Without Polyelectrolyte Solution

Additional polyelectrolyte may be added in order to fill all the void space in the theoretical cement cells. Table 8.9 shows the total weight of polyelectrolyte that would be needed to fill all void space in the glass filler combinations.

ASG Lattice	Filler Particle Shape	Weight (g)
BCC	Sphere	1.46
	Square / Cubic	0.58
	Triangular	0.77
FCC	Sphere	1.19
	Square / Cubic	0.68
	Triangular	0.84
HCP	Sphere	1.19
	Square / Cubic	0.90
	Triangular	0.95

Table 8.9: Weight of Polyelectrolyte Solution Needed to Fill All Interstitial Void Space in Solvent, Solute Combinations from Table 8.8

If the voids were filled by introduction of additional polyelectrolyte solution the final cement would have inferior properties compared with the control cement because of increased powder : liquid ratio.

8.3.2 Simulated Random Packing (MacroPac)

The process of GIC production involves large mechanical forces that may best be represented by a combination of algorithms provided by MacroPac.

The dry powder when in storage can be represented by a Monte Carlo Shake simulation (MCSP) with periodic boundary conditions. The maximum packing fraction can be found using an overlap minimisation pack (OMP) with periodic boundary conditions which is believed to best represent the mixed cement.

Preliminary analytical tests (*see* Appendix 4) have shown that a difference in packing fraction of up to 16% is achieved when comparing packing and boundary conditions. Differences between hard and periodic boundary conditions alone are also pronounced with a difference between 6% – 11% being observed.

Preliminary simulations (*see* Appendix 4) have shown that for a powder with a spherical monodispersion the packing density will not reach greater than 63% (PF, 0.63) and will, on average, be around 57% (PF, 0.57).

8.3.2.1 Spherical Particle Optimisation

This subsection is an extension of previous, ideally packed models, in the sense that a monodispersion of solvent particles (ASG glass) will be packed with spherical filler particles of changing dimension.

The packing fraction of uniform spherical particles is approximately 63% therefore the packing fraction will be similar to that of an unfilled BCC lattice. Any improvement will be apparent by an increase in packing fraction above 0.63.

Solute particle size(s) ranging from 90% – 10% diameter of the solvent particle (100 μm) will be used to find the maximum packing fraction for bimodal packing combinations.

The size and number of filler particles were adjusted so that the volume was maintained constant (equal to the void volume of an ideally packed BCC lattice); this ensured that only filler particle size effects were being calculated. The number of solvent particles remained constant throughout experimentation with 10 particles being used.

The size of the filler particle used can be seen to, on average, affect the packing fraction by 0.023 after each successive decline in filler size until a limit at 20% solvent particle size is reached as can be seen in Table 8.10. The addition of filler particles, 20% in size of the lattice forming particles produces a packing fraction similar to an FCC / HCP crystalline lattice.

Filler Particle Size (%)	Packing Fraction
90	0.614
80	0.621
70	0.625
60	0.640
50	0.653
40	0.680
30	0.691
20	0.747
10	0.684

Table 8.10: Packing Fraction Results from a Series of Spherical Filler Particles Ranging from 90% - 10% of the Solvent Particle Radius

The simulations results for the 20% filler addition can be seen in Figure 8.9 and demonstrate that although heavily populated with solvent and solute particles the packing fraction has not exceeded that of an FCC / HCP lattice (Figure 8.2 & Figure 8.3 respectively).

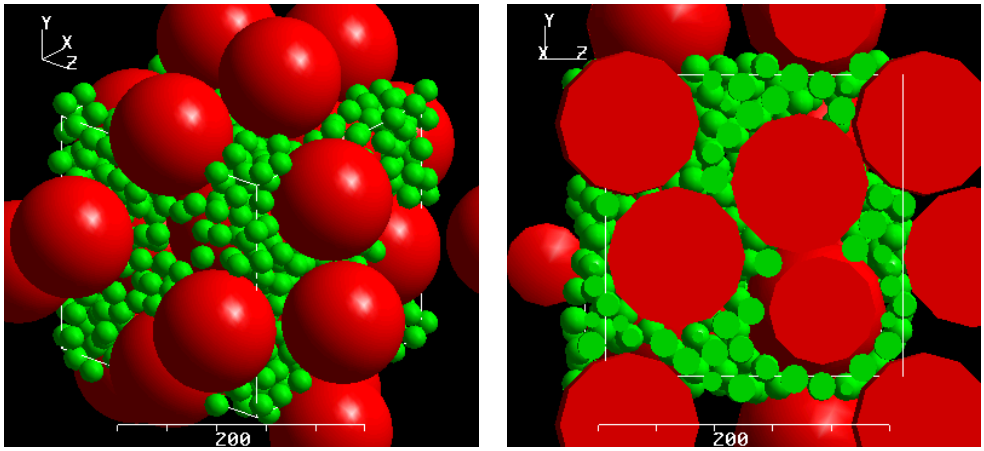

Figure 8.9: Simulation of the Packing Achieved in a System Where the Filler Particles are 20% the Size of the ASG Particles but the Volume of Filler Particles Matches that of an Un-Filled System.

ASG has an approximate packing fraction of 0.53 (Rocktron - Min Tron 7™, 2010) so solvent packing fractions smaller than those generated currently should be considered. Macropac is able to generate isotropic solvent lattices for packing with filler particles of a given packing fraction.

The above experiment was repeated for solvent lattices with packing fractions ranging between 0.30-0.74 which was subsequently populated with filler particles ranging in diameter between 10% - 30%.

The maximum void volume for each solvent lattice was calculated from the respective packing fraction. The volume of filler was adjusted to maintain a value approximately equal to the void volume. The volume of filler was decided in this way rather than an arbitrary value that may have been greater than the available space in well packed lattices or less than loose lattices.

Table 8.11 shows the results from the further bimodal simulations. All the results indicate that filler particle addition to a proposed ASG lattice with a packing fraction above 0.70 will cause a decrease in the packing density of the overall system.

The optimum particle size for filler incorporation remains as 20% the size of the solvent particle with the greatest improvements in packing fraction seen in this system.

The trend in results from filler particles 10% of the solvent size would suggest that small filler particles are able to affect the packing fraction to a greater extent by packing into solvent lattices with high packing fractions.

The results from filler particles 30% the size of the solvent do not show any significant trends over the range of packing fractions tested. The 30% particles do appear to be able to compensate for a reduction in solvent packing fraction better than the 10% filler particle inclusion.

Filler Particle Size (%)	Solvent Packing Fraction	System Packing Fraction
10	0.30	0.570
	0.40	0.574
	0.50	0.583
	0.63	0.684
	0.70	0.658
	0.74	0.671
20	0.30	0.707
	0.40	0.718
	0.50	0.737
	0.63	0.747
	0.70	0.726
	0.74	0.729
30	0.30	0.661
	0.40	0.670
	0.50	0.694
	0.63	0.691
	0.70	0.699
	0.74	0.663

Table 8.11: Results from a series of Simulations to Find Out What Affect the Filler Volume Has on the System Packing Fraction

An example (Figure 8.10) of the packing found in the 20% solvent particles size systems at the packing fraction extremes. The addition of filler particles to the ASG lattice with the lower (0.3) packing fraction can be seen to be more densely packed than the system with a high (0.74) ASG packing fraction. The filler addition in the ASG lattice with a packing fraction of 0.74 has disrupted the original packing causing a decrease in packing fraction that can be seen when comparing the images in Figure 8.10.

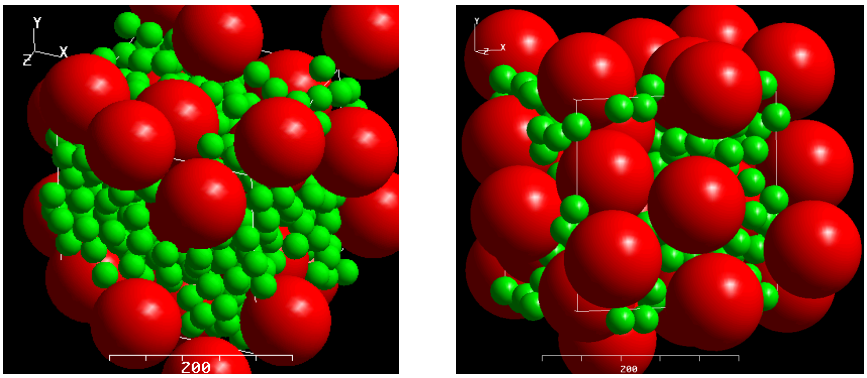

Figure 8.10: Bimodal Dispersion of a Packed Solvent Lattice with 20% Filler Addition – Solvent PF = 0.30 (left) and 0.74 (right)

The Andreasen's and Dinger-Funk continuous theory for particle packing is believed to achieve maximum packing of spherical particles (D. Dinger and J. Funk, 1993). The system proposed in Table 8.12 is similar to a Dinger-Funk system but is made up of tightly controlled discreet particle sizes instead of using a distribution range for each particle size. The stepwise addition of filler particles 80% smaller than the next largest particle (including filler particles) would be an ideal system to try given the results found thus far however, the time it would take to run a simulation with 44.9 million particles (starting with 10 of the largest particles) would not be economical.

Particle Size (µm)	Filler size (µm)	Number of Filler Particles
100.00	20.00	1.00×10^{1}
20.00	4.00	4.58×10^{2}
4.00	0.80	2.10×10^{4}
0.80	0.16	9.59×10^{5}
0.16	0.03	4.39×10^{7}

Table 8.12: A Trial System Incorporating Optimum Data from Previous Simulations

8.3.2.2 Shaped Particle Optimisation

The idealised theoretical modelling has covered shaped particles and has shown that there is some scope for their use as an effective filler particle. MacroPac will be used to simulate random packing of cements that have been optimised using square / cubic and triangular shaped filler particles.

The shaped particles were assumed to pack perfectly in the ideal model but this is unlikely to happen in reality. Simulations were run using filler particles alone with dimensions suitable to fit into the interstitial spacing's in a 100μm spherical lattice.

MacroPac constructs polyhedral shapes by joining several spherical particles in close proximity to one another to form the desired shape. The bulk particle, consisting of several spherical particles is then rendered with straight edges for visualisation purposes. This technique for constructing polyhedral shapes means that there are many more interaction taking place in simulation increasing the time and computational power needed to complete given tasks. It is for this reason that OMP simulations will not be performed on square / cubic and triangular particles, instead Dynamic drop simulations and MC Shake simulations were used to model how shaped filler particles would behave when packed together.

The results from these simulations can be seen in Figure 8.11, Figure 8.12 and Figure 8.13 and are summarised in Table 8.13.

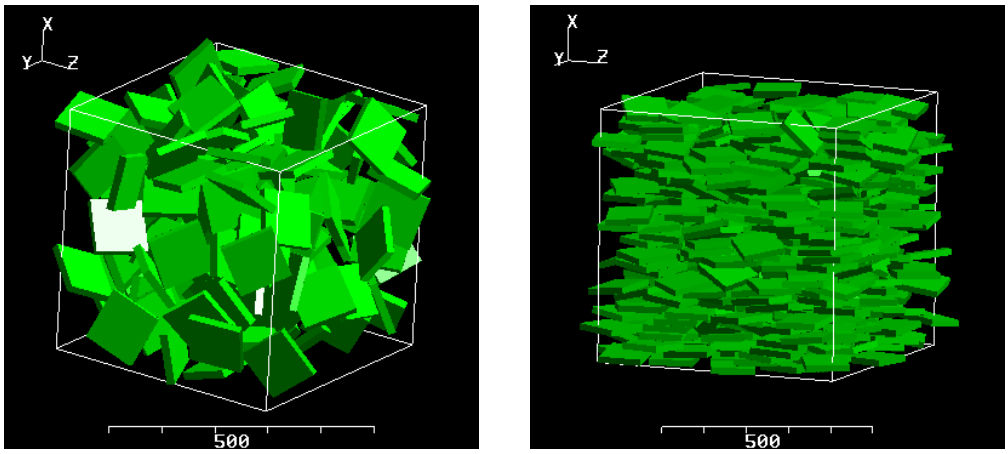

Figure 8.11: Dynamic Drop (left) and MC Shake (right) Simulations of Plate Shapped Filler Particles Packing Together

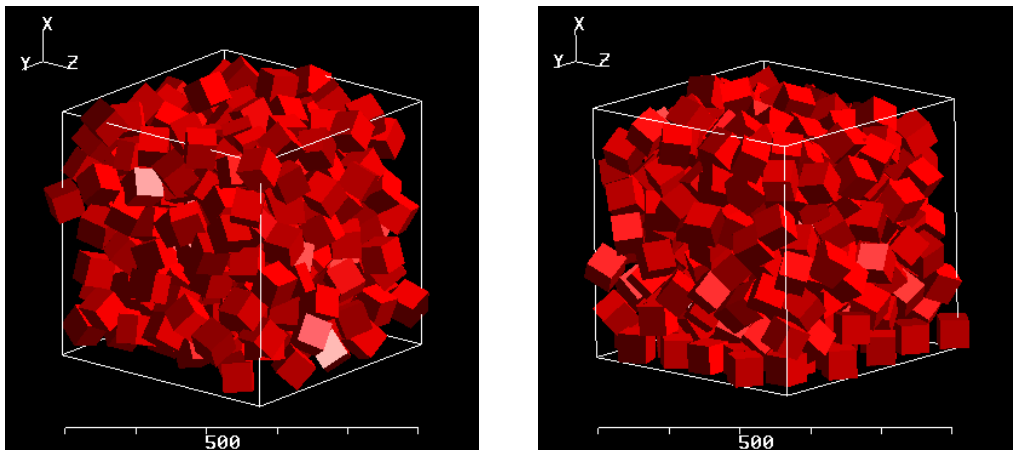

Figure 8.12: Dynamic Drop (left) and MC Shake (right) Simulations of Cube Shapped Filler Particles Packing Together

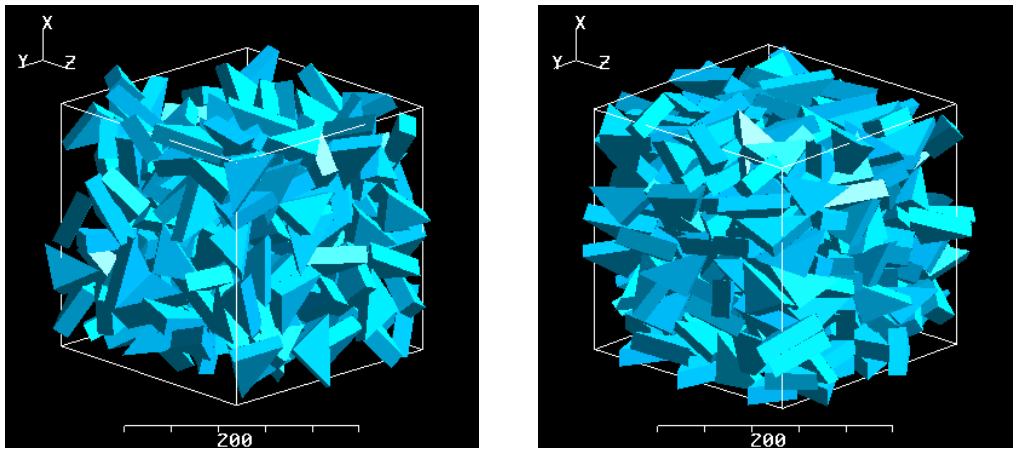

Figure 8.13: Dynamic Drop (left) and MC Shake (right) Simulations of Triangular Shapped Filler Particles Packing Together

The results in Table 8.13 show that cubic particles will pack together best (PF – 0.4) when subject to gravity alone and that plates will have the poorest packing fraction of only 0.2. Spherical and triangular particles have a similar packing density under gravity packing.

The MCS simulations are closer to that which would be expected from cement after it had been mixed and indicate that spherical particles come together (PF – 0.554) with the least resultant void volume. Cubic and triangular particles have a packing fraction not dissimilar to spheres (0.510 - 0.528) and plat shaped particles have the lowest packing fraction (PF – 0.410).

Interestingly spherical particles would be expected to pack together with smaller void volumes than the geometrical shaped filler particles that were originally expected to, tessellate and display optimum packing.

Filler only Packing		
Filler particle	Packing Fraction	
	Dynamic Drop	MC Shake
Plate	0.203	0.410
Cube	0.402	0.510
Triangle	0.366	0.528
Sphere	0.368	0.554

Table 8.13: Packing Fraction Results for Shaped Filler Particle Packing

In order to test the idea that shaped particles will produce better packing fractions than spherical particles a MCS simulation will be performed using the, now standard, 100µm ASG representative lattice and shaped particles suitable to fit into solvent solutions with particle sizes ranging from 20µm - 100µm.

The way in which the packing works in an MCS differs from that of an OMP. Particles are added successively in a MCS rather than all together and then rearranged as in an OMP. This means that MacroPac is given a number of particles and packs a cell until it is unable to fit anymore in, at this point the simulation is terminated. In practice, this means that although the particle selection is random the cell will become quickly occupied with ASG particles and then slowly loaded with filler an example of which can be seen in Figure 8.14.

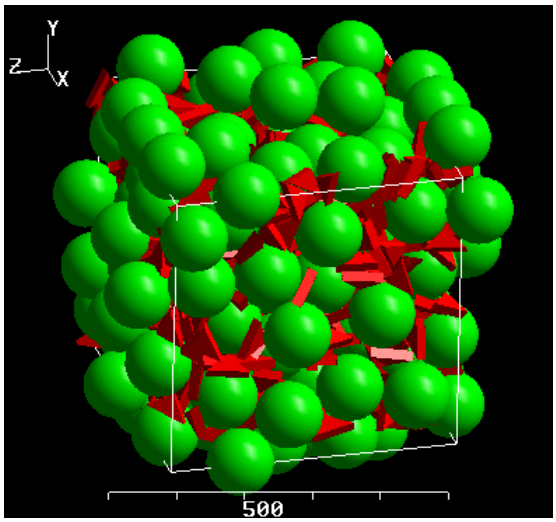

Figure 8.14: 100µm Spherical Lattice with Triangular Shaped Filler Particle Incorporation

The dimensions of the shaped filler particles has been calculated using the formula's found in Table 8.3 using the radii of solvent particles that can be found in the column titled 'solvent particle size' in Table 8.14.

Table 8.14 shows that triangular shaped filler particles produce slightly greater packing fractions than spherical particles (Table 8.11) and a noticeable increase when compared with plate and cubic particles contrary to the packing fractions obtained for a mono-dispersion of filler alone. The decreasing filler particle size increases packing fraction by 9.9% - 12.6% (Cube → Plate → Triangle) over a range of sizes suitable for glass lattices ranging from 20-100 µm.

Solvent Particle Size (μm)	Packing fraction		
	Plate	Cube	Triangular
100	0.601	0.583	0.647
90	0.610	0.594	0.664
80	0.613	0.626	0.649
70	0.622	0.638	0.709
60	0.644	0.641	0.697
50	0.646	0.653	0.728
40	0.698	0.669	0.763
30	0.702	0.671	0.767
20	0.708	0.682	0.773

Table 8.14: Packing Fraction of Filler Particles of Differing Size in a 100 μm Solvent Lattice - Filler Particle Size Based on Solvent Size

The minimum and maximum difference in packing fraction comparing shaped filler particles with the same solvent radius is 6.4% and 9.1% respectively. The effect to packing fraction seen when adding non-spherical filler particles to a disordered lattice (Figure 8.14) would suggest that the shape of the particle is equally important as the size.

8.3.3 Control Cement System

The particle size analysis of Diamond Carve (*see* Chapter 3) has shown that the mean particle size in the ASG used to formulate the cement lies in the range 38 - 16μm. The fractional composition of the ASG can be seen in Table 8.15 and can be used to simulate the packing undergone in a GIC.

Particle Size Distribution of ASG used in Diamond Carve GIC		
Particle Size (μm)		Fraction
Size Range	Median	
250-125	187.50	0.0067
125-63	94.00	0.0494
63-38	50.25	0.1397
38-16	26.75	0.2476
16-8	12.00	0.2089
8-4	6.00	0.1554
4-2	3.00	0.1059
2-1	1.50	0.0865

Table 8.15: Particle Size Analysis of ASG used to Formulate Diamond Carve

Particles of ASG have no uniform geometric shape so will be represented as spheres. The OMP algorithm will therefore give the best representation of the packing found in a mixed sample of the control material (Diamond Carve).

Hard and periodic boundary conditions (Figure 8.15 and Figure 8.18) were used so an understanding of the likely particle arrangement at the cement – dentin interface and the bulk cement can be made.

8.3.3.1 Dentin – Cement Interface

Hard boundary conditions have been used to represent the packing that will be achieved at the dentin – cement interface which is known (Wilson & Nicholson, 1993; Nicholson, 1998) to be the weakest point in a GIC restoration.

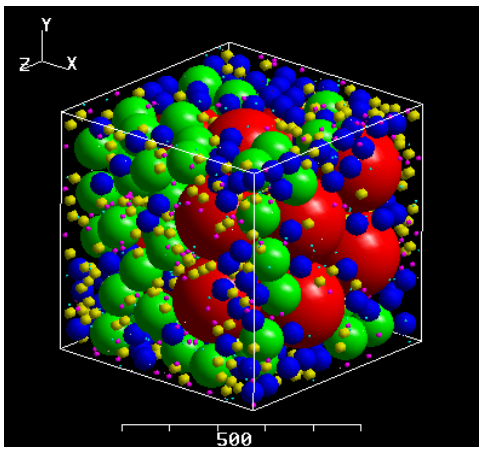

Figure 8.15: A Simulation of the Packing Achieved in ASG when mixed with a Polyelectrolyte (Hard Boundry Conditions)

Figure 8.16 shows 10% of the simulation results at the boundary interface. The packing density in the 10% slice is 0.446 meaning that there is a lot of free space (56% free space) at the cement interface. This free space is presumably filled with polyelectrolyte solution that binds the cement structure to the enamel or dentin substrate.

It is assumed that a contact area of 100% polyelectrolyte (gap between cement and tooth filled with polyelectrolyte) would produce the best bond between cement and substrate. This assumption is made because no interaction between ASG and dentin is known to take place; greater packing at the boundary interface would reduce the bond between restoration and tooth because of reduced exposure to polyelectrolyte solution.

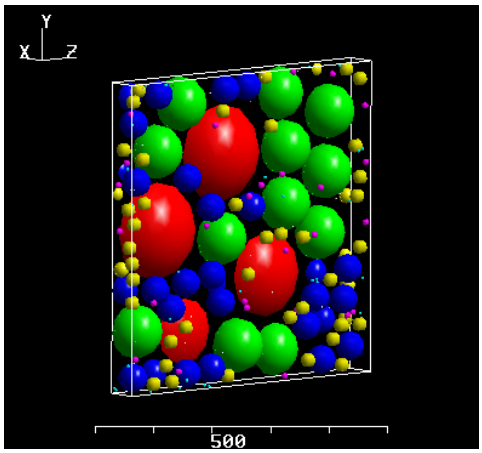

Figure 8.16: Sliced View of an OMP Simulation within 10% of the Simulated Dentin – Cement Boundary

The packing fraction rapidly increases as you move towards the bulk of the cement material (Figure 8.17) however the maximum PF of 0.582 for the entire cell does not accurately represent the bulk of the cement as this encompasses the edge (boundary interface) values.

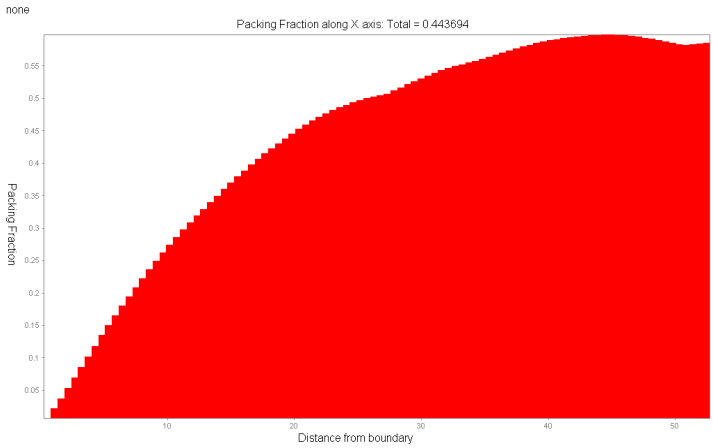

Figure 8.17: Packing Density of an OMP Simulation of ASG used in Diamond Carve

8.3.3.2 Bulk Cement Packing

The simulation of the bulk cement (Figure 8.16) resulted in a total packing fraction of 0.704 which is close to the theoretical maximum packing fraction of a mono-dispersed FCC/HCP lattice (0.74).

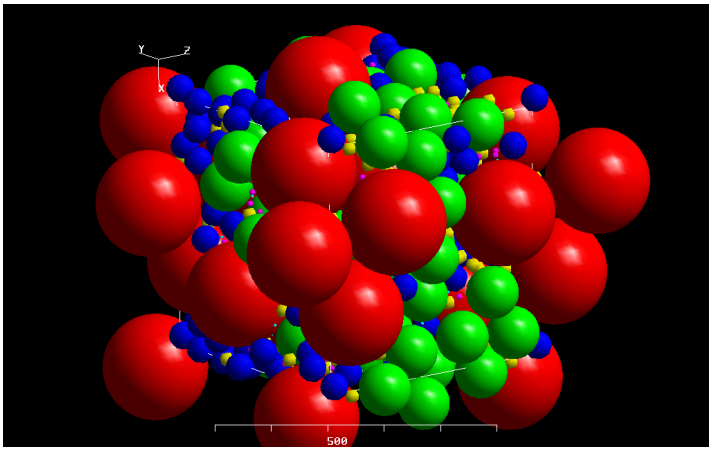

Figure 8.18: A Simulation of the Packing Achieved in ASG when mixed with a Polyelectrolyte (Periodic Boundary Conditions)

Addition of polyelectrolyte solution in a ration of 4:1 powder to liquid further increases the packing fraction from 0.704 to a possible 0.745.

The packing fraction of the bulk material is excellent considering that the particle size distribution has been formulated with handling properties as the main focus. A possible improvement of 0.2 (PF) could foreseeable be achieved given ideal packing circumstances (*see* Section 8.3.1.3) however this will have an unknown effect on the handling properties of the control material and may make the cement 'unusable'.

8.3.4 Optimisation of the Diamond Carve System

Simulations have been performed based on the experimental control material with the addition of spherical, square / cubic and triangular filler particles with the intention of increasing the packing fraction above the 0.704 found. The simulations include incorporation values (2.5% & 7.5% w/w) that have had mechanical tests performed on them so a comparison between the modelled cement and real data can be compared.

8.3.4.1 Spherical Filler Particle Addition

In practice, the replacement of ASG with TiO_2 was performed on a w/w basis for 2.5% and 7.5% TiGICs. The same principal has been applied in the models generated to simulate these cements; in a 2.5% TiGIC the mass of each particle size has been subject to a deduction of 2.5% which when totalled over the entire mass of ASG has a resultant reduction of 2.5% w/w. The mass of ASG is replaced equally with 1µm TiO_2 so a reduction in total volume will be observed because of the greater density associated with TiO_2.

The simulation results can be seen in Figure 8.19 to Figure 8.21 and are summarised in Table 8.16. TiO_2 is coloured pink in the images of simulation results.

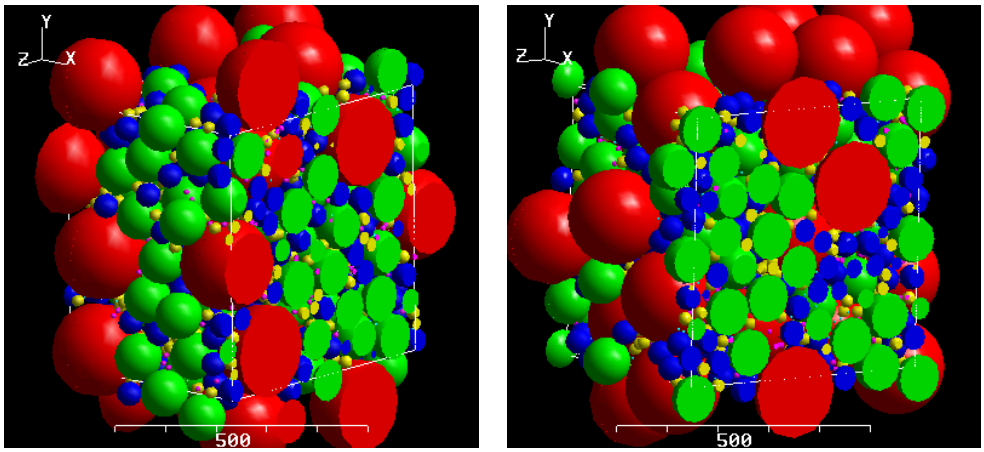

Figure 8.19: Left: 1%TiO_2 Incorporation into the DC System-Packing Fraction 0.707, Right: 2.5%TiO_2 Incorporation DC System-Packing Fraction 0.714

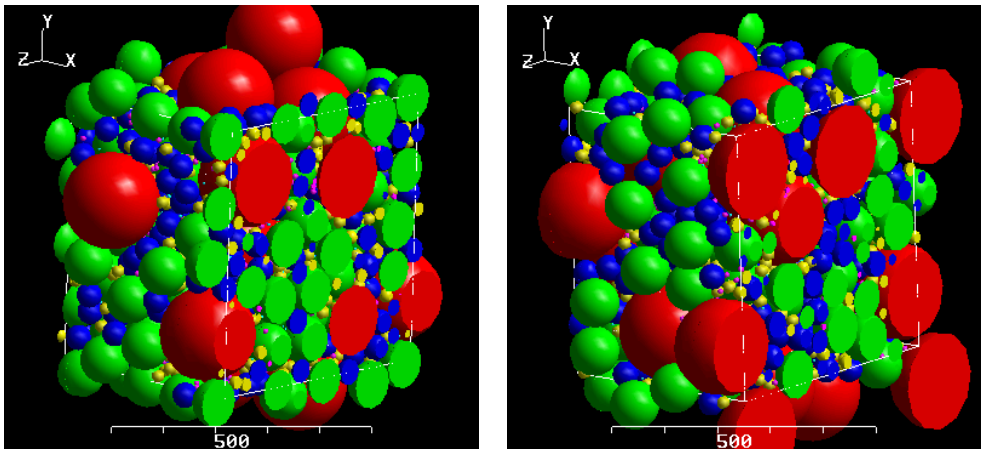

Figure 8.20: Left: 7.5%TiO_2 Incorporation into the DC System-Packing Fraction 0.711 Right: 12.5%TiO_2 Incorporation into the DC System-Packing Fraction 0.703

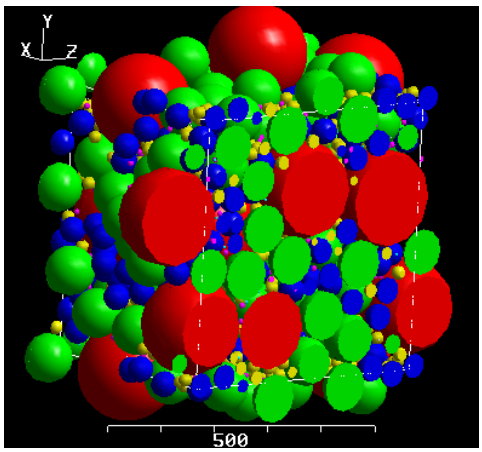

Figure 8.21: 15%TiO_2 Incorporation into the DC System-Packing Fraction 0.708

Sample	Packing Fraction
Diamond Carve	0.704
1.0% TiO_2 Incorporation	0.707
2.5% TiO_2 Incorporation	0.714
7.5% TiO_2 Incorporation	0.711
12.5% TiO_2 Incorporation	0.703
15.0% TiO_2 Incorporation	0.708

Table 8.16: Packing Fraction Values from Simulations Representing TiGICs Incorporating Between 1% - 15% w/w Filler Particles

The simulation data suggests that there will be a slight increase in the obtained packing fraction when 2.5 – 7.5% w/w filler incorporation is used. Incorporation volumes grater than 7.5% w/w produce similar results to the control material (0.704) which may possibly be caused by the disruption of the packing arrangement of the ASG.

The final packing fractions obtained for a 2.5% and 7.5% w/w TiGIC after mixing with polyelectrolyte solution with a powder to liquid ratio of 4:1 are 0.756 and 0.753 respectively.

The original hypothesis that packing density is directly related to compressive strength of the formed cement means that slightly better compressive strengths may be produced using an incorporation of 2.5% - 7.5% filler material.

8.3.4.2 Shaped Filler Particle Addition

The incorporation of shaped filler particles may increase the packing fraction beyond that achieved using spherical filler particles in a poly-disperse cement.

The inclusion of shaped filler particles has not been practically performed so unlike the control material models an average filler particle size is not available.

The analysis of a 2.5% and 7.5% w/w TiGIC incorporating shaped filler material has been performed using multiple sizes. The size of the shaped filler particles used in simulations has been calculated from median particle size values of the control cement found in Table 8.15 (8 in total). The removal of ASG and replacement with shaped TiO_2 has been calculated in the same manner as in section 8.3.4.1.

Figure 8.22 shows the simulation results from a 7.5% w/w incorporation of shaped filler particles based on an 187.5μm ASG diameter. The results from all simulations have been summarised in Table 8.17.

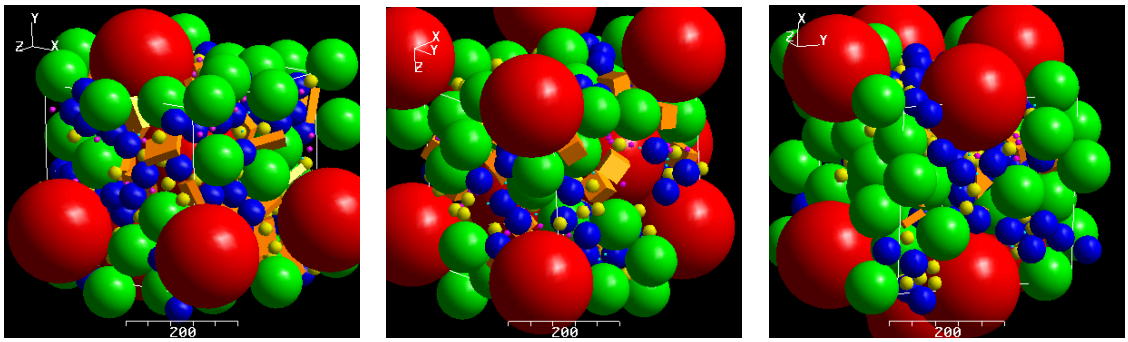

Figure 8.22: Simulation Results for 7.5% Incorporation of Plate (left), Cubic (centre) and Triangular (left) Shaped Filler Particles into Base Cement (oragne particles)

The simulations have identified that the addition of plate, cubic and triangular filler particles only increases the packing fraction to a greater value than the control cement 44%, 13% and 25% of the time respectively. Table 8.17 suggest that lower w/w incorporations of filler produce better packing fraction for plate shaped fillers whereas cubic fillers show no preference for higher or lower incorporation values and triangular fillers produce better packing fractions with greater filler incorporation. The standard deviations associated with each set of simulations lay within the range 0.025 – 0.007 so there can be no significant conclusions drawn when comparing filler particle size for each incorporation weight.

ASG Particle Size (µm)	2.5% Filler Incorporation			7.5% Filler Incorporation		
	Plate	Cube	Triangle	Plate	Cube	Triangle
187.50	0.698	0.672	0.685	0.689	0.69	0.711
94.00	0.701	0.69	0.679	0.707	0.698	0.703
50.25	0.701	0.699	0.705	0.686	0.626	0.700
26.75	0.700	0.683	0.681	0.695	0.683	0.714
12.00	0.716	0.693	0.688	0.704	0.703	0.658
6.00	0.711	0.696	0.674	0.685	0.715	0.697
3.00	0.706	0.697	0.684	0.711	0.694	0.694
1.50	0.717	0.688	0.684	0.700	0.706	0.704

Table 8.17: Packing Fraction Achieved After Addition of Shaped Filler Particles to a Representation of an Experimental Cement (ASG Size used to Calculate the Geometry of Shaped Particles)

8.4 Discussion / Conclusions

8.4.1 Idealised Packing

Idealised packing of mono-dispersed BCC, FCC and HCP lattices with maximum packing fractions have been used to find the volume of TiO_2 filler capable of filling interstitial spaces.

These results have indicated that 4.33g-5.33g's (26%-32% v/v) of spherical TiO_2 filler is capable of fitting into a spherical aluminosilicate glass lattice based on 1g of material (ASG). This level of incorporation would increase the packing fraction of the packed cement to a maximum of 0.79, an 8% reduction in void volume above the ASG lattice alone.

The addition of shaped filler particles further increases the packing fraction to 0.91, a significant improvement. The ideal packing model has shown that square/cubic particles would be the best shaped filler to improve the packing in ideal cement.

8.4.2 Random Packing Simulations

Preliminary simulations (*see* Appendix 4) have shown that a monodispersed spherical powder will reach a maximum packing fraction of 63% (PF, 0.63) but will, on average, be around 57% (PF, 0.57). The optimum sized spherical filler to pack the interstitial spaces in a ASG mono-dispersion will be 20% the size of the solvent particle. The addition of solute particles with a total volume not exceeding the void volume of an unpacked solvent lattice and 20% the size of the solvent diameter will produce a maximum packing fraction of 0.791 including polyelectrolyte addition.

Simulation of the control material (Diamond Carve) based on hard, non sticky spheres has indicated that a packing fraction of 0.75 or 0.70 is possible with and without polyelectrolyte addition respectively.

The addition of filler particles mimicking experimental systems further increased the packing fraction to 0.76 including polyelectrolyte addition. It was found that TiO_2 incorporations around 2.5% w/w and 7.5% w/w produced better packing densities that 1% w/w and larger incorporation values.

The optimum amount of filler needed to increase the packing fraction of the control cement is below that predicted using a mono-disperse ASG lattice. The idealised model suggests that up to 5 times the weight of TiO_2 can be used for every gram of ASG.

The inclusion of shaped fillers showed little increase in packing fraction when simulations were run using dimensions calculated from formula used throughout idealised packing.

8.4.3 General Discussion

The original hypothesis that the packing fraction will have a direct influence on the compressive strength of formed cements appears to be true when a comparison between simulated packing fractions is compared with compressive strength results from Chapter 5. The greatest packing fractions found follow the order 2.5% w/w , 7.5% w/w then the original material in descending order. The averaged results from experimental data (*see* Figure 5.4) also shows the above trend however, the error associated with experimental results prevents this from being a conclusive relationship.

The idealised packing results have indicated that a ratio of almost 5:1 filler to glass can be maintained without the disruption of ASG packing. The effect of TiO_2 addition has previously been found to be detrimental to both the working and setting times because of how the filler interacts with the cement forming liquid and the removal of Ca/Sr/Al rich ASG. The addition of high levels of TiO_2 would conceivably stop a cement from forming but would certainly stop the cement from being clinically useful (*see* Chapter 4).

The constant 4:1 powder to liquid ratio means that there is always an excess of ASG in formed GICs, therefore, porosity will always be an inherent problem with this type of cement.

Earlier in this chapter it was suggested that additional polyelectrolyte solution could be used to reduct the porosity of the formed cements and further increase the packing density. The alteration of the powder to liquid ratio is known to affect GICs handling characteristics (Wilson, 1974; Wilson & Nicholson, 1993; Chapter 4) therefore is not recommended as a viable alteration.

Practically, the best way to increase the packing fraction would be to generate a particle size distribution with ASG particles conforming to the Dinger-Funk equation. This will provide the maximum packing fraction without the addition of a non reactive filler particle, a further variable. The alteration/tailoring of the particle size distribution will likely cause a detrimental effect in handling characteristics.

Chapter 9

Conclusion

9.1 Introduction

In Chapter 1, the aim of the research presented in this thesis project was established as the improvement of a commercially available glass ionomer cement by inclusion of novel sub-micron sized titanium dioxide filler particles. In some cases the titania filler particles would be coated with a reactive aluminium hydroxide with the intention of assisting their incorporation into the GIC.

The motivation for this research was based on the following hypotheses:

- Inclusion of titania fillers would aid the mixing process via 'mechanical lubrication'
- Inclusion of titania fillers with a reactive aluminium hydroxide coating would enhance the particles' integration into the GIC during setting.
- A greater packing density would be obtained using titania fillers, resulting in a greater compressive strength.

Titania was selected as the novel filler material chosen as it has a low toxicity (it is widely used as a food pigment, and as a coating on dental implants), is readily available and has a tightly controlled particle size distribution. Aluminium hydroxide was selected as the titania coating material as it is known to react with polyacrylic acid, which is used in GICs (Equation 13) and therefore it was thought that this would bridge the interface between TiO_2 and GIC matrix.

$$\left[C_5O_4H_4\right]_n + \left[Al(OH)_3\right]_n \rightarrow \left[C_5O_4H_2Al_n\right]_n + nH_2O \qquad \text{Equation 13}$$

9.2 Outcomes

The most significant results from the experimental work described in this thesis can be summarised thus:

GICs containing aluminium hydroxide-coated titania filler particles display, in comparison to conventional GICs:

- A shorter working time
- A longer setting time
- A setting mechanism unchanged from the control material
- A reduction in total aluminium concentration
- A slight increases in the compressive strength and
- The theoretical possibility of high filler incorporations without disrupting the original cements packing.

9.2.1 Rheology

Wilson rheology was used to characterise both the working and setting time of control and TiGIC materials; this is the standard, ISO, method for calculating the working time. Given the rapid increase in viscosity of test samples, the simplicity of the test set-up was beneficial and a better method could not be found. The setting time was also calculated using a Wilson rheometer which is not the ISO standard for finding this variable however the absolute setting time of the control and new GICs was not thought to be as important as the working time. The working time of TiGICs formulations was found to be up to 60 seconds shorter than the control cement and have a standard deviation of around 10 seconds while the setting time was greater than 200 seconds longer than the control material and the deviation was as large as 73 seconds. A relatively large variation was found in the setting time when compared with the working times due to the large affect small errors had on the steep gradient of the rheogram at completion. A more suitable method and the ISO standard for finding the setting time of GICs is using a Gillmore needle which may have produced less error. The setting time of the TiGICs was extended greatly when compared to the control material that the need for a low standard deviation was not necessary.

An AR2000 advanced rheometer was used in conjunction with the Wilson rheometer to find additional data, such as storage and loss modulus, over a longer period of time than the Wilson rheometer was able to provide because of increased sensitivity. The AR2000 suggested that the TiGICs would have approximately 50% the compressive strength of DC at 1 hour. A difference of between 30% - 50% was confirmed by mechanical testing. The use of rheology was the most suitable way to monitor physical changes during the first hour of mixing because of the combination of rapid response and high sensitivity between the two techniques employed.

The shortening of the working time and elongation of the setting time were originally believed to be due to chemical means as low percentages of filler were being used. The hypothesis was that the working time was being shortened by a reaction between tartaric acid and $Al(OH)_3$ rapidly neutralising the acid solution. The neutralisation was causing the large polymer chains of PAA to unwind and increase the viscosity of the cement. The increasing viscosity prevents normal acid-based reaction between ASG and polyacid occurring due to reduced mobility which resulted in elongated setting times and poor strength development.

9.2.2 Spectroscopy

Two non-destructive spectroscopic methods were used to probe the setting mechanism of both the control and TiGIC cements. Infrared spectroscopy was used in an attempt to identify the rapid increase of aluminium tartrate, believed to cause the reduction in working time. It was also hoped that the use of IR monitoring during the curing process would passively identify the cause of setting time elongation. The IR analysis found that the setting mechanism in TiGICs largely precedes the same as in the control material with the exception of high concentrations of aluminium tartrate at the onset of mixing. The high concentration of Al-TA was also present in uncoated TiGICs so is not believed to be caused by $Al(OH)_3$. A major complication with the IR analysis was the overlap of major cement salts, no separate peak for aluminium hydroxide – PAA salts and shifting baselines caused by surface contact with the ATR window. The use of infrared spectroscopy to find the time to first appearance of cement salts is a valid experimental technique that has been used several times in conjunction with conventional and experimental GICs (Nicholson, 1999).

Confidence in the IR results may be increased by using shorter scan & sampling times or by using the spectrometer in transmission mode improving the experimental procedure. Shorter sampling & acquisition times would mean that rapid changes in cement salt concentration could be more closely monitored where as transmission experiments would provide a more stable baseline and easier sample acquisition due to the samples having to have the acid-base reaction stopped in order to form a potassium bromide (KBr) window; this would be beneficial in difference spectra. The use of chemometrics may also be beneficial as it is common place to use this technique to separate overlapping absorbencies. This has not previously been performed for GICs and is uncommon on mid-IR spectra however the applicability of the technique is still valid.

Solid state NMR was used to identify the setting mechanism of the control and experimental GICs. The results found were complimentary to those found from IR spectroscopy and identified that the experimental cements have the same reaction path as the control cement. NMR identified the cause of setting time elongation as a reduction in aluminium from the removal of ASG. The removal of ASG from the TiGICs reduces the amount of available aluminium and calcium/strontium for reaction, effectively lowering the ASG : polyacid ratio causing the elongation of the setting time. The amount of ASG in the TiGICs still has an excess of aluminium and calcium/strontium for the concentration of polyacid used however it is not readily available. Once the surface of the glass has become diminished it effectively ‘locks’ away the metal cations in the middle of what has become a glass filler particle.

The two spectroscopic techniques were unable to find a mechanistic reason for the shortening of the working time. Prentice *et al* (2005) have previously found similar results to those found in this study when adding ytterbium and barium sulphate nanoparticles to conventional GICs. Ytterbium and barium sulphates are inert particles so are expected to react in a similar way as TiO_2 used in this study. Adsorption isotherms are not present for PAA interacting with either of these particles however PAA is known to adsorb onto their surface (Wright *et al*, 1987).

Premature gelation by temporary cross-linking of PAA by adsorption onto the surface of $Y_2(SO_4)_3$ and $BaSO_4$ is a possible reason for the reduction in working time. The shortening of conventional GICs working time after the addition of sub-micron particles is not widely reported and the cause of this observation is unknown. Conventional GICs are made from particulate glass in a polymer matrix so the addition of sub-micron particles to an already heavily filled polymer system was overlooked and is still not fully understood. This is an area that needs to be further quantified before particulate matter can be used to fill GIC systems.

9.2.3 Compressive Strength

The compressive strength analyses of diamond carve and novel TiGIC formulations from 1 hour to 1 year identify key differences during the early and latter stages of cement maturation. The use of the AR2000 rheometer was successful in predicting the increase in compressive strength during the first hour of maturation. At the end of Chapter 4 subsection 4.3.3.2 the results predicted that the compressive strength of TiGICs would be 50% of the strength of DC. The compressive strength results found in Chapter 5 show that the compressive strength of TiGIC formulations ranged from 30-50% compared to DC. DC reaches approximately 80% of its maximum strength by 3 days where as the TiGICs have, on average, reached approximately 70% of their maximum strength. The compressive strength of TiGICs reaches comparable values to the control cement by 7 days.

The variation in the data makes it hard to say whether or not the TiGIC cements have significantly improved in strength however the average values do strongly suggest this is the case. The coated TiGICs displayed superior results to the uncoated TiGICs suggesting further, long term reaction of the coating with the cement forming acids. It was found that the 2.5% incorporation yielded higher compressive strengths than the larger 7.5%, incorporation. This is in agreement with the results from theoretic modelling of the system and is likely caused by the disruption of the ASG packing structure.

The cause of the large error associated with the data is not known however given the differences in particles size and distribution within individual samples and the unique way in which they fail may be a partial cause.

Other methods for determining the strength of GICs are available such a compressive shear testing and diametral tensile strength however these are not commonly used in dental material research so comparison with literature values would be difficult.

9.2.4 Theoretical Modelling

The question, 'what would happen if you put in more filler' gave rise to the modelling of the cement system.

The theoretical modelling used both ideal and random packing models to find the amount of filler that can be added to a monodispersed ASG lattice and a representation of the control cement. These models suggested that greater amounts of TiO_2 than currently used could be incorporated into the control cement without disrupting the packing achieved in the control material. This is approach to optimising GICs has not previously been published. The modelling approach allowed for optimisation of the existing GIC structure with spherical and irregularly shaped filler particles that were in agreement with experimental results. The development of uniform filler particles such as flat, square, shaped clay particles means that there is scope to further increase the packing in 'real' experimental cements increasing the achieved packing density and therefore the compressive strength.

The rheology chapters have shown that filler addition at any concentration caused the GIC to lose the 'snap set' property, decrease the working time and increase setting time so formulation changes would need to be made in order to incorporate fillers and still be clinically useful. The rapid working and long setting time were seen during the development of conventional GICs (Wilson & Nicholson, 1993) and was eventually solved by the inclusion of TA at a critical concentration to retard the early setting reaction whilst enhancing the setting mechanism.

9.2.5 Observations

9.2.5.1 Mixing Properties

A comment about the hand mixing of TiGICs compared with DC. This is not a property that can be analytically quantified and is generally performed by a panel of dental nurses and a overall opinion about mixing quality is reached. A clinical trial was never performed however, personally, the hand mixing of TiGICs was much easier than DC due to the cement forming a paste easily and flowing easily during the viscous, high shear mixing process.

9.2.5.2 Opacity

Titanium dioxide is known for having a high refractive index (η_D = 2.488, Handbook of Chemistry and Physics) which is why it is typically used as a white pigment in a wide variety of applications. Although the opacity of the TiGICs was not measured during this research it is worth noting that the addition of TiO_2 to the original DC cement made the restoration a opaque, brilliant white colour. One of the advantages of GICs has been the similar translucency to enamel hence the filler addition has diminished this property. Although GICs are becoming more widely used as a cavity liner before CR placement the unnatural opaque whiteness of the TiGICs currently limites them the only being used as cavity liners

9.3 Conclusion

The inclusion of reactive filler particles to a conventional glass poly-vinyl-phosphonate cement has improved the average compressive strength. The curing mechanism is the same as the control material during the early stages of maturation however a continued reaction between polyacid and $Al(OH)_3$ is believed to continue as compressive strength of TiGICs with hydroxide coating achieve a greater σ_C than those without.

The reduction in observed working times have likely been caused as a result of interactions between the filler and polyacid solution causing decreased mobility of polymer chains in a similar way to cross-links between PAA and ASG. The setting time has been elongated due to the reduction of available metal cations from ASG which was not compensated for by the addition of $Al(OH)_3$.

Chapter 10

Further Work

10.1 Introduction

Considering the relative novelty of the cement composition(s) used throughout this thesis, the possibilities for future work are very extensive. If time were not a concern then the further work could be divided into two categories: (1) further characterisation of the properties of current cement formulations, (2) research aimed at optimising the properties of the cements by modification to the current formulation. The further characterisation of the new TiGICs would consist of routine tests carried out to quantify the 'qualities' of these new cements and would include analysis of fluoride release and adhesion to enamel/dentin. These tests have been carried out previously and can be found in relevant literature (e.g. Acid-Base Cements by Wilson & Nicholson, 1993) and international standards for dental restoratives (e.g. BS EN ISO 9917-1:2003).

The second category would include further optimisation of the current TiGICs via particle size and polyelectrolyte alteration and the investigation of other possible improvements to the GIC system. This chapter will focus on the second category and will include brief outlines of the idea, its proposed purpose and how the research may be carried out.

10.2 Chemical Alteration

The easiest way to address the problems of shortened working time but elongated setting time would be the addition/subtraction of polyelectrolyte constituents. The most logical approach to resolve the aforementioned problem is the addition of TA and subtraction of PAA. This will have the effect of elongating the working time due to the retarding affect of TA and shortening of the setting time due to alteration of the powder to liquid ratio (ASG:PAA).

10.3 Filler Effects on Cement Rheology

The reduction in the working times of TiGICs is believed to be caused by the addition of sub-micron filler particles. The interaction between filler & polyelectrolyte and their affect on the cement viscosity may be accounted for experimentally. Three considerations must be accounted for during the setup due to the complexity of the acid-base reaction and electrolyte-filler interactions.

Firstly, the characterisation of interactions between ASG and TiO_2 with PAA. This has previously been performed in a number of ways including, UV/Vis and IR, Zeta Potential analysis and Absorption Isotherm measurements.

Secondly, the identification of alternatives to ASG or PAA that posses similar adsorptive properties whilst having minimal chemical reactivity negating the acid-base setting reaction.

Finally, the quantification of the viscosity change due to the addition of ASG and TiO_2 into the polymeric (PAA substituted) solution. This can be directly obtained using a viscometer or an oscillating rheometer can be used to find the complex viscosity and this can be back calculated to real viscosity.

10.4 Particle Packing Optimization

Theoretical modelling has indicated that there is sufficient room within a fully formed GIC for a considerable volume of filler to be added. However, this study has also identified that the alteration of the powder to liquid ratio (ASG:PAA) has the detrimental effect of elongating the setting time. Assuming that the setting time of the TiGICs can be accounted for chemically (*see* Section 10.2) then two further studies may arise.

An experimental trial of tailored ASG particle size distributions using those suggested in Chapter 8. The cements will consist of a large fraction of small diameter particles again affecting the speed of reaction and therefore handling properties. This will have to be accounted for during the formulation of the final GIC.

Further to this experimental study, the construction of a Finite Element (FE) model to predict the influence of particle size and volume of incorporation would be a novel, although extensive further study. Many unknown parameters would need to be found before the model could be constructed adding to the novelty as these properties have never been found before. Properties such as the Young's Modulus of the ASG and formed PAA-metal oxide cement matrix would need to be found using, for example, a nano indenter for a range of glasses, cements and filler particles. The poasions ratio of the cements would also need to be found should a full mechanical model be established.

10.5 Coatings and Coating Medium

Metal oxides and hydroxides of bivalent metals are known to react readily with PAA (Wilson & Nicholson, 1993; Wu *et al*, 1997); the order of reactivity increases from oxide to hydroxide. This entire thesis may be repeated with a different metal oxide coating on the filler material surface to better aid its addition to the cement without hindering the setting mechanism. However, it is foreseeable that the problem of decreased working time will be exaggerated as the binding of PAA will be immediate upon the initiation of mixing coupled with the unresolved filler addition affect.

A currently untried method of controlling the Acid-Base reaction is the coating of ASG directly with a less reactive substance such as aluminium hydroxide allowing the use of smaller particle sizes and tighter particle size distributions. The exact method and extent of coating would need to be researched as the same method as that used to coat TiO_2 base particles would result in deterioration of the ASG due to the initial acid conditions.

Chapter 10: *Further Work*

The coating would need to proceed via a basic coating process (see Appendix 1), a non-ionic coating method or a dry diffusion method. The simplest method able to be readily performed in any laboratory would be the basic coating using sodium aluminate via a sol-gel precipitation. The coating can then be further modified with application of fluorine to increase surface basicity. ASG would need to be suspended in solution using mechanical agitation alone as an acidic surfactant would be needed to reduce surface interaction.

A Non-ionic coating can be performed by dissolving aluminium isopropoxide in butanol along with ASG. This can subsequently be hydrolysed to form aluminium hydroxide by the addition of a little water. Alternatively, the placement of aluminium metal on the surface using a 2/3 component system similar to IPCOTE MSRR 9253 followed by a post-placement transformation to aluminium hydroxide by boiling in ‘pure’ water for several hours.

Aluminium can be applied via a low pressure Chemical Vapour Deposition (CVD) method. The CVD method would need to be closely controlled or the formation of a solid glass-aluminium composite would be formed and require mechanical grinding to obtain a suitable powder for mixing with PAA.

Bibliography

A

Abe. Y, Lambrechts. P, Inoue. S, Bream. M, Takeuchi. M, Vanherle. G, Van Meerbeek. B.
Dynamic Elastic Modulus of 'Packable' Composites
Dental Material 17(6), 520, 2001

Alexandera. M. R, Beamsonb. G, Blomfieldc. C. J, Leggettd. G, Duce T. M.
Interaction of Carboxylic Acids with the Oxy-hydroxide Surface of Aluminium: Poly(acrylic acid), Acetic Acid and Propionic Acid on Pseudoboehmite
Journal of Electron Spectroscopy and Related Phenomena 121, 19–32, 2001

Anstice. H, Nicholson. J.
Investigation of the Post-Hardening Reaction in Glass Ionomer Cements Based on Poly(vinylphosphonic) Acid
Journal of Materials Science: Materials in Medicine 6(7), 420, 1995

B

Balasubramanlan. D, Mlsra. C.
Chain Expansion of Neutral Polymer Coils upon Cation Binding
The Journal of Physical Chemistry, 81(24), 1977

Barnes. H. A.
Handbook of Elementary Rheology
University of Wales, Institute of Non-Newtonian Fluid Mechanics, 2000

Barry. T. I, Clinton. D. J, Wilson A. D.
The Structure of Glass Ionomer Cements and its Relationship to the Process
Journal of dental research, 58(3) 1072-1079, 1979

Barton. M. I, Quintard. P.
Infrared Evidence of Order-Disorder Phase Transitions in Al_2O_3
Journal of Molecular Structure, 79, 337-340, 1982

Bayne. S. C, Thompson. J. Y, Swift. E. J, Stamatiades. P, Wilkerson. M.
A Characterisation of First Generation Flowable Composites
129(5), 567, 1998

Bayraka. S, Tunca. E. S, Aksoyb. A, Ertasc. E, Guvencd. D, Ozere. S.
Fluoride Release and Recharge from Different Materials Used as Fissure Sealants
European Journal of Dentistry, 4, 245-251, 2010

Berenbaum. R, Brodie. I.
The Tensile Strength of Coal
Journal of the Institute of Fuel, 32, 320-327, 1959

Billington. R. W, Williams. J. A, Pearson. G. J.
Variation in Powder / Liquid Ratio of a Restorative Glass Ionomer Cement used in Dental Practice
British Dental Journal, 22, 169(6), 164-167, 1990

Billington. R. W, Williams. J. A, Pearson. G. J.
Ion Processes in Glass Ionomer Cements
Journal of Dentistry 34, 544–555, 2006

Borkowski
Dissociation Constants
http://www.chembuddy.com/?left=BATE&right=dissociation_constants
Accessed 13/4/10, Last Updated, 2005

Bibliography

Bowen. R. L.
Proceedings of a Workshop on Adhesive Restorative Dental Materials
National Institute, Bethesda, MD, 177-191, 1961

Braun. M, Hartmann. P, Jana. C.
F^{19} NMR Spectroscopy of Calcium Apatites.
Journal of Material Science: Mater Med, 6(4), 150, 1995

Bresciani. E, Barata. T. E, Fagundes. T. C, Adachi. A, Terrin. M. M, Lima Navarro. M. F.
Compressive and Diametral Tensile Strength of Glass Ionomer Cements
Journal of Applied Oral Science, 12(4), 9-17, 2004

Brouwers. H. J. H.
Particle-size distribution and packing fraction of geometric random packing's
Physical Review E 74, 2006

Brouwers. H.J.H, Radix. H.J.
Self-compacting Concrete: The Role of the Particle Size Distribution
First International Symposium on Design, Performance and Use of Self-Consolidating Concrete, SCC'2005 - China, 26 - 28 May 2005, Changsha, Hunan, China

Brown. R, Marjenhoff. W.
Dental Composites / Glass Ionomers: The Materials
Advances in Dental Research 6, 44, 1992

Brune. D.
Heat Treatment of Glass Ionomer, Silicate, Zinc Phosphate and Zinc Polycarboxylate Cements
Scandinavian Journal of Dental Research, 90, 409 – 412, 1982

BS EN ISO 9917-1:2003
Dentistry – Water Based Cements – Part 1: Powder/liquid Acid-base Cements

Buonocore. M, Wileman. W, Brudevold. F.
A Report on Dental Composition Capable of Bonding to Human Dentin Surfaces
35, 846, 1956

Buonocore. M.
A Simple Method of Increasing the Adhesion of Acrylic Filling Materials to Enamel Surfaces
34, 849, 1955

Buonocore. M. G, Davila. J.
Restoration of Anterior Teeth with Ultraviolet Light Polymerised Bonding Materials: A New Technique
Journal of the American Dental Association 86(6), 1349, 1973

C

CERAM Research Limited
http://www.ceram.com
Accessed 25/11/10

Chang. M.
Monte Carlo Simulation for the Pharmaceutical Industry: Concepts, Algorithms, and Case Studies
CRC Press, 26 July 2010

Clayden. J, Greeves. N, Warren. S, Worthers. P.
Organic Chemistry, 2004

Cody. G. D, Mysen. B, Saghi-Szabo. G, Tossell. J. A.
Silicate-Phosphate Interactions in Silicate Glasses and Melts: I. A Multinuclear (^{27}Al, ^{29}Si, ^{31}P) MAS NMR and ab initio Chemical Shielding (^{31}P) Study of Phosphorous Speciation in Silicate Glasses.
Geochimica et Cosmochimica Acta, 65(14), 2395–2411, 2001

Coldebella. C, Santos-pinto. L, Zuanon. A. C.
Effect of Ultrasonic Excitation on the Porosity of Glass Ionomer Cement: A Scanning Electron
Microscope Evaluation
Microscopy Research and Technique 74, 54–57, 2011

Cook, W. D, Brockhurst. P.
The Oscillating Rheometer - What Does It Measure?
Journal of Dental Research 59(5):795-799, 1980

Cook. W. D.
Dental polyelectrolyte cements: II: Effect of Powder/Liquid Ratio on their Rheology
Biomaterials, 4, 21-24, 1983
Coughian. A, Scanion. K, Mahon. B. P, Towler. M. R.
Zinc and Silver Glass Polyalkenoate Cements: An Evaluation of their Antibacterial Nature
Bio-medical Materials and Engineering, 20(2), 99-106, 2010

Criscenti. L. J, Brantley. S. L, Mueller. K, Tsomaia. T. N, Kubicki. J. D.
Theoretical and ^{27}Al CPMAS NMR Investigation of Aluminium Coordination Changes During Aluminosilicate Dissolution
Geochimica et Cosmochimica Acta 69(9), 2205–2220, 2005

Crisp. S, Wilson. A. D.
Reactions in Glass Jonomer Cements: III - The Precipitation Reaction
Journal of Dental Research 53, 1420, 1974

Crisp. S, Lewis. B. G, Wilson. A. D.
Glass Ionomer Cements: Chemistry of Erosion
Journal of Dental Research, 55(6), 1032-1041, 1976

Crisp. S, Lewis. B. G, Wilson. A. D.
Characterisation of Glass Ionomer Cements – Long term hardness and compressive.
Journal of Dentistry, 4, 162-166

Crisp. S, Prosser. H. J, Wilson. A. D
An infra-red Spectroscopic Study of Cement Formation between Metal Oxides and Aqueous Solutions of Polyacrylic Acid
Journal of Material Science, 11, 36-48, 1976

Crisp. S, Wilson. A. D.
Reactions in Glass Ionomer Cements – Decomposition of the Powder
Journal of Dental Research, 53, 1408, 1974

Cumberland. D. J
The packing of particles (Handbook of powder technology)
Elsevier, 1987

D

Davidson-Kaban. S, Davidson. C, Feilzer. A, DeGee. A, Erdilek. N.
The Effect of Curing Light Variations on Bulk Curing and Wall-to-Wall Quality of two types and Various Shades of Resin Composites
Dental Material, 13, 344, 1997

De Maeyer. E. A. P, Verbeeck. R. M. H, Vercruysse. C. W. J.
Reactivity of Fluoride-containing Calcium Aluminosilicate Glasses Used in Dental Glass-ionomer Cements
J Dent Res 77(12), 2005-2011, 1998

De Maeyer. E. A. P, Verbeeck. R. M. H, Vercruysse. C. W. J.
Infrared Spectrometric Study of Acid-degradable Glasses
Journal of Dental Research 81, 552, 2002

Deliperi. S, Bardwell. D.
An Alternative Method to Reduce Polymerisation Shrinkage in Direct Posterior Composite Restorations
Journal of the American Dental Association 133, 1387, 2002

Dinger, D. R, Funk J. E.
Particle Packing IV – Computer Modelling of Particle Packing Phenomena
Interceram, 42(3), 150–153, 1993

Doktycz. S. J, Suslick. K. S.
Interparticle Collisions Driven by Ultrasound
Science, 247, 1067–1069, 1990

Dollase. W. A, Merwin. L. H, Sebald. A.
Structure of Na_3-3xAl$P0_4$, x = 0 to 0.5
Journal of Solid State Chemistry, 83, 140-149, 1989

DuPont Titanium Technologies
Effect of TiO2 on Viscosity
http://www.specialchem4polymers.com/tc/titanium-dioxide/index.aspx?id=viscosity
Accessed 12/02/09

Dupree. R, Holland. D, Mortuza. M.G, Collins. J. A, Lockyer. M.W.G.
The Chemistry and Binding Properties of Aluminium Phosphates
Journal of Non-Crystalline Solids, 112, 111-119, 1989

E

Eliades. P. G.
In Vitro Characterisation of Visible Light Cured Glass Ionomer Liners
Dental Materials 9, 198, 1993

Ellakuria. J, Triana. R, Minguez. N, Soler. I, Ibaseta. G, Mazab. J, Garcia-Godoy. G.
Effect of One-Year Water Storage on the Surface Microhardness of Resin-Modified Versus Conventional Glass-Ionomer Cements
Dental Material 19(4), 286, 2003

Ellis. J, Wilson. A. D.
The formation and properties of metal oxide poly(vinylphosphonic acid) cements
Dental Material 8, 79-84, 1992

F

Fennell. B, Hill. R.G, Akinmade. A.
Failure and Fracture Characteristics of Glass(vinylphosphonate) Cements
Dent. Mater. 14, 358, 1998

Ferracane. J. L, Moser. J. B, Greener. E. H,
Rheology of Composite Restoratives.
Journal of Dental research 60(9), 1678-1685, 1981

Finch. S. D, Oreskovic. T, Ramadurai. K, Herrmann. C. F, Steven M. George. S. M, Mahajan. R. L.
Biocompatibility of atomic layer-deposited alumina thin films
National Institute of Standards and Technology
Journal of Biomedical Materials Research Part A, 100-107

Fleming. G, Farooq. A, Barralet. J.
Influence of Powder / Liquid Mixing Ratio on the Performance of a Restorative Glass Ionomer Dental Cement
Biomaterials 24(23), 4173, 2003

Fleming. G, Farooq. A, Barralet. J, Fusayama. T, Katayoni. T, Nomoto. S.
Corrosion of Gold and Amalgam Placed in Contact with each other
Journal of Dental Research 42, 1183-1197, 1963

Forss. H.
Release of Fluoride and other Elements from Light Cured Glass Ionomers in Neutral and Acidic Conditions
Journal of Dental Research 71, 1257, 1993

Franenberger. R, Kramer. N, Pelka. M.
International Adaptation and Overhang Formation of Direct Posterior Resin Composite Restorations
Clin. Oral. Investig. 3, 208, 1999

Futatsuki. M, Nozawa. M, Ogata. T, Nakata. M.
Wear of Resin-Modified Glass Ionomers: An in Vitro Study
25(4), 297, 2001

G

German. R. M.
Particle Packing Characteristics
Metal Powder Industry, 1989

Glasel. H, Hartmann. E, Mehnert. R, Wennrich. A, Prager-Duschke. A, Khalil. H, Hallmeier. K. H, Makhova. L, Thieroff. C, Buchmeiser. M. R.
Synthesis of Polar and Non-Polar Nano-Corundum and Uses for Aluminium Carboxylate Hybrid Nanocomposites with Enhanced Surface Mechanical and Viscoelastic Properties
Macromolecular Materials Engineering 292, 1140–1148, 2007

Goodwin J W, Hughes R W
Rheology for Chemist.
The Royal Society of Chemistry, 2000
Thomas Graham House, Cambridge

Gray. W. A.
Packing of Solid Particles (Powder Technology)
Chapman and Hall, 1968

Griffin. S.G, Hill. R.G.
Influence of glass composition on the properties of glass polyalkenoate cements. Part II: influence of phosphate content.
Biomaterials, 21, 399 – 403, 2000

Grippo. J, Simring. M, Schreiner. S.
Attrition, Abrasion, Corrosion and Abfraction Revisited: A New Perspective on Tooth Surface Lesions
Journal of the American Dental Association 135(8), 1109-1118, 2004

Guggenberger. R, May. K, Stephan. R.
New Trends in Glass Ionomer Chemistry
Biomaterials, 19, 479, 1998

H

Hales T. C.
An overview of the Kepler conjecture
Mathematics - Metric Geometry

Hatton. P.V., Brook. I. M.
Characterisation of the Ultrastructure of Glass-Ionomer (Poly-alkenoate) Cement
British Dental Material, 173, 275–277, 1992

Hem. S. L.
Physicochemical Properties of Antacids
Journal of Chemical Education, 52(6), 382-387, 1975

Hill. R. G.
The Fracture Properties of Glass Polyalkenoate Cements as a Function of Cement Age
Journal Material Science 28, 3851–3858, 1993

Hill. R. G, Labok. S. A.
The Influence of Polyacrylic Acid Molecular Weight on the Fracture of Zinc Polycarboxylate Cements
Journal of Material Science 28, 67, 1992

Hill. R. G, Stamboulis. A, Law. R. V.
Characterisation of Fluorine Containing Glasses by ^{19}F, ^{27}Al, ^{29}Si and ^{31}P MAS-NMR Spectroscopy
Journal of Dentistry, 34, 525-532, 2006

Hill. R.G, Stamboulis. A, Law. R.V, Clifford. A, Towler. M. R, Crowley. C.
The Influence of Strontium Substitution in Fluorapatite Glasses and Glass-Ceramics
Journal of Non-Crystalline Solids 336, 223–229, 2004

Hill. R. G, Warrens. C. P, Wilson. A. D.
The Influence of Poly(acrylic acid) Molecular Weight on the Fracture Toughness of Glass-ionomer Cements
Journal Material Science 24, 363, 1989

Hill. R. G, Wilson. A. D.
A Rheological Study of the Role of Additives on the Setting of Glass-Ionomer Cements.
Journal of Dental research 67(12), 1446-1450, 1988

Hirayama. C.
Properties of Aluminoborate Glasses of Group 11 Metal Oxides: Glass Formation and Thermal Expansion.
Journal of the American Ceramic Society. 44, 602–606, 1961

Hofmann. N, Markert. T, Hugo. B, Klaiber. B.
Effect of High Intensity vs. Soft Start Halogen Irradiation of Light-Cured Resin-Based Composites. Part 1: Temperature Rise and Polymerisation Shrinkage
Am. J. Dent 16(6), 421, 2003

Holt. R., Roberts. G, Scully. C.
ABC of Oral Health: Dental Damage, Sequelae and Prevention
British Medical Journal, 320, 1717, 2000

Hornsby. P. R.
A Study of the formation and properties of ionic polymer cements
Thesis for PhD, Brunel University, Middlesex, England, 1977

Hse. K, Leung. S, Wei. S.
Resin-Ionomer Restorative Material for Children: A Review
Aus. Dent J. 44(1), 1, 1999

Hu. H, Saniger. J. M, Castaiio. V. M.
Characterization of the Mechanical Properties of Polyacrylic Acid-Metal Oxide Concretes
Materials Letters 14, 83-87, 1992

I

J

Jones. F. H.
Teeth and Bones: Applications of Surface Science to Dental Materials and Related Biomaterials
Surface Science Reports 42(3-5), 75, 2001

Jones. F. H, Hutton. B, Hadley. P, Eccles. A, Steele. T, Billington. R, Pearson. G.
Fluoride Uptake by Glass Ionomer Cements: A Surface Analysis Approach
Biomaterials 24(1), 107, 2003

Jones. R. M, Zheng. L, Newlands. M. D.
Comparison of particle packing models for proportioning concrete constituents for minimum voids ratio
Materials and Structures 35, 301-309, 2002

Jones. S.
The Story of Adhesion and Developments in Dentistry
International Journal of Adhesion and Adhesives, 15(2), 109, 1995

K

Kan. K, Messer. L, Messer. H.
Variability in Cytotoxicity and Fluoride Release of Resin-Modified Glass-Ionomer Cements
Journal of dental research, 79, 1502, 1997

Kelsey. K. E., Allward. J. R, Stebbins. J. F.
Ca–Mg Mixing in Aluminosilicate Glasses: An Investigation using ^{17}O MAS and 3QMAS and ^{27}Al MAS NMR
Journal of Non-Crystalline Solids 354, 4644–4653, 2008

Kendall. K.
Complexities of compression measurements,
361, 245, 1978

Kenneth J. D. MacKenzie, Mark E. Smith
Multinuclear solid-state NMR of inorganic materials
Elsevier Science LTD Oxford, 2002

Kent. B. E, Lewis. B.G, Wilson. A. D.
The Properties of a Glass Ionomer Cement
British Dental Journal, 161, 322-326, 1973

Kent. B. E, Lewis. B. G, Wilson. A. D.
Glass Ionomer Cement Formulations: I. The Preparation of Novel Fluoroaluminosilicate Glasses High in Fluorine. Journal of dental research, 58(6), 1607-19, 1979

Kerby. R. E, Bleiholder. R. F.
Physical Properties of Stainless-Steel and Silver Reinforced Glass Ionomer Cements
Journal of Dental Research, 70(10),1358-61, 1991

Kiczenski. T. J, Du. L, Stebbins. J. F.
^{19}F NMR Study of the Order of High Field Strength Cations at Fluoride Sites in Silicate and Aluminosilicate Glasses
Journal of Non-Crystalline Solids, 337, 142-149, 2004

King. H. W.
Quantitative Size-Factors for Interstitial Solid Solutions
Journal of Material Science 6, 1157-1167, 1971

Kingery W. D.
Fundamental Study of Phosphate Bonding in Refractory's, II: Cold Setting Properties
Journal of the American Ceramic Society, 33, 242-247, 1950

Kirkpatrick RJ, Brow RK.
Nuclear Magnetic Resonance Investigation of the Structures of Phosphate and Phosphate Containing Glasses: A Review.
Solid State Nuclear Magnetic Resonance, 5, 9–21, 1995

Kleverlaan. C. J, Duinen. V. A, Feilzer. A. J.
Mechanical Properties of Glass Ionomer Cements Affected by Curing Methods
Dental Materials 20(1), 45–50, 2004

L

Labella. R, Lambrechts. P, Van Meerbeek. B, Vanherle. G.
Polymerisation Shrinkage and Elasticity of Flowable Composites and Filled Adhesives
Dental Material 15(2), 128, 1999

Larson. R. G.
The Structure and Rheology of Complex Fluids
Oxford University Press, New York, 1999

Leach. A.
Molecular Modelling: Principles and Applications
Prentice Hall; 2 Edition, 2001

Lea. S. C, Price. G. J, Walmsley. A. D.
A Study to Determine Whether Cavitation Occurs Around Ultrasonic Instruments
Journal of Dental Research 82, 90, 2003

Lee. I, Son. H. H, Um. C. M.
Rheological Properties of Flowable, Conventional Hybrid and Condensable Composite Resins
Journal of Dental Material 19, 298, 2003

Lee. J. H, Paik. U, Hackley. V. A.
Effect of Poly(Acrylic Acid) on Adhesion Strength and Electrochemical Performance of Natural Graphite Negative Electrode for Lithium-ion Batteries
Journal of Power Sources 161, 612–616, 2006

Lee. J. H, Um. C. M, Lee. I. B.
Rheological properties of resin composites according to variations in monomer and filler composition
Dental Materials 22, 515-526, 2006

Lee. S. K, Stebbins. J. F.
Al-O-Al and Si-O-Si Sites in Framework Aluminosilicate Glasses with Si/Al = 1: Quantification of Framework Disorder
Journal of Non-Crystalline Solids 270, 260-264, 2000

Leinfelder. K. L, Prasad. A.
A New Condensable Composite for the Restoration of Posterior Teeth
Dentistry Today 17(2), 112, 1998

Leinfelder. K. L, Radz. G. M, Nash. R. W.
A Report on a New Condensable Composite Resin
Compendium, 19(3), 230, 1998

Lewandowski. H, Koglin. E.
Adsorption of Polyacrylic Acid on Aluminium Oxide: DRIFT Spectroscopy and Ab Initio Calculations
Modern Methods and Algorithms of Quantum Chemistry, NIC Series, 2000

Li. J, Naito. Y, Chen. J. R, Goto. T, Ishida. Y, Kawano. T, Tomotake. Y, Ichikawa. T.
Journal of Dental Material 2010

Liu. X, Qian. L, Shu. T, Tong. Z
Rheology Characterisation of sol-gel Transition in Aqueous Alginate Solutions Induced by Calcium Cations through situ Release
Polymer 44, 407-412, 2003

Liufu. S, Xiao. H, Li. Y.
Adsorption of Poly(Acrylic Acid) onto the Surface of Titanium Dioxide and the Colloidal Stability of Aqueous Suspension
Journal of Colloid and Interface Science 281, 155–163, 2005

Lohbauera U., Walkerb J., Nikolaenkoa S., Wernerc J., Clareb A., Petschelta A., Greilc P.
Reactive Fibre Reinforced Glass Ionomer Cements
Biomaterials 24, 2901–2907, 2003

Lorton. L, Moore. B. K, Swartz. M. L, Phillips. R. W.
Rheology of Luting Cements
Journal of Dental Research 9(59), 1486-1492, 1980

Lowenstein. W.
The Distribution of Aluminium in the Tetrahedra of Silicates and Aluminates
American Mineralogist 39, 92-96, 1954

M

Macosko, W.
Rheology: Principles, Measurements and Applications
Wiley-VCH, New York, 1994

MacroPac – Simulating Particle Packing
Intelligensys Ltd
Springboard Business Centre, Stokesley Business Park
Ellerbeck Way
Stokesley, North Yorkshire
TS9 5JZ,

Matsuya. S, Maeda. T, Ohita. M.
IR and NMR Analysis of Hardening and Maturation of Glass-ionomer Cement
Journal of Dental Research 75(12), 1920-1927, 1996

Matsuya. S, Stamboulis. A, Hill. R. G, Law. R. V.
The Structural Characterisation of Ionomer Glasses by Multinuclear Solid-State MAS NMR Spectroscopy
Journal of Non-Crystalline Solids 353, 237-243, 2007

McCabe. J.
Resin-Modified Glass Ionomers
Biomaterials, 19, 521, 1998

McCabe. J, Rusby. S.
Water Absorption, Dimensional Change and Radial Pressure in Resin Matrix Dental Restorative Materials
Biomaterials 25(18), 4001, 2004

McKinney. E, Antonucci. J. M, RUPP. N. W.
Wear and Microhardness of Glass-Jonomer Cements
Journal of Dental Research 66(6), 1134-1139, 1987

McKinney. J. E.
Apparatus for Measuring Wear of Dental Restorative Materials,
Wear 76, 337-347, 1982

McKinney. J. E, Wu. W.
Chemical Softening and Wear of Dental Composites
Journal of Dental Research 64(11), 1326-1331, 1985

McLean. J. W, Gasser. O.
Glass-Cermet Cements
Quintessence Int 16, 333-343, 1985

MEMS and Nanotechnology Exchange
http://www.mems-exchange.org
Accessed 12/02/10

Mitra. S.
In Vitro Fluoride Release from a Light Cured Glass Ionomer Liner / Base
70, 75, 1991

Mitchell. C.A, Douglas. W. H.
Comparison of the porosity of hand mixed and capsulated glass-ionomer luting cements
Biomoterials 18, 1127-1131, 1997

Mitsuhhashi. A, Hanaoka. K, Teranaka. T.
Fracture Toughness of Resin-Modified Glass Ionomer Restorative Materials: Effect of Powder/Liquid Ratio and Powder Particle Size Reduction on Fracture Toughness
Dent Mater, 19(8), 747, 2003

Momoi. Y, Hirosaki. K, Kohno. A, McCabe. J.
In Vitro Toothbrush-Dentifrice Abrasion of Resin Modified Glass Ionomer
Dent Mater, 13(2), 82, 1992

Momoi. Y, McCabe. J.
Fluoride Release from Light Activated Glass Ionomer Restorative Cements
Dent Mater 9(3), 151, 1993

Moses. H, Ashby. W. C, Bogner. M. A.
Dewpoint Temperature Inversions
Journal of Applied Meteorology 7, 1967

Mountjoy. G.
The Local Atomic Environment of Oxygen in Silicate Glasses from Molecular Dynamics
Journal of Non-Crystalline Solids 353(18-21), 1849-1853, 2007

Mutlu. G, Huggett. R, Harrison. A.
Rheology of Acrylic Denture-Base Polymers.
Dental Materials 6, 288-293, 1990.

Mysen. B.O, Cody. G. D.
Silicate-Phosphate Interactions in Silicate Glasses and Melts: II. Quantitative,
High-Temperature Structure of P-bearing Alkali Aluminosilicate Melts
Geochimica et Cosmochimica Acta, 65(14), 2413–2431, 2001

N

Nagaraja Upadhya. P, Kishore. G.
Glass Ionomer Cement – The Different Generations
Trends in Biomaterials 18(2), 2005
http://www.sbaoi.org

Neve. A, Piddock. V, Combe. E.
The Effect of Glass Heat Treatment on the Properties of a Novel Polyalkenoic Cement
Clinical Materials, 12, 113-115, 1993

Nicholson. J. W.
Adhesive Dental Materials – A Review
International Journal of Adhesives, 18, 229, 1998

Nicholson. J. W, Anstice. H. M.
The Chemistry of Modern Dental Filling Materials
Journal of Chemical Education, 76(11), 1497, 1999

Nicholson. J. W, Brookman. P. J, Lacy. O. M, Wilson. A. D.
Fourier Transform Infrared Spectroscopic Study of the Role of Tartaric Acid in Glass-ionomer Dental Cements
Journal of Dental Research 67(12), 1451-1454, 1988

Nolan. G. T, Kavanagh. P. E.
Computer Simulation of Random Packing of Hard Spheres
Powder Technology 72, 149-155, 1992

Nomotoa. R, Komoriyamaa. M, McCabeb. J. F, Hiranoa. S.
Effect of mixing method on the porosity of encapsulated glass ionomer cement
Dental Materials 20, 972–978, 2004

O

O'Neill. I. K, Prosser. H. J, Richards. C. P, Wilson. A. D.
NMR Spectroscopy of Dental Materials. I. ^{31}P Studies on Phosphate-Bonded Cement Liquids
Journal of Biomedical Materials Research, 16, 39-49, 1982

O'Donnell. M. D, Hill. R. G, Law. R. V, Fong. S.
Raman Spectroscopy, ^{19}F and ^{31}P MAS-NMR of a Series of Fluorochloroapatites
Journal of the European Ceramic Society 29, 377–384, 2009

O'Donnell. M. D, Watts. S. J, Law. R. V, Hill. R. G.
Effect of P_2O_5 Content in two Series of Soda Lime Phosphosilicate Glasses on Structure and Properties – Part I: NMR
Journal of Non-Crystalline Solids 354, 3554–3560, 2008

P

Packier. A, Dhillon. H. S.
Studies on Amorphous Aluminium Hydroxide Precipitates (Gels) – Kinetics of Dissolution by Sodium Hydroxide Solutions
Kolloid-Zeitschrift und Zeitschrift fur Polymere, Band 239, Heft 1 (1969) – Translated to English by the West Ham College of Technology

Pefferkorn. E, Widmaier. J, Elfarissi. F.
Aluminium Ions at Polyelectrolyte Interfaces II – Role in the Surface-Area-Exclusion Chromatography of Humic Acid
Colloid and Polymer Science 279, 493-497, 2001

Peterson. C. L, Perry. D. L, Masood. H, White. J. L, Hem. S. L, Fritsch. C, Haeusler. F.
Characterisation of Antacid Compounds Containing Both Aluminum and Magnesium II – Codried Powders
Pharmaceutical Research 10(7), 1993

Peutzfeldt. A, Garcia-Godoy. F, Asmussen. E.
Surface Hardness and Wear of Glass Ionomers and Compomers
American Journal if Dentistry, 10(1), 15, 1997

Pires. R, Nunes. T. G, Abrahams. I, Hawkes. G. E, Morais. C. M, Fernandez. C.
Stray-field Imaging and Multinuclear Magnetic Resonance Spectroscopy Studies on the Setting of a Commercial Glass-ionomer Cement
Journal of Material Science: Materials in Medicine 15, 201-208, 2004

Poirier. T, Labrador. N, Alvarez. M. A, Lavelle. C, Enet. N, Lira. J.
Formation of Crystalline Phases in (SiO_2-CaO-Fe_2O_3)-TiO_2 Based Glasses.
Material letters, 59:308-12, 2005

Prentice. L. H, Tyas. M. J, Burrow. M. F.
The Effect of Particle Size Distribution on an Experimental Glass-ionomer Cement
Dental Materials 21, 505–510, 2005

Prosser. H. J., Jerome. S. M., Wilson. A. D.
The Effect of Additives on the Setting Properties of a Glass-Ionomer Cement
Journal of Dental Research 61, 1195-1198, 1982

Prosser. H. J., Powis. D. R, Wilson. A. D.
Glass-ionomer Cements of Improved Flexural Strength
Journal of Dental Research, 65, 146-148, 1986

Prosser. H. J, Richards. C. P, Wilson. A. D.
NMR Spectroscopy of Dental Materials: 2. The Role of Tartaric Acid in Glass-ionomer Cements
Journal of Biomedical Materials Research 16, 431-445, 1982

Q

Qvist. V, Manscher. E, Teglers. P.
Resin-modified and Conventional Glass Ionomer Restorations in Primary Teeth: 8-Year Results
Journal of Dentistry 32(4), 285, 2004

R

Ray. N. H.
Inorganic Glasses as Ionic Polymers, in Chap. 8,
Ionic Polymers (Ed., L. Holliday),
Appl. Sci. Publishers, Ltd., London 1975

Rock. W. P.
The use of Ultraviolet Radiation in Dentistry
British Dental Journal, 136, 455, 1974

Rubbi. E, Baffa. O, Vinha. D, Camargo-Thome. L. H.
Rheological Studies of Photopolymerised Dental Composites
Dental materials 9, 361-364, 1993

Rueggeberg. F.
Contemporary Issues in Photocuring
Comp. Cont. Educ. Dent. 20(25), 4, 1999

S

Sakida. S, Hayakawa. S, Yoko. T.
^{125}Te, ^{27}Al and ^{71}Ga NMR Study of M_2O_3-TeO_2 (M=Al and Ga) Glasses
Journal of the American Ceramic Society 84(4), 836-42, 2001

Sarkar. N. K, El-Mallakh. B, Graves. R.
Silver Release from Metal Reinforced Glass Ionomers
Dental materials, 4(2), 103-104, 1988

Sasanaluckit. P, Albustany. K. R, Doherty. P. J, Williams. D. F.
Biocompatibility of Glass Ionomer Cements
Biomaterials 14(12), 906-16, 1993

Sato T.
Preparation of Aluminium Hydroxide by Reacting Sodium Aluminate Solutions with Mineral Acid
Journal of Chemical Technology and Biotechnology, 31, 670-675, 1981

Sato. T.
The Thermal Transformation of Gelatinous Aluminium Hydroxide
Zeitschrift für Anorganische und Allgemeine Chemie 391, 167-173, 1972

Schaller. T, Stebbins. J. F.
The Structural Role of Lanthanum and Yttrium in Aluminosilicate Glasses: A ^{27}Al and ^{17}O MAS NMR Study
Journal of Physical Chemistry B, 102(52):10690-97, 1998

Schmalz. G, Arenholt-Bindslev. D.
Biocompatibility of Dental Materials
Springer-Verlag Berlin Heidelberg, 2009

Schmitt. W, Purrmann. R, Jochum. P, Gasser. O.
Calcium Depleted Aluminium Fluorosilicate Glass Powder for use in Dental or Bone Cements
US Patent N^0: 4376835, 1983

Silikas. N, Watts. D. C.
Rheology of Urethane Dimethacrylate and Diluent Formulations.
Dental Materials 15, 257-261, 1999

Simmelink. J. W.
Oral Development and Histology
Thieme Medical Publishers Inc. New York, 1994

Simmons. J. J.
The Miracle Mixture – Glass Ionomer and Alloy Powder
Texas Dental Journal 1, 6-12, 1983

Singh. N. B, Rai. S, Singh. N.
Highly Reactive β-Dicalcium Silicate
Journal of the American Ceramic Society, 85(9), 2171-76, 2002

Skinner. E. W, Phillips. R. W
The Science of Dental Materials, 5th Edition
Philadelphia and London
W.B. Saunders Company

Smith. D. C.
A New Dental Cement
British Dental Journal 124, 381-384, 1968

Smith. S.
Development of Glass-Ionomer Cement Systems
Biomaterials 19(6), 467, 1998

Smitha. D. C.
Development of Glass-ionomer Cement Systems
Biomaterials 19(6), 467-478, 1998

Sourial. E, Peres. T, Capobianco. J. A, Speghini. A, Bettinelli. M.
A Structural Investigation of $Mg(PO_3)_2$, $Zn(PO_3)_2$ and $Pb(PO_3)_2$ Glasses using Molecular Dynamic Simulation
Physical Chemistry, Chemical Physics, 1, 2013-18, 1999

Stamboulis. A, Matsuya. S, Hill. R. G, Law. R. V, Udoh. K, Nakagawa. M. Matsuya. Y.
MAS-NMR Spectroscopy Studies in the Setting Reaction of Glass Ionomer Cements
Journal of Dentistry 34, 574-581, 2006

Stamboulis. A., Law. R. V, Hill. R. G.
Characterisation of Commercial Ionomer Glasses using Magic Angle Nuclear Magnetic Resonance (MAS-NMR)
Biomaterials 25, 3907–3913, 2004

Stebbins. J. F, Kroeker. S, Lee. S. K, Kiczenski. T. J.
Quantification of Five- and Six-coordinate Aluminium Ions in Aluminosilicate and Fluoride-containing Glasses by High Field, High Resolution ^{27}Al NMR.
Journal of Non-crystalline Solids 275, 1-6, 2000

Stebbins. J. F, Xu. Z.
NMR Evidence for Excess Non-bridging Oxygen in an Aluminosilicate Glass
Nature 390, 60-62, 1997

Stebbins. J. F, Zeng. Q.
Cation ordering at fluoride sites in silicate glasses: a high-resolution ^{19}F NMR Study.
Journal of Non-crystalline Solids 262, 1-5, 2000

Stebbins. J. F, Zhao. P, Lee. S. K, Oglesby. J. V.
Direct Observation of Multiple Oxygen Sites in Oxide Glasses: Recent Advances from Triple-Quantum Magic Angle Spinning Nuclear Magnetic Resonance
Journal of Non-crystalline Solids 293(295), 67-73, 2001

St-Georges. A. J, Swift. E .J, Thompson. J. Y, Heymann. H. O.
Irradiance Effects on the Mechanical Properties of Universal Hybrid and Flowable Hybrid Resin Composites
Dental Matterial 19(5), 406, 2003

Strauss. H, Heegn. H, Strienitz. I.
Effect of PAA Adsorption on Stability and Rheology of TiO_2 Dispersions
Chemical Engineering Science 48(2), 323-332, 1993

Suslick KS, Price GJ.
Application of Ultrasound to Materials Chemistry
Annual Review of Material Science, 29, 295 – 326, 1999

T

Takaishi. T, Jin. J, Uchino. T, Yoko. T.
Structural Study of $PbO\text{-}B_2O_3$ Glasses by X-ray Diffraction and ^{11}B MAS NMR Techniques
Journal of the American Ceramic Society, 83(10), 2543-48, 2000
Tanner. D. A, Rushe. N, Towler. M. R.
Ultrasonically set glass polyalkenoate cements for orthodontic applications
Journal Material Science 17, 313–318, 2006

Tanumiharja. M, Burrow. M, Tyas. M.
Micro-tensile Bond Strengths of Glass Ionomer (Polyalkenoate) Cements to Dentin using Four Conditioners
Journal of Dentistry 28(5), 361, 2000

Ten Cate. A.
Oral Histology: Development, Structure and Friction
Mosby, 1994

Tikhov. S. F, Fenelonov. V. B, Sadykov. V. A, Yu. V, Potapova. V, Salanov. A. N.
Porous Al_2O_3/Al Metal Ceramics Prepared by the Oxidation of Aluminum Powder under Hydrothermal Conditions Followed by Thermal Dehydration: I. Composition and Macrocharacteristics of Composites
Kinetics and Catalysis, 41(6), 826–834, 2000 (Translated from Kinetika Kataliz)

Tomlinson. S. K.
Dental Cements Based on Cyanoacrylates
PhD Thesis – University of Exeter (2007)

Tomlinson. S. K, Ghita. O. R, Hooper. R. M, Evans. K. E.
The use of Near-infrared Spectroscopy for the Cure Monitoring of an Ethyl Cyanoacrylate Adhesive
Vibrational Spectroscopy 40, 133–141, 2006

Toplis. M. J, Schaller. T.
A ^{31}P MAS NMR Study of Glasses in the System $xNa_2O–(1- x)Al_2O_3–2SiO_2–yP_2O_5$
Journal of Non-Crystalline Solids 224, 57–68, 1998
Towler. M. R, Bushby. A. J, Billington. R.W, Hill. R.G.
A Preliminary Comparison of the Mechanical Properties of Chemically Cured and Ultrasonically Cured Glass Ionomer Cements, using Nano-indentation Techniques
Biomaterials 22(11), 1401-1406, 2001

Towler MR, Crowley CM, Hill RG.
Investigation into the Ultrasonic Setting of Glass Ionomer Cements: Part I Postulated Modalities
Journal Material Science 22(7), 539–541, 2003

Twomey. E, Towler. M. R, Crowley. C. M, Doyle. J, Hampshire. S.
Investigation into the Ultrasonic Setting of Glass Ionomer Cements: Part II Setting Times and Compressive Strengths
Journal Material Science 39, 4631–4632, 2004

Tyas. M. J.
Clinical Performance of Glass-ionomer Cements
Journal of Applied Oral Science 14, 10-13, 2006

U

Uno. S, Finger. W, Fritz. U.
Long Term Mechanical Characteristics of Resin-modified Glass Ionomer Restorative Materials
Dental Material 12(1), 64, 1996

Unterbrink. G, Muessner. R.
Influence of Light Intensity on Two Restorative Systems
Journal of Dentistry 23, 183, 1995

V

Vallittu. P. K, Sevelius. C.
Resin-bonded, Glass Fiber-reinforced Composite Fixed Partial Dentures: A Clinical Study
The Journal of Prosthetic Dentistry 12, 413, 2000

Van Noort. R.
Dental Materials
Mosby, 1994

Venkataraman. B. H, Varma. K. B. R.
Structural and Optical Properties of $(100-\chi)(Li_2B_4O_7) - \chi(SrO\text{-}Bi_2O_3\text{-}0.7Nb_2O_5\text{-}0.3V_2O_5)$ Glasses and Glass Nanocrystal Composites
Optical Materials, 28, 1423-31, 2006

Vermilyea. S. G, Powers. J. M, Koran. A,
The Rrheological Properties of Fluid Denture-base Resins
Journal of Dental Research 57(2), 227-231, 1978

Versluis. A, Douglas. W, Cross. M, Sakaguchi. R.
Does an Incremental Filling Technique Reduce Polymerisation Shrinkage Stresses?
Journal of Dental Research 75(3), 871, 1996

W

Wang. L, D'Alpino. P, Lopes. L, Pereira. J.
Mechanical Properties of Dental Restorative Materials: Relative Contribution of Laboratory Tests
Journal of Applied Oral Science 11(3), 162-7, 2003

Wasson. E. A, Nicholson. J. W
New Aspects of the Setting of Glass-Ionomer Cements
Journal of Dental Research 72(2), 481-483, 1993

Wazer. J. R, Lyons. J. W, Kim. K. Y, Colwell. R. E.
Viscosity and Flow Measurements
Interscience Publishers, London. 1963

Wilder. A. D, May. K. N, Leinfelder. K. F.
Three Year Clinical Study of UV Cured Composite Resins in Posterior Teeth
Journal of Prosthetic Dentistry 50, 26, 1983

Williams. J, Billington. R, Pearson. G.
The Glass Ionomer Cement: The Sources of Soluble Fluoride
Biomaterials 23(10), 2002

Wilson. A. D
A Hard Decade's Work: Steps in the Invention of the Glass-lonomer Cement
Journal of Dental Research 75(10), 1723-1727, 1996

Wilson. A. D.
Resin-modified Glass-ionomer Cements
International Journal of Prosthodontics 3, 425, 1990

Wilson. A. D.
Dental Silicate Cements: VII. Alternative Liquid Cement Formers
Journal of Dental Research 47, 1133-1136, 1968

Wilson. A. D
Poly-vinylphosphonic Acid and Metal Oxide or Cermet or Glass Ionomer Cement
United States Patent: 5079277

Wilson. A. D.
Characterisation of Glass Ionomer Cements: 2 – Effect of Powder to Liquid Ratio on Physical Properties
Journal of Dentistry 4(6), 287-290, 1976

Wilson. A. D, Groffman. D. M, Powis. D. R, Scott. R. P.
A Study of the Variables Affecting the Imparting Jet Method for Measuring the Erosion of Dental Cements
The Journal of Prosthetic Dentistry 80(3), 280-301, 1998

Wilson. A. D, Hill. R. G, Warrens. C. P, Lewis. B. G.
The Influence of Polyacid Molecular Weight on Some Properties of Glass-ionomer Cements
Journal of Dental Research 68(2), 89-94, 1989

Wilson. A. D, Kent. B. E.
A New Translucent Cement for Dentistry. The Glass Ionomer Cement.
British Dental Journal 132, 133-135, 1972

Wilson. A. D, Kent. B. E, Clinton. D, Miller. R. P.
The Formation and Microstructure of Dental Silicate Cements
Journal of Material Science, 7, 220-238, 1972

Wilson. A. D, Nicholson. J. W.
Acid – Base Cements
Cambridge University Press, 1993

Wilson. A. D, Prosser. H. J.
A Survey of Inorganic and Polyelectrolyte Cements
British Dental Journal 157, 449-454, 1984

Wilson. A. D, Prosser. H. J, Crisp. S, Lewis. B. G, Merson. S. A.
Aluminosilicate Glasses for Polyelectrolyte Cements
Industrial and Engineering Chemical Research 19, 263, 1980

Wilson. M. A, Combe. E. C.
Effects of Glass Composition and Pre-treatment on the Reactivity of Novel Glass Polyalkenoate (Glass Ionomer) Dental Cements
Clinical Materials, 7, 15-21, 1991

Wood. D, Hill. R.
Glass Ceramic Approach to Controlling the Properties of a Glass Ionomer Cement
Biomaterial, 12, 164-170, 1991

Wright, J. A. Harron, R. Williams, P. A. Pass, G. Robb, I. D.
Exchange and competitive adsorption of polyelectrolytes on barium sulphate
Colloids and Surfaces, 24(2-3), 249-258, 1987

Wu. H. S, Jone. H. C, Hwang. J. W
Reaction of Polyacrylic Acid and Metal Oxides: Infrared Spectroscopic Kinetic Study and Solvent Effect
Journal of Applied Polymer Science 63, 89–101, 1997

X

Xie. D, Chung. I, Wu. W, Lemons. J, Puckett. A, Mays. J.
An Amino Acid-modified and Non-HEMA Containing Glass-ionomer Cement
Biomaterials 25(10), 1825-1830, 2004

Xie. W, Brantley. D, Culbertson. B, Wang. G.
Mechanical Properties and Microstructure of Glass Ionomer Cement
Dental Materials 16(2), 129, 2000

Y

Yan. Z, Sidhu. S. K, Carrick. T. E, McCabe. J. F
Response to Thermal Stimuli of Glass Ionomer Cements
Dental Materials 23(5), 597-600, 2007

Yap. A. U. J, Cheang. P. H. N, Chay. P. L.
Mechanical Properties of Two Restorative Reinforced Glass-ionomer Cements
Journal of Oral Rehabilitation 29(7), 682-8, 2002

Yli-Urpo. H, Vallittu. P. K, Narhi. T. O.
Release of Silica, Calcium, Phosphorus, and Fluoride from Glass Ionomer Cement Containing Bioactive Glass
Journal of Biomaterials Applications 19, 5-20, 2004

Young. A. M, Rafeeka. S. A, Howlett. J. A.
FTIR Investigation of Monomer Polymerisation and Polyacid Neutralisation Kinetics and Mechanisms in Various Aesthetic Dental Restorative Materials
Biomaterials 25, 823–833, 2004

Youngman. R. E, Dejneka. M. J.
NMR Studies of Fluorine in Aluminosilicate-Lanthanum Fluoride Glasses and Glass-ceramics
Journal American ceramic society, 85(5), 1077-82, 2002

Z

Zainuddina. N, Karpukhina. N, Hill. R. G, Law. R. V.
A Long-term Study on the Setting Reaction of Glass Ionomer Cements by ^{27}Al MAS-NMR Spectroscopy
Dental Materials 25(3), 290-295, 2009

Zhang. W, Nilsson. S.
Helix-Coil Transition of a Titrating Polyelectrolyte Analyzed within the Poisson-Boltzmann Cell Model - Effects of pH and Counterion Valency
Macromolecules 26 (2003), 2866-2870

Numerical

3M ESPE
http://solutions.3m.com/wps/portal/3M/en_US/3M-ESPE/dental-professionals/products/category/cement.
Accessed 25th April 2007 at 1709 hours

Appendices

Appendix 1

Materials

This appendix contains the procedure for the hand mixing of GICs and the full FETEM analysis of 1%, 3% and 9% coated TiO_2 particles including energy dispersive x-ray analysis (EDX).

1.1 Hand Mixed Cements

The cement is prepared by weighing out quantities of cement powder and liquid so that a ratio of 4:1, powder to liquid is maintained. Typical amounts of powder and liquid to make one aliquot of cement for clinical use are 0.2 ± 0.005g powder and 0.05 ± 0.005g liquid.

The cement was mixed mechanically by hand on a glass slab (20mm x 50mm x 100mm) using a dental spatula. The clinical procedure, as demonstrated by Doctor Gavin Pearson (University of Bristol Dental School, Fixed Prosthodontics Tutor), for correct mixing of GICs was as follows,

1. Weigh out 0.2 ± 0.005g of cement powder and 0.05 ± 0.005g of cement liquid and place on a glass mixing slab separately.
2. Mixing is initiated by introducing ½ of the cement powder to the cement liquid. A stop watch is initiated at this time.
3. The cement powder is mixed by applying pressure to the constituents in a shearing motion.
4. The remainder of the cement powder is included in small increments until the powder has been fully incorporated into the mixed cement.
5. At the point where thorough mixing is achieved the mixed cement should be sheared to form a thin layer across the glass slab to remove any air pockets.
6. The entire mixing process should take no longer than 60s for DC (cements should be mixed to manufacturers guidelines).

The mixed cement should posses,

- Putty like consistency
- Non-sticky to instruments
- Slight translucency

1.2 Transmission Electron Microscopy

1.2.1.1 Imaging

Bright field imaging was performed at a range of magnifications, up to high resolution (lattice fringe) magnifications (Figures A1, A3, A5, A6, A8). Due to the number of samples to be analysed, it was not possible to wait a significant amount of time for full thermal stability of the sample holder to be achieved, so a short exposure time was required for frames, which will consequently show more noise than with a longer exposure.
On higher Al content samples, a webbing-like structure could be seen around some samples. Due to the amorphous nature of the aluminium oxide, it is difficult to observe this layer against the background of the amorphous carbon film.

1.2.1.2 EDX Analysis (Presented in Chapter 3, Fig 3.6)

Al was found to be present in the samples, particularly associated with the edge in transmission view from area spectra analysis. This is consistent with an Al rich phase around the outside of the particles. However, in the 9% content samples, this Al phase was only around three times the detection limit. As such, it was not felt that EDX on the lower content samples would be productive.

1.2.1.3 HAADF

HAADF imaging (Figures A2, A4, A7, A9) revealed the presence of a darker layer around the particles, visible when one particle overlapped another. EDX area analysis of these regions indicates that they are relatively rich in Al, which along with the z-contrast effects strongly suggests that these layers are the Al rich layer expected.

1.2.1.4 Potential Artefacts

The samples showed (Figure A 1 & Figure A 2) some signs of charging under the beam, and some beam-induced carbon build up was observed, leading to an amorphous layer around the samples after being exposed to the beam for some time. No major structural changes to the samples were noticed during beam exposure.

The control sample did not disperse well in acetone, settling to the bottom of the vial shortly after ultrasonicating. Although some material was left in suspension to be picked up on the TEM grid, this may not be characteristic of the material as a whole.

1.2.2 FETEM Images

Uncoated base material (TiO_2)

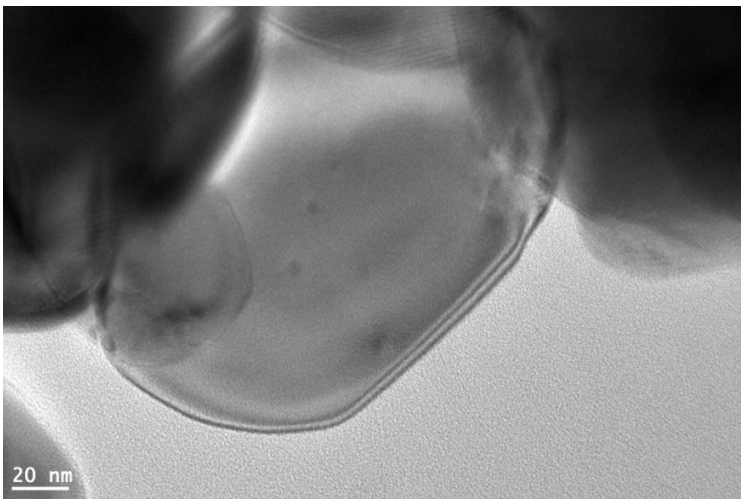

Figure A 1: Uncoated TiO_2 (100,000 x Magnification, Bright Field Image)

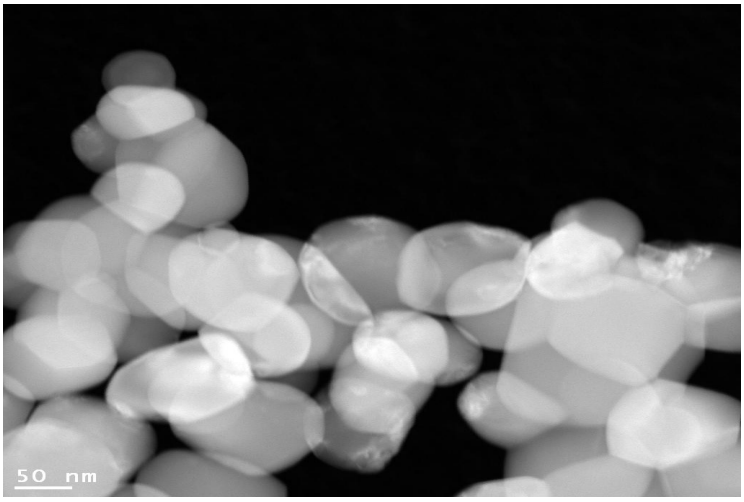

Figure A 2: Uncoated TiO2 (250,000 x Magnification, HAADF Image)

1% Coated TiO_2

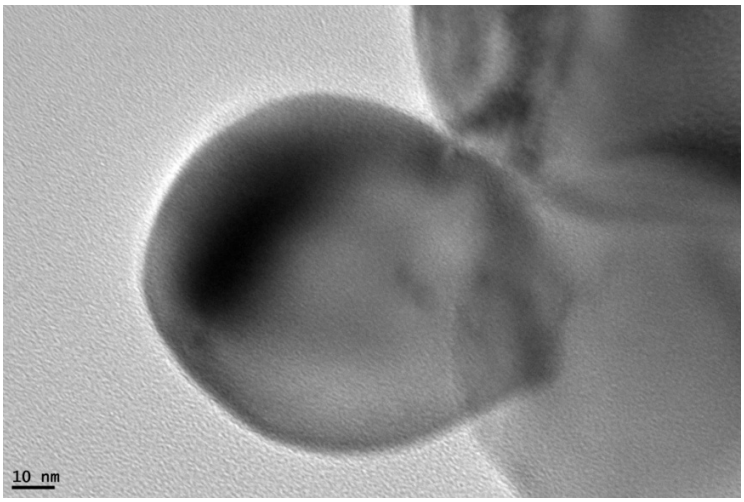

Figure A 3: 1% coated TiO_2 (150,000 x Magnification, Bright Field Image)

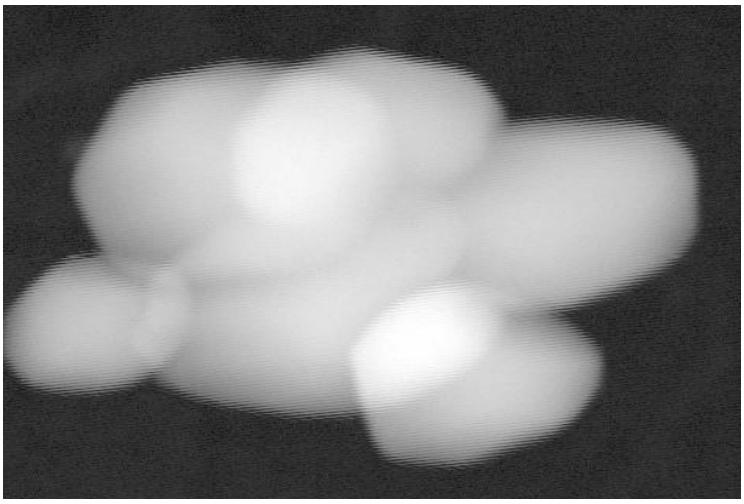

Figure A 4: 1% coated TiO2 (500,000 x Magnification, HAADF Image)

3% Coated TiO_2

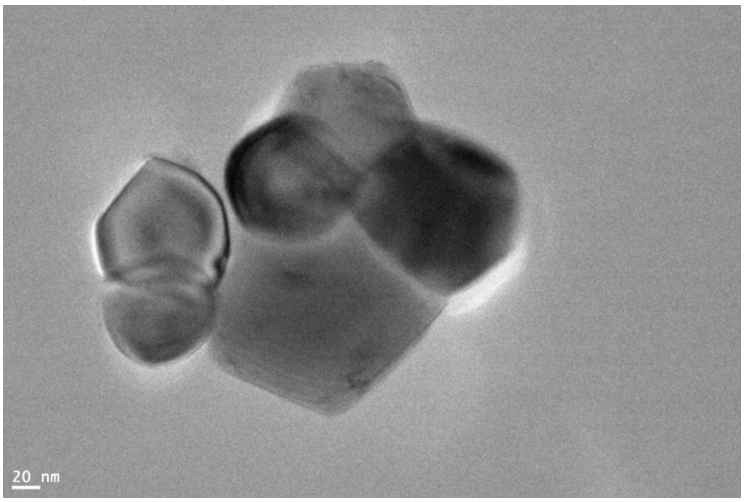

Figure A 5: 3% coated TiO_2 (50,000 x Magnification, Bright Field Image)

Figure A 6: 3% coated TiO_2 (250,000 x Magnification, Bright Field Image)

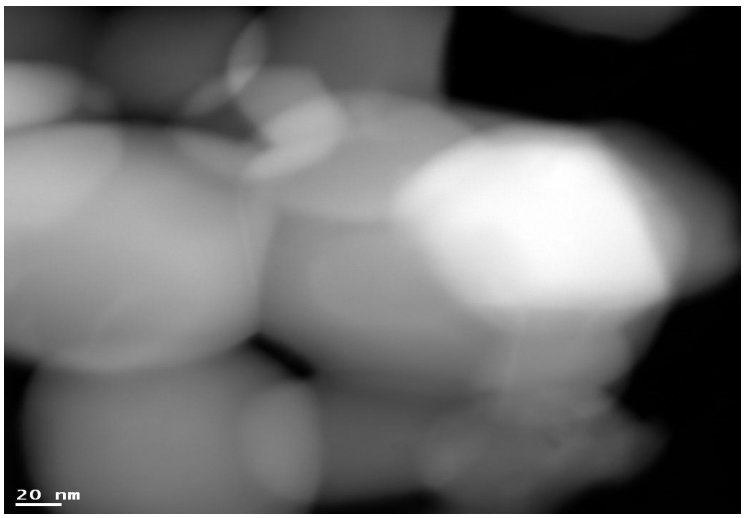

Figure A 7: 3% coated TiO_2 (500,000 x Magnification, HAADF Image)

9% Coated TiO_2

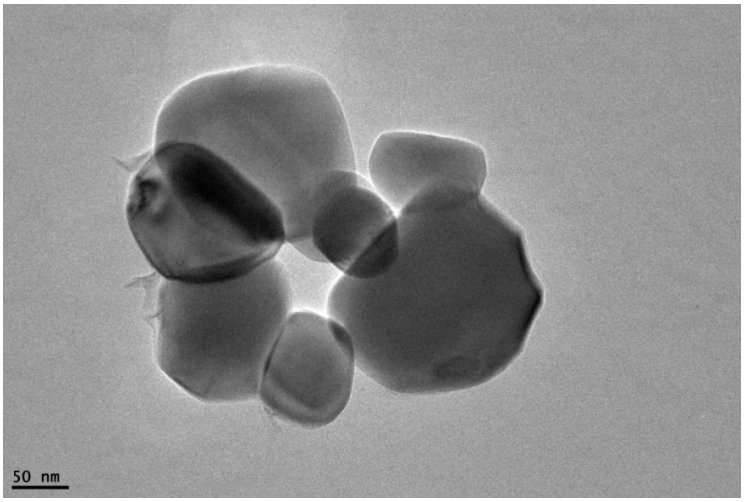

Figure A 8: 9% coated TiO_2 (40,000 x Magnification, Bright Field Image)

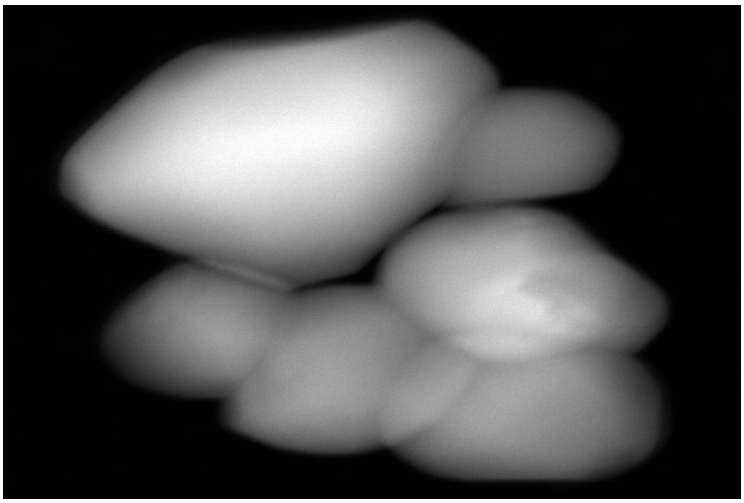

Figure A 9: 9% coated TiO_2 (400,000 x Magnification, HAADF Image)

Appendix 2

Rheology

2.1 Investigatory Experiments

2.1.1 Rheometer Plate Material

The standard material used to make the oscillating plates on the AR2000 rheometer is aluminium because it is a light weight material therefore reducing the inertia of the spinning plate making the system more sensitive to change. The Wilson rheometer uses serrated brass plates because of the high wear resistance (CRC press, 1999).

The AR2000 rheometer is unable to be used with serrated plates. This is because the parallel plate configuration (Figure A 10) makes calculation of standard material properties (e.g. elastic and plastic modulus, viscosity). This is because the AR2000 calculates the shear velocity from the edge of the plates (which is used for calculation of material properties); the instrument is unable to calculate the velocity at the edge of a serrated plate.

The best plate material to be used with a flat / non serrated face in conjunction with the AR2000 needed to be found.

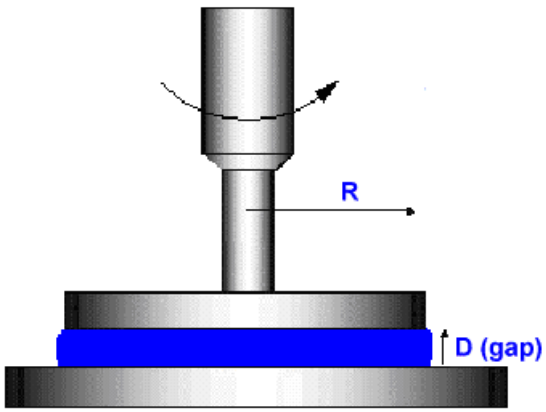

Figure A 10: Parallel Plate Configuration used with the AR2000 Rheometer.
R – Contact Surface Radius, D – Space Between Plates

Appendix 2: Rheology

Plates were fabricated as illustrated in Figure A 11 from both brass and aluminium. The dimensions used mimic the standard sized plates supplied with the AR2000 rheometer and the contact surface used with a Wilson rheometer.

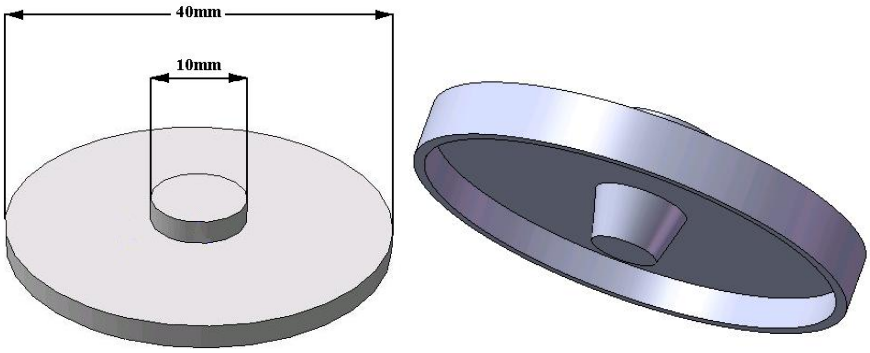

Figure A 11: Design of Fabricated Plates to be used with the AR2000 rheometer.

An applied shear stress of 1000 and 5000 Pascal's (Pa) was used with both the brass and aluminium plates. Hand mixed DC was used and the ETC was set to maintain a temperature of 20ºC using liquid nitrogen.

The applied shear stresses of 1000 Pa and 5000 Pa were chosen so that the strain response was not high enough to unfasten the cement from the rheometer plates.
Figure A 12 shows that the brass plates produce a higher strain and phase separation at the onset of experimentation than the aluminium plates. This observation is however more likely caused by a variation in room temperature when the cements were being prepared. Table A 1 shows that the room temperature during aluminium plate experimentation was 4ºC greater than the brass. The temperature greatly affects the rate of reaction as can be seen in Section 5.3.2; Table 4.1.

Disregarding any possible temperature effects, it is possible to see that the brass results become noisy around 1200 seconds as a result of plate slippage (plate inertia is accounted for in the instrument mapping process). If the brass plate results were super-positioned (set back by approximately 300 seconds) over the aluminium results the delta values would match and the strain values would only differ slightly in initial gradient.

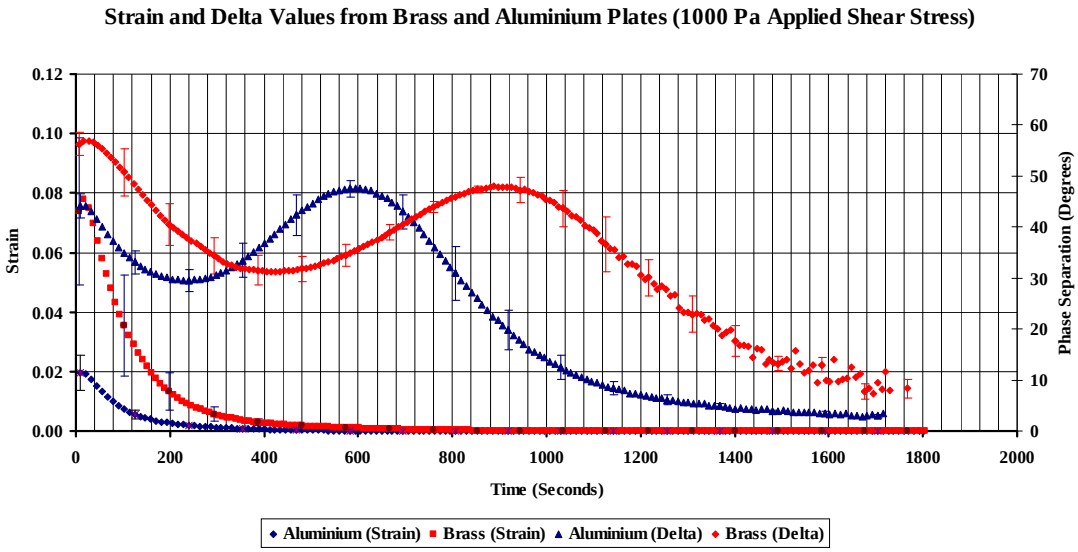

Figure A 12: Strain and Delta Values from Aluminium and Brass Plates (1000 Pa Applied Shear Stress)

Table A 1 shows that the samples prepared for testing at 1000 Pa will have a marked variatoin in the level of cure at experimental onset were as the samples prepared for the 5000 Pa tests will be directly comparable.

The temperature difference wasn't expected to have such a distinct affect on the results however the cement becoming unfastened from the brass plates before the aluminium is a temperature independent effect.

Room Temperature during Sample Preparation				
Applied Stress	1000 Pa		5000 Pa	
Plate Material	Aluminium	Brass	Aluminium	Brass
°C	22.80	20.60	24.60	24.10
	24.30	20.30	22.80	24.50
	24.40	20.40	24.50	24.90
Average	23.83	20.43	23.97	24.50
SD	0.90	0.15	1.01	0.40

Table A 1: Room Temperature during Sample Preparation

The results from the 5000 Pa applied stress test Figure A 13 vary only slightly, the brass plates produce a slightly higher strain than the aluminium plates at the beginning of data acquisition.

The standard deviation (SD) of the aluminium plate results are greater than the brass plates results which can be accounted for because of the difference between room temperatures during sample preparation (Table A 1). The brass plates produce a larger error in the phase separation results than aluminium after 600 seconds and the signal becomes increasingly noisy after 900 seconds; this is most likely due to the cement separating from the rheometer plates.

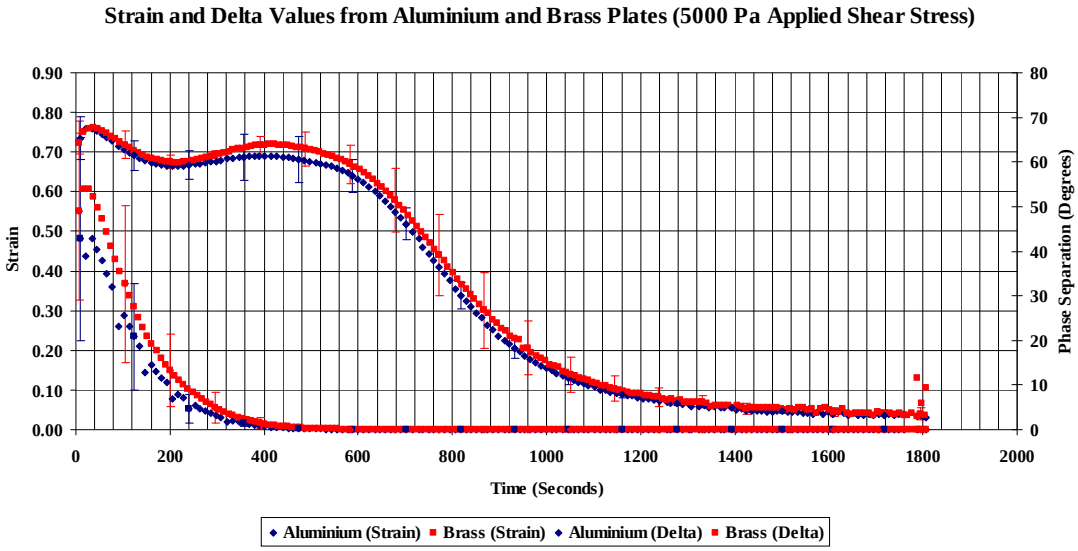

Figure A 13: Strain and Delta Values from Aluminium and Brass Plates (5000 Pa Applied Shear Stress)

The storage modulus (Figure A 14) shows that both the brass plate results are below the aluminium plate results. The storage modulus results from the 1000 Pa brass plates produce a noisier signal than the other stresses and plate materials. The setting profile of the cement remains constant (Figure A 14 and Figure A 15) so the resultant strain will dominate the storage modulus with lower values resulting in higher storage moduli. The sensitivity of the instrument is therefore interrelated with how well the cement bonds to the plates.

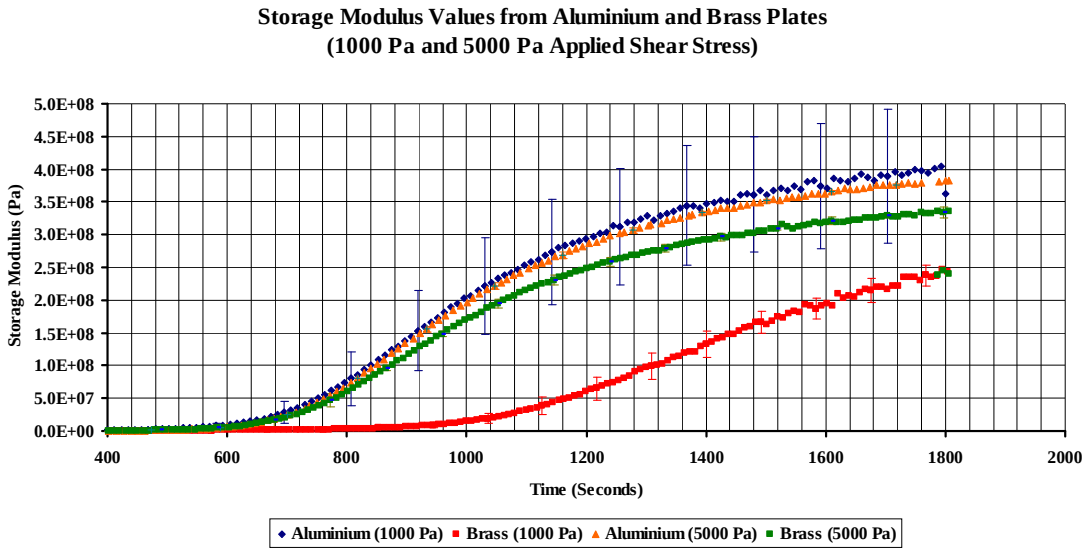

Figure A 14: Storage Moduli from Aluminium and Brass Plates over Time (1000 Pa and 5000 Pa Applied Shear Stress)

The loss modulus values in Figure A 15 show that the cement does not bond to the brass plates as well as aluminium.

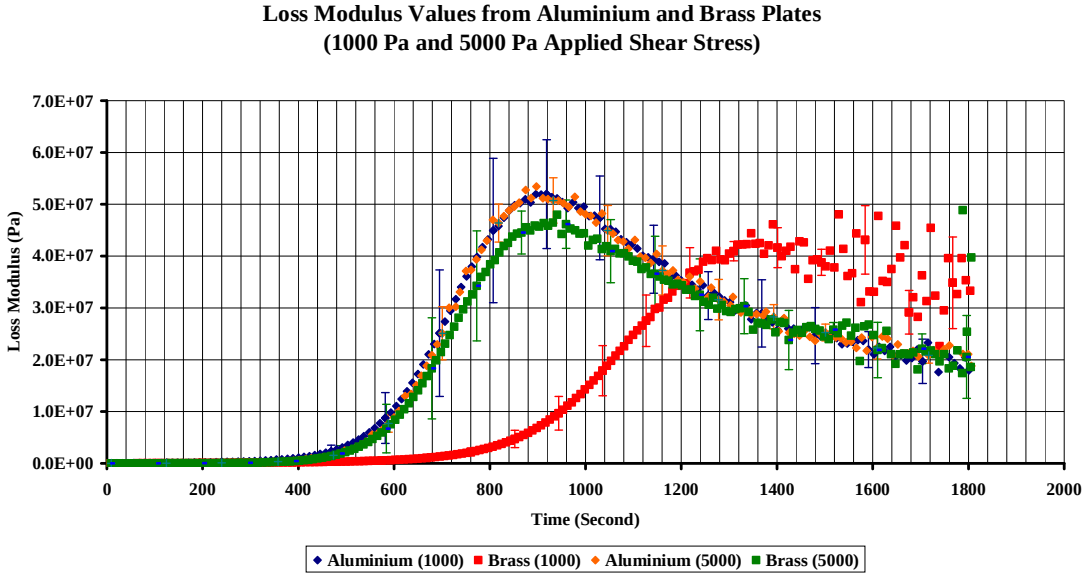

Figure A 15: Loss Moduli from Aluminium and Brass Plates over Time (1000 Pa and 5000 Pa Applied Shear Stress)

The aluminium plates produce higher moduli and less noisy results than the brass plates. This is due to a greater degree of bonding between the plate materials. The best choice plate material is therefore aluminium for use in conjunction with the AR2000 rheometer.

2.1.2 Applied Shear Stress

The results produced by an oscillating rheometer are directly related to the applied torque and angular frequency. The frequency remained constant throughout experimentation therefore the best applied shear stress to use without damaging the internal structure of the cement needs to be found.
A range of applied shear stresses were used in conjunction with Hand Mixed DC. The stresses were 1000 Pa, 2000 Pa, 3000 Pa, 5000 Pa, 10000 Pa, 15000 Pa, 17500 Pa, 19000 Pa, 20000 and 25000 Pa.

The larger shear stresses produce % strain values over 100 (Table A 2) so the rheometer completes over one rotation, twisting and damaging the structure of the cement. The two largest values had large erroneous results caused by the cement separating across its diameter.

Shear Stress	% Strain
1,000	0.98
2,000	8.70
3,000	11.26
5,000	20.69
10,000	124.04
15,000	134.60
17,500	163.22
20,000	252.10
25,000	607.36

Table A 2: Maximum Strain at the onset of Experimentation

Applied stresses greater than 10,000 Pa are not considered because of the large strain likely causing damage to cement network.

The results from experiments with an applied stress of 1 KPa, 2 KPa, 3 KPa and 5 KPa follow an inverse trend with the strain response. The largest strain is produced by the greatest force and vice versa (**Error! Reference source not found.**).

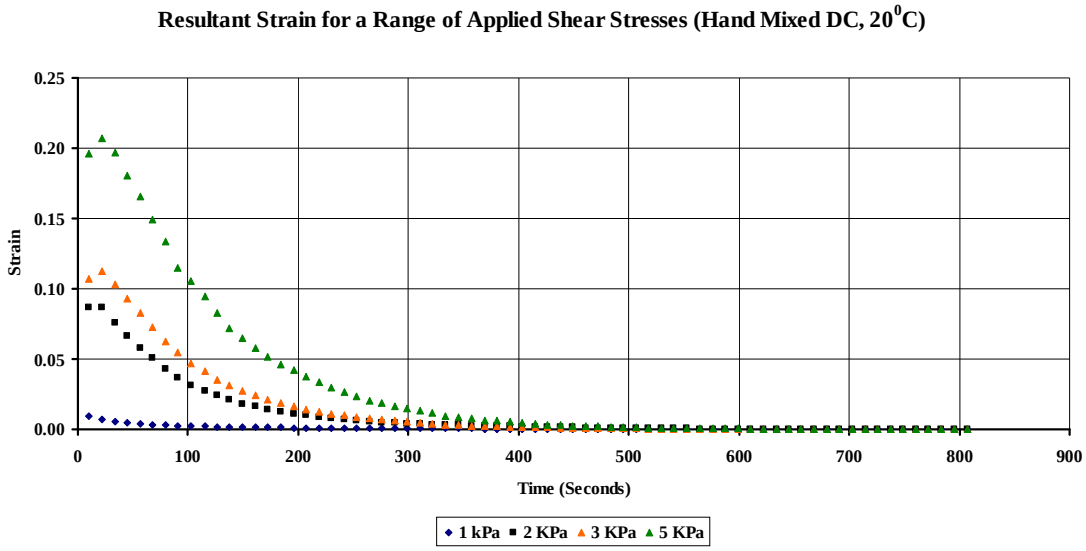

Figure A 16: Strain Response from an Applied Oscillating Stress of 1000, 2000, 3000 and 5000 Pa

The phase separation (Figure A 17) from the chosen applied stresses show that applied stresses above 3,000 Pa start to reduce sensitivity as can be seen by the loss of the periodic increase in the phase separation. The value of the phase separation is proportional to the apply shear stress.

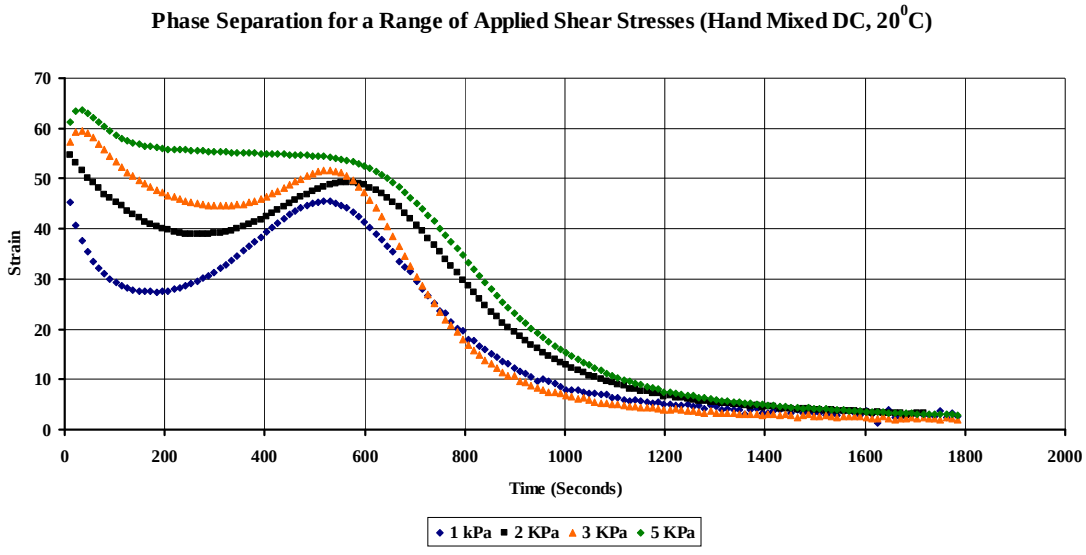

Figure A 17: Phase Separation for a Range of Applied Shear Stresses (Hand Mixed DC, 20°C)

The storage modulus shows that the applied stress has an effect on the setting profile of the storage modulus (Figure A 18). The storage modulus is related to the strain by Equation 1 herefore the maximum value should follow 5,000 to 1,000 because once the strain magnitude and phase separation equate the G' values will rely solely on the applied stress. The onset of the G' (500 – 800 seconds) is also dominated by the strain which will be dependent on the applied shear stress because the lager force will displace the same viscosity cement a greater amount and therefore have a lower G'. The middle of Figure A 18 (800 -1400) shows that the more force applied to the system the greater the rate of increase in G' which is related to the strain as can be seen in Equation 1.

$$G' = \frac{\sigma_0}{\gamma_0}\cos\delta \qquad \textbf{Equation 1}$$

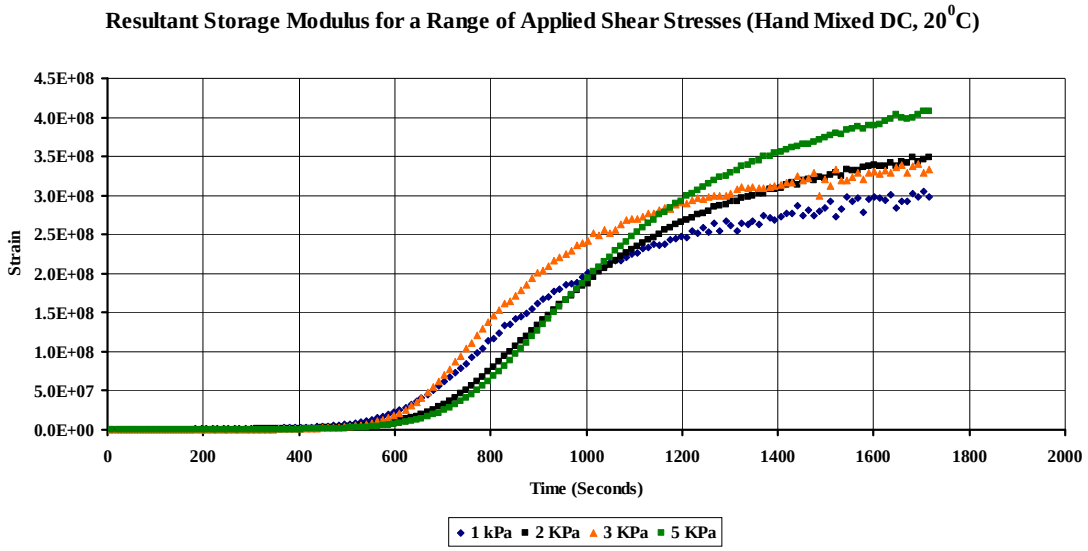

Figure A 18: Storage Modulus Produced from a Range of Applied Oscillatory Stresses

The loss modulus (**Error! Reference source not found.**) shows that there is a marked difference between the 1000, 2000, 3000 Pa results when compared to the 5000 Pa results. The height of the peak in the G'' is the point where the cement is able to dissipate the most energy and is therefore related to the amount of energy being put into the system. Interestingly the 5000 Pa trace has its peak almost 200 seconds after all the other applied stresses.

Appendix 2: Rheology

This separation is also seen in the mid section of the storage modulus and phase separation; a rapid increase is observed in the G', strain and δ values and can only be explained by the increased force sharpening the snap set characteristics of the cement. The 2000 and 3000 Pa results are both almost identical and these plus the 1000 Pa values all have their G'' peaks around 770 seconds unlike the 5000 Pa values (900 seconds). The 1000 Pa values are lesser than that of the others caused by much lower strain values than the others in the series (Figure A 19

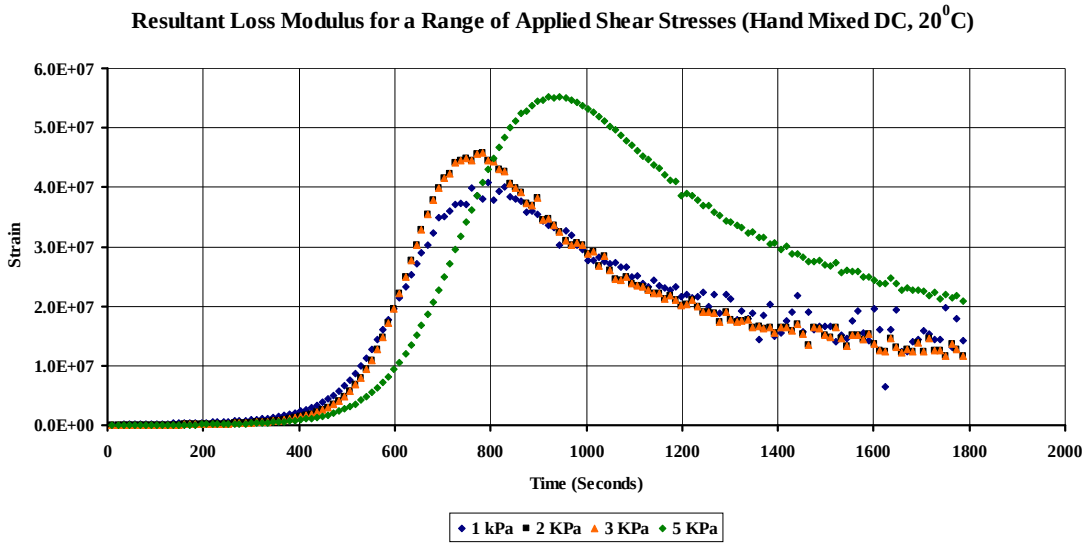

Figure A 19: Loss Modulus Produced from a Range of Applied Oscillatory Stresses

It is therefore apparent that the choice of what applied shear stress should be chosen is going to be a choice between signal strength (5000 Pa) and sensitivity (1000 Pa). The 1000 Pa stress produces to weak a signal and the 5000 Pa is exaggerating the snap set characteristic disproportionally to the other applied forces. The choice is therefore between 2000 and 3000 Pa; the decision was made to use 2000 Pa because of the increased sensitivity over the 3000 Pa and a slower rate of increase caused as a result of higher applied forces.

2.2 Advanced Rheometer Inconsistency

Initial experimentation using hand mixed DC generated results that were inconsitent. Figure A 20 and Figure A 21 show the storage and loss modulus of DC hand mixed cement respectively. These inconstancies were unexpected as the cements were all mixed in the same manor and experimentation began at the same time relative to the beginning of cement mixing.

The rapid rate of cure (increasing viscosity) prevented the gel point[2] and any other unexpected (*see* Chapter 6) results from being observed.

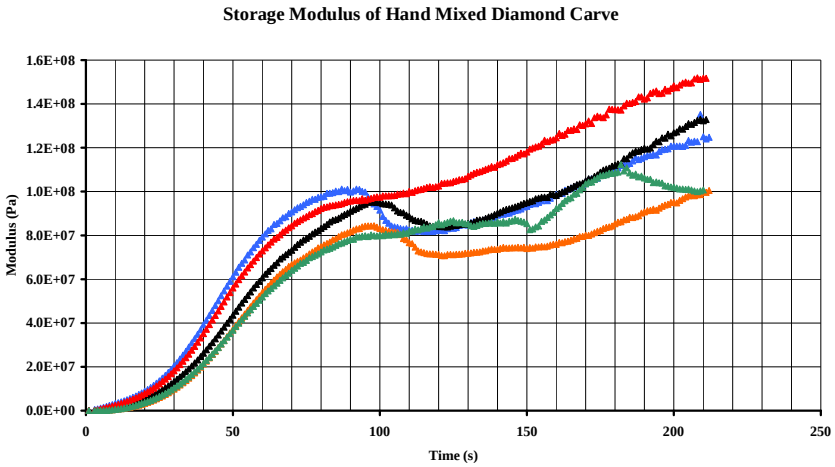

Figure A 20: Storage Moduli Obtained from Five Repeats of Hand Mixed DC (20°C, 2MPa Applied Shear Stress)

[2] The gel point can be found on a rheogram plot of storage moduli and loss moduli against time. The point where the loss moduli value becomes less than the storage moduli (intersection of the two plot lines) is considered the gel point. The significance of the gel point is as a time dependent measure of when the cement stops being viscous dominated and become elastically dominated.

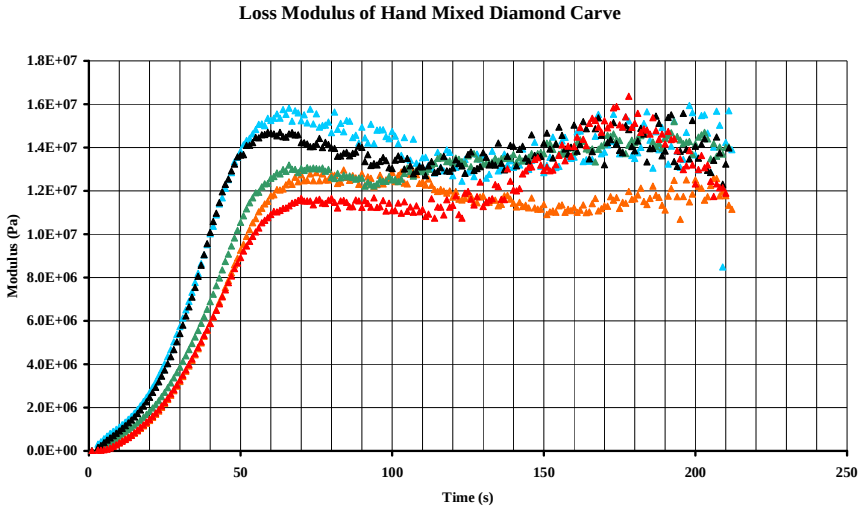

Figure A 21: Loss Moduli Obtained from Five Repeats of Hand Mixed DC (20ºC, 2MPa Applied Shear Stress)

A method was needed to slow the onset of the reaction during the early stages of cure so that the gel point could be identified and inconsistencies in the produced data could be surpressed.

2.3 Reaction Retardation

Two attempts were made to slow the reaction rate,

(i) Chemical Retardation
(ii) Temperature Retardation

Glass ionomers contain tartaric acid (TA) which is included to introduce the property of a snap set. This property can be seen by comparing two examples; A Wilson Rheogram, one with TA and one without is shown in Figure A 22. DC has approximately 2.5% TA inclusion to provide the snap set property.

Appendix 2: Rheology

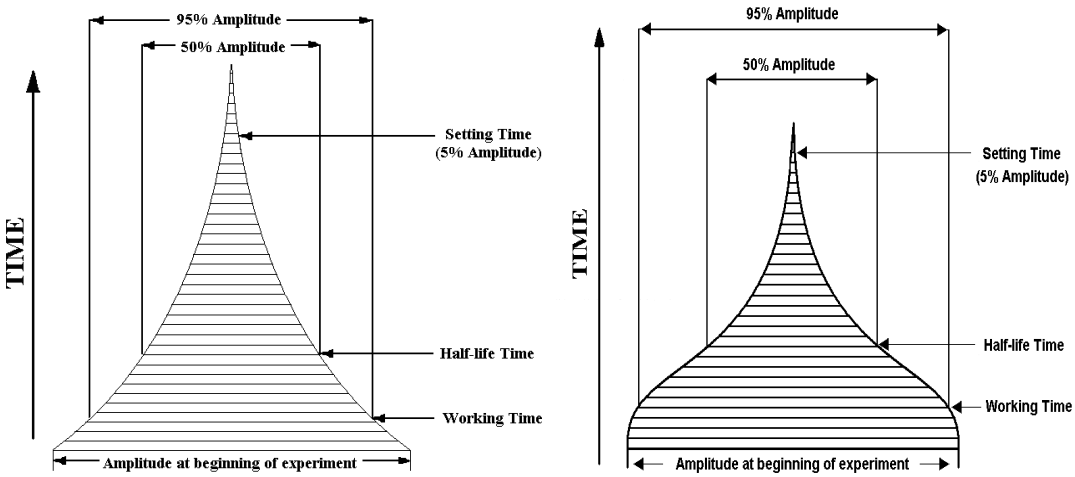

Figure A 22: Example of the Wilson Rheogram Obtained for a GIC without (Left) and with (Right) Tartaric Acid

The rheogram without tartaric acid has a continuous rapid increase in viscosity until the amplitude of the signal tends to zero. The rheogram with tartaric acid has had its working time elongated followed by a rapid increase in viscosity. The snap set property is vital to the commercial usefulness of GICs otherwise the cement would set to rapidly.

Using TA as a chemical retardant to offset the rapid initial increase in viscosity would allow time for the rheometer to be closed and data acquisition begun. Incorporation of 5% w/w and 10% w/w addition tartaric acid was included in the original control material.

This has had the effect of elongating the onset of reaction by approximately 400 seconds per 5% increase in TA.Figure A 23, Figure A 24 and Figure A 26 illustrate the differences between the increased TA percentage cements and the control (Averages).

Table A 3 shows the amount of glass powder and polyelectrolyte liquid used to form the sample cement. The gel point, room temperature (RT), mixing plate temperature (PT), relative humidity (RH) and dew points (DP) are given to show the variation between samples and experimental conditions. All experiments were run with an oscillation frequency of 0.1667Hz and an applied oscillation stress of 2KPa. The ETC was maintained at 20ºC for non-chilled experiments and 15ºC for chilled.

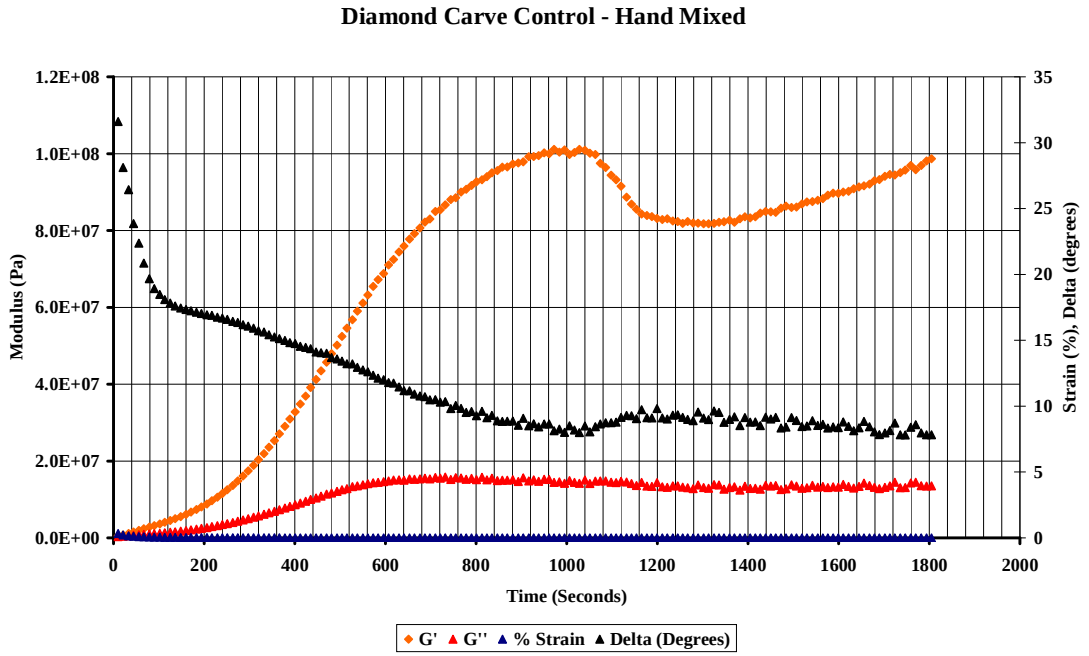

Figure A 23: Hand Mixed Diamond Carve - Mixed at Room Temperature (24.32 ± 0.13ºC)

No gel point was present in the control material because the cement will have proceeded past this point and the recorded data started with the cement being elastically dominated. It can be seen from the phase separation at the beginning of the acquisition (32º) that the cement was viscoelastic and closer to being an elastic solid (0º) than a Newtonian fluid (<90º). The % strain value begins at 0.3% so the amount of oscillatory movement (strain) is very minimal. The signal is noisy and the traces are not smooth likeFigure A 24 and Figure A 25. The dip in storage modulus at ≈1040 seconds is caused by an increase in strain and phase separation translating as a decrease in viscosity. This decrease in viscosity has not been reported and cannot be directly related to the setting mechanism (Hill & Wilson, 1988; Nicholson *et al*, 1988; Wilson & Nicholson, 1993; Stamboulis *et al*, 2006 and Zainuddin. N, 2008; *see* Chapter 2) until further in vitro tests have been performed (*see* Chapter 6).

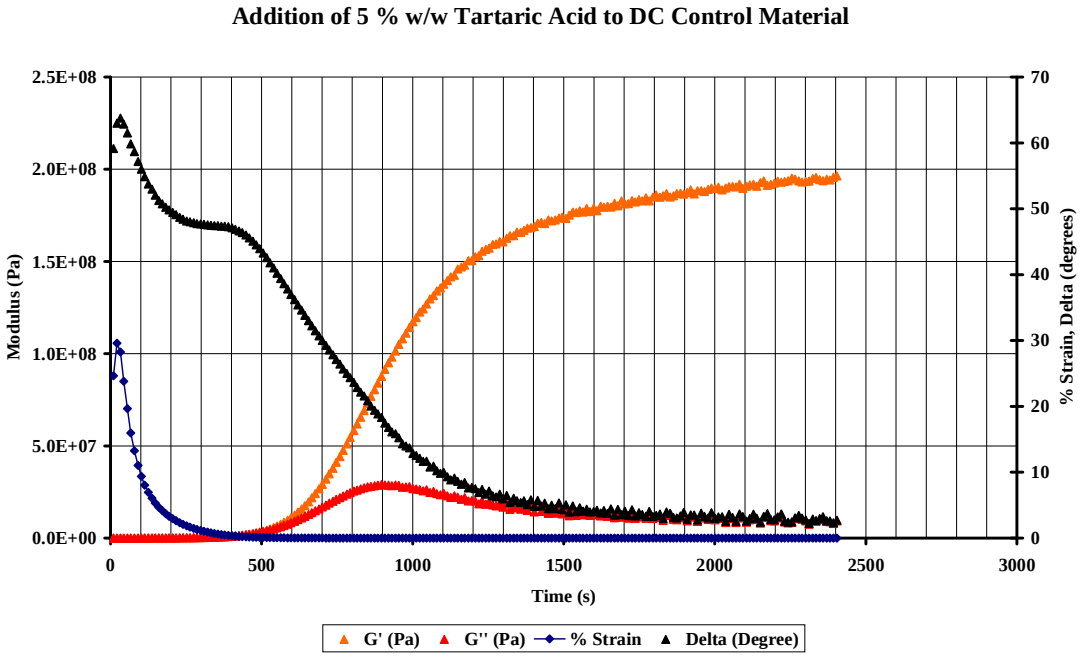

Figure A 24: Hand Mixed Diamond Carve with 5% w/w Additional TA - Mixed at Room Temperature (24.64 ± 0.34ºC)

The phase separation begins (peak) at 64º which is double the maximum phase separation of the control material (32º). The maximum strain at the beginning of experimentation was 43%. The cement was a factor of ten less viscous in the 5% w/w addition cement when compared to DC (Table A 4). The phase separation has a period (240 - 448 s) where the phase separation flattens identifying an area of maintained fluid like characteristic of the cement although this levelling is not mimicked by the strain (Figure A 25) indicating that the cement was still increasing in viscosity (setting). No influence is seen in the G' due to the subtle nature of the phase separation compared to the large influence from the decreasing strain in the complex modulus.

The complex viscosity modulus (η^*) is calculated by dividing the oscillation stress σ_0 by the oscillatory strain response (γ_0) multiplied by the oscillation frequency (ω).

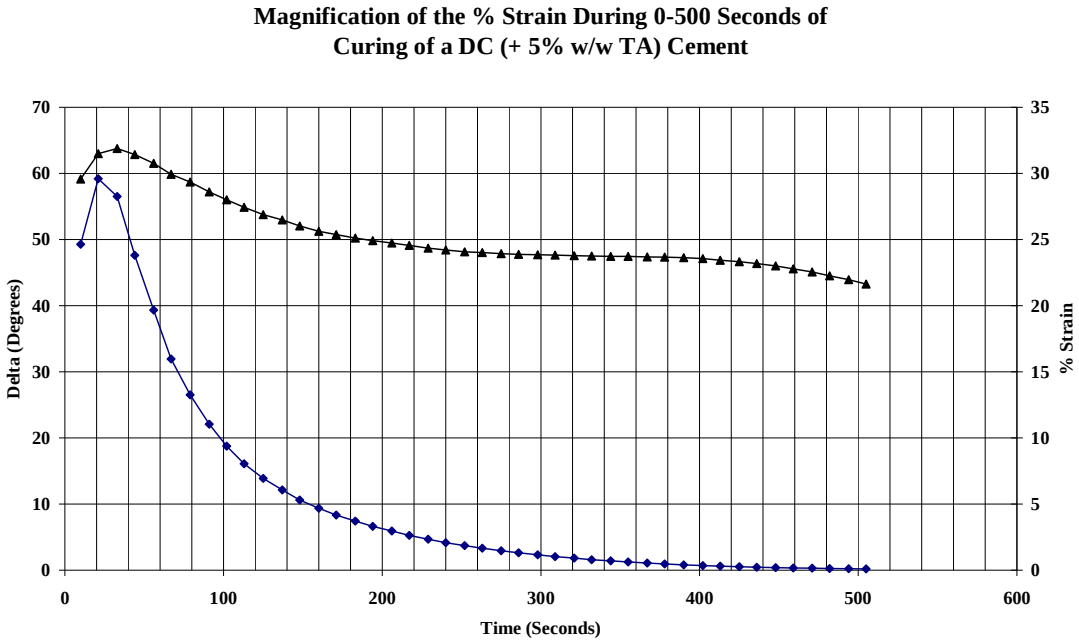

Figure A 25: % Strain and Phase Separation (Degrees) of DC (+ 5% w/w TA) Whilst Curing (0-500 Second Zoom)

This periodic levelling in the phase separation (Figure A 25) is not observed in the storage or loss modului because the cosine of the small phase separation change does not have a significant effect on the large complex modulus which changes with respect to strain.

The addition of 5% w/w additional tartaric acid has delayed the onset of the storage and loss moduli by approximately 400 seconds. The additional TA has affected the maximum value (Pa) that the storage and loss moduli attain within the experimental time scale. The peak in loss modulus is representative of the strength (Goodwin and Hughes, 2000) of the material however; given how the cement will be used (compression) the storage moduli may give a better indication of the compressive strength. The additional TA has therefore produced a cement with an increased compressive strength within the first 30 minutes of reaction compared to the control material.

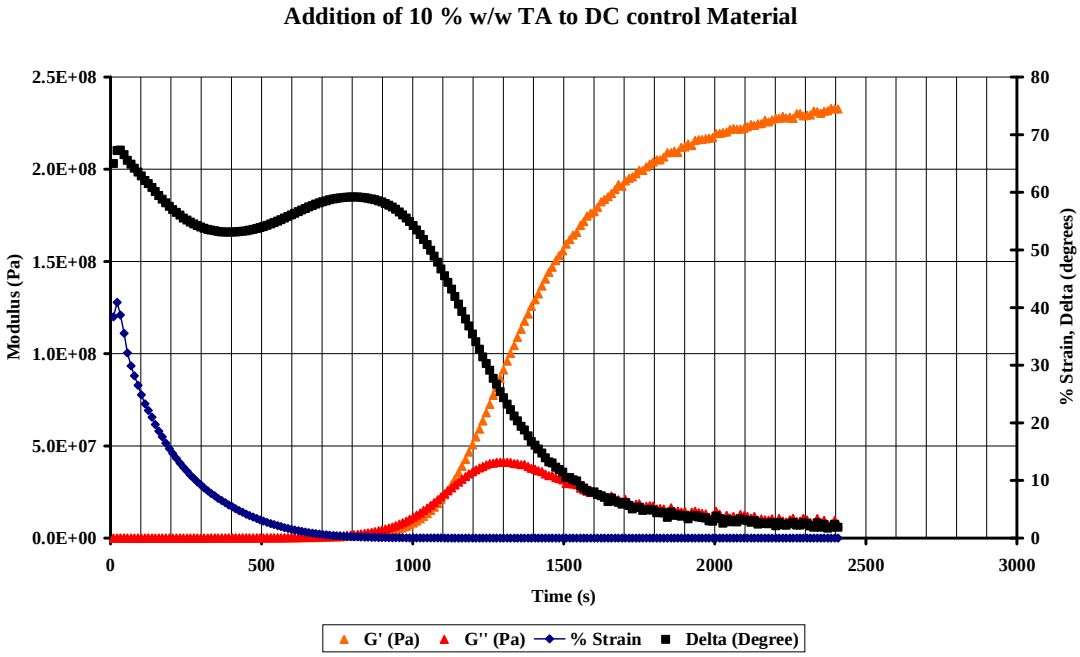

Figure A 26: Hand Mixed Diamond Carve with 10% w/w Additional TA - Mixed at Room Temperature (24.36 ± 0.16ºC)

The affect of 10% w/w TA addition to DC has caused the onset of cure to be delayed by 800 seconds. The cement is less viscous than both the control material and the 5% w/w cement with a % strain and phase separation of 40% and 67º respectively. The plateu seen in the phase separation of the 5% w/w cement has become more pronounced in the 10% w/w cements. The strain continues to decrease as in the 5% w/w cement although the phase separation increases identifying a move away from elastic behaviour. This behaviour is clearly related to the chemical effect of TA and therefore must relate to the replacement of the weak Tartrate salts formed with calcium and aluminium (Crisp & Wilson, 1976) by stronger polyacrylic salts formed at higher pH's. This periodic increase in delta last approximately twice as long as in the 5% w/w addition cement which supports the increase being due to TA content.

The TA has been reported to decrease apparent viscosity at the onset of reaction (Cook, 1983a, b; Hill & Wilson, 1988; Crisp & Wilson, 1976 and Wilson *et al*, 1976) dependent on the inclusion amount.

Appendix 2: Rheology

The phase separation increase / plateau, storage modulus periodic decrease loss and increased storage and loss moduli values prompted the abandonment of chemically retarding the setting reaction because it was apparent that the data was no longer characteristic of the base material. The decision to move away from chemically retarding the reaction rate lead to the use of a chilled mixing slab.

Figure A 27 shows the average results from DC mixed on a cooled glass block. Table A 3 shows the mixing variable for cements prepared using a chilled block. Particular attention should be drawn to the MPT and DP temperatures. The ETC was maintained at 15ºC during experimentation.

The affect of mixing the cement on a cool glass block has reduced the onset of cure by approximately 400 seconds; a similar effect as 5% TA addition. The starting strain and phase separation have peaks at 29 % and 68º respectively. The viscosity (Table A 4) at the beginning of experimentation is fifteen times less viscous than DC mixed at room temperature. The shape of the storage modulus has regained the periodic decrease as seen in the room temperature sample but not in the +TA cements. There is no pronounced peak in the loss modulus as is seen in the +TA cements. There is a small disturbance in the phase separation response; this is likely the case for room temperature DC but the experiment proceeds with such speed that it is not seen.

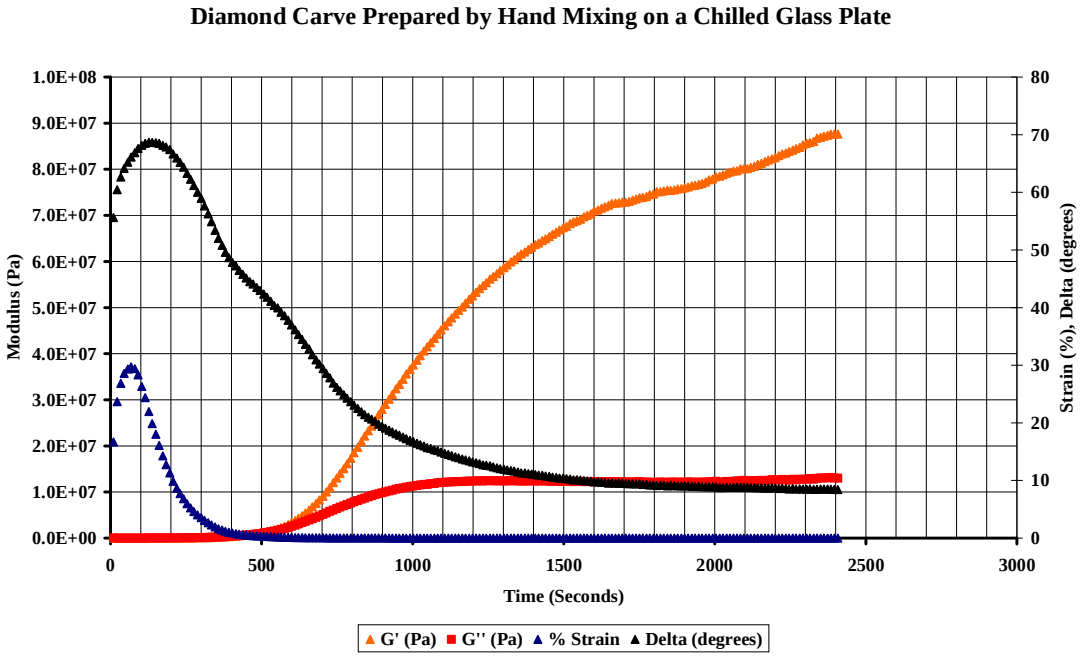

Figure A 27: Diamond Carve Prepared by Hand Mixing on a Chilled Glass Plate

The cements mixed on a chilled plate are characteristic of DC although repeatability between samples remains a problem. The cool mixing block method is also flawed, Table A 3 shows that the dew point is only fractionally below the temperature of the glass block used to prepare the cements. The glass plate was cooled by refrigeration for 30 minutes before experimentation and the temperature was taken using a thermocouple stuck to the surface of the slab. It was found that condensation was forming during mixing was subsequently mixed into the cement leading to the variation in gel point standard deviation.

Appendix 2: Rheology

Mixing Variables for DC and Cements Prepared with Additional Tartaric Acid								
Material	**Powder (g)**	**Tartaric Acid (g)**	**PVPA -PAA (g)**	**RT (^{0}C)**	**MPT (^{0}C)**	**RH (%)**	**DP (^{0}C)**	**Gel Point (s)**
Diamond Carve (DC)	0.2001	N/A	0.0501	24.32	24.72	N/A	N/A	N/A
SD	0.0001	N/A	0.0001	0.13	0.28	N/A	N/A	N/A
DC (Cooled Plate)	0.2000	N/A	0.0501	24.1	10.92	41.78	10.32	444
SD	0.0000	N/A	0.0001	0.22	0.46	0.40	0.26	65
DC (+ 5% TA)	0.2001	0.0125	0.0500	24.64	25.24	N/A	N/A	375
SD	0.0001	0.0000	0.0001	0.83	0.34	N/A	N/A	213
DC (+ 10% TA)	0.2000	0.0249	0.0501	24.36	25.50	N/A	N/A	1101
SD	0.0000	0.0000	0.0001	0.16	0.54	N/A	N/A	18

Table A 3: Mixing Variables for DC and Cements Prepared with Additional Tartaric Acid (Room Temperature, RT; Mixing Plate Temperature, MPT; Relative Humidity, RH; Dew Point, DP)

The gel points from Table A 3 can be used to follow the extent of retardation and the repeatability of the method. The inclusion of TA produced an exaggerated intermediate phase separation plateau and the 5% w/w inclusion produced a very large standard deviation (56% SD). It was concluded that the +TA cements were not representative of the DC control material so therefore should not be used. The cooled mixing block method produced results representative of the control material although a 15% standard deviation was still produced and was believed to be a result of condensation formation and subsequent inclusion in the sample cement.

Sample	% Strain	Average |n*| (Pa.s)
Diamond Carve	1.98	16068
DC (Chilled Plate)	29.72	1071
DC (+ 5% w/w)	18.85	1688
DC (+ 10% w/w)	36.51	872

Table A 4: Complex Viscosity at Maximum Strain

The best method for reducing the initial viscosity is therefore the use of a cooled mixing block as this produced an initial viscosity 15 times less than the initial viscosity of DC mixed at room temperature (Table A 4). There is however still a relatively large repeatability problem with this method (Figure A 28).

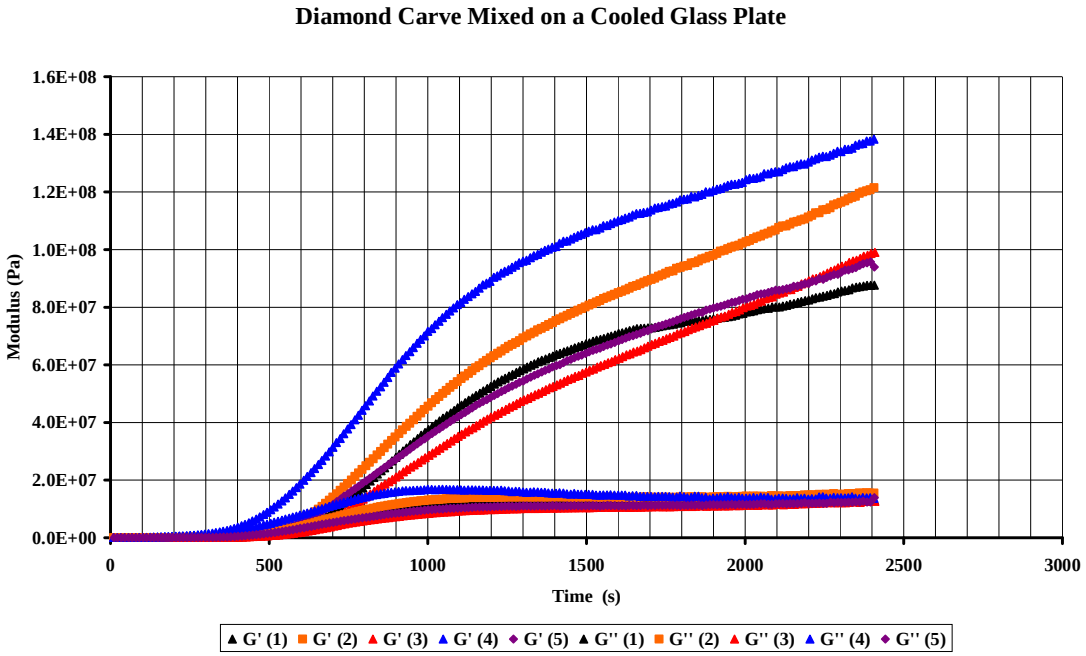

Figure A 28: Storage and Loss Moduli for Five Repeats of Diamond Carve Mixed on a Cooled Glass Plate

2.4 Capsulated Cements

The use of encapsulated Diamond Carve produced much more repeatable results (Figure A 29) The gel point was unable to be found using these experimental conditions. The capsules were refrigerated in an attempt to lower the reaction rate further however longer mixing times were required to fully mix the cement and the final formed cement was the same temperature as the capsules mixed from room temperature. The ETC was held at 15ºC to avoid the formation of condensation on the rheometer plates (Moses *et al*, 1967). Using encapsulated DC with the ETC held at 15ºC gives the most representative characterisation of the control material with the highest repeatability between samples.

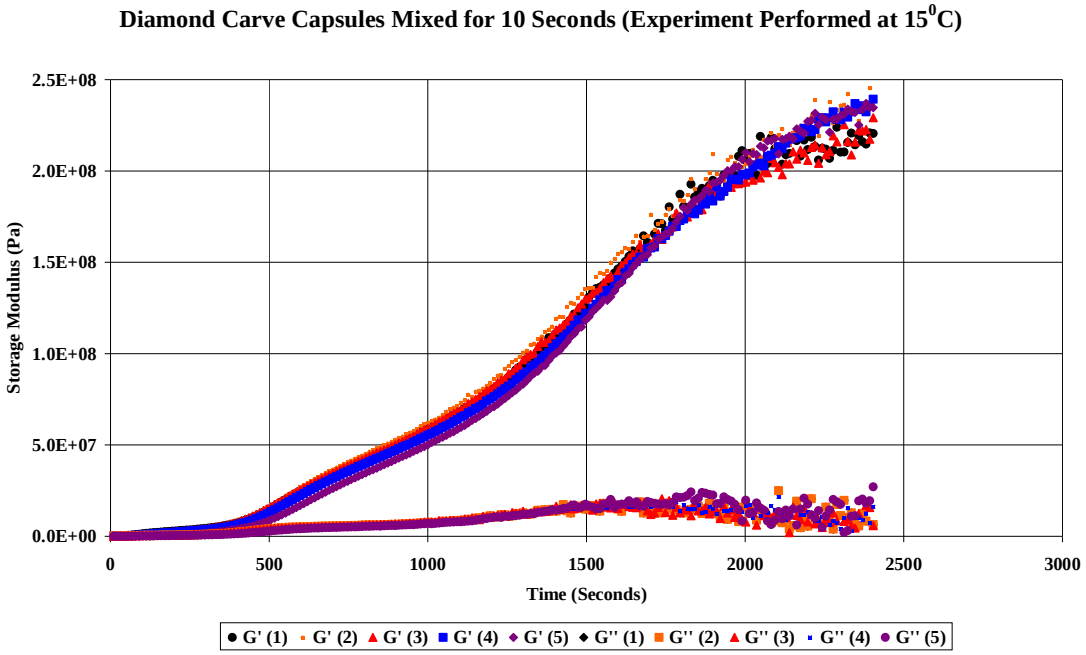

Figure A 29: Encapsulated Diamond Carve Mixed for 10 Seconds at 3280 RPM. Experiment was Performed at 15ºC using the ETC

The data is subtly different from hand mixed cements; both the storage and loss modulus have periods of rapid increase unseen in the hand mixed cements (Figure A 30 and Figure A 31). The linear period between 400-1200 seconds in the storage is caused by the rate of viscosity increase, decreasing during this period. The factor cos δ (real part of modulus) has little affect on the storage modulus. Cos δ starts at 0.95 (400 seconds) and rises to 0.99 approximately 400 seconds latter and maintains at this value for the rest of the acquisition.

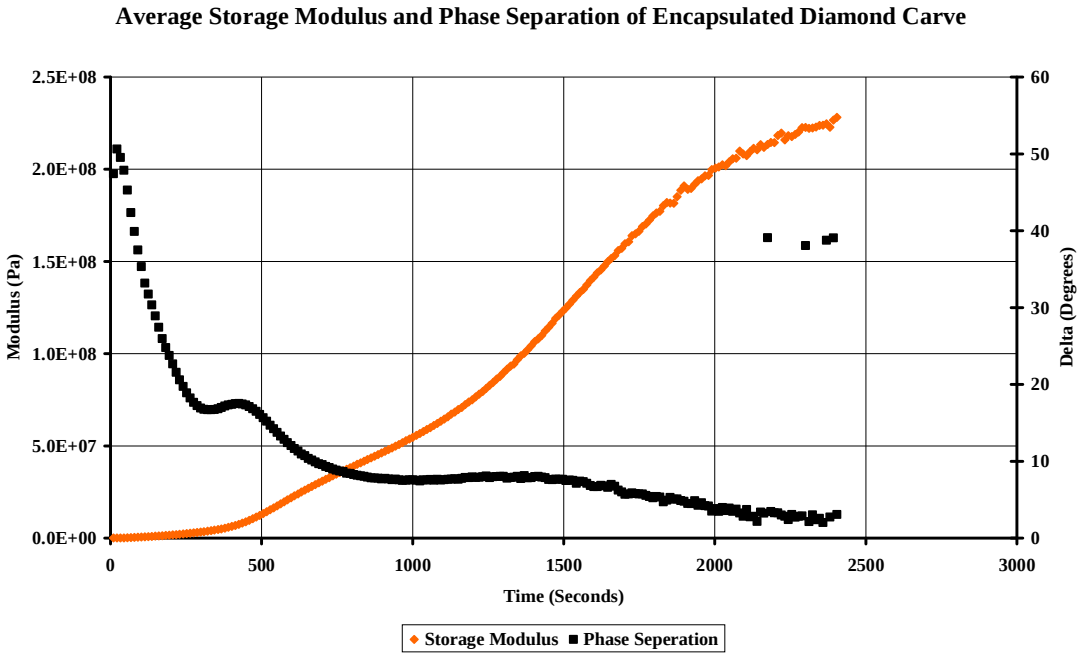

Figure A 30: Storage Modulus and Phase Separation of Encapsulated DC

The increase in the loss modulus around 400 -900 is not observed in the hand mixed cement. The cause of this increase is due to the slowing of the complex modulus during this period and the sin δ factor. The sin δ factor has a large impact on the loss modulus, the values follow the trend in the phase separation results and range from 0.31 to 0.18 with a peak around 0.30. this has the effect of driving the data around the peak in the phase separation peak down highlighting the periodic increase in viscous character.

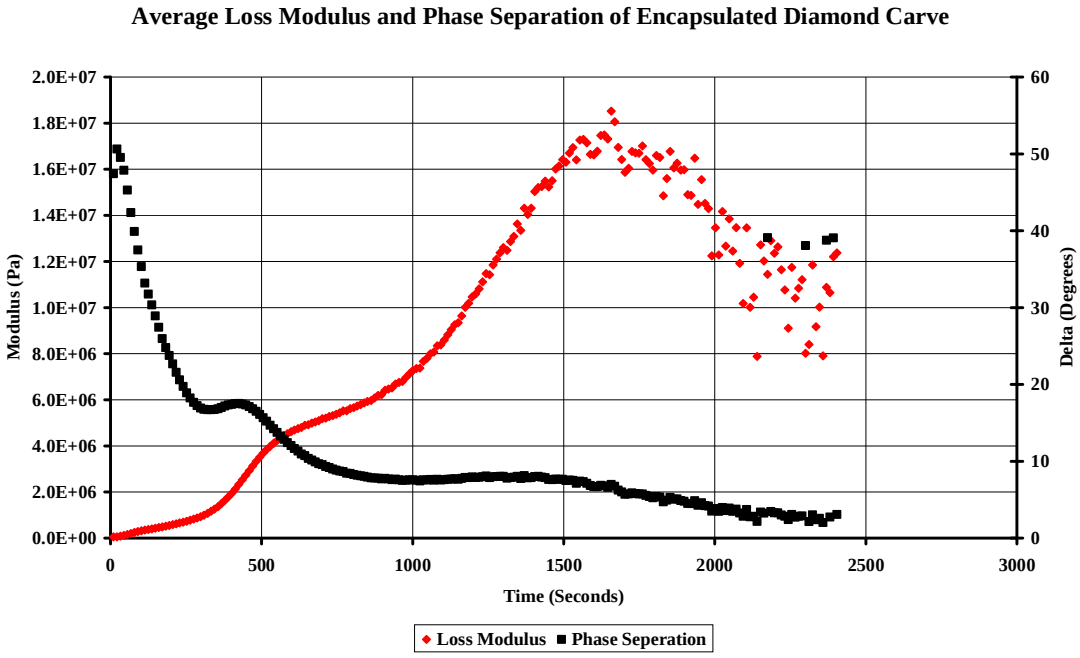

Figure A 31: Loss Modulus and Phase Separation of Encapsulated DC

The results from the encapsulated form of DC provide consistent results without the need to alter the chemical make up of the cements or powder to liquid ratio. It is therefore prudent to continue all experimentation using capsules to mix experimental and control materials.

Appendix 3

Infrared Investigation of Cure

3.1 ATR Signal to Absorbance Conversion

$$A = \varepsilon c \ell \qquad \textbf{Equation 2}$$

where A is absorbance, ε is the molar absorptivity coefficient, c is the analyte concentration and ℓ is the path length. The path length in an ATR measurement is the depth the sample is penetrated (d_p) by the IR beam which is a function of the wavelength (Equation 2)

$$d_p = \frac{\lambda}{2\pi n_1 \sqrt{\sin\phi - (n_2 / n_1)^2}} \qquad \textbf{Equation 3}$$

where λ is the wavelength, Φ is the incident angle and $n_{1\&2}$ are the refractive index of the diamond crystal and sample. The measured absorbance (intensity) from the ATR signal is found by Equation 3

$$A = (\log_{10} e)\frac{n_2}{n_1}\frac{E_0^2}{\cos\phi}\frac{d_p}{2}\alpha \qquad \textbf{Equation 4}$$

where E_0 and α are the electric fields of the evanescent wave at the boundary and the absorption coefficient per unit thickness of the sample, respectively.

ATR spectra is converted to absorbance using Equation 4

$$AB = ATR\frac{1000}{x} \qquad \textbf{Equation 5}$$

where *x* is the wavelength expressed as a wavenumber ($x = 1/\lambda$, cm^{-1}).

3.2 Additional Tartaric Acid

The periodic increase in the phase separation observed in the rheological analysis of DC has been further investigated using additional TA which was originally used to retard the setting reaction in the rheological exploratory tests (Appendix 5)

IR Spectra of DC with 5% w/w and 10% w/w additional TA have shown periodic increases in the phase separation at 6 and 13 minutes respectively when investigated using a oscillating rheometer (*see* chapter 5)

3.2.1 Diamond Carve Plus 5% w/w TA Addition

The difference spectra of DC +5% w/w TA (Figure A 32) is dominated by tartrate salts. The increase in TA concentration has brought about the quick development of Al-TA which is not seen until much later in the reaction process of unmodified DC (obscured by water H_2O bend). The increased TA salt intensity has dwarfed any peaks produced from Sr/Ca-PAA.

The point at which the rate of consumption is no longer accelerating occurs at approximately 6 minutes (Figure A 33) which coincides with the occurrence of the periodic increase in phase separation seen in rheological results.

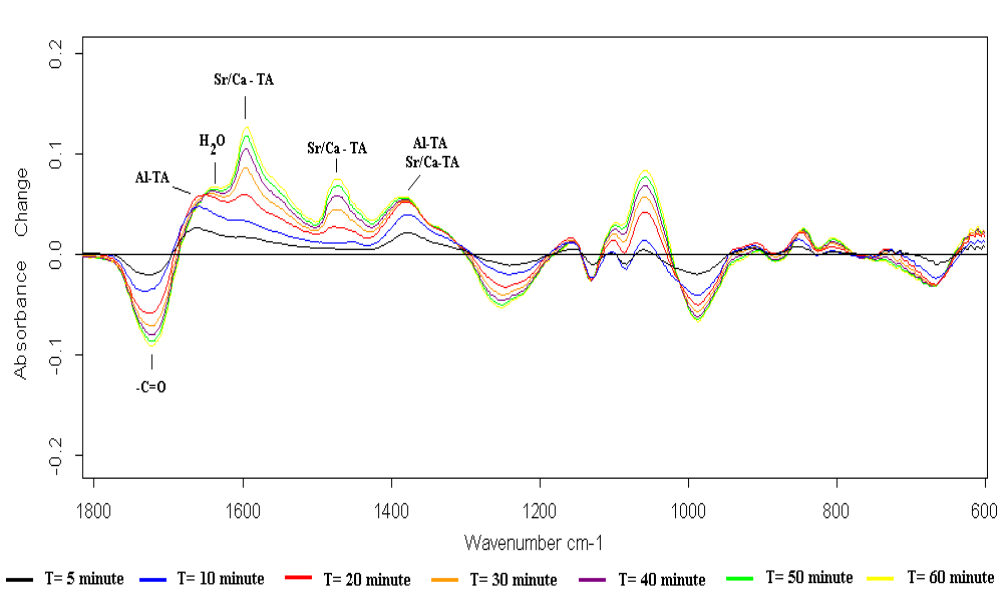

Figure A 32: Difference Spectra of DC + 5% TA during 60 Minutes of Cure Monitoring

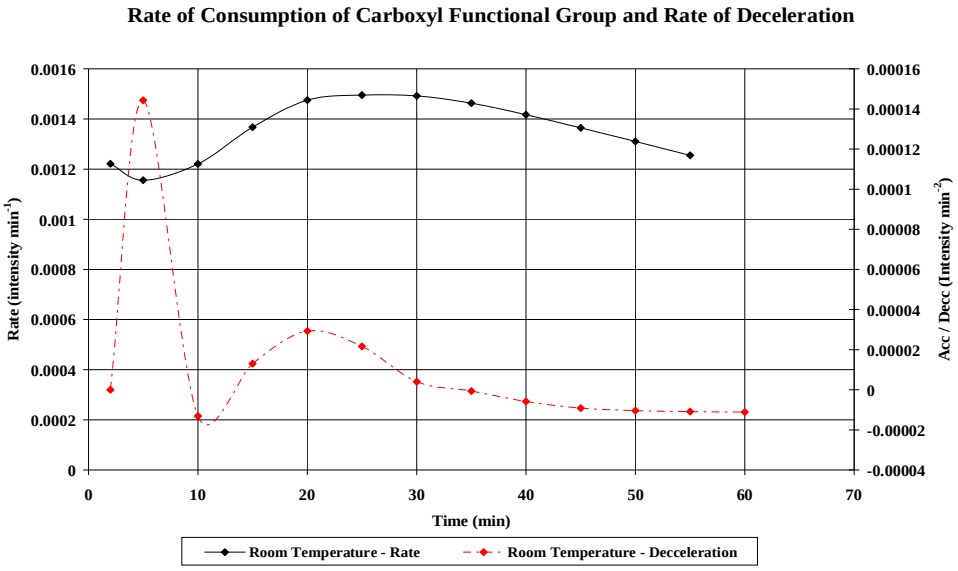

Figure A 33: Rate of Consumption of Carboxylic Acid and Change in Rate over 60 Minutes

An obvious switch in dominant salt species in the time period 5 - 10 minutes has not been seen in the +5% TA cement (Figure A 34). The rates do however experience a rapid change around 9 minutes when Al-TAs rate of formation decelerates past that of Sr/Ca-TA (Figure A 35). Subsequently the rate of Sr/Ca-TA formation increases when the rate of Al-TA formation continues to decelerate.

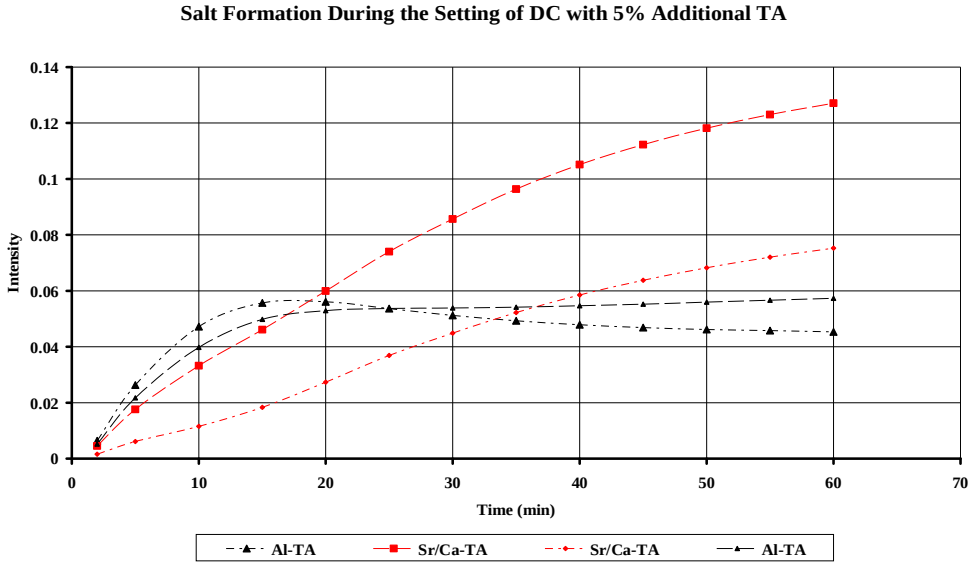

Figure A 34: Salt Formation during the Setting of DC + 5% TA

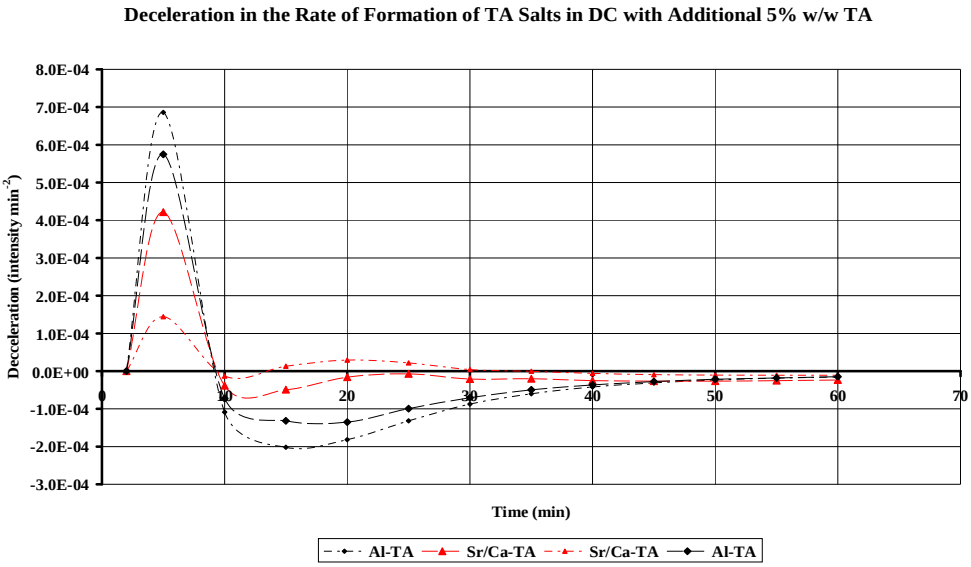

Figure A 35: Deceleration in the Rate of Formation of TA Salts in DC with 5% Additional TA (Asymmetric Stretch – Dashed Line, Symmetric Stretch – Solid Line)

3.2.2 Diamond Carve Plus 10% w/w TA Addition

The difference spectra from DC +10% TA look almost identical Figure A 36 to the +5% TA spectragram with the exception of greater intensity at the Al-TA peak at 1378 cm^{-1}. The reaction progresses at a similar rate to the +5% cement (Figure A 37 and Figure A 38). The point at which the rate of consumption of carboxylic acid begins to decelerate happens at approximately 13 minute which coincides with the periodic increase in phase separation in rheological results.

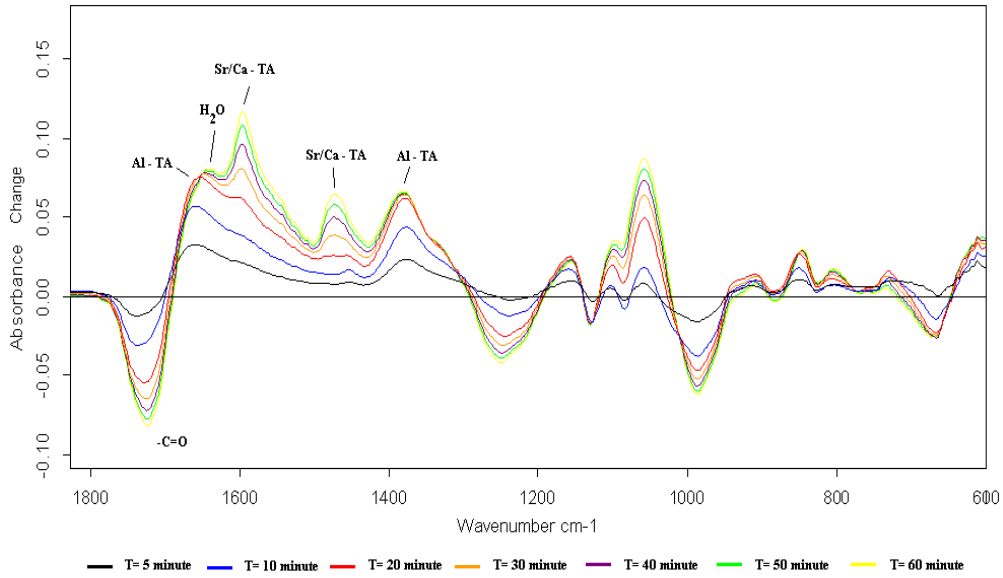

Figure A 36: Difference Spectra of DC + 10% TA During 60 Minutes of Cure Monitoring

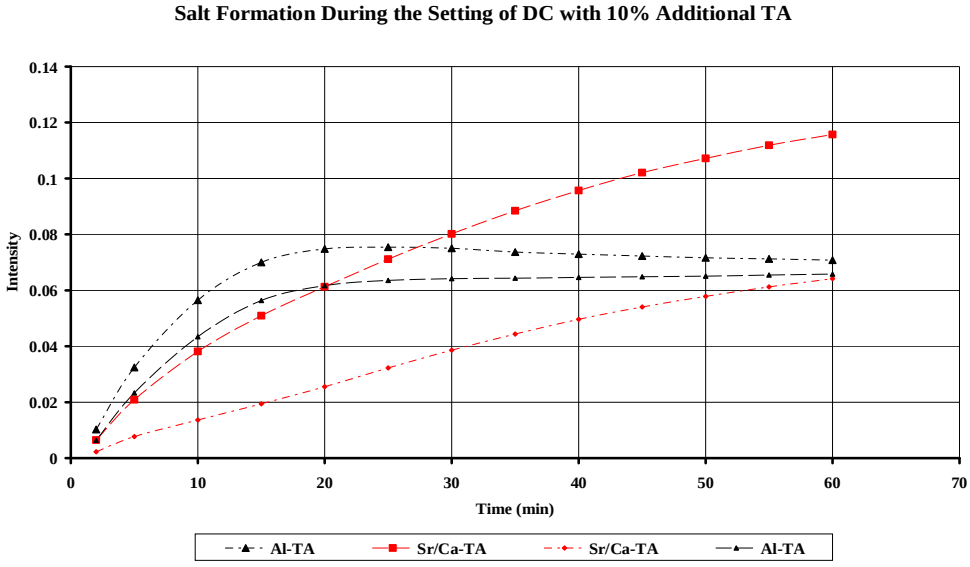

Figure A 37: Salt Formation during the Setting of DC + 10% TA

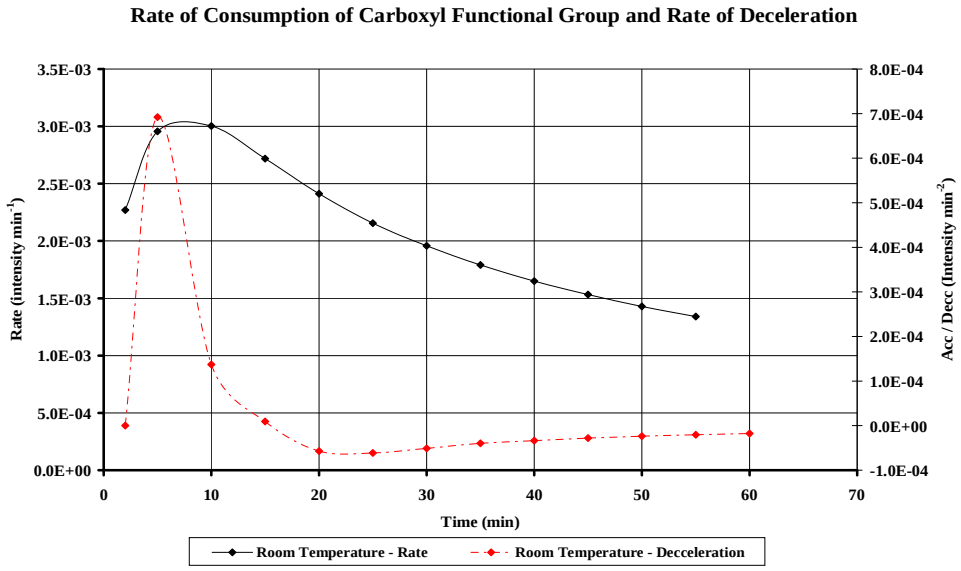

Figure A 38: Rate of Consumption of Carboxylic Acid and Change in Rate over 60 Minutes

The swap between dominant salt species at the same time as a decrease in the consumption of carboxylic acid has been seen in chilled DC. The increased concentration of TA in the retarded DC samples has effectively blocked the appearance of the PAA salts by a combination of prolonged reaction with the metal cations from ASG and obscuring them from view because of the increased TA salt intensity.

The increase in phase separation can be attributed to the

3.2.3 Conclusion

The observed periodic increase in the rheological phase separation is coincident with the deceleration in the rate of carboxyl group consumption. Figure A 33 and Figure A 38 both show that the point where the rate of carboxyl conversion ceases to be accelerating and instead turns to a negative / deceleration is incident with the observered periodic increase at approximately 6 and 13 minutes for 5% w/w and 10% w/w addition respectively. The cause of the deceleration is believed to be related to the swap between the rate of Al-TA and Sr/Ca-TA formation. The formation of Al-TA was found to be greater than Sr/Ca-TA in both the experimental TiGICs and the altered DC cements (TA addition) during the very early stages of observation.

Figure A 34 and Figure A 37 highlight the rapid decrease in the rate of Al-TA formation around the time of the periodic increase when the rate of Sr/Ca-TA becomes the fastest forming salt in the cement for the majority of the observation period (40-60 minutes). The decrease in Al-TA formation and the deceleration of C=O would indicate that the initial high consumption of the carboxyl groups is caused by the formation of Al-TA.

3.3 Control Material Analysis

The exploratory tests positively identified the presence and location of aluminium tartrate at 1672 cm^{-1} in deuterated combinations of Al(OH) and TA. It is therefore presumed that the peak of irresolution at 1670 cm^{-1} is caused by Al-TA.

DCL has been broken down into its constituent parts (Table A 6 & Table A 7) for analysis because the clear identification of the species formed in the wavenumber range 1600 –1680 cm^{-1} and 1380-1460 cm^{-1} have possible confusion. The multiple peaks found in the range 1380-1460 cm^{-1} can be confused between Sr-PAA and a $–CH_2$ scissoring vibration of PAA; also within this range, peaks are present from Ca-PAA and Al-TA which are not able to be separated (Tomlinson, 2007).

The control materials (Table A 5) were chosen based on the constituent parts of DC and their ability to form aluminium and calcium salts independently to mimic the salts formed by a GIC so the characteristic absorbencies could be found.

Substance	**CAS-NO**	**Supplier**
Calcium Hydroxide	1305-62-0	Sigma-Aldrich (C7887-500G)
Aluminium Hydroxide	21645-51-2	Prepared in chapter 3
Aluminosilicate Glass	NA	Kemdent (Swindon)
Polyacrylic Acid	9003-01-4	Acumer 1510 (25% Solids, MW-60,000)
PAA-PVPA Co-Polymer	NA	Kemdent (Swindon)
Tartaric Acid	147-71-7	Aldrich (T206)
Distilled Water	7732-18-5	Produced in house
Deuterium Oxide	7789-20-0	Aldrich (435767-25g)

Table A 5: Control Materials for IR Analysis

Appendix 3: Infrared Investigation of Cure Monitoring

Solutions of PAA, TA, PAA-PVPA and DCL were made up so that the concentrations mimic that found in the commercial DC product. The solutions were made from distilled water and deuterium oxide as shown in Table A 6 and Table A 7.
There is a difference between the densities of water and deuterium oxide so the weight of deuterium oxide was increased in order to maintain a constant volume of fluid.

Distilled Water Solutions				
Solution	PAA (g)	PVPA-PAA (g)	TA (g)	H_2O (g)
PAA	1.509	0.000	0.000	5.00
TA	0.000	0.000	0.826	5.00
PVPA-PAA	0.000	0.064	0.000	5.00
DC Liquid	3.018	0.000	1.651	10.00

Table A 6: Control Solutions Dissolved in Distilled Water

Deuterium Dioxide Solutions				
Solution	PAA (g)	PVPA-PAA (g)	TA (g)	D_2O (g)
PAA	0.682	0.000	0.000	2.50
TA	0.000	0.000	0.373	2.50
PVPA-PAA	0.000	0.029	0.000	2.50
DC Liquid	2.045	0.000	1.119	7.50

Table A 7: Control Solutions Dissolved in Deuterium Oxide

All the cements formed from the control materials were mixed by hand in the same manner as described in chapter 3. Cements without tartaric acid were mixed with a large excess of polyelectrolyte solution because without the retarding effect of TA the cements were uncontrollable and set rapidly. The average weight of basic powder and acidic polyelectrolyte used to form a cement was 0.4g and 0.1g respectively. Cements formed with calcium hydroxide were mixed on a chilled glass block using chilled polyelectrolyte solutions because the speed of reaction was uncontrolled at room temperature and formation of a reasonable homogeneous cement was not possible.

3.3.1 Aluminosilicate Glass

The IR spectrum of the aluminosilicate glass used in DC was recorded (Figure A 39). Two strong peaks can be seen at 692 and 966 cm^{-1}. The identification of these peaks was complex because the amorphous glass lacked long range order therefore broad indistinct peaks are formed. The inclusion of phosphorus in the glass network will increase the amount of disorder, further broadening characteristic peaks (De Maeyer, 2002). The peak at 692 cm^{-1} has been assigned to a strong –Al-O stretch from octahedral aluminium with a underlying combination of –O-Si-O bending and asymmetric / symmetric –Si-O-Si stretching from amorphous silica. The peak at 966 cm^{-1} is assigned to a strong –Al-O stretch from tetrahedral aluminium with a weak signal from bonding –Si-O-Si and non-bonding –Si-O oxygen causing the deformation of the peak. (Gritco *et al*, 2005; Day & Rindone, 1962; De Maeyer *et al*, 2002; Hwa *et al*, 1998; Yipa & Tob, 2005; Young *et al*, 2005).

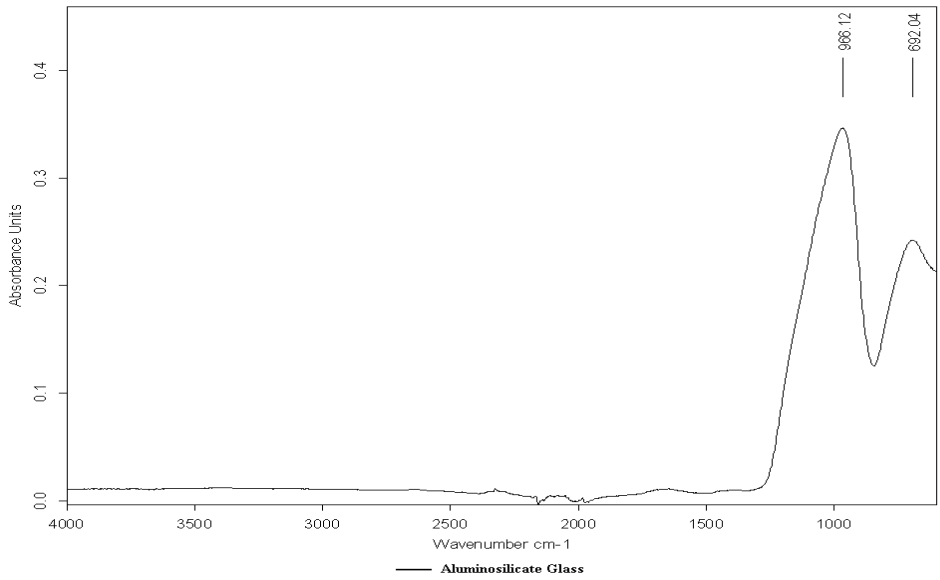

Figure A 39: Aluminosilicate Glass used in the Production of DC Powder

3.3.2 Distilled Water and Deuterium Oxide Polyelectrolyte Solutions

The solvent properties of deuterium oxide are almost identical to that of water but the additional weight of the deuterium atom causes the characteristic scissoring frequency at 1634 cm^{-1} in water to become present at the longer wavelength of 1203 cm^{-1} (Figure A 40). The use of deuterium oxide as a solvent to prepare polyelectrolyte solutions for use with ASG will remove the scissoring vibration of water around 1634 cm^{-1} in the spectrum therefore avoiding any overlapping signals with the –C=O stretch from carboxylic acid functional groups, aluminium tartrate and strontium / calcium tartrate.

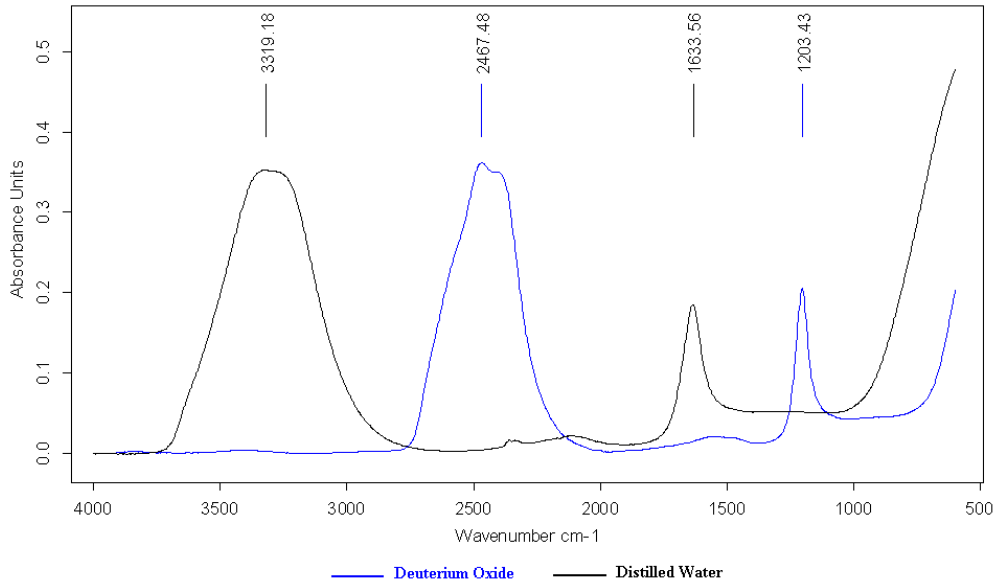

Figure A 40: IR Absorption Spectrum of Deuterium Oxide and Distilled Water

DCL contains polyacrylic acid, tartaric acid and water (Table A 6). Individual solutions of these constituent acids were prepared using quantities from Table A 6 and Table A 7.

Water based solutions of polyacrylic acid have a large peak based around 3365 cm^{-1} caused by symmetric (sym) and asymmetric (asym) –O-H stretches dominantly from water (Figure A 41). The peak at 1634 cm^{-1} is from a scissoring vibration of water; this peak has a pronounced shoulder at 1700 cm^{-1} from the carboxyl group of PAA.

The two peaks at 1453 cm^{-1} and 1260 cm^{-1} are from $–CH_2$ scissoring in the PAA backbone; the latter vibration is broadened by an –C-O stretch around 1188 cm^{-1}. Deuterated PAA has equivalent peaks at the wave-numbers found in Table A 8.

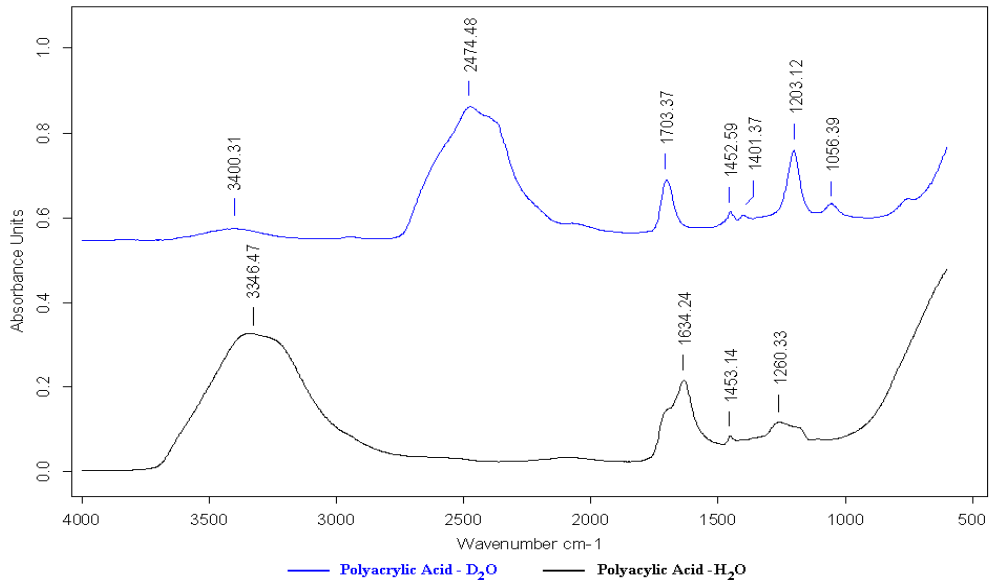

Figure A 41: Deuterium Dioxide and Water Solutions of Polyacrylic Acid

Wavenumbers (cm^{-1})	Peak Assignment	Remarks
H_2O PAA		
3365	-O-H	Sym and Asym stretching vibrations
1700	-C=O	Carboxyl stretch from polycarboxylate
1634	H-O-H	Scissoring vibration
1453	$-CH_2$	PAA carbon backbone
1260	$-C(OH) / -CH_2$	OH bending from carboxylate group
1188	-C-O	Stretch
D_2O PAA		
3400	$-CH_2$	Stretching vibration
2474	-O-D	Sym and Asym stretching vibrations
1703	-C=O	Carboxyl stretch from polycarboxylate
1452	$-CH_2$	PAA carbon backbone
1401	$-CH_2$	PAA carbon backbone
1203	D-O-D	Scissoring vibration
1056	Unassigned	Likely –C-O stretch (Stuart, 2004)

Table A 8: Peak Assignment for PAA Dissolved in Distilled Water and Deuterium Oxide

Water solutions of tartaric acid (Figure A 42) have two peaks from various –OH vibrations at 3331 cm^{-1} and 1633 cm^{-1}. A shoulder present at 1724 cm^{-1} is caused by an –C=O vibration from the carboxyl group present within the acid.

There is a peak present at 1262 cm^{-1} due to a combination of –C-H and –O-H deformations from the secondary alcohol groups of TA, this peak has been assigned the combination frequency HCOH. Two –C-O(H) stretching vibrations at 1136 cm^{-1} and 1088 cm^{-1} due to asymmetric and symmetric stretches of the secondary alcohol groups respectively. The removal of the –OH vibrations in the deuterated acid has reviled two previously hidden peaks. The two peaks at 1379 cm^{-1} and 1316 cm^{-1} have been assigned to a –C-O stretch from transverse placement at opposite ends of the TA molecule.

The peaks present in tartaric acid (Figure A 42) are presented in Table 18.

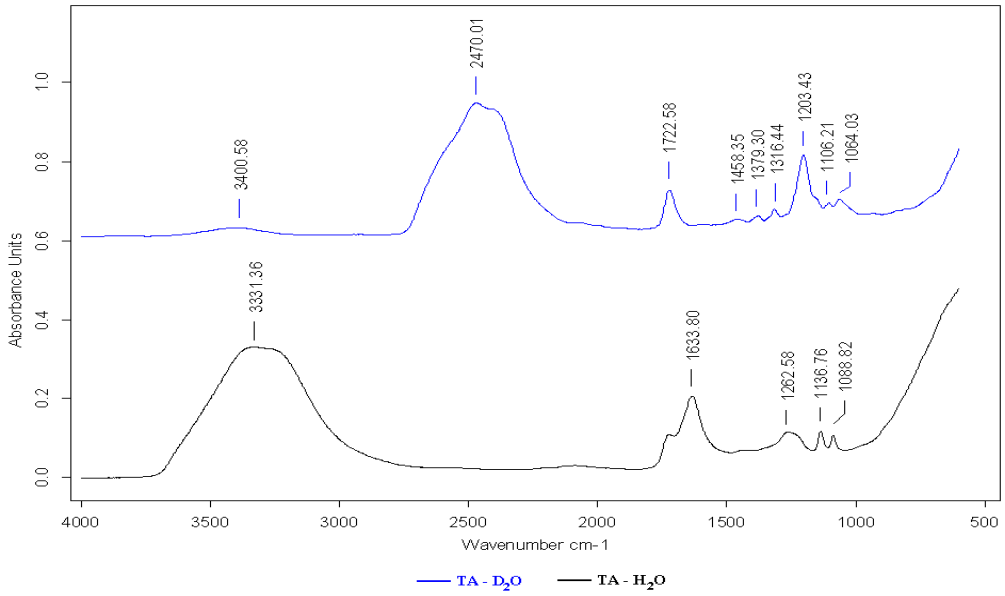

Figure A 42: Deuterium Dioxide and Distilled Water Solutions of Tartaric Acid

Wavenumbers (cm^{-1})	Peak Assignment	Remarks
H_2O TA		
3331	-OH	Sym and Asym stretching vibrations from water
1724	-C=O	Carboxyl stretch from TA
1633	H-O-H	Scissoring vibration
1262	HCOH	Deformation of –C-H and –O-H from alcohol group
1136	-C-O(H)	Asym –CO stretch from secondary alcohol
1088	-C-O(H)	Sym –CO stretch from secondary alcohol
D_2O TA		
3400	-OH	Stretching vibrations from carbonyl and secondary alcohol
2470	-O-D	Sym and Asym stretching vibrations of solvent
1722	-C=O	Carboxyl stretch from TA
1458	-CH	TA carbon backbone
1379	-C-O	Valence stretch of carboxylate group at transverse orientations.
1316	-C-O	
1203	D-O-D	Scissoring vibration
1106	-C-O(H)	Asym –CO stretch from secondary alcohol
1064	-C-O(H)	Sym –CO stretch from secondary alcohol

Table 18: Peak Assignment for TA Dissolved in Distilled Water and Deuterium Oxide

The concentration of PAA-PVPA co-polymer (Table A 6) is relatively low within the DC cement. Only one characteristic peak is present from the vinyl phosphate functional group; a hydrogen bonded P-OH (-O-H) vibration (Figure A 43) at 2503 cm^{-1}. The peak at 1459 cm^{-1} is thought to be due to the $–CH_2$ vibration of the co-polymer carbon backbone. The phosphate peak is not visible in the deuterate PAA-PVPA solution because of the sym and asym –O-D stretches within the solvent overlapping the absorbance. The presence of any absorbencies due to the presence of the vinyl phosphate group will be obscured by cement salt absorbencies with greater concentrations.

Appendix 3: Infrared Investigation of Cure Monitoring

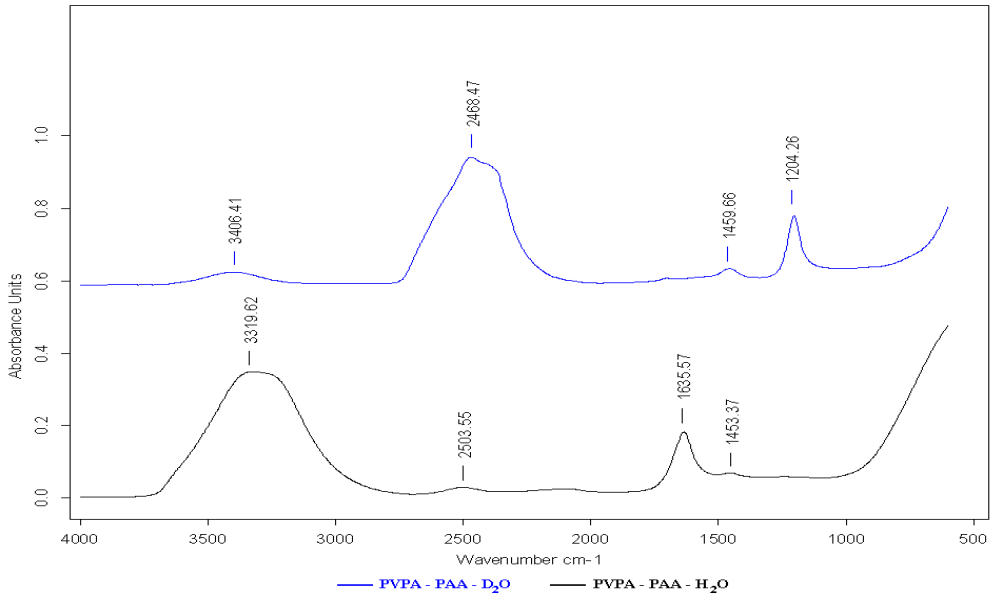

Figure A 43: PAA-PVPA Solutions Dissolved in Distilled Water and Deuterium Oxide

3.3.3 Calcium Hydroxide Cements

3.3.3.1 Polyacrylic Acid Cement

Calcium hydroxide is known to react rapidly with PAA when compared with aluminium hydroxide (Wu *et al*, 2007). Rapid cement formation between $Ca(OH)_2$ and PAA was of practical difficulty when mixing the cement. A great excess of PAA was used to try and 'dilute' the $Ca(OH)_2$ as a colloidal dispersion rather than form a cement as used by Prosser *et al* (1982).

The reaction proceeded rapidly during the first 5 minutes of reaction (Figure A 44). The total removal of the –C=O stretching vibration within 5 minutes of reaction demonstrates the strong reaction between Ca^{2+} and $–COO^-$. The high rate of reaction is due to the highly basic nature of CaO which has a pH of 12.7 compared to pH 8 for Al_2O_3 (Wu *et al*, 2007). Four well defined peaks at 1538 cm^{-1}, 1454 cm^{-1}, 1407 cm^{-1}, and 1325 cm^{-1} with a pronounced shoulder at 1352 cm^{-1} have been identified in Table A 9 (Saniger *et al*, 1991). The assignment of the peak at 1407 cm^{-1} has previously been given to the $–CH_2$ symmetric vibration of the PAA backbone but the change in the intensity and shape has been predicted to be caused by an overlap with a symmetric –C-O stretch from PAA (Saniger *et al*, 1991).

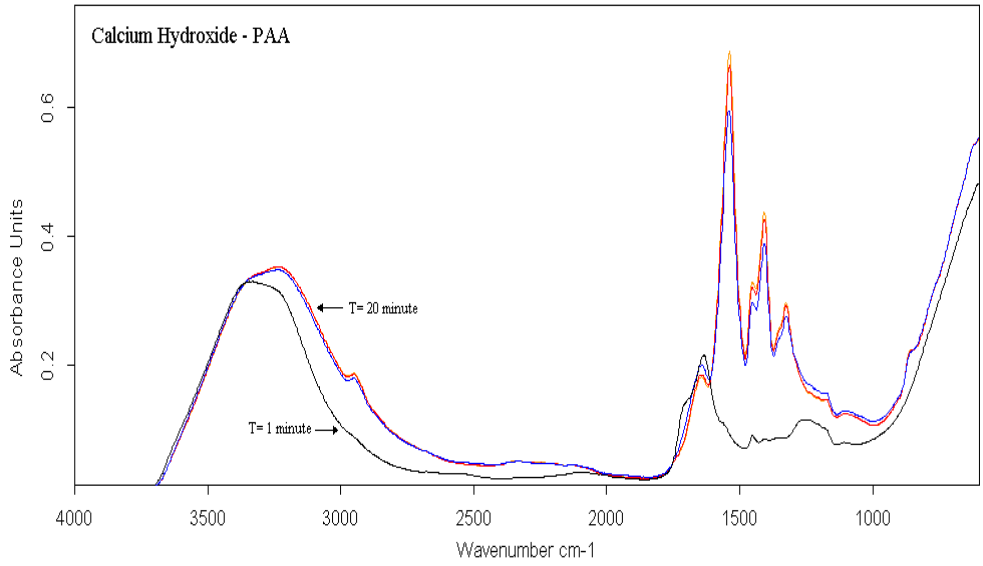

Figure A 44: Rapid Formation of Reaction Products from a Calcium Hydroxide - PAA Cement

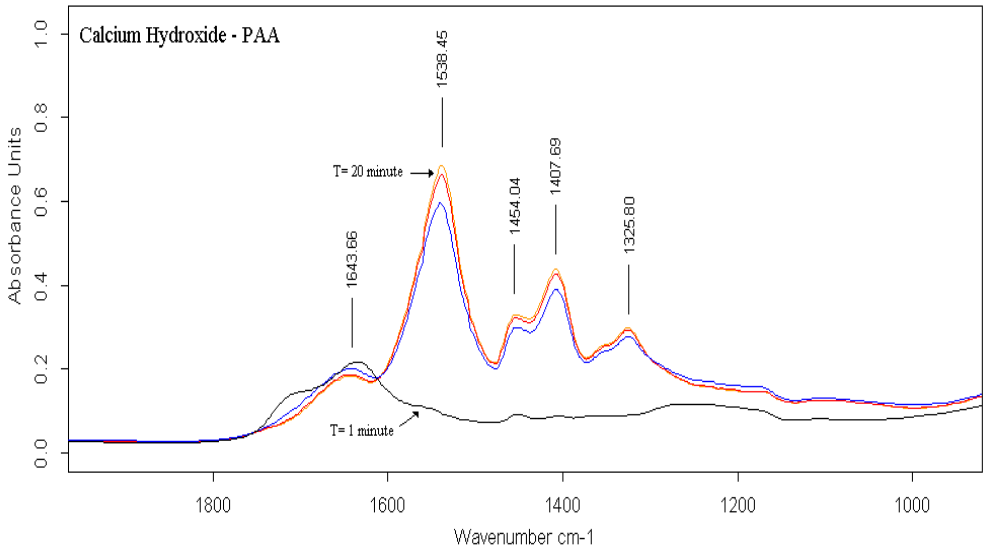

Figure A 45: Zoomed View of Reaction Products Forming within the Range 1000-1800 cm^{-1}

If the carboxylic peak is used as a measure of reaction completeness and the rate of consumption as an indication of the rate of reaction then the peak is best separated from the water bend present in original DCL (Figure A 45 and Figure A 46). The carboxyl peak of deuterated PAA is present at 1686 cm^{-1} and after 20 minutes of reaction the peak is still visible therefore carboxylic groups are still available for reaction. This is common with clinical formulations of calcium hydroxide cements (Akashi *et al*, 1990).

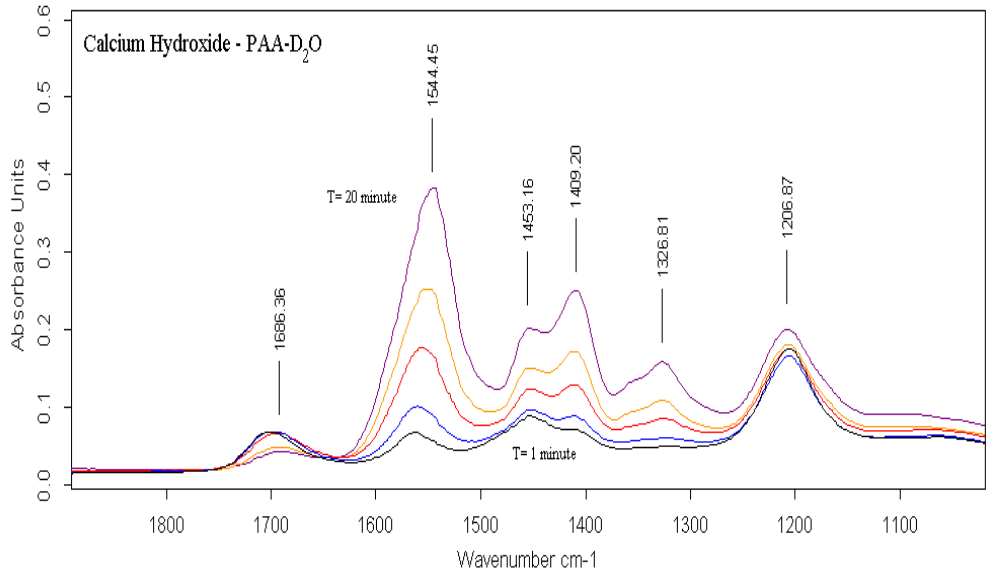

Figure A 46: Reaction between Calcium Hydroxide and PAA-D_2O Confirming Peak Formation without a Water Overlap

Wavenumbers (cm^{-1})	Peak Assignment	Remarks
1695	-C=O	Stretching
1642	H-O-H	-O-H Bending
1538	-C-O	Asymmetric 2(–C-O^-)Ca^{2+}
1453	-CH_2	PAA Backbone (Scissoring)
1407	-C-H, -C-O	Hydrogen Bend from α Carbon; overlapping with symmetric –C-O
1352	-C-O	Symmetric 2(-C-O^-)Ca^{2+}
1326	-C-O	

Table A 9: Peak Assignment for Calcium Hydroxide Reacted with PAA

3.3.3.2 Tartaric Acid Cement

The cements formed from TA and $Ca(OH)_2$ were lumpy, non-homogeneous pastes that were difficult to handle and load onto the ATR window. This is due to increased acid strength of TA (low pKa) and high reactivity of $Ca(OH)_2$ forming calcium tartrate salt at an unmanageable rate.

The reaction ceases to progress after 10 minutes of reaction with no visible change in absorption intensities between 10-20 minutes. The difficulty experienced when mixing and handling Ca-TA cements is translated as a noisy IR spectrum caused by poor contact with the ATR window.

The peak allocation of Ca-TA is difficult because of the number of peaks present. Nicholson (1998), Deb & Nicholson (1999) and Tomlinson (2007) have assigned peaks to general GIC salt species whose absorption wavelength co-insides with the observed Ca-TA absorbencies (**Error! Reference source not found.**). Examples are the assignment of the peaks present at 1405 cm^{-1} and 1055 cm^{-1} to Al-TA / Ca-PAA and Si-O-Si respectively. This is due to the strong overlapping absorbencies in these areas because all the cement salts are formed from the same two carboxylate groups (TA / PAA) that only differ by the strength of attraction to a bi or tri valent cation.

The identification of several un-assignable peaks (Table A 10) will not be made unless these peaks are observed in the experimental cement spectra. There increasing intensity would mean that they can only be Ca-TA or an increase in secondary alcohol formation as hydrogen bonding decreases and acid species are neutralised.

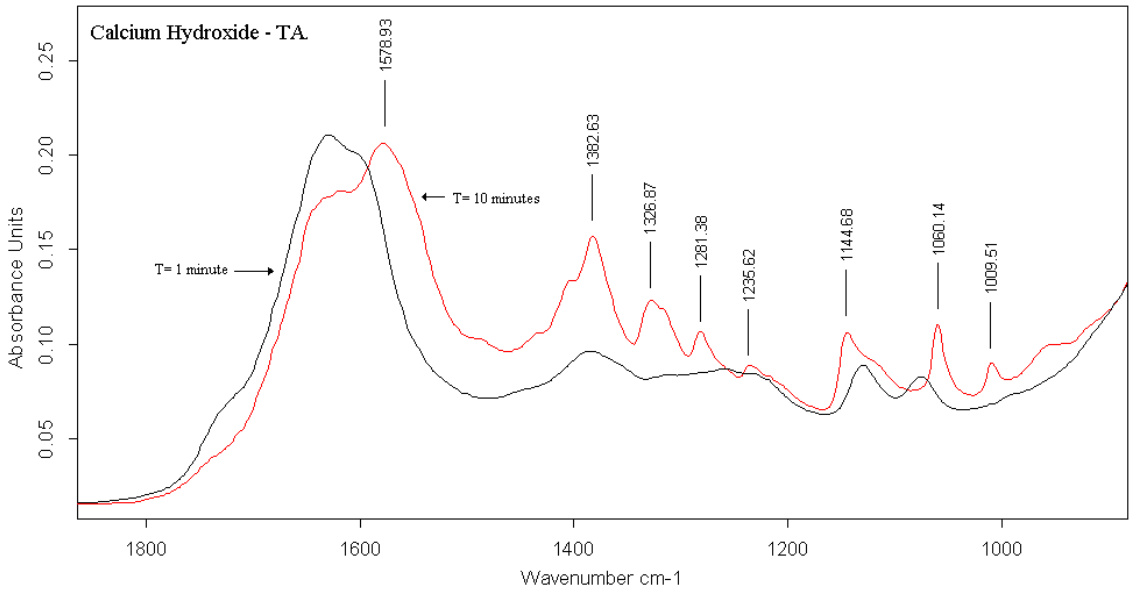

Figure A 47: Reaction between $Ca(OH)_2$ and TA Forming Multiple Calcium Salt Peaks

Wavenumbers (cm^{-1})	Peak Assignment	Remarks
1724	-C=O	
1633	H-O-H	
1600 moving to 1579	-C-O	Asym Stretch of Ca-TA
1486	Unassigned	
1435	Unassigned	
1403	$-C-O^- Ca^{2+}$	Asym stretch
1380	-C-O	Asym carbonate stretch
1324	-C-O	Sym carbonate stretch
1283	HCOH	TA combined deformations
1233	Unassigned	
1143	Unassigned	
1060	-C-O(H)	Asym –CO stretch from secondary alcohol
1009	-C-O(H)	Sym –CO stretch from secondary alcohol

Table A 10: Peak Assignment for Ca-TA Cements forming over 10 Minutes of Reaction

3.3.3.3 Diamond Carve Liquid Cement

The major peaks present in DCL mixed with calcium hydroxide are the most dominant peaks from PAA and TA (Figure A 48). The peak assignment has been made (Table A 11) based on the peaks present in $Ca(OH)_2$ – PAA / TA. The unassigned peak at 1146 cm^{-1} was not present in the control samples of TA; the intensity of this peak does not change so it is assumed to be from the TA backbone and has become visible because of decreased hydrogen bonding due to salt formation. Reference tables suggest that the peak is due to a –C-OH stretch from the secondary alcohol of TA (Williams & Fleming, 1995).

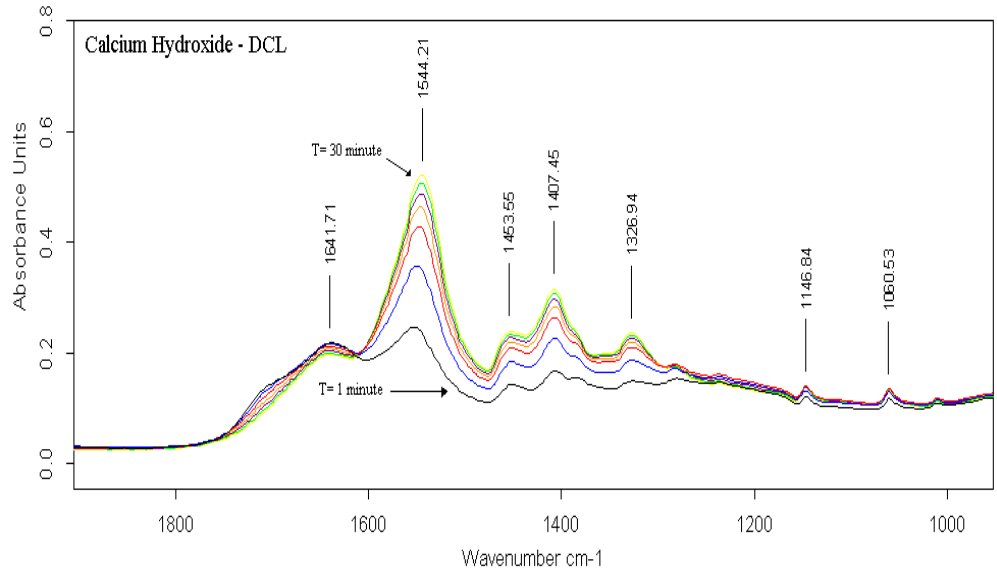

Figure A 48: Maturation of Ca-DCL Cement over a 30 Minute Period

Wavenumbers (cm^{-1})	Peak Assignment	Remarks
1704	-C=O	Dominated by carboxyl group on PAA
1640	H-O-H	Water bend
1544	-C-O	Asym Ca-PAA stretch
1453	$-CH_2$	PAA backbone (scissoring)
1406	-HCOH, -C-O	Hydrogen bend from PAA and $2(COO^-)Ca^{2+}$ of Ca-TA
1385	-C-O	Asym –C-O from Ca-TA
1327	-C-O	Sym –C-O from Ca-TA
1146	Unassigned	Present in TA – constant intensity
1060	-C-O(H)	Sym –C-O(H) stretch from TA secondary Alcohol

Table A 11: Peak Assignment for the Major Absorbance's Present in DCL Mixed with Calcium Hydroxide

3.4 Aluminium Hydroxide Cements

3.4.1 Polyacrylic Acid Cement

The reaction between freshly prepared $Al(OH)_3$ and PAA happens slowly (Figure A 49). It is possible to see a slight decrease of carboxylic acid intensity at 1695 cm^{-1} over a 20 minute period. The loss of the –C=O stretch (Figure A 50) would mean that a neutralisation reaction is taking place although the appearance of reaction products at the expected absorbance's are not observed. A change does however take place at 2363 cm^{-1}, 2344 cm^{-1} and 2327 cm^{-1}; the assignment of these peaks has not previously been carried out. The peaks occurring at 2327 cm^{-1} and 2344 cm^{-1} are both found in the spectrum of aluminium hydroxide (Figure A 51); possible causes are a –O-H stretch (Wefers & Misra, 1987) and carbon dioxide respectively. However, PAA-H_2O also contains these two peaks so positive identification cannot be made. The increase in the intensity of the peak occurring at 2363 cm^{-1} is a new absorbance (not seen in either $Al(OH)_3$ nor PAA-H_2O) and is therefore considered a product of the acid-base reaction between $Al(OH)_3$ and PAA-H_2O so will tentatively be assigned to aluminium polyacrylate.

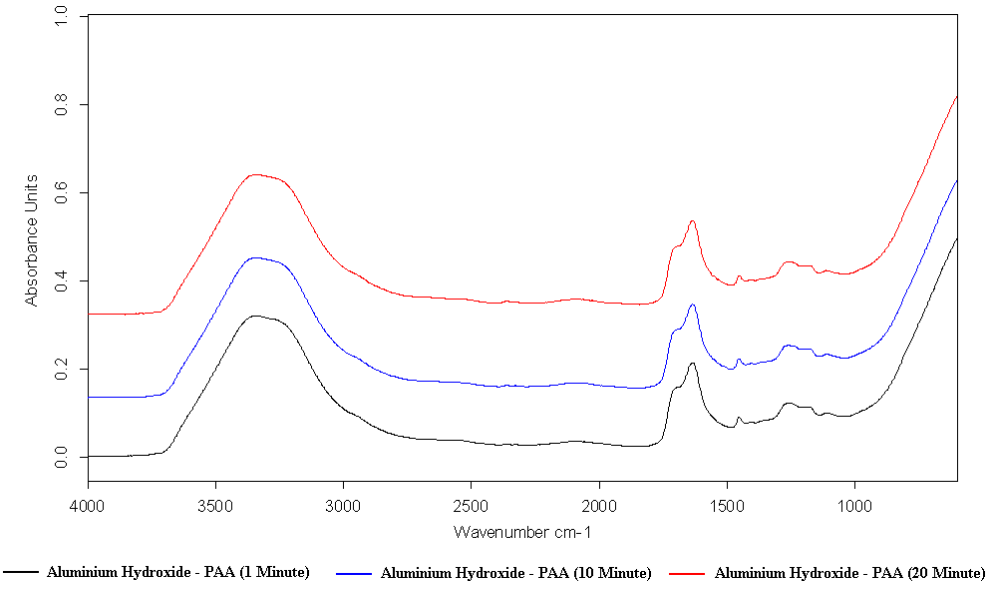

Figure A 49: Aluminium Hydroxide Reacted with PAA-H_2O for 20 Minutes (Room Temperature - 24.3°C)

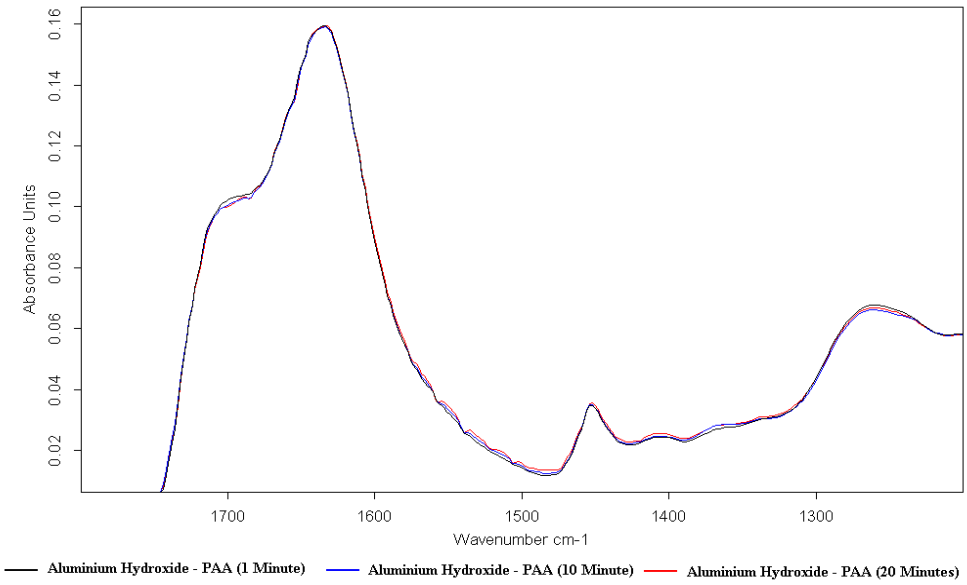

Figure A 50: Zoomed Section of Carboxyl and -CH_2 Absorptions

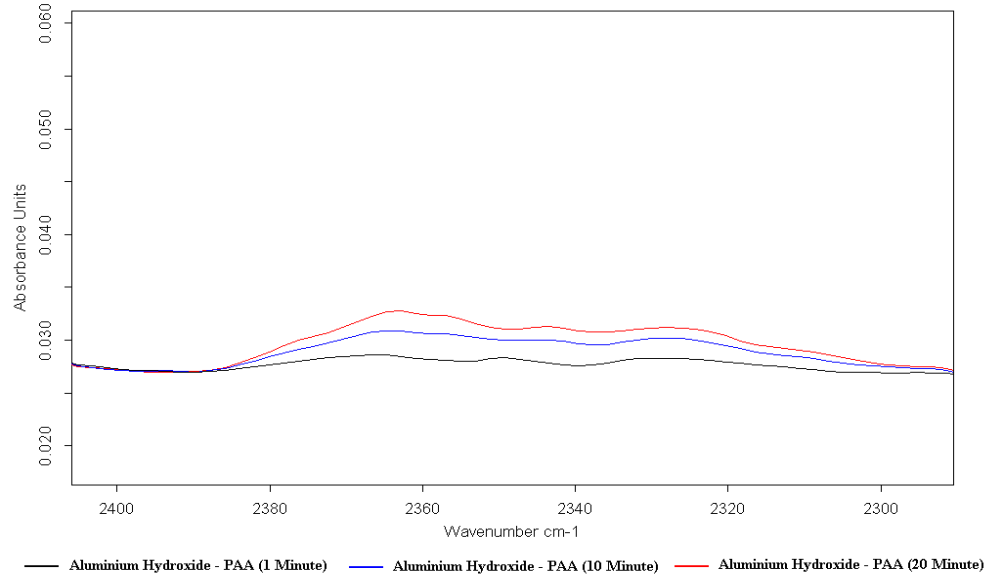

Figure A 51: Peaks at 2363 cm^{-1}, 2344 cm^{-1} and 2327 cm^{-1} in a Aluminium Hydroxide - PAA Cement

3.4.2 Tartaric Acid Cement

The reaction between TA and $Al(OH)_3$ (Figure A 52) progresses much more rapidly than PAA and $Al(OH)_3$. This is because TA (pKa = 2.96) is a stronger acid than PAA (pKa = 4.25), Mandel, 1970) as described in chapter 2 and can overcome the energy barrier for the reaction to progress more easily than PAA.

The carboxyl peak at 1725 cm^{-1} has almost totally vanished after 30 minutes of reaction suggesting total reaction of all carboxylic groups present in TA. The rapid consumption of –C=O is accompanied with the rapid production of water and Al-TA ($3(COO^-)Al^{3+}$) at 1634 cm^{-1} and 1380 cm^{-1} respectively. The presence of two peaks at 2341 cm^{-1} and 2360 cm^{-1} are observed and have been assigned to carbon dioxide and Al-TA respectively as had previously been done for $Al(OH)_3$ and PAA cements. The slow production of another peak at 1333 cm^{-1} has been attributed to the asymmetric stretch of Al-TA (Nicholson, 1998 & Ana *et al*, 2003). The decrease in the peak at 1260 cm^{-1} is in agreement with its assignment as a –C-O stretch.

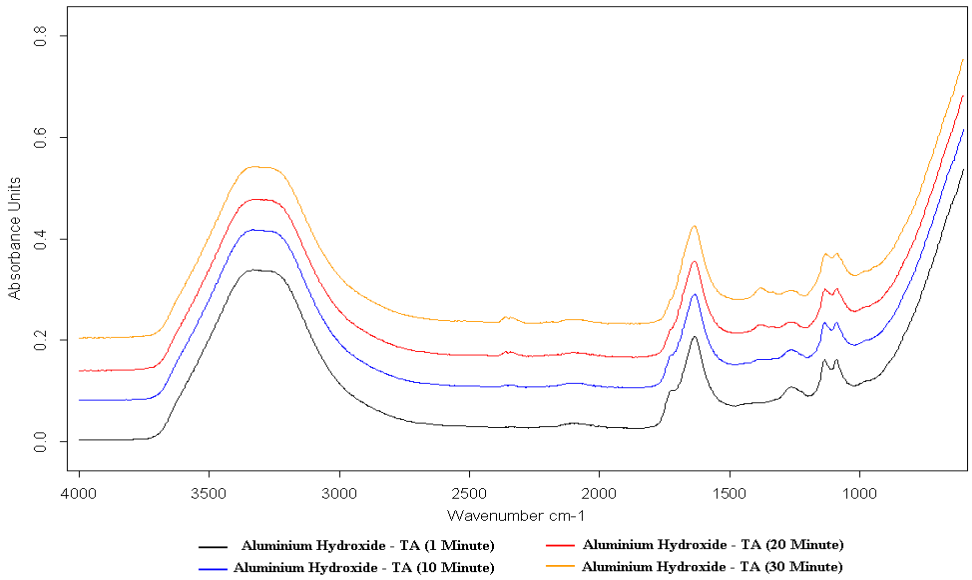

Figure A 52: IR Spectra of the Reaction between Aluminium Hydroxide and Tartaric Acid over 30 Minutes

The vibration from water at 1607 cm^{-1} masks most of the Al-TA absorbencies. Peaks are observed at 1670 cm^{-1}, 1387 cm^{-1}, 1341 cm^{-1} and 1137 cm^{-1} (Figure A 53).

The peaks have been assigned to monodentate –C-O$^-$ Al^{3+} (1670cm^{-1}), transverse –C-O$^-$ Al^{3+} (1387 cm^{-1} & 1341 cm^{-1}) and asymmetric –C-O$^-$ Al^{3+} (1137 cm^{-1}) from a secondary alcohol (Kozhevina *et al*, 1981).

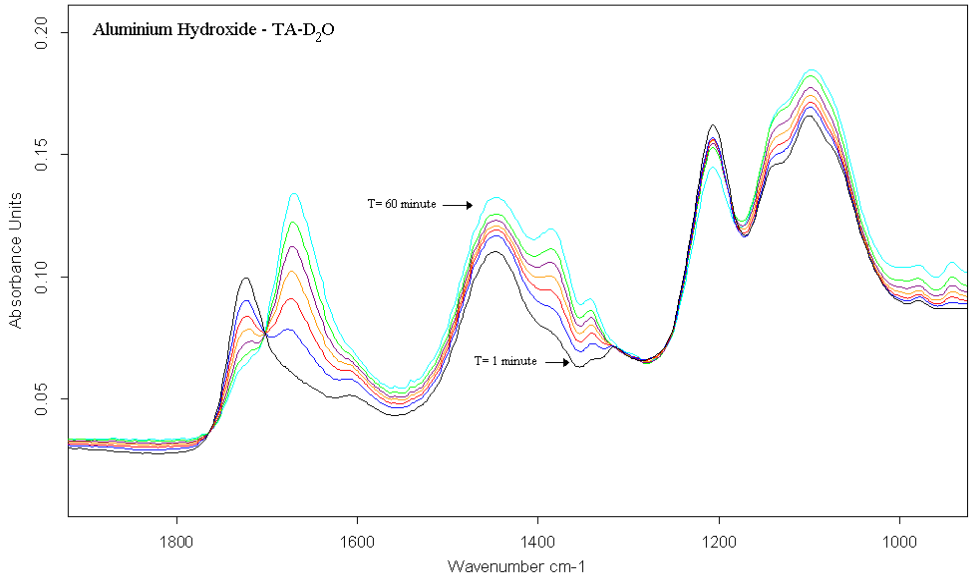

Figure A 53: Generation of Multiple Peaks formed between Al(OH)$_3$ and Deuterated TA

3.4.3 Polyvinylphosphonic Acid Cement

PVPA-PAA reacts with Al(OH)$_3$ producing two peaks of changing intensity. The peaks observed in the PAA and TA aluminium hydroxide cements around 2340 cm^{-1} – 2365 cm^{-1} are also present in the PAA-PVPA, Al(OH)$_3$ cement at 2341 cm^{-1} 2360 cm^{-1}. The positive assignment of these peaks is still not possible as they are present in all samples and localised noise around these frequencies in Al(OH)$_3$ (Figure 6.6) means they may be an artefact from the basic material. The second peak of interest at 1102 cm^{-1} (Figure A 54) has been assigned to the stretching vibration (sym, asym or bridging) of –P-O(Al). The identification of a –P=O stretch in DC by Tomlinson (2007) at 1088 cm^{-1} aids this assignment.

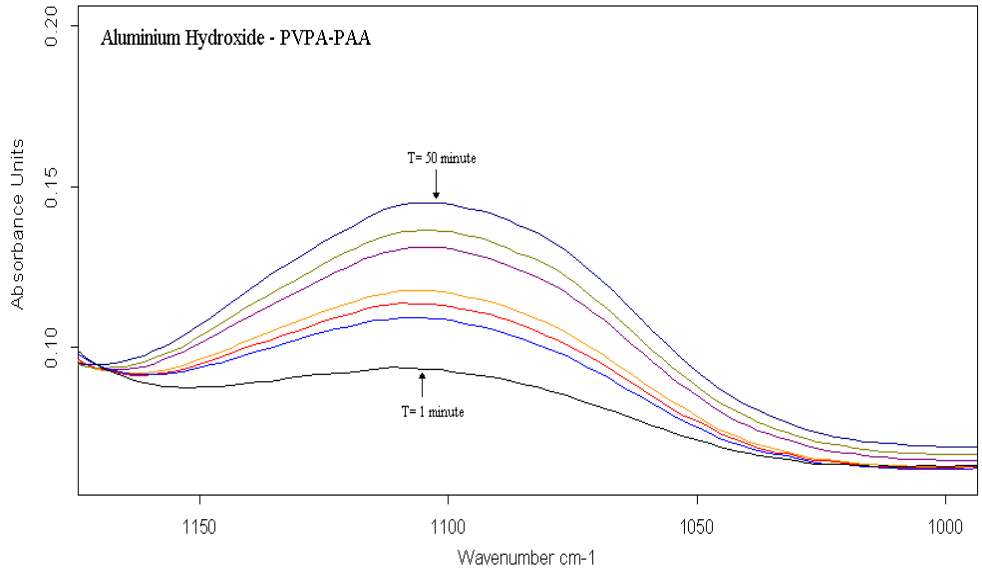

Figure A 54: Aluminium Hydroxide Reacted with PVPA-PAA for 1-50 Minutes (Peak at 1102 cm^{-1})

3.4.4 Diamond Carve Liquid Cement

The reaction between water based DCL and $Al(OH)_3$ has produced a relatively large increase in the intensities of symmetric and asymmetric Al-TA at 1337cm^{-1} and 1367cm^{-1} respectively (Figure A 55). A small decrease in the –C=O stretch at 1706cm^{-1} and a increase of the water vibration at 1635cm^{-1} will be a result of setting reaction between carboxylic acid; predominantly from TA. The relative intensity of the carboxyl peak will be dominated by PAA because of the relative concentration within DCL. No effect from PVPA-PAA is observed because of its absence in DCL (included in DC powder). A small asymmetric Al-TA peak at 1682cm^{-1} is starting to occur after 60 minutes of reaction (Nicholson, 1998). The only discernable influence from PAA is the increase in absorbance around 1408cm^{-1} although this is strongly overlapped by Al-TA absorptions (Figure A 56).

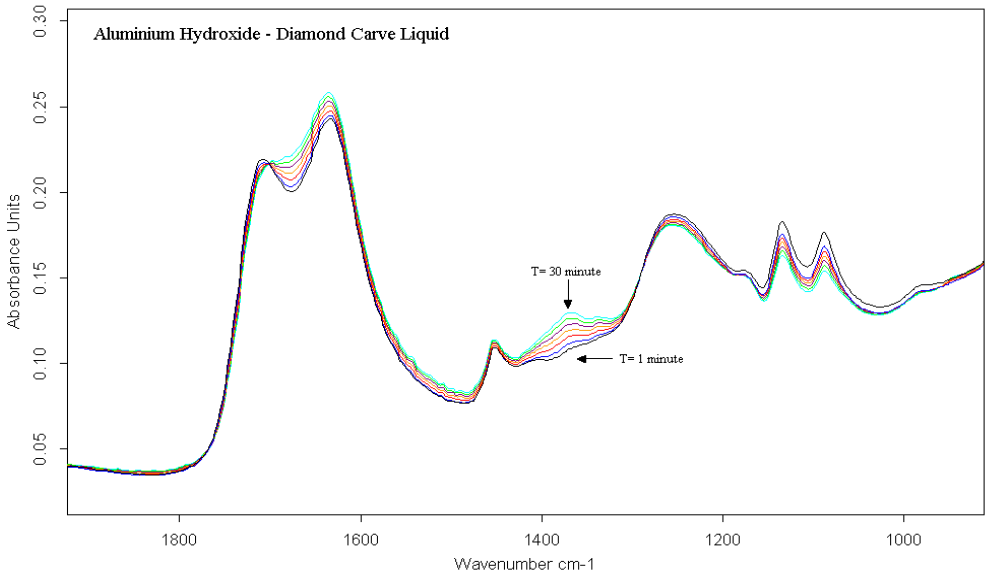

Figure A 55: Reaction between Aluminium Hydroxide and Diamond Carve Liquid

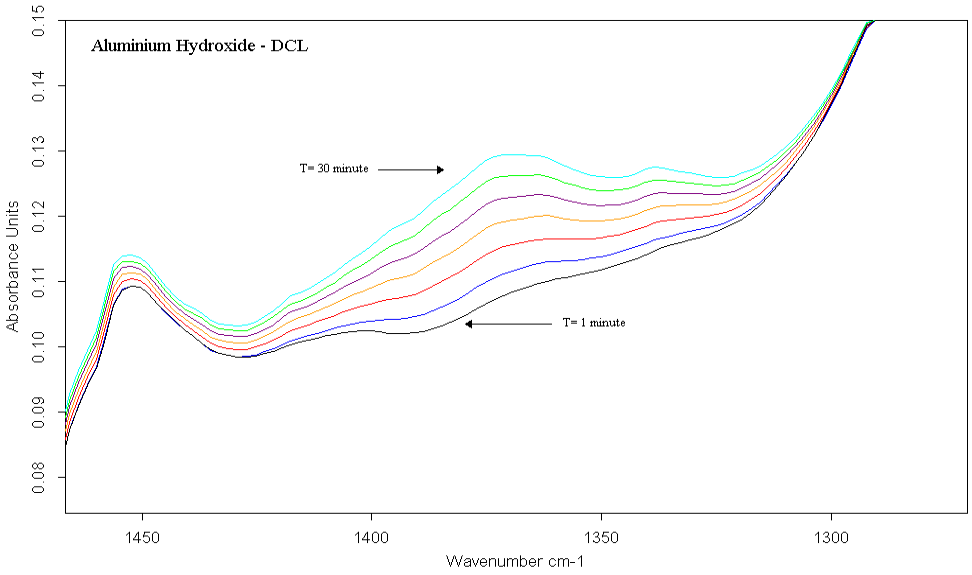

Figure A 56: Zoomed View between 1300-1450 cm^{-1} from the Reaction between $Al(OH)_3$ and DCL

3.5 Aluminosilicate Glass Cements

The aluminosilicate glass used in DC contains Na^{+}, Ca^{2+}, Sr^{2+}, Al^{3+} and Si^{4+} (*see* chapter 3) all possible of complexing with the polyelectrolyte's used in DCL. The cation percentage of sodium and calcium are relatively low compared to strontium, aluminium and silicon. Any absorption from Na^{+} and Ca^{2+} will be masked by the absorptions from the higher concentration cations.

3.5.1 Polyacrylic Acid Cement

The reaction between ASG and PAA produces similar results to that seen when PAA was mixed with $Al(OH)_3$ (Figure A 57). The increased intensity of the shoulder on the dominant water bend at 1632 cm^{-1} has been assigned to Al-PAA at 1559 cm^{-1} and Sr-PAA at 1550 cm^{-1}. The reaction between PAA and ASG was so slow that barely any progress was seen over 30 minutes.

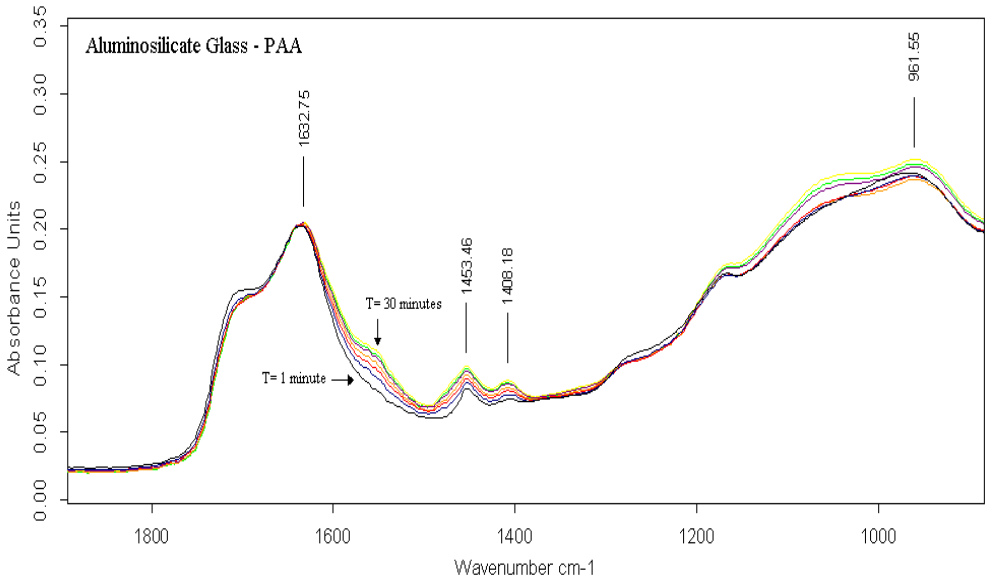

Figure A 57: Aluminosilicate Glass Reacting with PAA

3.5.2 Tartaric Acid Cement

The relative reactivity of TA towards Sr/Ca and Al translates as the much quicker production of cement forming salts. The reaction reached completion within 15 minutes from the initiation of mixing. The formation of peaks at 1725 cm^{-1} from –C=O, 1643 cm^{-1} from H-O-H scissoring, 1476 cm^{-1} from the unassigned Ca-TA cements, 1385 cm^{-1} from Al-TA and 1266 cm^{-1} from –C-O disappearing as Al-TA is growing (Figure A 58). The breakdown of the ASG is also accompanied with the increase in Si-O(H) stretching vibrations at 949 cm^{-1}.

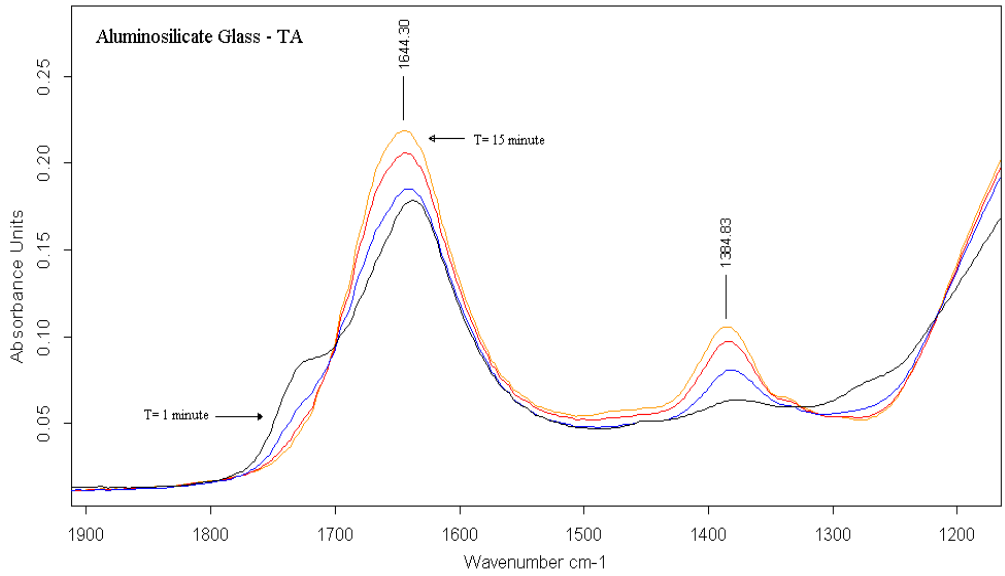

Figure A 58: Aluminosilicate Glass Reacting with Tartaric Acid

3.5.3 Diamond Carve Liquid Cement

There are multiple peaks formed in the reaction of ASG with DCL (Figure A 59). The loss of peaks in the 1500's cm^{-1} from the formation of Sr/Ca-TA, Sr/Ca-PAA and Al-TA as seen in DC cements was unexpected. The presence of the aforementioned peaks are present but in small quantities and are overlapped by the H-O-H absorption. The removal of the water peak (Figure A 60) reveals the formation of Sr/Ca-TA at 1606 cm^{-1} and the broadening of the carboxylate peak towards 1658 cm^{-1} as Al-TA is formed and –C=O is consumed. The peak at 1452 cm^{-1} remains constant throughout reaction and is assigned to the $–CH_2$ vibration of PAA. The peaks at 1378 cm^{-1} 1242 cm^{-1} 1170 cm^{-1} 1133 cm^{-1} 1063 cm^{-1} 945 cm^{-1} have been assigned to Al-TA, $-CH_2$ (PAA) overlapped by Sr/Ca-TA, -C-O from PAA, asym -C-O(H) from TA, sym –C-O, Si-O-Si respectively.

The presence of additional TA, PAA and PVPA-PAA contained within the DC powder must help the degradation of the ASG therefore accelerate the formation of cement forming salts.

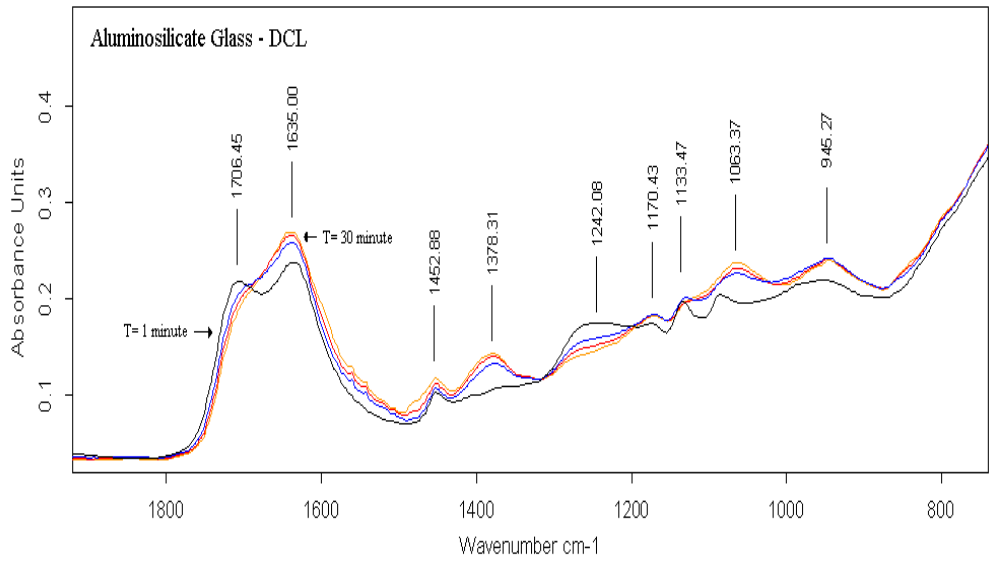

Figure A 59: Zoomed Section of the Fingerprint Region of the Reaction Progress of ASG and DCL over a 30 Minute Period

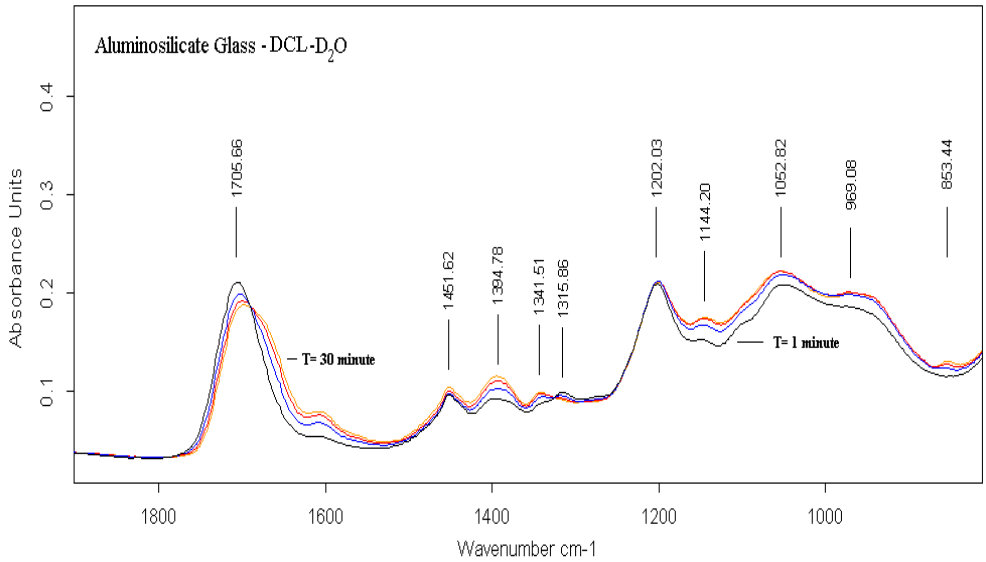

Figure A 60: Zoomed Section of the Fingerprint Region of the Reaction Progress of ASG and Deuterated DCL over a 30 Minute Period

Appendix 4

Theoretical Modelling

4.1 Theory (unit cell)

Crystalline materials such as metals and ceramics are made up of a repetitive structure called a crystal lattice. The smallest divisible unit that possesses the symmetry and properties of the entire crystal lattice when stacked together in three dimensions is called the unit cell.

The atoms in the unit cell may be at the corners, on the edges, on the faces, or wholly enclosed in the box, and each cell in the crystal is identical.

There are three general unit cells that can be used to describe most crystalline structures (i) Body Centred Cubic (BCC) (**Error! Reference source not found.**), (ii) Face Centred Cubic (FCC) (Figure A 62(iii) Hexagonal Close Packed (HCP) (Figure A 63).

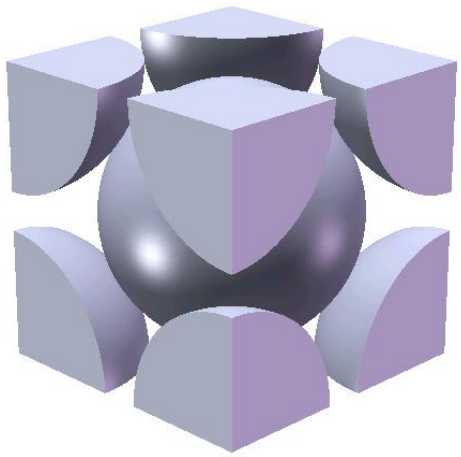

Figure A 61: Body Centred Cubic Unit Cell (BCC)

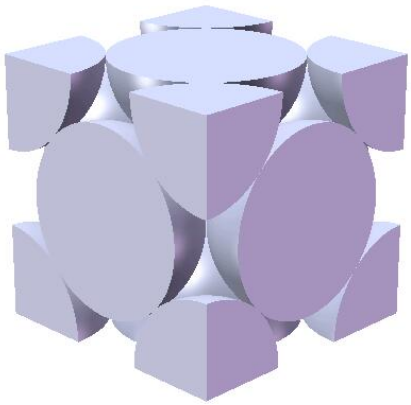

Figure A 62: Face Centred Cubic Unit Cell (FCC)

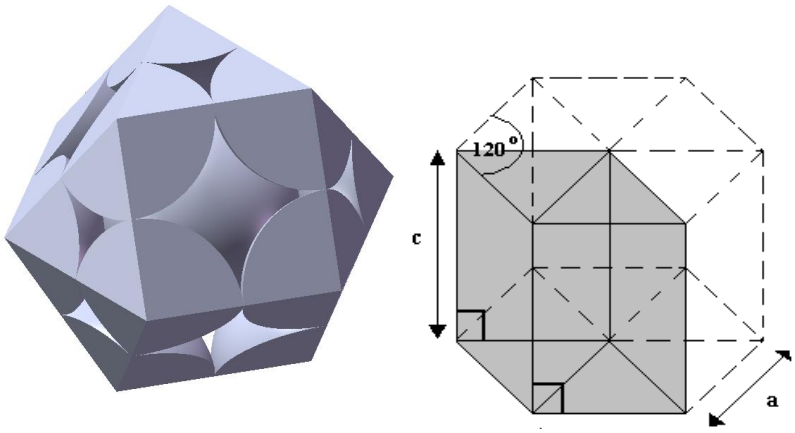

Figure A 63: Hexagonal Close Packed Unit Cell (HPC)

The unit cell dimensions, particle size, volume and void space are all related and can be calculated when the base materials (**Solvent**) particle size is known.

4.1.1 Unit Cell Dimensions

The first assumptions made before starting this investigation is that the solvent particles size will remain constant for individual lattices (not including simulation modelling). This simplifies the calculation for the unit cell dimensions because only the radius of one solvent atom must be considered. The cell dimensions can be calculated using;

Body Centred Cubic, $a = \frac{4r}{\sqrt{3}}$ Equation 5

Face Centred Cubic, $a = 2r\sqrt{2}$ Equation 6

Hexagonal Close Packed, $a = 2r$ Equation 7.1

$c = 4r\sqrt{\frac{2}{3}}$ Equation 7.2

HCP has two lattice constants (Figure A 63) because a = b ≠ c unlike BCC and FCC where a = b = c.

4.1.2 Unit Cell Volume and Void Volume

The dimensions of the unit cell can be calculated using equations 1-3 dependent on the type of lattice under investigation. If the size of the solvent particle is known then the volume of the spheres in the unit cell can be calculated using equation 4.

$$\text{Volume} = \frac{4}{3}\pi r^3 = \frac{1}{6}\pi d^3 \qquad \text{Equation 8}$$

where ***r*** and ***d*** are radius and diameter respectively.

The different unit cells contain different numbers of complete spheres; BCC has 2 complete spheres, HCP has 3 complete spheres and FCC has 4 complete spheres.

The volume of the unit cell is calculated;

$$V_{BCC} = \left(\frac{4r}{\sqrt{3}}\right)^3 = \frac{64r^3}{\sqrt{27}} \qquad \text{Equation 9}$$

$$V_{FCC} = \left(2r\sqrt{2}\right)^3 = 16r^3\sqrt{2} \qquad \text{Equation 10}$$

$$V_{HPC} = \left(6\sqrt{3}r^2\right)\left(2\left(2r\sqrt{\frac{2}{3}}\right)\right) \qquad \text{Equation 11}$$

Once the volume of the unit cell is known and the volume of the spheres in the unit cell has been calculated then the void volume is calculated by:

$$\text{Void Volume } (V_v) = \text{Unit Cell Volume - Sphere Volume} \qquad \text{Equation 12}$$

4.2 Idealised Conditions

Idealised calculations were performed assuming the highest possible packing density for the unit cell. The packing factor can be described as:

$$\text{PF} = \frac{\text{Volume of Spheres in Unit Cell}}{\text{Volume of Unit Cell}} \qquad \text{Equation 13}$$

Unit cells differ in appearance but the number of spheres and size of the cells differ only slightly providing optimal packing is applied. The highest possible packing factor is 0.74 (William & Callister, 2000) which is achieved in the FCC and HCP lattice structure. The BCC lattice structure has a packing factor of 0.68.

4.2.1 Interstitial Gaps

An interstitial gap is a void that remains in the unit cell because the particles are unable to fill the space.

There are two different types of interstitial gaps that are present in the unit cells under investigation which can be seen in Figure A 64, Figure A 65 and Figure A 66.

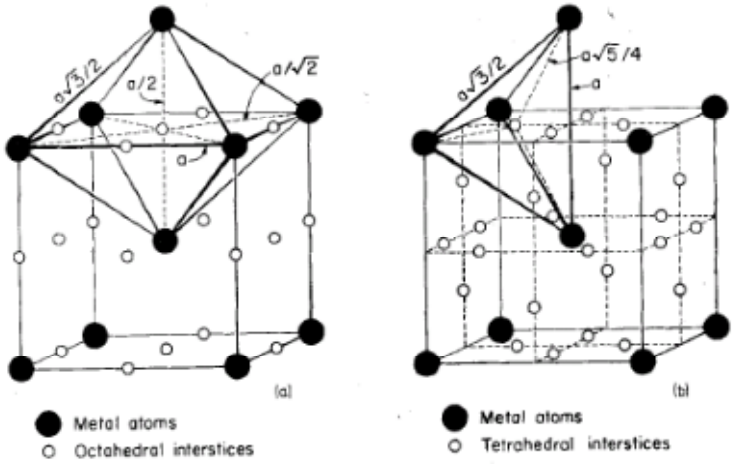

Figure A 64: Interstitial holes in the BCC structure, (a) Octahedral holes at face centres and cell edges. (b) Tetrahedral holes on cell faces.

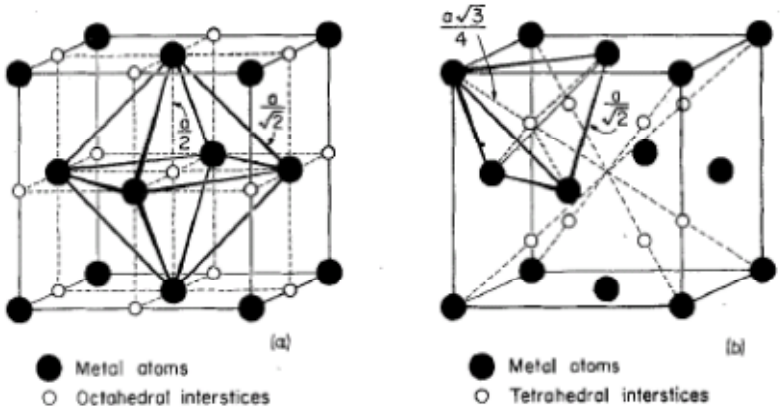

Figure A 65: Interstitial holes in the FCC structure, (a) Octahedral holes at body centre and mid-points of cell edges. (b) Tetrahedral holes on body diagonals.

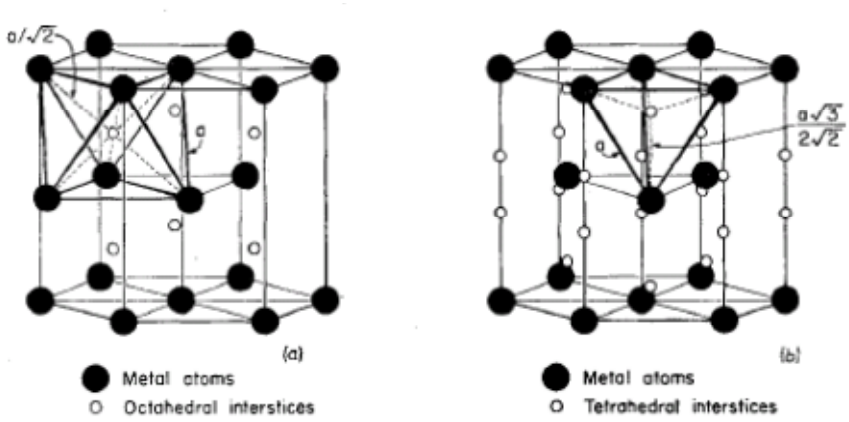

Figure A 66: Interstitial holes in the HCP structure, (a) Octahedral holes within the cell. (b) Tetrahedral holes along cell edges.

4.2.2 Spherical Interstices

The radius of the largest spherical particle that can fit into these interstitial gaps can be calculated using,

$$R_O = S_O - R_A \text{ or } R_T = S_T - R_A \qquad \text{Equation 14}$$

where R_O or R_T are the radius of the largest particle that can fit in the interstitial gap in either an octahedral or tetrahedral position. S_O or S_T is the distance to the centre of the nearest solvent atom in either the octahedral or tetrahedral neighbouring position. R_A is the radius of the solvent atom.

The lattice constants can be calculated using equation(s) 5 – 7 and then the size of the interstices can be calculated using Table A 12 and equation 14.

Relationships for Interstices Calculations

BCC	FCC	HCP
$R_A = a \times \frac{\sqrt{3}}{4}$	$R_A = \frac{\sqrt{2}}{4}$	$R_A = a \times \frac{1}{2}$

$S_{O1} = a \times \frac{1}{2}$ or $S_{O2} = a \times \frac{\sqrt{2}}{2}$	$S_O = a \times \frac{1}{2}$	$S_O = a \times \frac{\sqrt{2}}{2}$	
$R_{O1} = 0.067a$ or $R_{O2} = 0.274a$	$R_O = 0.1464a$	$R_O = 0.207a$	
$S_T = a \times \frac{\sqrt{5}}{4}$	$S_T = a \times \frac{\sqrt{3}}{4}$	$S_T = a\frac{\sqrt{3}}{\sqrt{8}}$	
$R_T = 0.126a$	$R_T = 0.0794a$	$R_T = 0.1124a$	

Table A 12: Relationships for Interstices Calculations (King, 1971)

In the BCC structure, the octahedral interstices are irregular and two different sized particles can be accommodated (R_{O1} & R_{O2}).

4.2.3 Non-spherical Interstices

In order to understand what the most effective shape filler to add to the control GIC so as the interstices have the lowest void volume attainable and highest surface / area ratio shapes other than spherical must be considered.

Triangular, square and cylindrical rods can be located into the interstitial gaps in the glass lattice and using the assumption that TiO_2 particles will tend to group together and act as a bulk material the most favourable shape can be determined.

4.2.3.1 Body Centred Cubic

The maximum size of the shaped filler materials in a BCC lattice (Figure A 67, Figure A 68, Figure A 69) can be found below from Tables A13, A14, A15 :

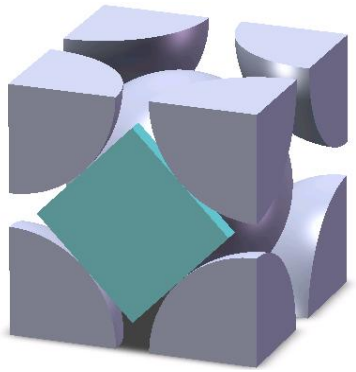

Figure A 67: Square Plate Interstitial Particle in a BCC Lattice

Height	Width	Depth
$\left(\sqrt{\frac{32}{3}}r\right)-2r$	$\left(\sqrt{\frac{32}{3}}r\right)-2r$	$\frac{2r}{\sqrt{3}}-r$

Table A 13: Square Plate Interstitial Gap Geometries in a BCC Lattice

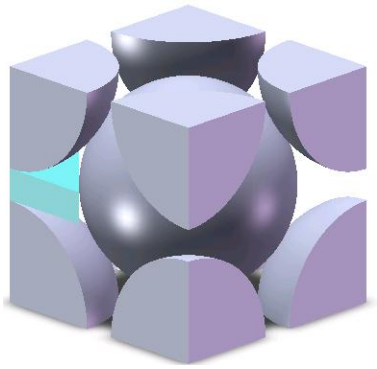

Figure A 68: Triangular Section of a Square Plate Interstitial Particle in a BCC Lattice

Vertical Height	Hypotenuse Length	Distance to centre particle
$\frac{4r}{\sqrt{3}}-2r$	$\left(\sqrt{\frac{32}{3}}r\right)-2r$	$\sqrt{2}\frac{2r}{\sqrt{3}}-r$

Table A 14: Triangular Section Gap Geometries in a BCC Lattice

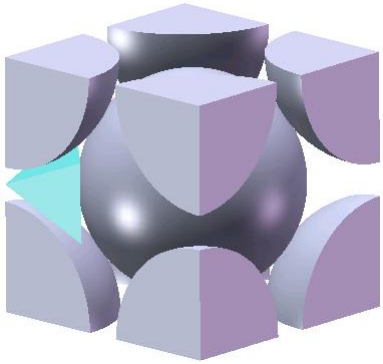

Figure A 69: Triangular Bar Interstitial Particle in a BCC Lattice

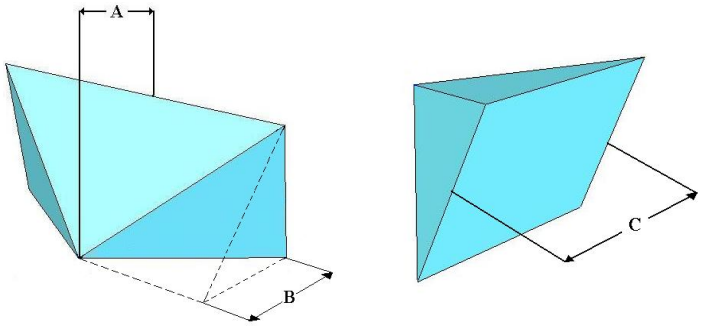

Figure A 70: Triangular Bar Interstitial Geometries in a BCC Lattice

Depth (A)	Equilateral Side (B)	Horizontal Length (C)
$\sqrt{2}\frac{2r}{\sqrt{3}} - r$	$\frac{2\left[\sqrt{2}\frac{2r}{\sqrt{3}} - r\right]}{\sqrt{3}}$	$\left(\sqrt{\frac{32}{3}}r\right) - 2r$

Table A 15: Triangular Bar Interstitial Geometries in a BCC Lattice

4.2.4 Face Centred Cubic and Hexagonal Closed Packed

FCC and HCP lattices have interstitial spacing's that have been called internal and external based on their position within the unit cell. If the cells were segmented differently than there would be no internal or external designation, therefore these terms are for illustrating the position and geometry of the equations given.

4.2.4.1 Internal Spacing

Internal spaces in the FCC unit cell are capable of accomodating a cubic filler (Figure A 72) and a triangular rod (Figure A 73). The size of these filler particles can be calculated from the radius of the solvent aprticles using Tables A16 and A17.

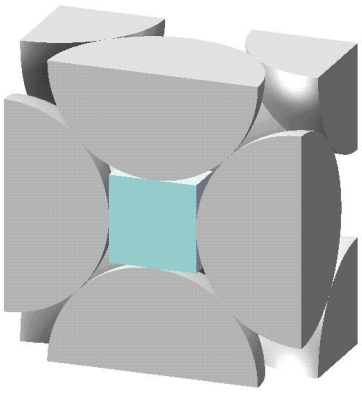

Figure A 71: Internal Interstices of an FCC Lattice Filled With a Square Block

Cube Dimensions
$2r\left(\sqrt{2}-1\right)$

Table A 16: Internal Geometries in an FCC Lattice

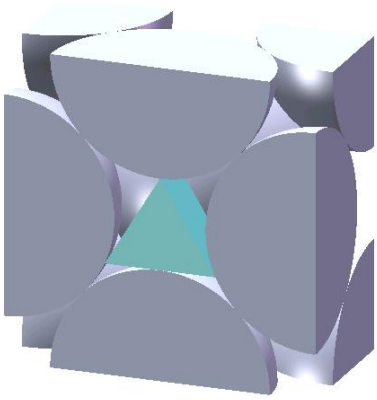

Figure A 72: Internal Interstices of an FCC Lattice Filled With a Triangular Rod

Height	Width (Base)	Depth

$$2r\left(\sqrt{2}-1\right) \quad 2\left[r\sqrt{2}-\sqrt{r^2-r\left(\sqrt{2}-1\right)^2}\right] \quad 2r\left(\sqrt{2}-1\right)$$

Table A 17: Internal Geometries in an FCC Lattice Filled With a Triangular Rod

4.2.4.2 External Spacing

The external spaces of the unit cell shown in Figure A 74 and A75 show are able to hose square bar and triangular rod shapped filler particles respectively. It is however possible to accomodate particles four times the size of those calculated in Table A18 and A19 due toi the way unit cells are joined together.

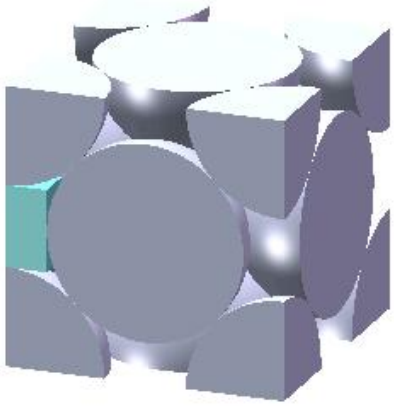

Figure A 73: External Geometry for a Square Rod Filler in a FCC Lattice

Height	Width	Depth
$r\left(\sqrt{2}-1\right)$	$r\left(\sqrt{8}-2\right)$	$r\left(\sqrt{2}-1\right)$

Table A 18: External Geometry for a Square Rod Filler in a FCC Lattice

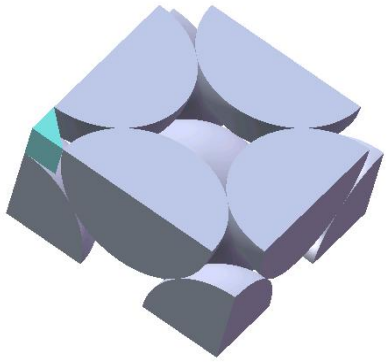

Figure A 74: FCC Lattice with a Triangular Rod Filler in an External Interstices

Height	Horizontal Length	Depth
$2r\left(\sqrt{2}-1\right)$	$\sqrt{\left(6-4\sqrt{2}\right)r^2}$	$r\left(\sqrt{2}-1\right)$

Table A 19: External Geometry for a Triangular Rod

4.2.4.3 Hexagonal Closed Packed

HCP lattices can be imagined as a FCC latice with the top layer offset by the radius of a solvent particle so it sit in the middle of the bottom row. The HCP lattice has been further broken down for ease of illustration in Figures A76, A77, A78 and A79. The geometry of the particles housed in these figures can be calculated using Tables A20, A21, A22 and A23.

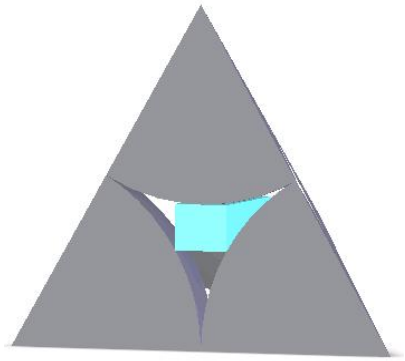

Figure A 75: Hexagonal Closed Packed Interstitial Geometry for a Square Rod

Width (Base)	Height	Depth
$2r - r\sqrt{3}$	$\frac{\sqrt{3}}{2}\left(2r - r\sqrt{3}\right)$	$\sqrt{2}\frac{2r}{\sqrt{3}} - r$

Table A 20: Hexagonal Closed Packed Interstitial Geometry for a Square Rod

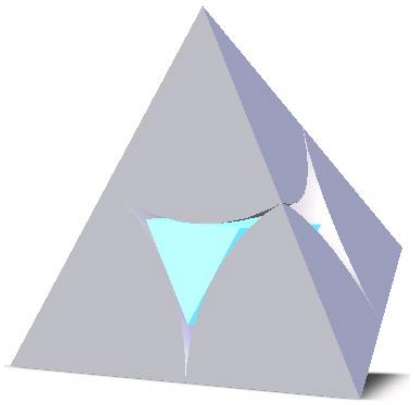

Figure A 76: Hexagonal Closed Packed Interstitial Geometries for a Triangular Bar

Width (Equilateral)	Depth
$4r - 2r\sqrt{3}$	$\sqrt{2}\frac{2r}{\sqrt{3}} - r$

Table A 21: Hexagonal Closed Packed Interstitial Geometries for a Triangular Bar

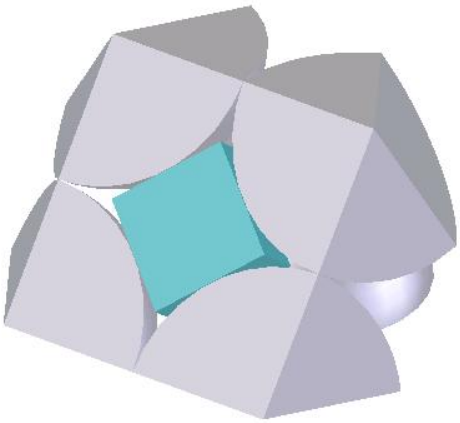

Figure A 77: Hexagonal Closed Packed Lattice Geometry for a Square Bar

Side Length(s)	Depth
$2r\left(\sqrt{2}-1\right)$	$r\left(\sqrt{2}-1\right)$

Table A 22: Hexagonal Closed Packed Lattice Geometry for a Square Bar

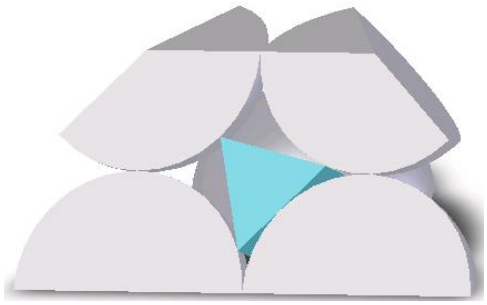

Figure A 78: Internal Geometries in an HCP Lattice Filled with a Triangular Rod

Height	Width (Base)	Depth
$2r\left(\sqrt{2}-1\right)$	$2\left[r\sqrt{2}-\sqrt{r^2-r\left(\sqrt{2}-1\right)^2}\right]$	$r\left(\sqrt{2}-1\right)$

Table A 23: Internal Geometries in an HCP Lattice Filled with a Triangular Rod

4.3 Surface Area

It is well known that the surface area of the glass particles used with GICs is one of the rate controlling variables. The surface coating on the titanium dioxide base materials is predicted to enhance the acid – base reaction within the GIC therefore; the surface area of the coating may be used as a method to control the reactivity of the GIC hybrid.
The surface coating is not uniformly layered over the entire base particle as previous experiments using SEM and TEM have indicated (Figure A 80).

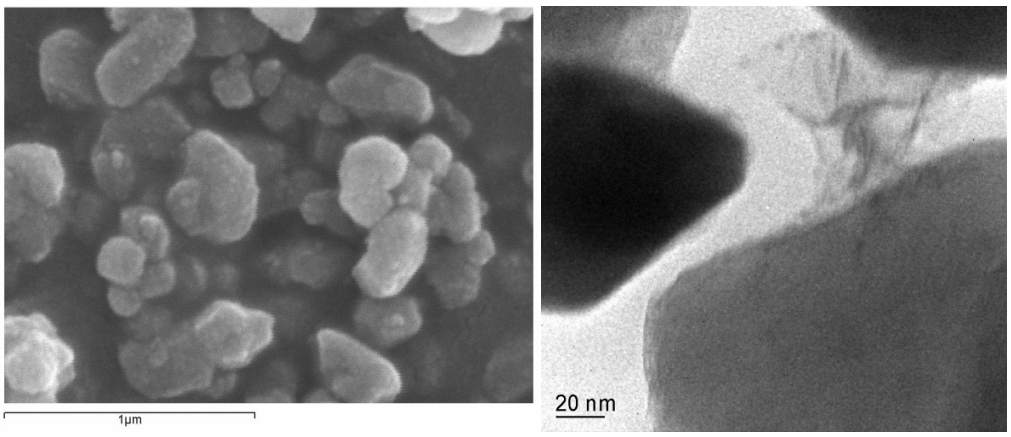

Figure A 79: SEM (left) and TEM (right) images of $Al(OH)_3$ coated TiO_2

There is a mixture between small droplets of coating on the surface of the base particle and totally coated base particles. Reaction kinetics dictate that the contact area (surface area) will affect the reaction rate therefore a full understanding of how the surface area changes with changing morphology is needed.

Two assumptions have been made, (i) the coating will cover the entire base particle or (ii) go on as small hemispherical droplets; these droplets never come within one radii distance of each other, otherwise the surface tension / surface interaction will cause the $Al(OH)_3$ to merge into a single coating.

The volume of the coating remained constant (9% w/w) throughout experimentation therefore if the number of coating droplets increased, the diameter of the hemispheres become smaller to keep the volume constant.

The size of the coated TiO_2 particle is known so the surface area and volume can be calculated using equations 15 and 16.

The mass of TiO_2 can be calculated given that the bulk density TiO_2 is 4.23×10^{-12} gμm^{-3}.

Once the mass of the TiO_2 base particle is known the mass and volume of the $Al(OH)_3$ coating can be calculated given that the density of $Al(OH)_3$ is 2.42×10^{-12} gμm^{-3}.

$$\text{Volume of a Sphere} = \frac{4}{3}\pi r^3 = \frac{1}{6}\pi d^3 \qquad \text{Equation 15}$$

$$\text{Surface Area of a Sphere} = 4\pi r^2 \qquad \text{Equation 16}$$

The limiting number of coating hemispheres that can fit on the surface of the TiO_2 particle can be calculated using the surface area of the base of the coating hemisphere. The surface area of the coating hemispheres base can be calculated using equation 19 although the diameter of the hemisphere needs to be calculated first using equations 17 & 18.
To calculate the surface area of the coating droplets equation 20 can be used;

$$\text{Diameter of Sphere } (d) = \sqrt[3]{\frac{6V}{\pi}} \qquad \text{Equation 17}$$

$$\text{Diameter of Hemisphere } (d_{Hemi}) = \sqrt[3]{2d^3} \qquad \text{Equation 18}$$

$$\text{Area of Base of Hemisphere } (A_{Base}) = \frac{\pi d^2{}_{Hemi}}{4} \times N^O Hemi \qquad \text{Equation 19}$$

$$\text{Surface Area of Hemisphere } (A_{Hemi}) = \frac{\pi d^2{}_{Hemi}}{2} \times N^O Hemi \qquad \text{Equation 20}$$

Once the surface area of the individual particles has been calculated the surface area of the total 'bulk' filler content needs to be considered. Due to the size of TiO_2 being used there will be a high surface energy therefore dry or suspended TiO_2 will tend to agglomerate into a structure representative of a larger particle (Figure A 81).

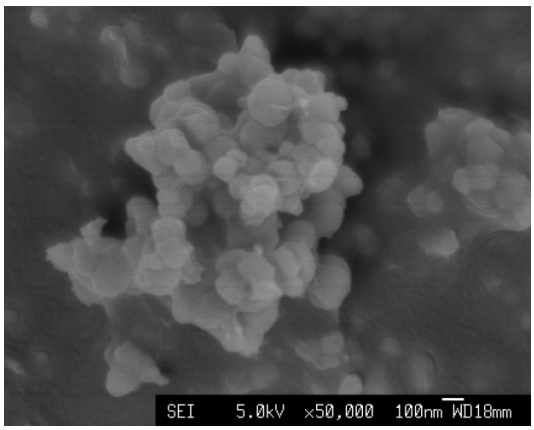

Figure A 80: Agglomerated TiO_2 Filler Particles (Coated)

4.4 Packing Algorithm

4.4.1 Dynamics Drop Pack

In Dynamics Drop pack mode, when an object is placed into the box, it "drops" along the given axis and stops only when it comes to rest balanced on other objects and/or a boundary wall. Therefore this mode can be used to model systems in which the objects are subject to gravity or some other such force along an axis.

One object is dropped at a time and this object is the only moving object in the simulation. Therefore the collisions between the dropped object and other objects result only in a change in velocity to the dropped object (not of the rest of the system), and when the object comes to rest it is fixed in position.

4.4.2 The Monte-Carlo Simulation

For each Monte Carlo step an object is selected at random, and then it is moved in a random direction by a random distance between zero and a value DRMax (the maximum starting distance that an object may be moved in the box). Non-spherical objects are also randomly rotated, by plus or minus 22.5 degree. The move is rejected if there are collisions with other objects. It is accepted if the potential energy decreases, i.e. the particle's centre of mass moves in the direction of the force, down the axis

In Monte Carlo (MC) Shake pack mode the objects already packed are "shaken" during the packing process using a Monte Carlo algorithm. In a similar fashion to Dynamics Drop mode, a force (e.g. gravity) can be applied along an axis in the box. This mode can be used for all shape types.

The Monte Carlo Shake pack mode will result in higher packing fractions than the Static pack mode. If a "shake" occurs along an axis, objects will settle down along that axis. If a random axis is used then gaps between objects will be opened thereby allowing more objects to be packed into the box.
As well as randomly moving previously packed objects, non-spherical particles are randomly rotated. Therefore this mode can be used to model systems where non-spherical objects are subject to gravity or some other such force along an axis, and it should be used rather than Dynamics Drop mode for such systems.

4.4.3 Overlap Minimization Pack

The Overlap Minimization pack mode differs fundamentally from the other modes of packing. It aims to find the maximum packing fraction for the given number of objects that you add to the box. In this mode the target number of objects is always packed even if this leads to objects overlapping one another.

The overlap minimization routine runs over a given number of loops, where a loop is the process of moving the objects around in the box and scaling their size to reduce overlaps to zero.

To obtain random close packing of spheres you should use populations bigger than 50. Even then, results may depend on the size of the box compared to the population size.

4.5 Boundary Conditions

Lower and Upper values - are required when there are two opposing walls – for example, the Lower value might apply to the bottom, and the Upper value to the top, or the Lower value might apply to the left-hand boundary while the Upper value corresponds to the right-hand boundary opposing it.

Hard boundary - the whole of the object must lie within the container.

Soft boundary - objects can cross the boundary as long as the centre of mass of the object lies inside the container

Periodic boundary conditions - allow particles to cross the container wall, but the portion of the particle which leaves the container re-enters from the other side of that container. For this reason it is necessary that periodic conditions be specified on both opposing walls. You cannot have a periodic boundary condition along an axis in which gravity is being applied, either in Dynamics Drop or in MC Shake pack modes.
Periodic boundary conditions can be used to represent packing in the bulk of a system where wall effects can be neglected.

A range of population sizes, simulation algorithms and boundary conditions were tried and the individual method is reported with the data set.

4.5.1 Boundary Conditions

In order to understand the effects that the packing algorithms and boundary conditions will have on the final packing density a series of simulations were run to highlight differences. Table A24 shows the number of packed particles and the packing fraction achieved when a thousand shperical particles with a diameter of twenty were attempted to be packed into a $10{,}000^3$ cell.

Packing Algorithm	Boundary Condition			
	Hard		Periodic	
	Number Packed	Packing Fraction	Number Packed	Packing Fraction
DDP	875±6.01	$0.535 \pm 3.68 \times 10^{-3}$	933±6.81	$0.570 \pm 4.16 \times 10^{-3}$
MCSP	873±2.31	$0.533 \pm 1.41 \times 10^{-3}$	937±2.52	$0.572 \pm 1.54 \times 10^{-3}$
OMP	1000±0.00	$0.565 \pm 6.46 \times 10^{-3}$	1000±0.00	$0.634 \pm 2.75 \times 10^{-3}$

Table A 24: Comparison between Hard and Periodic Boundary Conditions and the Affect had on the Subsequent Packing Fraction

Table A 24 shows that there can be a difference of up to 16% when comparing packing algorithms and boundary conditions. There is a difference of between 6% – 11% when comparing the boundary conditions alone.

Different number fractions and sized particles have been packed using the DDP, MCSP and OMP simulations to calculate an average packing density for a single particle system under the influence of gravity.

4.6.4.1 Dynamic Drop

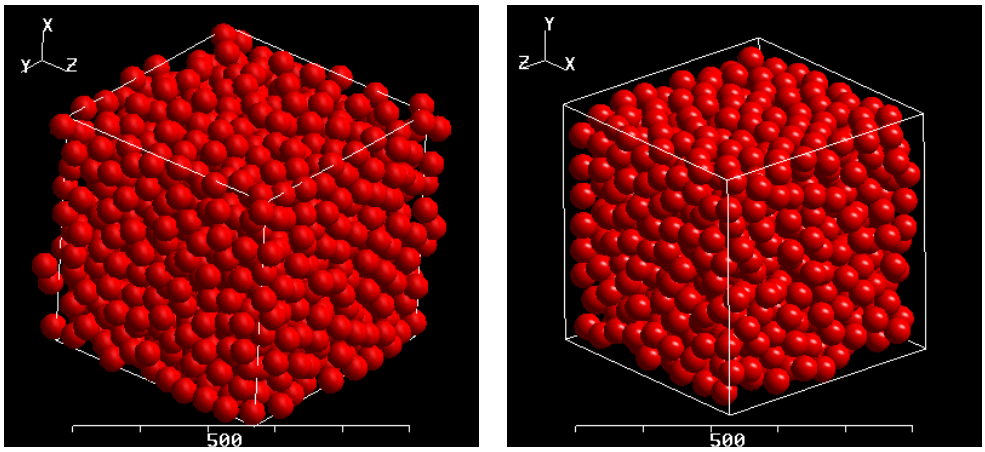

Figure A 81: Dynamics Drop Packing of 1000 Spherical Particles.
(Left) Hard Boundary Conditions (Right) Periodic Boundary Conditions

The use of periodic boundary conditions accurately represents the bulk packing achieved by the spheres assuming that the cell is representative of a small section of a much larger quantity of particles.

4.6.4.2 Monte Carlo Shake Simulation

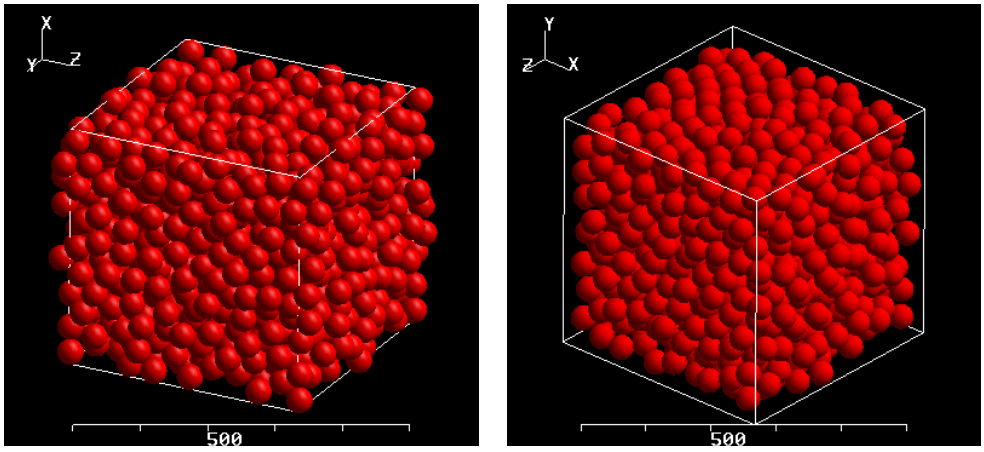

Figure A 83: Monte Carlo Shake Simulation of 1000 Spherical Particles.
(Left) Periodic Boundary Conditions (Right) Hard Boundary Conditions

The hard boundary conditions introduce excess space around the edges of the cell as can be seen in Figure A81 and A83.

4.6.4.3 Overlap Minimisation Packing

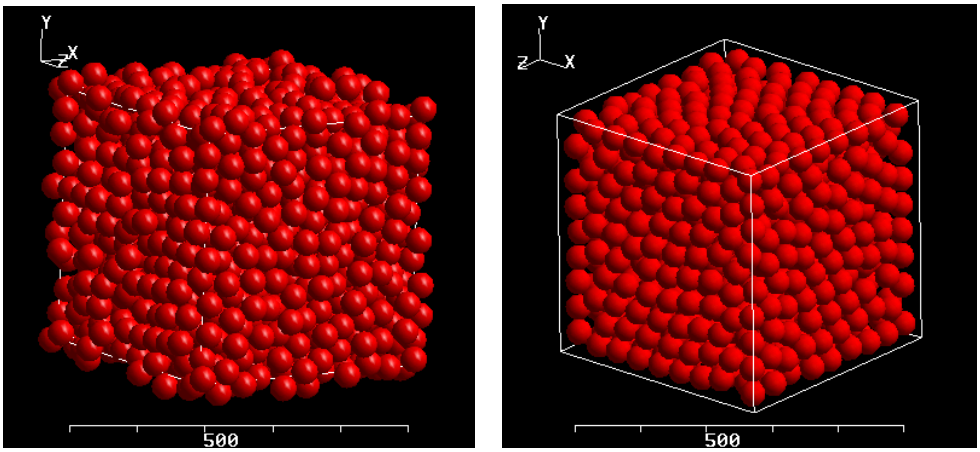

Figure A 84: Overlap Minimisation Simulation of 1000 Spherical Particles.

The excess space around the boundaries will also be present in real situations but the affect on the packing fraction will not be as pronounced. This is due to the wall effects being reduced in large cells when the particle size(s) remain constant.
Figure A 84 indicates that the OMP produces a more uniform lattice when compared to DDP (Figure A 81) and MCSP (Figure A 83) therefore may not be an accurate representation of a real system subjected to just gravitational forces.

The simulations have shown that for a powder with a single particle size the packing density will not reach greater than 63% and will, on average, be around 57%.

4.6 Particle and Cell Constants for Aluminosilicate Glass Packing

The calculation of the cell dimensions, volume and void volume are presented as these are the base calculations for filler incorporation (Table A 25).

Lattice Structure	Particle Size (μm)	Cell Dimensions (μm)	Cell Volume (μm^3)	Void Volume (μm^3)
BCC	40	*a* - 46.19	9.85×10^4	3.15×10^4
	35	*a* - 40.41	6.60×10^4	2.11×10^4
	30	*a* - 34.64	4.16×10^4	1.33×10^4
FCC	40	*a* - 56.57	1.81×10^5	4.70×10^4
	35	*a* - 49.50	1.21×10^5	3.15×10^4
	30	*a* - 42.43	7.64×10^4	1.98×10^4
HCP	40	*a* - 40 *c* - 65.32	1.36×10^4	3.53×10^4
	35	*a* - 35 *c* - 57.15	9.10×10^4	2.37×10^4
	30	*a* - 30 *c* - 48.99	5.73×10^4	1.49×10^4

Table A 25: Cell Dimensions, Volume and Void Volume for BCC, FCC and HCP Unit Cells

4.6.1 Spherical Filler Particle Size

BCC Interstitial Gap Radii			
ALG Particle Size (μm)	**Radius Octahedral (1) (μm)**	**Radius Octahedral (2) (μm)**	**Radius Tetrahedral (μm)**
30	3.094	12.660	4.220
35	2.707	11.077	3.693
40	2.321	9.495	3.165

Table A 26: Maximum Radius of the Interstitial Particle Capable of Fitting into a BCC Lattice

FCC and HCP Interstitial Gap Radii		
ALG Particle Size (µm)	**Radius Octahedral (µm)**	**Radius Tetrahedral (µm)**
30	8.284	4.495
35	7.249	3.933
40	6.213	3.371

Table A 27: Maximum Interstitial Particle Capable of Fitting into a FCC or HCP Lattice with the given radius (R_A)

4.6.2 Shaped Filler Particles

4.6.2.1 Body Centred Cubic Lattice

BCC Plate			
ALG Particle Size (µm)	**Dimensions**		
	Height (µm)	**Width (µm)**	**Depth (µm)**
30	37.980		4.641
35	44.310		5.415
40	50.639		6.188

Table A 28: Dimensions of Plate Shaped Interstitial Particles Capable of Fitting into A BCC Lattice

BCC Cubic			
ALG Particle Size (µm)	Dimensions		
	Vertical Height (µm)	Hypotenuse Length (µm)	Distance to centre particle (µm)
30	9.282	37.980	18.990
35	10.829	44.310	22.155
40	12.376	50.639	25.320

Table A 29: Dimensions of Cubic Shaped Interstitial Particles Capable of Fitting into A BCC Lattice

BCC Triangle			
ASG Particle Size (µm)	Dimensions		
	Depth (A)	Equilateral Side (B)	Horizontal Length (C)
30	18.990	21.928	37.980
35	22.155	25.582	44.310
40	25.320	29.237	50.639

Table A 30: Dimensions of Triangular Shaped Interstitial Particles Capable of Fitting into A BCC Lattice

4.6.2.2 Face Centred Cubic Lattice

FCC Cube (Internal)			
ASG Particle Size (µm)	Dimensions		
	Height (µm)	Width (µm)	Depth (µm)
30	24.853		
35	28.995		
40	33.137		

Table A 31: Dimensions of Internal Cubic Shaped Interstitial Particles Capable of Fitting into a FCC Lattice

FCC Cube (External)			
ASG Particle Size (µm)	**Dimensions**		
	Height (µm)	**Width (µm)**	**Depth (µm)**
30	12.426	24.853	12.426
35	14.497	28.995	14.497
40	16.569	33.137	16.569

Table A 32: Dimensions of External Cubic Shaped Interstitial Particles Capable of Fitting into a FCC Lattice

FCC Triangle (Internal)			
ASG Particle Size (µm)	**Dimensions**		
	Height (µm)	**Width (Base) (µm)**	**Depth (µm)**
30	24.853	30.242	24.853
35	28.995	35.282	28.995
40	33.137	40.323	33.137

Table A 33: Dimensions of Internal Triangular Shaped Interstitial Particles Capable of Fitting into a FCC Lattice

FCC Triangle (External)			
ASG Particle Size (µm)	**Dimensions**		
	Height (µm)	**Width (Base) (µm)**	**Depth (µm)**
30	24.853	17.574	12.426
35	28.995	20.503	14.497
40	33.137	23.431	16.569

Table A 34: Dimensions of External Triangular Shaped Interstitial Particles Capable of Fitting into a FCC Lattice

4.6.2.3 Hexagonal Closed Packed Lattice

HCP Cube (Small)			
ASG Particle Size (µm)	**Dimensions**		
	Height (µm)	**Width (µm)**	**Depth (µm)**
30	8.038	6.962	6.563
35	9.378	8.122	7.657
40	10.718	9.282	8.751

Table A 35: Dimensions of Small Cubic Shaped Interstitial Particles Capable of Fitting into a HCP Lattice

HCP Cube (Big)			
ASG Particle Size (µm)	**Dimensions**		
	Height (µm)	**Width (µm)**	**Depth (µm)**
30	24.853		12.426
35	28.995		14.497
40	33.137		16.569

Table A 36: Dimensions of Large Cubic Shaped Interstitial Particles Capable of Fitting into a HCP Lattice

HCP Triangular Rod (Small)		
ASG Particle Size (µm)	**Dimensions**	
	Width (Equilateral) (µm)	**Depth (µm)**
30	16.077	6.563
35	18.756	7.657
40	21.436	8.751

Table A 37: Dimensions of Small Triangular Rod Shaped Interstitial Particles Capable of Fitting into a HCP Lattice

HCP Triangular Rod (Big)			
ASG Particle Size (µm)	**Dimensions**		
	Height (µm)	**Width (Base) (µm)**	**Depth (µm)**
30	24.853	30.242	12.426
35	28.995	35.282	14.497
40	33.137	40.323	16.569

Table A 38: Dimensions of Large Triangular Rod Shaped Interstitial Particles Capable of Fitting into a HCP Lattice

4.6.3 Size of interstitial particles

Size of Shaped Filler Particles Used in the Optimisation of Diamond Carve Glass Ionomer									
Size of Filler Particle	Plate			Cube			Triangle		
	Height (µm)	Width (µm)	Depth (µm)	Height (µm)	Width (µm)	Depth (µm)	Thickness (µm)	Bottom Length (µm)	Height (µm)
1	63.29	63.29	15.47	41.42	41.42	41.42	15.47	63.29	31.65
2	56.96	56.96	13.92	37.27	37.27	37.27	13.92	56.96	28.48
3	50.63	50.63	12.37	33.13	33.13	33.13	12.37	50.63	25.32
4	44.31	44.31	10.82	28.99	28.99	28.99	10.82	44.31	22.15
5	37.98	37.98	9.28	24.85	24.85	24.85	9.28	37.98	18.99
6	31.65	31.65	7.73	20.71	20.71	20.71	7.73	31.65	15.82
7	25.32	25.32	6.18	16.56	16.56	16.56	6.18	25.32	12.66
8	18.99	18.99	4.64	12.42	12.42	12.42	4.64	18.99	9.49

Table A 39: Dimensions of Shaped Filler Particles used throughout Optimisation

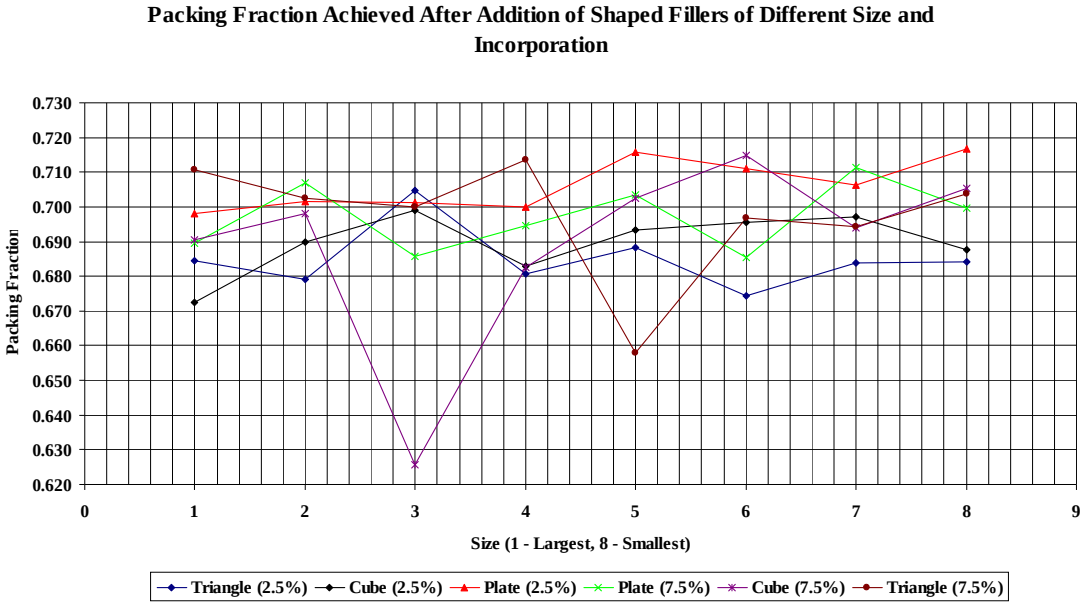

Figure A 85: Packing Fraction Achieved After Addition of Shaped Fillers of Different Size and Incorporation

4.7 Diamond Carve Control Material

The volumes of individual components (Table A 40) can be calculated for Diamond Carve which has been used as the control material.

0.2g Powder				
	Weight (g)	Density ($g/\mu m^3$)	Volume (μm^3)	Vol. (cm^3)
Aluminosilicate Glass	1.76E-01	1.70E-13	1.03E+12	1.03E+00
PAA Powder	1.79E-02	1.05E-12	1.70E+10	1.70E-02
TA Powder	4.74E-03	1.79E-12	2.65E+09	2.65E-03
PVPA Powder	1.76E-03	1.39E-12	1.26E+09	1.26E-03
Total	0.20	4.40E-12	1.05E+12	1.05E+00

0.05g Liquid				
	Weight (g)	Density ($g/\mu m^3$)	Volume (μm^3)	Vol. (ml)
PAA Powder	4.12E-02	1.05E-12	3.92E+10	3.92E-02
TA Powder	5.63E-03	1.79E-12	3.14E+09	3.14E-03
Water	3.22E-03	1.00E-12	3.22E+09	3.22E-03
Total	0.05	3.84E-12	4.55E+10	4.55E-02

Table A 40: Volume Calculations for Diamond Carve

Wilson & Nicholson (1998) have shown that the powder to liquid ratio will improve the strength of the cement as the ratio increases (i.e. greater powder incorporation). Diamond Carve has a powder to liquid ratio of 4:1 by weight. The volume ratio is however 23:1 powder to liquid which can provide an ideal of how much powder is able to mix with a relatively small quantity of liquid.

The volume of the liquid phase cannot be divided into small cells like the idealised mono-disperse ASG so the entire volume needs to be considered. This means that the unit cell calculations need to be performed and then applied to a real system.

The particle size distribution for the aluminosilicate glass used in Diamond Carve (base material) can be seen in Figure A 86.

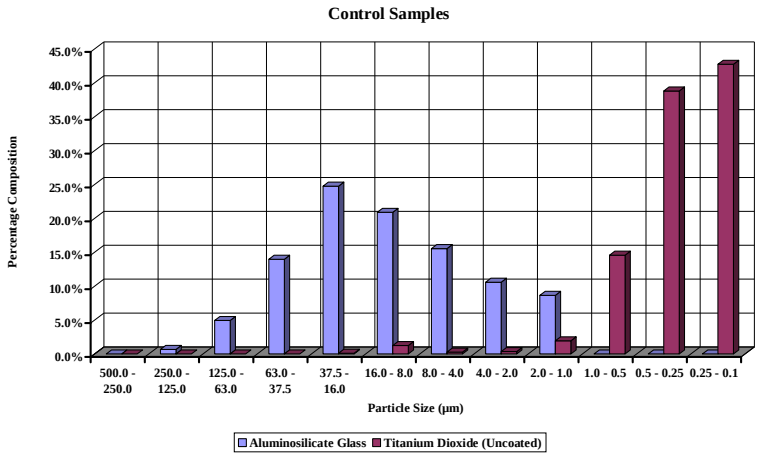

Figure A 86: Particle Size Distribution for Base Materials used in the Production of TiO_2 Incorporated GIC (TiGIC).

The mean particle size of the glass is in the range 30 - 40µm therefore, the calculations will be based on particle sizes of 30, 35 and 40µm. The TiO_2 has a mean in the range 0.10 – 0.25µm although, due to the vast difference in size between glass and filler all the TiO_2 sizes will be considered (1.00, 0.75, 0.50, 0.25 and 0.10µm) so any significant differences can be observed.

Agglomerates form because small powder particles are more mobile than larger, heavier particles. The small TiO_2 particles are therefore drawn together by attractive forces such as van der whaals forces and ionic charges which reside on the surface of individual particles; large particles do not succumb to these forces because of their weight giving them enough energy to overcome these attractive forces.